

(2)



Naval Research Laboratory

Washington, DC 20375-5000

NRL Memorandum Report 6628

AD-A221 287

DTIC FILE COPY

Physical and Computational Investigation of the Wall Pressure Fluctuations in a Channel Flow

MICHAEL P. HORNE

Laboratory for Computational Physics and Fluid Dynamics

April 26, 1990

DTIC
ELECTE
MAY 02 1990
S D D
D q

6a. NAME OF PERFORMING ORGANIZATION NAVAL RESEARCH LABORATORY			6b. OFFICE SYMBOL (If applicable) CODE 4420		7a. NAME OF MONITORING ORGANIZATION		
6c. ADDRESS (City, State, and ZIP Code) Washington, DC 20375-5000					7b. ADDRESS (City, State, and ZIP Code)		
8a. NAME OF FUNDING / SPONSORING ORGANIZATION Office of Naval Research			8b. OFFICE SYMBOL (If applicable)		9. PROCUREMENT INSTRUMENT IDENTIFICATION NUMBER		
8c. ADDRESS (City, State, and ZIP Code) Arlington, VA 22217-5000					10. SOURCE OF FUNDING NUMBERS		
			PROGRAM ELEMENT NO. 61153N		PROJECT NO.		TASK NO. RR023- 01-41
							WORK UNIT ACCESSION NO DN158-015
11. TITLE (Include Security Classification) Physical and Computational Investigation of the Wall Pressure Fluctuations in a Channel Flow							
12. PERSONAL AUTHOR(S) Horne, M. P.							
13a. TYPE OF REPORT Final		13b. TIME COVERED FROM 1/88 TO 1/90		14. DATE OF REPORT (Year, Month, Day) 1990 April 26		15. PAGE COUNT 173	
16. SUPPLEMENTARY NOTATION							
17. COSATI CODES			18. SUBJECT TERMS (Continue on reverse if necessary and identify by block number)				
FIELD	GROUP	SUB-GROUP	Noise cancellation				
			Wall pressure				
			Direct numerical simulation				
			Turbulent flow				
			Hydrodynamic flow noise				
19. ABSTRACT (Continue on reverse if necessary and identify by block number)							
<p>Wall pressure fluctuations within an equilibrium rectangular channel flow geometry were investigated. The overall objective of this investigation was to obtain experimentally for the first time, the statistical properties of the wall pressure fluctuations for a generic turbulent flow within a rectangular channel and to directly compare the results with those obtained from a full solution to the Navier-Stokes equations via Direct Numerical Simulation (DNS). For both the physical and computational experiments, serious limitations on the quality of the results were identified related to facility generated noise, transducer resolution, Reynolds number effects and constraints imposed by the computational technique.</p> <p style="text-align: right;">(Continues)</p>							
20. DISTRIBUTION / AVAILABILITY OF ABSTRACT <input checked="" type="checkbox"/> UNCLASSIFIED/UNLIMITED <input type="checkbox"/> SAME AS RPT <input type="checkbox"/> DTIC USERS					21. ABSTRACT SECURITY CLASSIFICATION UNCLASSIFIED		
22a. NAME OF RESPONSIBLE INDIVIDUAL Michael P. Horne					22b. TELEPHONE (Include Area Code) (202) 767-2352		22c. OFFICE SYMBOL Code 4420

19. ABSTRACT (Continued)

An extensive data base was obtained from the physical experiment. Profiles for the mean and fluctuation components of the streamwise velocity were obtained at a number of spanwise locations and served to establish the existence of equilibrium flow conditions over a range of Reynolds numbers. An array of flush-mounted pressure transducers was utilized to measure the two point spectral characteristics in the stream-wise direction. A unique signal processing scheme was developed and used to cancel facility generated noise which resulted in new information being recorded at low frequencies for the Reynolds numbers investigated.

Two issues of fundamental importance were examined. First, the results from both experiments were compared directly. The computational results were found to be somewhat underdeveloped for the higher order statistics for the particular data investigated. Resolution problems were shown to exist at both ends of the frequency spectrum. The computational grid spacing was insufficient to resolve the small scale structure at high frequencies and the limited size of the computational box resulted in contamination at the low end of the frequency spectrum by sensing the periodic boundary conditions as "noise" peaks. Secondly, the spectral results for rectangular channel flow were compared directly to results obtained from typical outer flow regimes as represented by flat plate boundary layers. Two fundamental results were established. Although similarity scaling was shown to exist, the turbulence structure was shown to decay approximately twice as fast as obtained in external flows. Various scaling laws were examined which were found to collapse respective spectral content separately, but no "universal" law was found to exist which brings both internal and external flow regimes into coincidence.

This investigation has provided new information not previously recorded in the literature. An extensive high quality data base was obtained for generic channel flow at low Reynolds numbers which may be used to assess the quality of typical Direct Numerical Simulation (DNS) results. A careful examination of the results will prove useful in characterizing the proper governing parameters necessary for future DNS initiatives.

TABLE OF CONTENTS

	Page
LIST OF FIGURES.....	v
LIST OF TABLES.....	vii
ACKNOWLEDGEMENTS.....	viii
NOMENCLATURE.....	ix
ABSTRACT.....	xii
 Chapter 1. INTRODUCTION	
1.1 Background.....	1
1.2 Review of Wall Pressure Studies.....	3
1.3 Theoretical Studies and Numerical Simulation	11
1.4 Objectives of Research.....	14
 Chapter 2. EQUATIONS OF TURBULENCE	
2.1 Turbulence Definitions and Corresponding Equations.....	16
2.1.1 General Equations for Turbulent Flows.....	17
2.1.2 Channel Flow.....	19
2.1.3 Higher Moments.....	20
2.2 Statistical Relationships of Turbulence	22
2.3 Macro/Micro Length and Time Scales.....	27
2.4 Relevant Measured Time-Dependent and Statistical Quantities	29
2.5 Statistical Error Definitions.....	30
 Chapter 3. DESCRIPTION OF PHYSICAL AND COMPUTATIONAL EXPERIMENTS	
3.1 Physical Experiment.....	36
3.1.1 Channel Description	36
3.1.2 Operational Characteristics	38
3.1.3 Test Section	39
3.1.4 Wall Shear Stress Measurements	40
3.1.5 Measurement and Data Acquisition of the Mean Flow and Turbulence.....	42
3.1.6 Measurement and Data Acquisition of the Wall Pressure Fluctuations	43



A-1

<div style="position: relative; height: 100px;"> <div style="position: absolute; top: 0; right: 0; width: 20px; height: 20px; border: 1px solid black; background-color: white;"></div> <div style="position: absolute; top: 20px; right: 20px; width: 20px; height: 20px; border: 1px solid black; background-color: white;"></div> <div style="position: absolute; top: 40px; right: 20px; width: 20px; height: 20px; border: 1px solid black; background-color: white;"></div> </div>	<div style="border-bottom: 1px solid black; padding-bottom: 5px;">Codes</div> <div style="border-bottom: 1px solid black; padding-bottom: 5px;">or</div> <div style="border-bottom: 1px solid black; padding-bottom: 5px;">Serial</div>
--	---

	Page
3.1.7 Software Approach for Spectral Computations	45
3.1.8 Cancellation Methodology	45
3.2 Computational Experiment	50
3.2.1 Methodology of Solution	50
3.2.2 Description of Physical Model	51
 Chapter 4. EXPERIMENTAL RESULTS FOR VELOCITY	
4.1 Introduction	66
4.2 Mean Velocity Profiles	68
4.3 Streamwise Velocity Fluctuations	70
4.4 Shear Velocity	72
 Chapter 5. EXPERIMENTAL RESULTS FOR PRESSURE	
5.1 Introduction	87
5.2 Correction Analysis and <i>rms</i> Pressure Levels	89
5.2.1 Auto-Spectrum and Magnitude Squared Coherence	89
5.2.2 Root-Mean-Square Pressure Levels (<i>rms</i>)	92
5.3 Spectral Features of Channel Flow Wall Pressure	93
5.3.1 Single Point Frequency Spectra	93
5.3.2 Cross-Spectral (two-point) Pressure Measurements	97
5.3.3 Convection Velocity (narrow-band)	99
5.4 Temporal Features of Channel Flow	101
5.4.1 Correlation Analysis (broad-band)	101
5.4.2 Length and Time Scales	104
5.4.3 Probability and Time Series Analysis	105
 Chapter 6. SUMMARY AND CONCLUSIONS	
6.1 Summary of Accomplishments	150
6.2 Major Conclusions	152
6.3 Original Contributions and Concluding Remarks	154
 REFERENCES	156

LIST OF FIGURES

	Page
2.1a Space-Correlation for Fixed Time Delay	33
2.1b Time-Correlation for Fixed Spatial Separation	33
2.2 Full Space-Time Covariance Contours, $R(\xi, \tau)$	34
2.3 Auto Time-Correlation Coefficient for Velocity (zero spatial separation)	35
3.1 Rectangular Water Channel Facility	53
3.2 Turbulence Management and Test Sections	54
3.3 Channel Flow Bulk Velocity Control	55
3.4 Test Section Configuration	56
3.5 Test Plate With Pressure Transducer Taps	57
3.6a Transducer Calibration for Bulk Velocity Control	58
3.6b Transducer Calibration for Channel Pressure Gradient	58
3.7 Channel Pressure Gradient Using Multiple Taps for a Range of Bulk Velocities	59
3.8 Friction Coefficient for Rectangular Channel	60
3.9 Schematic of LDV Orientation With Respect to Tunnel Walls	61
3.10 Block Diagram of Wall Pressure Data Acquisition	62
3.11 Dynamic Calibration of Wall Pressure Transducers	63
3.12 Power Spectral Density of Three Transducers at Two Typical Velocities	64
3.13 Transducer Alignment for Signal-Free Cancellation	65
4.1 Velocity Profile at $R_h = 5,000$ at Each Station Across the Channel	74
4.2 Velocity Profile at $R_h = 10,000$ at Each Station Across the Channel	75
4.3 Velocity Profile at $R_h = 15,000$ at Each Station Across the Channel	76
4.4 Velocity Profile at $R_h = 20,000$ at Each Station Across the Channel	77
4.5 Velocity Profile Across Channel at $Y_o = 0.1$ inches From Upper Wall	78
4.6 Velocity Profile Across Channel at $Y_o = 0.5$ inches From Upper Wall	79
4.7 Velocity Profile at Station B for All Reynolds Numbers, to Include Numerical Data	80
4.8 Universal Velocity Profile at All Reynolds Numbers Including the Numerical Data	81
4.9 Velocity Defect for All Data	82
4.10 Rms Profile Versus Outer Variables	83

	Page
4.11 Rms Profile Versus Local Variables.....	84
4.12 Rms Profile Versus Inner Variables.....	85
4.13 Friction Velocity Versus Reynolds Number	86
5.1 Power Spectral Density at $R_h = 10,000$	107
5.2 Power Spectral Density at $R_h = 15,000$	108
5.3 Power Spectral Density at $R_h = 20,000$	109
5.4 Power Spectral Density at $R_h = 25,000$	110
5.5 Highest Resolution Power Spectral Density (corrected)	111
5.6 Magnitude Squared Coherence, $R_h = 10,000$	112
5.7 Magnitude Squared Coherence, $R_h = 15,000$	113
5.8 Magnitude Squared Coherence, $R_h = 20,000$	114
5.9 Magnitude Squared Coherence, $R_h = 25,000$	115
5.10 Comparison of Rms Levels.....	116
5.11 Outer Variable Similarity	117
5.12 Mixed Variable Similarity.....	118
5.13 Mixed Variable Similarity With Hydraulic Diameter on Both Axes	119
5.14 Mixed Variable Similarity With Hydraulic Diameter on X-axis Only	120
5.15 Inner Variable Similarity.....	121
5.16 Comparison of Spectral Resolution.....	122
5.17 Streamwise Coherence, $R_h = 15,000$	123
5.18 Streamwise Coherence, $R_h = 20,000$	124
5.19 Streamwise Coherence, $R_h = 25,000$	125
5.20 Narrow Band Convection Velocity of Computational Experiment (Outer units)	126
5.21 Narrow Band Convection Velocity of Physical Experiment At $R_h = 15,000$ (Outer units)	127
5.22 Narrow Band Convection Velocity of Physical Experiment At $R_h = 20,000$ (Outer units)	128
5.23 Narrow Band Convection Velocity of Physical Experiment At $R_h = 25,000$ (Outer units)	129
5.24 Narrow Band Convection Velocity of Computational Experiment (Inner units).....	130

	Page
5.25	Narrow Band Convection Velocity of Physical Experiment At $R_h = 15,000$ (Inner units).....131
5.26	Narrow Band Convection Velocity of Physical Experiment At $R_h = 20,000$ (Inner units).....132
5.27	Narrow Band Convection Velocity of Physical Experiment At $R_h = 25,000$ (Inner units).....133
5.28	Time Correlation for Physical Experiment at $R_h = 10,000$134
5.29	Time Correlation for Physical Experiment at $R_h = 15,000$135
5.30	Time Correlation for Physical Experiment at $R_h = 20,000$136
5.31	Time Correlation for Physical Experiment at $R_h = 25,000$137
5.32	Time Correlation for Computational Experiment at $R_h = 2,129$138
5.33	Outer Unit Correlation Versus Reynolds Number for the Physical Experiment139
5.34	Outer Unit Correlation; Computational and Physical Experiments.....140
5.35	Inner Unit Correlation Versus Reynolds Number for the Physical Experiment141
5.36	Inner Unit Correlation; Computational and Physical Experiments142
5.37	Broadband Convection Velocity for Both Experiments143
5.38	Probability Distribution Normalized With <i>rms</i> Pressure144
5.39	Probability Distribution Normalized With Dynamic Head145
5.40	Computational Temporal Data at Station 1146
5.41	Computational Temporal Data at Station 4147
5.42	Temporal Data at $R_h = 15,000$148
5.43	Temporal Data at $R_h = 25,000$149

LIST OF TABLES

4.1	Parameters for Computational Experiment67
4.2	Governing Parameters for Physical Experiment68
5.1	Possible Record Size and Ensemble Averages89
5.2	Parameters Governing Both Experiments93

ACKNOWLEDGEMENTS

This thesis effort could not have been possible without the many contributions I have received from colleagues and friends. To them I wish to express my sincere appreciation.

I would like to express gratitude to my many colleagues at the Naval Research Laboratory who have assisted me in the development of my professional career. Of these people, special appreciation goes to Dr.'s Skop, Hansen and Griffin. They have not only willingly given of their professional and technical skills but have shown a great deal of patience in the support of this long, somewhat arduous endeavor. Dr. Skop was instrumental in my overall career development by seeing that support was obtained through an advanced training program of study. Dr. Hansen convinced me that an advanced program of doctoral research was possible and provided continued inspiration throughout the initial phases of this research effort. Special thanks is expressed to Dr. Owen Griffin who in the last phases of the research gave me his unequivocal support as well as encouragement to carry this project to completion.

The generous support of the Naval Research Laboratory training office is gratefully acknowledged. I was fortunate to be awarded a position in the Edison Memorial Training program of advanced research study which provided the means for participating in this extended training both at the laboratory and at Catholic University.

I wish to express special appreciation to my dissertation director, Professor Mario Casarella. Prof. Casarella supervised my work with patience and a great deal of perseverance over the last few years. He assisted in the organization of the effort particularly in the last stages and this support is greatly appreciated.

I wish to thank Dr.'s Krishnamurthy and Hansen for taking the time to review the dissertation. Their comments improved the work and helped to formulate the important conclusions from the results. I also wish to express my gratitude to the many people at the University for their support and cooperation during the course of this research effort.

Finally, I would like to thank my wife and son for their love and support throughout this endeavor at higher education and in particular, their patience during the long process that led to a finished dissertation. My absence for many weekends and holidays was most difficult for them. Hopefully, the completion of this dissertation was worth their sacrifice.

NOMENCLATURE

A_s	channel aspect ratio, $A_s = w/2h$
$B(u)$	probability density function
C	correlation covariance
C_o	exponential decay coefficient for streamwise coherence
d_h	hydraulic diameter
d_t	transducer diameter
d^+	non-dimensional transducer diameter, $d^+ = d_t u^* / \nu$
F, f	frequency (Hz)
F_{max}	maximum frequency for which turbulence information exists
h	channel half-height
i	$\sqrt{-1}$
k	wavenumber, $k = \sqrt{k_1^2 + k_3^2}$
K	kurtosis (flatness factor)
k_o	ω/U_c , (Taylors's hypothesis)
k_1, k_x	streamwise wavenumber
k_3	spanwise wavenumber
l_x	streamwise micro length scale
L_x	streamwise macro length scale
N	number of ensemble averages or records
N_p	number of points per record
p	fluctuation component of pressure
P	total pressure
p_{rms}	root-mean-square of fluctuating pressure
\bar{P}	mean pressure
Q	average dynamic head, $Q = 1/2 \rho U_{avg}^2$
Q_∞	dynamic head, $Q_\infty = 1/2 \rho U_\infty^2$
R	correlation function
R_h	channel Reynolds number, $R_h = U_\infty h / \nu$
R_{dh}	channel Reynolds number based on hydraulic diameter, d_h
R_{dh}^*	R_{dh} modified by friction factor
R^*	shear velocity Reynolds number, $R^* = u^* h / \nu$
rms	root-mean-square

r_1	transducer spacing
S	skewness
t	time variable
T	period of integration
\mathcal{T}_o	macro time scale
U	total velocity, $U = U(\bar{U}, \bar{V}, \bar{W}, u, v, w)$
u, v, w	fluctuating components of velocity
$\bar{U}, \bar{V}, \bar{W}$	mean components of velocity
U_{avg}	channel average or bulk velocity
U_c	convection velocity
U_∞	channel centerline velocity, (maximum velocity)
U^+	\bar{U}/u^*
u^*, u_τ	shear velocity, $u^* = \sqrt{\tau_{wall}/\rho}$
Y^+	yu^*/ν
x, y, z	streamwise, wall-normal and spanwise coordinate directions
α	cross-spectrum phase angle (radians)
γ^2	coherence function
δ	boundary layer thickness
δ^*	boundary layer displacement thickness
ϵ	statistical error
κ	von-Karman's constant
λ	wavelength parameter, $\lambda = 2\pi/k$
ν	kinematic viscosity
$\xi_x, \Delta x$	separation in streamwise direction
ξ^*	non-dimensional streamwise separation, $\xi^* = \Delta x u^*/\nu$
π	3.14159.....
ρ	fluid density
σ^2	variance
τ	time delay
τ_{min}	micro time scale
τ_{wall}	wall shear stress
Φ	spectral function

$\Phi(\omega), \Phi(f)$	frequency spectrum
Φ_{pp}	wall pressure spectrum
ω	angular frequency
$\langle \dots \rangle$	time or ensemble average

ABSTRACT

Wall pressure fluctuations within an equilibrium rectangular channel flow geometry were investigated. The overall objective of this investigation was to obtain experimentally for the first time, the statistical properties of the wall pressure fluctuations for a generic turbulent flow within a rectangular channel and to directly compare the results with those obtained from a full solution to the Navier-Stokes equations via Direct Numerical Simulation (DNS). For both the physical and computational experiments, serious limitations on the quality of the results were identified related to facility generated noise, transducer resolution, Reynolds number effects and constraints imposed by the computational technique.

An extensive data base was obtained from the physical experiment. Profiles for the mean and fluctuation components of the streamwise velocity were obtained at a number of spanwise locations and served to establish the existence of equilibrium flow conditions over a range of Reynolds numbers. An array of flush-mounted pressure transducers was utilized to measure the two point spectral characteristics in the streamwise direction. A unique signal processing scheme was developed and used to cancel facility generated noise which resulted in new information being recorded at low frequencies for the Reynolds numbers investigated.

Two issues of fundamental importance were examined. First, the results from both experiments were compared directly. The computational results were found to be somewhat underdeveloped for the higher order statistics for the particular data investigated. Resolution problems were shown to exist at both ends of the frequency spectrum. The computational grid spacing was insufficient to resolve the small scale structure at high frequencies and the limited size of the computational box resulted in contamination at the low end of the frequency spectrum by sensing the periodic boundary conditions as "noise" peaks. Secondly, the spectral results for rectangular channel flow were compared directly to results obtained from typical outer flow regimes as represented by flat plate boundary layers. Two fundamental results were established. Although similarity scaling was shown to exist, the turbulence structure was shown to decay approximately twice as fast as obtained in external flows. Various scaling laws were examined which were found to collapse respective spectral content separately, but no "universal" law was found to exist which brings both internal and external flow regimes into coincidence.

This investigation has provided new information not previously recorded in the literature. An extensive high quality data base was obtained for generic channel flow at low Reynolds numbers which may be used to assess the quality of typical Direct Numerical Simulation (DNS) results. A careful examination of the results will prove useful in characterizing the proper governing parameters necessary for future DNS initiatives.

ADMINISTRATIVE INFORMATION

This work is a dissertation submitted to the faculty of the School of Engineering and Architecture of the Catholic University of America in partial fulfillment of the requirements for the degree Doctor of Philosophy and has been reproduced here, with minor modifications, as a Naval Research Laboratory (NRL) Memorandum Report. The entire research effort was conducted at NRL while the author was involved in long term training via the Edison Memorial Graduate Training program. Additional funding for the research as well as the publication of this report has been supported by the NRL 6.1 Basic Research Program; Task Area RR023-01-41, Fluid Dynamics; Work unit 2985, Modification and Control of Shear Flow.

PHYSICAL AND COMPUTATIONAL INVESTIGATION OF THE WALL PRESSURE FLUCTUATIONS IN A CHANNEL FLOW

CHAPTER 1 INTRODUCTION

1.1 Background

Wall pressure has received a considerable amount of attention by experimentalists in the last few years. Most of this interest has attempted to characterize and/or otherwise explain fluid/structure interaction in relation to the coupling phenomena as represented by the generation of vibration and sound. In a practical sense, the origins of these phenomena may be expected whenever there is relative motion between adjacent bodies of fluid, such as a free shear flow, or between a fluid flowing within or external to a body. If the flow and subsequent body motions (such as vibrating panels) become coupled, a particularly deleterious condition termed "flow-induced noise" may exist. The resultant motion of the body may approach resonance in which case the motion itself becomes quite large. In these circumstances, fatigue of the body's surface may occur, or at the least, high intensity sound waves radiate to the farfield. Thus, any study related to these physical features of fluid/structure coupling can be characterized as the interactions of the following basic physical phenomena:

- o Unsteady fluid mechanics (turbulence)
- o Structural response (impedance, energy distribution, damping)
- o Radiative acoustic field related to fluid/structure interaction

A major motivation of studying such flow interactions lies in a desire to improve the basic understanding of the structure of turbulent flows and their relation to flow-induced noise, and help to resolve problems of practical engineering significance. An example of an engineering application may be found in the area of hydroacoustics where the sound radiating to the farfield is attributed to pressure fluctuations at the wall coupling with the natural resonances of the wall structure. A related example of extreme importance is the "flow noise" associated with the flow of water over a sonar platform or hydrophones mounted on the surfaces of ships or submarines. Flow noise takes on special significance in towed array topology, where the turbulent flow about the array so contaminates the pressure signature being recorded that it becomes difficult to extract worthwhile information.

Since the early work of Kraichnan (1956a,b), disagreement has persisted on the identification of the turbulence source terms that uniquely contribute to the wall pressure field and the

length scales and locations within the boundary layer in which this energy transfer takes place. It was originally thought that the spatial structure of the pressure field was not as fine-grained as that of the velocity field and received most of its energy from the low frequency velocity spectrum (Corcos, 1963). If one examines the Poisson equation for the wall pressure fluctuations, it can be shown that the pressure generated at the wall is coupled to velocity fluctuations throughout the boundary layer. Furthermore, integrating this equation over the unbounded half-space above the boundary wall shows that effective contributions decrease with distance away from the wall. Typically, 80 percent of the energy contributed to the wall pressure appears to occur within the near wall buffer region ($Y^+ < 50$) at length scales much smaller than the boundary layer thickness. Recently, it has been argued that the Burst/Sweep events in the near-wall region are a major contributor to the high frequency, high amplitude pressure fluctuations (Her, 1986).

Theoretical work in the past has mainly been confined to semi-empirical turbulence models which are strongly dependent on experimental data for closure of the problem. These models have resulted in only marginal success. Recent numerical solutions to the full time-dependent Navier-Stokes equations with no closure assumptions have had modest success (Handler, *et al.* 1984). Several characteristic features such as root-mean-square (*rms*) wall pressure, convection velocity and spectral content of the pressure field have compared favorably to experimental data. This numerical work appears promising, both in terms of reproducing measured properties of the wall pressure field as well as giving insight into physical features of this field which are not amenable to experimental measurements.

A major difficulty encountered in evaluating recent numerical methods is the absence of detailed experimental studies of the wall pressure field for a generic flow. The small body of existing wall pressure data is for high Reynolds number external flows which are typically two orders of magnitude higher than can be achieved in the present calculations. In addition, these previous experiments are poorly documented and contain measurements of only some of the relevant quantities.

The purpose of this investigation is to conduct a comparison/analysis of two wall pressure fluctuation experiments; one computational simulation experiment and one physical laboratory experiment that are of the same order magnitude in Reynolds number. For the first time, detailed measurements of the wall pressure field in a low-noise, low Reynolds number, fully developed turbulent channel flow will be compared to the results obtained from Direct Numerical Simulations (DNS) of the Navier-Stokes equations.

In this introduction, an attempt will be made to review the more salient characteristics and important results of past experiments on wall pressure. In particular, efforts will be made to point to those classical studies which are considered as standards in the literature. In addition, a brief synopsis of theoretical and computational work done to date will be given, including Direct Numerical Simulations (DNS) as it exists at this time. Finally, the specific objectives of this study will be put forth.

1.2 Review of Wall Pressure Studies

Kraichnan (1956 a,b) performed probably the earliest complete analysis, in a qualitative sense, of the important features of the wall pressure fluctuation structure within boundary layer flow over a smooth flat plate. His reasoning and dimensional arguments for scales and orders of magnitude of various parameters has set the foundation for much of the present work. Combining the equation of continuity with the divergence of the incompressible Navier-Stokes equations, he derived a Poisson equation for the unsteady pressure in a turbulent field which was a function of the velocity fluctuations throughout that field. At this point, Kraichnan resorted to an analysis based on similarity arguments and orders of magnitude, since detailed measurements of the fluctuating velocity field and related gradients were not, at the time, well documented. He showed that if the equation for pressure was written in integral form, a relation for wall pressure was obtained which showed the fluctuating pressure to be coupled to velocity fluctuations throughout the flow region being investigated, with those effects closest to the wall contributing the major share.

Kraichnan's work on the theoretical estimate of the *rms* value of the wall pressure in relation to the velocity fluctuations via similarity arguments was extremely innovative. Furthermore, he was the first to obtain values for these ratios and speculate that they were Reynolds number dependent. He determined that the ratio of *rms* pressure to the wall shear stress should be of the same order of magnitude, approximately equal to six, and that for the same class of similarity flows, this ratio should be a constant. One of the more interesting observations of Kraichnan's analysis was that the integration of the correlation function over the wall for all time delay should vanish, and therefore, the total mean square force per unit area exerted on the wall should be zero. This observation is still open to discussion within the literature.

Willmarth (1959) performed one of the first experiments on wall pressure within a flat plate boundary layer. He speculated that there were two basic mechanisms for the generation

of noise by turbulent boundary layers in general. In relation to rigid walls, he determined that a rapid change of fluid properties by the turbulent flow field caused noise generated by turbulence only. On the other hand, for more flexible walls, the wall acted as a diaphragm or speaker and hence coupled with the low wave number harmonics of turbulence which amplified this sound and radiated to the farfield. The subsequent generation of sound may be a resonance phenomena involving moving waves and ripples in the wall which are produced and amplified by a convected pattern of pressure fluctuations within the boundary layer. Willmarth found that the high frequency end of the spectrum was attenuated due to the spatial limitations of the large transducers available at that time ($d_t/\delta^* = 1.1$ to 4.6). He found $p_{rms}/Q_\infty = .00425$ but as d_t/δ^* decreased to the order of 1.1 , he obtained a value approaching $.0055$. Willmarth further proposed that in the limit as the transducer diameter approached zero, this ratio should reach a constant value of 0.006 and be independent of Reynolds number, contrary to Kraichnan's findings. Willmarth further suggested that the turbulent pressure fluctuations lost half their identity in traveling two boundary layer thicknesses and almost all of it by 10δ . In agreement with Kraichnan's work, Willmarth suggested that one can not compare pressure fluctuations to those of velocity in terms of amplitudes or frequency content, since the pressure fluctuations depend on an integral relationship with the velocity throughout the boundary layer.

As interest began to develop in the wall pressure field, it became apparent that at this early stage in experimentation, state-of-the-art pressure transducers lacked resolution capability due to their large diameters. In addition, as mentioned earlier, turbulence acted as a source mechanism of unwanted acoustic sound which, in most cases, contaminated the low end of the frequency spectrum. In 1962 Willmarth and Wooldridge conducted one of the first extensive investigations of wall pressure on a flat plate, wherein care was taken to investigate transducer size effects and minimize background contaminating acoustic noise. Their ratio of boundary layer thickness to transducer diameter was $\delta/d_t = 30$, one of the smallest transducers used until that time. They obtained ratios of p_{rms}/τ_{wall} and p_{rms}/Q_∞ of 2.64 and $.00561$ respectively. They found only a slight Reynolds number effect in the ratio of p_{rms} to τ_{wall} which decreased as the Reynolds number increased. Of course, with increasing Reynolds number, the frequency content of the wall pressure would extend to a higher frequency range. Since the transducer diameter was fixed, more attenuation would be apparent at the higher frequencies, so this result was not totally unexpected.

Willmarth and Wooldridge addressed the issue of low frequency acoustic contamination by cutting off the spectrum at that frequency where the contamination began, and assumed a constant spectrum amplitude for all lower frequencies. They made combined spatial and temporal

cross-correlation measurements which showed that pressure fluctuations were convected downstream. These measurements were hi-pass filtered, hence low frequency, turbulence-related pressure data was eliminated from their results. In any case, they determined that the convection speed of a pressure producing eddy varied from approximately 0.56 to 0.83 and that eddies of a certain size decayed on the order of four to six boundary layer thicknesses. The large convection velocity suggested that significant contributions came from the large scale motion in the outer region. Finally, Willmarth and Wooldridge found that longitudinal and transverse macro scales were of the same order of magnitude and suggested that for future studies, the transducer should be of the order of $d_t = U_\infty / 2F_{max}$ (where F_{max} equals the maximum frequency for which turbulence information is present in the flow) in order to prevent high frequency attenuation.

Corcos (1962) presented a quasi-theoretical scheme which addressed the issue of finite resolution of the high frequency content of the wall pressure field. Using the results of Willmarth and Wooldridge (1962), Corcos derived functional relationships which allowed all statistical averages related to the space-time covariance of the wall pressure field to be systematically corrected for finite size transducers. These corrections were found to be a very sensitive function of the convection velocity, generally non-linear and to a large extent, over corrected in those regions which had been highly attenuated.

Bakewell, *et al.* (1963) conducted one of the first comprehensive experiments in a fully developed pipe flow. They applied Corcos's (1962) corrections to all data but found minimal effect even though their ratio of pipe radius to transducer diameter was only 25 : 1, which was slightly smaller than Willmarth and Woodridge's. Over a broad band analysis, Bakewell found the convection velocity to be $U_c/U_\infty = 0.7$ and appeared to be somewhat Reynolds number dependent. On the other hand, for a narrow frequency band, *e.g.*, low-passed at 500 Hz, only large structures were present moving at close to the maximum velocity hence, $U_c/U_\infty = 0.98$. For a high frequency band represented by hi-passing at 7000 Hz, only the small scale (high frequency) structure was present, and a much lower convection speed was obtained on the order of 0.63. The *rms* value of the wall pressure was computed by averaging the time history data from sets of octave bands and found $p_{rms}/Q_\infty = 0.0048$ to 0.0063 which was somewhat Reynolds number dependent.

At that time, an interest was beginning to develop in the actual structure of the wall pressure field and whether it scaled with definable similarity variables. Corcos (1963) reviewed a large compendium of work done to that date, with some attempt at explaining similarities

and differences in the results. He substantiated that p_{rms}/τ_{wall} was weakly Reynolds number dependent and that length scales within the inner region of a boundary layer seemed to be impressed by the outer flow. Corcos hypothesized that the pressure field was not as fine-grained as the velocity field and that the spectrum should peak at a value of $\omega\delta^*/U_\infty = 0.2$ to 0.3 . He found that mixed inner/outer variables for the magnitude and outer variables for the frequency appeared to collapse all Reynolds number flows into coincidence. However, he further theorized that this was most likely due to the cancellation effects of finite size transducers. Corcos felt that these differences at high frequencies were not resolvable and that similar differences at the low frequency end of the spectrum were due to secondary flows in the free stream and/or radiated noise.

Although other authors had made cross-spectral density measurements, Corcos pointed to the importance of this function as indicative of the true convective nature of the flow and that measurement of the cross-spectrum phase quantified a narrow-band measure of convection velocity $U_c(\omega, \xi)$. Corcos finally concluded that the lack of similarity between various Reynolds number flows was due to the fact that as pressure patterns convect downstream, evidence seems to suggest that instead of becoming incoherent, the dispersive nature of the source terms causes the pattern to spread out and become dispersive instead.

Willmarth and Roos (1965) made the assumption that if the transducer responds linearly to the pressure, then a complete and accurate set of wall-pressure measurements can be corrected for transducer size effects. They tested four different size transducers in the range $0.122 < d_t/\delta^* < 0.442$. They found that as the transducer diameter approached zero, the ratio of p_{rms} to τ_{wall} approached the limiting value of $p_{rms}/\tau_{wall} = 2.66$ for $R_\theta = 38,000$. They also found that the similarity corrections of Corcos (1962) were not valid when $\omega\delta^*/U_\infty > 3$ for spatial separations such that $\Delta x < 0.1\delta$, and that there existed departures even as low as $\omega\delta^*/U_\infty = 1$.

Schloemer (1966) investigated pressure gradient effects on wall pressure fluctuations along a flat plate. His conclusion was that convection velocities were changed due to the distortion of the mean velocity profiles, which were caused by imposed pressure gradients. With respect to zero pressure gradient flows, U_c/U_∞ was higher in the favorable gradient and lower in the adverse case. Schloemer determined that loss of coherence or decay in the flow direction was more rapid in the adverse than in zero pressure gradient case and, as expected, the favorable pressure gradient demonstrated slower rates of decay. The most important result of his work was that he was one of the first to establish or hypothesize that convection velocity was a function of some non-dimensional frequency based on boundary layer thickness. He also argued

that smaller eddies at higher frequencies must "physically" exist closer to the wall in lower speed regions, therefore, U_c/U_∞ should drop to zero as the velocity goes to zero.

Bull (1967) concluded that the wall pressure field has a structure produced by contributions from turbulent sources in the boundary layer with a wide range of convection velocities and therefore comprise two families of convected wave number components. The first, at high wave number, is associated with turbulent motion in the constant stress layer and is coherent for times proportional to the time to be convected a distance $\delta = \lambda$. The second family, composed of λ 's greater than twice the boundary layer thickness lose coherence as a group more or less independent of wave length and are associated with large scale eddy motion outside the constant stress region. By referring to these definitions, Bull could address the issue of where in the flow field the pressure source terms were likely to be located.

Both Bakewell (1968) and Clinch (1969) investigated wall pressure fluctuations in water flow. Bakewell's experiment was on the exterior surface of a cylinder for which in the flow direction, agreement with flat plate data was obtained. Only in the spanwise statistical properties did curvature effects become dominant. Clinch investigated fully developed pipe flow and found p_{rms}/Q_∞ to be independent of Reynolds number, on the order of 0.007. Clinch found macro and micro length scales in the longitudinal direction to exceed those in the transverse direction by 6 and 1.5, respectively.

Blake (1970) made wall pressure measurements on a flat plate with both smooth and rough walls. In order to address the issue of transducer resolution, his experiment was the first to use small pin-hole microphones which provided resolution approximately three times better, relative to displacement thickness, than had been previously accomplished. He determined that the space-time decay rate was considerably higher than previously reported. Blake found, as Schloemer (1966) first noted, that convection velocity for small separations dropped off sharply at low frequencies. Blake gave three definitions of convection velocity. If one draws a curve tangent to the space-time correlation curves then:

1. $U_c(r_1) = \partial r_1 / \partial \tau$ — instantaneous broad band convection velocity,

and

2. $U_c(r_1) = r_1 / \tau$ — average broad band convection velocity.

Blake's third definition was a narrow band convection velocity defined from the cross-spectral density function, where $U_c = -r_1\omega/\alpha$, which was in agreement with Corcos's definition (1963). Blake further found that the low frequency pressure spectra scaled on variables mixed from the inner as well as outer flow, but that the smaller scale, high frequency components scaled only on the inner variables $l \propto \nu/u^*$ and $v \propto u^*$. Blake's results were probably the most definitive work done in which great care was taken to minimize flow disturbances and in which an attempt was made to improve transducer resolution by an order of magnitude. Indeed, even to this day, Blake's results for flat plate flow are still used as baseline data for comparative purposes.

Willmarth and Yang (1970) conducted a comparison experiment between the flow on a flat plate to that external to a cylinder. They found that longitudinal and transverse scales were less for the cylinder than a plane boundary layer which they interpreted as the transverse curvature reducing the size of the pressure producing eddies. In addition, they determined p_{rms}/τ_{wall} to approach 2.5 for both experiments.

Wills (1970) made measurements of the wave-number/phase velocity spectrum. Up to this point in time, most experimentalists had evaluated pressure data by computing the space-time, $R(r, \tau)$, correlation function and had integrated (Fourier transformation) to obtain the pressure spectrum. Wills chose to integrate twice (ie., with multiple transducers) to obtain, for the first time, the full (wave number, frequency) spectrum. Thus one could look at a contour map for which a definition of $U_c(k)$ was depicted explicitly. Wills found that convection velocity at low wave number (low frequency) was as high as $0.9U_\infty$ and asymptoted to $0.55U_\infty$ at the largest wave number components. His data also showed that at lower wave numbers, there was a "decreasing" trend of the convection velocity indicated, thereby collaborating Schloemer and Blake's earlier work with pin-hole transducers. Wills's method provided a means for making corrections both for transducer effects as well as low frequency contaminating noise.

Willmarth (1975) gave a comprehensive review of the extensive effort towards investigating wall pressure fluctuations. He outlined that it was not possible to measure pressure fluctuations within the flow field due to the intrusive nature of the probe and that at the wall, resolution problems were still the rule rather than the exception. He further showed that the pressure at any one point is produced by momentum fluctuations at many other points and that theoretical work, up to that point, mostly employed turbulence models based on experimental work. Summarizing the efforts of many experimentalists, Willmarth suggested that the sound field at low frequencies contaminates most data and is difficult, if not impossible, to eliminate and

that although pin-hole effects were still not well known or understood, he commended Blake's (1970) results as then the best resolvable. Willmarth pointed out that other than Schloemer, Blake and Wills, experimenters for the most part were calculating convection velocity from correlation curves rather than from the cross-spectral density functions; i.e., a broad-band analysis only.

From the review by Willmarth, it became apparent that the two overriding important themes for making high quality measurements of the wall pressure field was first to eliminate the low frequency contaminating acoustic sound and secondly, placing a more careful emphasis on obtaining smaller transducers. During this past decade, technological advances in piezo-electronics has provided much smaller transducers and a number of new noise cancellation techniques were combined with facility redesign to reduce or eliminate the effects of the facility-generated noise.

Willmarth and Yang (1970) made one of the earliest attempts at reducing facility-generated noise from interfering with low frequency wall pressure content. Willmarth showed that a finite correlation was obtained for negative time delay between flush-mounted transducers separated in the streamwise direction. By combining this temporal quantity with the spatial separation between the two sensors, a velocity was derived equal to the sound speed (relative to the flow velocity) in the fluid. Willmarth interpreted this quantity as flow-generated acoustic noise and subtracted it from the original output to eliminate its contribution to the overall signal. However, this technique is somewhat subjective, and in reality, can only be applied to correlation measurements when it is known a priori that the low frequency noise is composed of a single frequency component.

A new technique, which employs a signal processing scheme, was introduced first by Wambganss and Zaleski (1970), and later refined by Wilson *et al.* (1979) and Horne and Hansen (1981). Utilizing three pressure transducers located in a plane perpendicular to the flow direction, simple subtraction of the time-dependent pressure signals provided a means of separating the individual signals due to turbulent wall pressure, background acoustic, and electronic noise, respectively. The method may be applied to wider band noise but relies on the belief that the low frequency noise only propagates as a plane wave. Wilson *et al.* investigated air flow in an annular pipe flow configuration at a Reynolds number of 300,000. The turbulent pressure signal was some 20dB less than their overall signal from a single transducer, resulting in the subtraction of very large numbers to obtain a much smaller one. Their values for p_{rms}/Q_{∞}

ranged from .005 to .0062 also indicating a Reynolds number dependence. Although an innovative technique, this method requires the noise to propagate as a plane wave which is somewhat restrictive. Furthermore, as will be shown later in this study, the subtraction scheme involves a major source of potential error (although subtle) which involves "all" signal processing subtraction techniques.

Panton *et al.* (1980) investigated the low-frequency region of the wall pressure spectrum on the external fuselage of a sailplane. The zero-pressure gradient flow had low free-stream turbulence intensity and showed the pressure spectra to decrease with decreasing frequency in agreement with calculations relative to a turbulence-mean shear interaction mechanism. The measurements showed virtually no acoustic contamination at low frequency and were among the first to show an approximate " ω^2 " dependence with rising frequency. An important point made by Panton, was how the pressure fluctuations act as a foot-print of the velocity fluctuations throughout the boundary layer, thereby providing a convenient mechanism by which the flow structure in the outer region can influence events going on within the inner layer close to the wall.

Schewe (1983) investigated the resolution problem inherent with high frequency wall pressure measurements by testing small (non-pinhole) flush mounted transducers ranging from 25.4mm to 1mm in diameter. These sizes correspond to viscous diameters ($d^+ = d_t u^*/\nu$) of $d^+ = 19$ to 333 and are considered to be the most definitive work on transducer resolution to date. Schewe showed that as the transducer diameter decreased, the probability distribution function exhibited considerable expansion. In other words, not only does the larger diameter transducer filter off the higher frequency (smaller structure) components of the wall pressure, but it filters out very large pressure amplitudes which contribute significantly to the *rms* level of pressure but have short life times. For the smallest transducer, ($d^+ = 19$), Schewe found $p_{rms}/Q_\infty = 0.0102$. However, he used Corcos's (1962) corrections to adjust all data with a five percent error in the smallest transducer. If one compares his spectral data (scaled on inner variables) with the work of Blake (1970) and Emmerling (1973), it appears that the low frequency part of the spectrum is somewhat low. In other words, all the transducers appear to be somewhat attenuated at low frequency which could be indicative of a slight calibration problem. Nevertheless, Schewe's resolution of the high end of the spectrum was pursued with great care and may be regarded as a standard for zero-pressure gradient wall bounded flows.

Farabee (1986), investigated wall pressure fluctuations beneath a non-equilibrium turbulent flow. He conducted experiments with pinhole transducers similar to those used by Blake,

in a flow passing over a backward-facing step. The objective of such a study was to identify those turbulent structures in the flow that contribute to the source terms of the wall pressure field. Data was taken for both the perturbed and non-perturbed states for comparison purposes. The high frequency wall pressures were found to scale on inner variables suggesting that the sources for this frequency range can be found within the inner layer of the boundary layer close to the wall. The maximum in the non-perturbed boundary layer was found to occur at $\omega \delta^+ / U_\infty = 0.3$. The extensive two-point statistics were in excellent agreement with the work of Blake, Bull and Emmerling, and provided some guidance for the present work.

1.3 Theoretical Studies and Numerical Simulation

For the most part, analytical studies have attempted to understand the relationships existing between the different scales of turbulence and how they induce and/or affect pressure fluctuations. As illustrated above, wall pressure fluctuation experiments have been more or less limited to examining the statistical properties of the pressure field and by conjecture, relate them to turbulence structures known to exist. This level of understanding has for the most part, been limited to equilibrium type boundary layers for high Reynolds numbers and very little evidence exists tying shear layers and internal/external wall flows together in a balanced theory.

Following the pioneering work of Kraichnan (1956), Landahl (1967) attempted to numerically solve the nonhomogeneous Orr-Sommerfeld equation for a turbulent boundary layer and assumed that the least damped eigenvalues of the problem would be the dominant sources of the wall pressure field. His results for the pressure cross-spectral density for a flat plate boundary layer agreed favorably with Willmarth and Wooldridge's experimental results. Landahl's calculated streamwise decay rates agreed well with the experimental results of Bull (1967). However, the calculated convection velocities were found to be too low by 30 percent.

Panton and Linebarger (1974) calculated the one-dimensional wavenumber (streamwise wavenumber) spectrum of pressure fluctuations beneath equilibrium turbulent boundary layers. They numerically solved the Poisson equation for wall pressure, following the development of Kraichnan, by using empirical models for the turbulence velocity source terms in the equation. An interesting feature of their work is that they showed the contributions to the total pressure, as a function of wavenumber, that come from various regions of the boundary layer. The inner portion of the boundary layer dominates the contributions at the highest wavenumbers. When

contributions come entirely from the wall layer and log region, a universal overlap region in the pressure spectrum was shown to exist. The presence of an overlap region can be argued following the same dimensional arguments that are used to show the presence of an overlap region for the mean flow velocity profile. Within this overlap region, the spectrum should scale as ω^{-1} . Interestingly, the contributions to the low wavenumber components come from the wake region, yet the contribution to the lowest wavenumber components come from the middle region of the boundary layer.

Chase (1980) conducted an extensive theoretical work attempting to model the wall-pressure field utilizing known facts extracted from detailed experimental work. His objective was to provide a description of the pressure spectrum that would be valid for both the convective (high wavenumber) components as well as for low wavenumber components. Chase used the Poisson equation formulation given by Kraichnan and modeled the fluctuation velocities as propagating waves, as suggested by Morrison and Kronauer (1969). An analytical expression for the pressure spectrum was obtained containing adjustable constants that were evaluated from experimental results. Chase's model agreed well with experiments, predicted the " ω^2 " dependence of the pressure spectrum at low frequencies, and deduced that the phase convection velocity should tend to zero at low frequencies.

Ffowcs-Williams (1982) used the similarity model of Corcos (1962) to model the turbulent sources of pressure, not the pressure itself, so that a Corcos-like description of the pressure spectrum could be derived that was consistent with the constraints imposed by the governing equations. The relation which was derived, resulted in a fairly compact specification of the pressure spectrum with a set of constants similar to Chase's (1980) model, which are dependent on experimental results. He concluded that the existing body of literature formed an inadequate base for determining these constants explicitly and that new experiments were needed. Ffowcs-Williams showed that the surface spectrum was proportional to the square of frequency at low wavenumbers with subsonic phase speed, $U_c = \omega/k$. He further showed that the acoustics of the problem determines the strength of all those low-wavenumber elements with supersonic phase velocities. The sound radiated by turbulence and the ability to discriminate against self-noise for incoming acoustic waves is therefore set entirely by spectral elements whose magnitude can not be determined experimentally unless the experiment is conducted in a facility that is acoustically anechoic.

Since the equation for pressure at the wall is a Poisson type, it is natural to expect the evolution of various attempts to solve this equation to take the path as indicated above.

However, all such methods resulted in undefined constants that must rely on experimental measurements to explicitly predict the pressure spectra.

Direct numerical simulations (DNS) of turbulent shear flows have recently provided researchers with a new tool that has been used to study the dynamics of turbulence in greater detail. DNS represents three-dimensional, time-dependent numerical solutions of the full Navier-Stokes equations that attempt to compute all significant scales of motion without using any turbulence models for closure. In some cases, these calculations have provided information that would be difficult or impossible to obtain from experiments and in other cases, provided new results later confirmed by experiments. As a review, a brief synopsis follows of the principal efforts that have been undertaken by numerous investigators in the direct numerical simulation of turbulence, with special emphasis on a simulation of wall bounded turbulence. The reader may refer to reviews by Rogallo and Moin (1984) and Schumann and Friedrich (1987) for a more exhaustive review of Direct Numerical Simulation (DNS) techniques and results.

Orszag and Patterson (1972) performed the first simulation of homogeneous isotropic turbulence which required " 32^3 " grid points. A spectral Galerkin approach was used based upon trigonometric functions. Orszag and Kells (1980) and Orszag and Patera (1980) investigated turbulent channel flow in which one of the homogenous coordinates used Chebyshev polynomials in place of trigonometric functions. Orszag and Kells investigated the problem of transition to turbulence and Orszag and Patera extended this work to a full turbulence calculation.

Marcus (1984) investigated the rotating cylinder problem represented as Taylor-Couette flow and satisfactorily predicted wave speeds. Marcus's use of Green functions, or so-called influence matrix methods, were an improvement to DNS by a more acceptable implementation of the necessary boundary conditions.

Handler *et al.* (1984,1988) and Hansen *et al.* (1987) performed the first analysis of the wall pressure field from a DNS calculation. The single and two-point spectra were obtained for a channel flow Reynolds number of $R_\lambda = 5000$ with a 32^3 calculation. The dominant features to include the general convective nature of decaying turbulence was successfully demonstrated. However, the smallest scales of motion were unresolved, resulting in a much slower, broadband decay rate than experiments have shown. They speculated that increased spatial resolution would improve the results at high frequency. They were the first to suggest that aliasing errors were possible due to spatial filtering when transferring back and forth between the Fourier computational space and the "physical" domains as is typically carried out in direct

numerical simulation calculations. They further speculated that both direct as well as large eddy simulations (LES) of the Navier-Stokes equations could provide the means of studying and interpreting the underlying physical processes taking place within the turbulent velocity field. Thus, evaluating results from such calculations might give information about the physics of wall pressure generation not easily obtained within the laboratory.

For the most part, investigations involving DNS for the incompressible case result in a number of time point realizations for which all three components of velocity and the pressure are solved. Many of the statistical functions of turbulence involving velocity have been investigated with the results from DNS. However, other than the work of Handler *et al.*, no detailed analysis of the wall pressure field has evolved from any of the calculations to date.

1.4 Objectives of Research

The review of the literature reveals that a number of questions about the wall pressure field remain unresolved. It has been shown that wall pressure fluctuations appear to be generated by velocity fluctuations throughout the boundary layer. To this date, it has not been substantiated how events within the flow field, such as burst-sweep events affect these fluctuations. It also has not been resolved whether pressure convected patterns are similar or directly related to velocity convected patterns. Taking into account all of the past experimental and theoretical work, some specific questions could be asked. Do axial and transverse length scales for wall pressure have limiting values for higher Reynolds number flows? Do in fact, unique length, velocity and/or time scales exist for both internal and external flows such that all wall bounded flows have universal features? For example, it has been shown both via experiments and to a certain extent, with theoretical modeling that eddies of a specific size decay over a distance proportional to their size. Do external and internal flows exhibit the same characteristics, and what are the Reynolds number effects?

Our current understanding of these fluctuations is specific to high Reynolds number, external wall-bounded flows and free shear layers. Anomalies that may exist at lower speeds can not be addressed realistically by examining the past literature. In light of new analytical techniques (DNS), studies of the wall pressure field and turbulence/turbulence and turbulence/pressure interaction are now being pursued. A full experimental study close to the Reynolds number range of a typical DNS calculation would prove invaluable for code validation as well as for documentation. Therefore, a generic wall pressure experiment would prove useful for critiquing

DNS as well as for comparing future DNS applications to wall roughness and non-Newtonian applications.

The specific objectives of this research are:

- o to extend the present data base by comparing for the first time, two wall pressure experiments; one physical experiment in the laboratory and one computational simulation on a high speed computer;
- o to document detailed measurements of the wall pressure field at a range of Reynolds numbers (based on channel half-width) from 10,000 to about 25,000 in a turbulent channel flow;
- o to document spectral statistics in the wavenumber and frequency domains for both experiments, where possible;
- o to utilize novel signal processing techniques in order to examine the low frequency range of the pressure spectrum thus contributing to our fundamental understanding of the mechanism of flow-induced noise;
- o to conduct a direct comparison between experiments at similar Reynolds numbers that will prove useful in assessing both qualitatively and quantitatively the validity of the recent theoretical work;
- o to examine scaling laws for both flows to address their range and validity, and to determine whether similarity laws have common features for both internal and external flows.

CHAPTER 2 EQUATIONS OF TURBULENCE

2.1 Turbulence Definitions and Corresponding Equations

Laminar and turbulent flow may be classified as one, two or three dimensional, depending on the number of spatial coordinates needed to describe the flow. In the steady laminar case, the fluid streamlines exhibit a constancy in time with no superimposed fluctuations or random interplay of any one streamline with another. For unsteady flows, the streamlines become time dependent, but still remain relatively smooth with no apparent fluctuations superimposed on the overall flow pattern.

By contrast, turbulent flow is depicted by disorder, randomness and unsteady fluctuations, and this added complexity precludes any simple analysis as in the laminar case. Turbulent flows are predominant over external surfaces such as airfoils, turbine and compressor blades, ship hulls and missiles; and through internal configurations such as ducts, pipes, nozzels and diffusers. Beyond certain critical Reynolds numbers, most laminar flows, whether external or internal, become unstable when subjected to small flow disturbances and move through a transition phenomenon towards the more prevalent turbulent flow characterization.

There are two alternatives in proceeding with any turbulent flow analysis. The first involves a practical semi-empirical analysis which attempts to predict the macro properties of the flow such as mean velocity and temperature profiles, boundary layer thicknesses, skin friction and heat transfer coefficients. Once this information is extracted, the more useful properties of engineering significance such as lift, drag, flow separation and heat transfer may be determined. The second alternative involves a statistical theory of turbulent correlation functions which seek to analyze these random flow fluctuations. This mode of solution endeavors to discover the structure of turbulence in a scientific knowledge-accumulating fashion. There are many flow investigations for which both these theories of solution overlap but almost always at a rather advanced frontier-research level of fluid mechanics. As a general rule, engineering studies involve the former, for the method of analysis lends itself nicely in producing the parameters of engineering significance, whereas, the latter method is the predominant form of analysis in a more functional investigation of the origins of turbulence to include its relative scales and energy content. However, one of the most complicated and important aspects of experimental turbulence is that quantities that are usually obtained in the laboratory are measured because

they are "easy" to get rather than of fundamental significance. In other words, the important quantities which may further our understanding are not necessarily easily obtained.

In molecular motion, molecules at most, only affect the motion of their immediate neighbors. On the other hand, within turbulence, the motion at any point within the flow affects motion at other points within the flow via the pressure field and therefore is only "quasi-random". No two realizations of turbulent flow parameters (i.e., velocity or pressure) are the same. In this case, statistical descriptions of the distributions of mean values are all that make sense. Finally, one hears turbulence characterized as "homogeneous" and "isotropic". These terms do not have the same or similar meanings. The first means a particular turbulent flow is invariant or independent of one or more coordinates in space and/or time. The second means that turbulent "scales" are invariant in space. Various size scales with quasi-organized motion or convection depending on size may exist within homogeneous turbulence, but only one size scale may exist in isotropic turbulence.

The general relationships for a generic flow will now be presented, and when appropriate, reduced to appropriate forms for a 2D-channel flow environment.

2.1.1 General Equations for Turbulent Flows

In the solution of a typical turbulent flow problem, the basic equations of mass, motion and energy for a viscous fluid are assumed valid at any instant of time. These must be transformed into alternate forms by averaging over a time interval consistent with our ability to study such flows experimentally. This time averaging is really a necessary consequence of our inability to track the instantaneous fluctuations of the real turbulent flow. In general, let any flow variable, G , be subdivided into mean and fluctuating components, \bar{G} , and g , respectively such that the following definitions hold true.

$$G = \bar{G} + g \quad (2.1)$$

$$\bar{G} = \lim_{T \rightarrow \infty} \frac{1}{T} \int_0^T G dt \quad (2.2)$$

$$0 = \lim_{T \rightarrow \infty} \frac{1}{T} \int_0^T g dt \quad (2.3)$$

$$0 = \lim_{T \rightarrow \infty} \frac{1}{T} \int_0^T \bar{G} g dt \quad (2.4)$$

$$\overline{G^2} + \overline{g^2} = \lim_{T \rightarrow \infty} \frac{1}{T} \int_0^T G^2 dt \quad (2.5)$$

The period T over which the integration is performed must be chosen significantly larger than the largest period of the fluctuating component, g , and the integration refers to taking the time average of the variable in question. The instantaneous equations of motion for an incompressible, Newtonian fluid, with constant viscosity, can be written in Cartesian tensor notation as,

$$\frac{\partial V_i}{\partial t} + V_j \frac{\partial V_i}{\partial x_j} = -\frac{1}{\rho} \frac{\partial P}{\partial x_i} + \nu \frac{\partial^2 V_i}{\partial x_j^2} \quad (2.6)$$

where $V = V(V_1=U, V_2=V, V_3=W)$ represents the velocity vector, P , pressure, ρ , density, and ν , the kinematic viscosity. Equation (2.6), representing the Navier-Stokes equations, is time dependent, incompressible with constant viscosity and consists of three equations for the four independent variables U, V, W and P . If we take the divergence of equation (2.6), we obtain a Poisson equation for the pressure as,

$$\nabla^2 P = -\rho \frac{\partial V_j}{\partial x_i} \frac{\partial V_i}{\partial x_j} \quad (2.7)$$

One may note, that as written, equations (2.6) and (2.7) involve the instantaneous variables U, V, W and P which themselves are implicit functions of time, t , and the spatial coordinates, x, y , and z . We will leave until section 3.2, a description of the difficulties and complexities involved with any attempt to solve the above two equations. Suffice it to say, that only in the last decade with the advent of high speed computers have these two equations been amenable to computational solutions directly, and only at extremely low Reynolds numbers for very restrictive flow geometries.

As depicted above, all four variables represent pseudo random functions of both space and time, and the equations defining them usually require some manipulation in order to make their solution more tractable. Following Reynolds (1895), we decompose both variables, velocity V and pressure P , according to the definitions of a mean and fluctuating component as outlined in equation (2.1). Paying close attention to the rules specified in equations (2.2) to (2.5) we substitute $V = \overline{V} + v$ and $P = \overline{P} + p$ into equations (2.6) and (2.7), take the time average, and obtain the following equations for the velocity and pressure respectively.

$$\frac{\partial \overline{V}_i}{\partial t} + \overline{V}_j \frac{\partial \overline{V}_i}{\partial x_j} = -\frac{1}{\rho} \frac{\partial \overline{P}}{\partial x_i} + \nu \frac{\partial^2 \overline{V}_i}{\partial x_j^2} - \frac{1}{\rho} \frac{\partial}{\partial x_j} (\overline{\rho u_i u_j}) \quad (2.8)$$

$$\nabla^2 \overline{P} = -\rho \left[\frac{\partial \overline{V}_j}{\partial x_i} \frac{\partial \overline{V}_i}{\partial x_j} + \frac{\partial v_j}{\partial x_i} \frac{\partial v_i}{\partial x_j} \right] \quad (2.9)$$

As indicated, we have introduced nine new variables (as represented by the last terms in both equations) into an already complicated set of equations which prevents any simple solution, since they require additional knowledge of the turbulence structure. There are no a priori analytical representations for these terms, and hence, they are usually modeled empirically. These new variables cause what has been termed the "closure" problem of solving the time mean Navier-Stokes equations. Two relatively simple and similar empirical models are based on the eddy viscosity and mixing length hypotheses based on a 1st order closure method. The reader may refer to any text on advanced fluid mechanics for a presentation of this and higher order models of closure for various geometric configurations.

2.1.2 Channel Flow

The derivation of a solvable set of relations for the internal flow through a channel is relatively simple due primarily to the fact that geometry prohibits a continuous growth of a characteristic thickness. We assume that x is in the direction of flow, y , normal to the surface, and z lies in the plane of the channel walls which extend to infinity. If this channel is long enough, there is no further growth in the boundary layer as it stretches to the centerline, and we would expect all variables and derivatives thereof, to be independent of x except for the mean pressure. The only component of mean velocity we expect is \bar{U} and the flow lies entirely in the xy -plane, with no variation in a direction normal to that plane. Recognizing that \bar{V} and \bar{W} are zero, it can be shown that equation (2.8) reduces to the following set of equations for steady flow.

$$0 = -\frac{1}{\rho} \frac{\partial \bar{P}}{\partial x} - \frac{d}{dy}(\bar{uv}) + \frac{\nu d^2 \bar{U}}{dy^2} \quad (2.10)$$

$$0 = -\frac{1}{\rho} \frac{\partial \bar{P}}{\partial y} - \frac{d}{dy}(\bar{v^2}) \quad (2.11)$$

Integrating equation (2.11) with respect to y , results in,

$$\frac{\bar{P}(x, y)}{\rho} + \bar{v^2} = \frac{\bar{P}_o(x)}{\rho} \quad (2.12)$$

Since $\bar{v^2}$ is independent of x , differentiating equation (2.12) with respect to x shows $\frac{\partial \bar{P}}{\partial x}$ to be equal to $\frac{d\bar{P}_o}{dx}$, which is constant in magnitude, otherwise the flow would accelerate. Using this information, equation (2.10) may be integrated once with respect to y to obtain,

$$0 = -\frac{y}{\rho} \frac{d\bar{P}_o}{dx} - \bar{uv} + \frac{\nu d\bar{U}}{dy} - u^2 \quad (2.13)$$

Due to symmetry, the total shear $-\overline{uv} + \nu \frac{d\overline{U}}{dy}$ must equal zero at the channel centerline, hence equation (2.13) reduces to the well known relation for shear velocity and shear-stress at the wall as,

$$\tau_{wall} = \rho u_*^2 = -h \frac{d\overline{P}_o}{dx} \quad (2.14)$$

In the inertial sublayer, it can be shown that $\overline{U}(y)$ must satisfy both a logarithmic law related to inner variables, and a velocity defect law in the core region, similar to the flow along a flat plate. The resultant relations are,

$$\text{Log - Layer} \quad \frac{\overline{U}(y)}{u_*} = \frac{1}{K} \ln \left(\frac{yu_*}{\nu} \right) + a \quad (2.15)$$

$$\text{Core - region} \quad \frac{\overline{U}(y) - \overline{U}_o}{u_*} = \frac{1}{K} \ln \left(\frac{y}{h} \right) + b \quad (2.16)$$

where \overline{U}_o is the centerline velocity, κ is von Karman's constant, and the constants 'a' and 'b' are finite, yet independent of Reynolds number. The reader may refer to the works of Schlichting (1955), Townsend (1956), or Tennekes and Lumley (1972) for a detailed derivation of these results. In the literature, there is some scatter in the constants 'a' and 'b' which may be due to a shortage of experiments being conducted at large enough Reynolds number to ensure their independence. A second reason for the scatter, is that it becomes difficult to ideally match parameters between one facility and another, even to the extent of matching day to day conditions for the same facility.

An attempt may be made to solve equation (2.13) provided one assumes some eddy viscosity or mixing length model for the \overline{uv} term to effect closure. Using finite differencing or finite element techniques, solutions to this equation have been shown to be relatively simple and straightforward, provided an accurate set of initial and pressure gradient conditions can be found. In the next chapter, we will present the methodology for solving equations (2.8) and (2.9) by the method of DNS with no "closure" assumptions. We proceed now to review the definitions of higher order statistics of a time dependent function.

2.1.3 Higher Moments

As discussed previously, the details of the turbulent velocity field can not be reproduced instantaneously. It's only in the mean, or on average, that the mean values within stationary time independent flows can be obtained. The mean value (over time) of velocity is the first moment, but higher moments for variance σ^2 , skewness S , and the kurtosis or flatness factor

K , can also be defined. Since any variable has been defined to equal the sum of its mean value and a fluctuating component about the mean, the higher moments of interest, are those due to the fluctuations themselves. These moments serve to describe the amount of disorder or randomness present and characterize the turbulence more definitively. All the moments can be defined either through time averages or the probability density function $B(u)$, as illustrated below.

$$(\text{mean}) \quad \bar{u} = \lim_{T \rightarrow \infty} \frac{1}{T} \int_0^T u \, dt = \int_{-\infty}^{\infty} u B(u) du \quad (2.17)$$

$$(\text{mean - square}) \quad \sigma^2 = \overline{u_i u_i} = \overline{u^2} \quad (2.18a)$$

$$\overline{u^2} = \lim_{T \rightarrow \infty} \frac{1}{T} \int_0^T u^2 \, dt = \int_{-\infty}^{\infty} u^2 B(u) du \quad (2.18b)$$

$$\text{variance} = \sigma = \sqrt{\overline{u^2}} \quad (2.19)$$

$$(\text{skewness}) \quad S = \frac{\overline{u^3}}{\sigma^3} = \lim_{T \rightarrow \infty} \frac{1}{T} \int_0^T \frac{u^3 dt}{\sigma^3} = \frac{1}{\sigma^3} \int_{-\infty}^{\infty} u^3 B(u) du \quad (2.20)$$

$$(\text{kurtosis}) \quad K = \frac{\overline{u^4}}{\sigma^4} = \lim_{T \rightarrow \infty} \frac{1}{T} \int_0^T \frac{u^4 dt}{\sigma^4} = \frac{1}{\sigma^4} \int_{-\infty}^{\infty} u^4 B(u) du \quad (2.21)$$

The probability density function $B(u)$ represents the number of u 's found over an interval u_i and $u_i + \Delta u_i$, weighted by the width of the interval, and is a function of all u_i 's tested. The function thus defined, has unit area under the curve as depicted below.

$$\int_{-\infty}^{\infty} B(u) \, du = 1 \quad (2.22)$$

As shown, σ is a measure of the *rms* value of the fluctuation, and the skewness S , gives a representation of the symmetry of u . Positive skewness means the left side of the probability curve is steeper than the right side and vice versa. $S = 0$, is a symmetric probability density as represented by a truly Gaussian-like random function with zero skewness. K , otherwise known as the Kurtosis or flatness factor, is a measure of the curvature of $B(u)$ (or how rounded it is) at its maximum value. We expect K for the velocity to have high curvature (very sharp profile)

close to the centerline and very low curvature (less sharp or very rounded) as one approaches the wall.

Only a complete set of moments of all orders, contain all the turbulent information. However, some distributions can be described by a finite set of moments. A Gaussian distribution is completely described by the 2nd moment σ . All odd moments are equal to zero and all even moments $n > 2$ are equal to a constant times the 2nd moment. For instance, $S = 0$ and $K = 3$. The departure of turbulence from Gaussian in nature, is a manifestation of the highly non-linear behavior of turbulence. Note, the 2-parameter probability density functions at a point also exist as shown by,

$$R_{u_i, u_j} = \overline{u_i u_j} = \lim_{T \rightarrow \infty} \frac{1}{T} \int_0^T u_i u_j dt = \int_{-\infty}^{\infty} \int_{-\infty}^{\infty} u_i u_j B(u_i, u_j) du_i du_j \quad (2.23)$$

Here, R_{u_i, u_j} equals the normal pressure stresses due to velocity for $i = j$ and the Reynolds stress terms when $i \neq j$. The same definitions hold true for the pressure \bar{P} . Schewe (1983) showed that the probability density function $B(p)$ can be a very important indicator of transducer cancellation effects related to the size of the transducer. $B(p)$ shows that the pressure signature contains amplitudes as high as 15σ which have very short lifetimes and contribute significantly to the value of σ calculated, depending on transducer size.

2.2 Statistical Relationships of Turbulence

As illustrated above, the derived averages are all first-order time mean values with the end result equal to some constant, depending on the parameter being measured and on some independent variable, *e.g.* time, or a spatial coordinate. However, when conducting a detailed analysis of a turbulent flow, we are interested in the various scales of turbulence, their energy content and convective properties, and how these various scales interact one with another. It becomes necessary to investigate the wave-like behavior using second order statistical functions obtained with fourier transformations. We start by characterizing a turbulent flow in such a way as to give meaning to the following statistical relationships.

The turbulence quantities of interest are random functions of both space and time and are considered to be stochastic processes. A stochastic process refers to dealing with functions (such as pressure or velocity components) which are functions of an independent variable or a specified combination of independent variables such that,

$$Y = Y(s_1, s_2, s_3, \dots, s_n) \quad (2.24)$$

It may also mean that a series of functions Y_i exist with independent variables s_i such that an ensemble average can be characterized through appropriate statistical properties. This means that we are dealing with some statistical comparison between dependent variables such as Y_1 and Y_2 which are functionally dependent on the same prescribed set of independent variables s_i throughout the comparison process. Since "statistics" implies a time average, it's not surprising that one of the independent variables of most interest, is the variable depicting time such as t or $\tau = t + \Delta t$. We further restrict our averaging process to be stationary in time. This means a process for which the defining statistics remain the same by shifting the independent variable by Δt . For instance, suppose we have a dependent variable $Y = Y(t)$ for which we collect a series of snapshots over a time period T in sequential time slots and then form an ensemble average by summing all the snapshots as follows,

$$\begin{aligned}
 Y_1 &= Y(t_0, t_1, t_2, \dots, t_{a_1}) \\
 Y_2 &= Y(t_{a_1}, \dots, t_{a_2}) \\
 Y_3 &= Y(t_{a_2}, \dots, t_{a_3}) \\
 &\dots\dots\dots \\
 &\dots\dots\dots \\
 Y_{n-1} &= Y(t_{a_{n-2}}, \dots, t_{a_{n-1}}) \\
 Y_n &= Y(t_{a_{n-1}}, \dots, t_{a_n})
 \end{aligned}$$

$$Y(t) = \langle Y_i \rangle = \sum_i^n Y_i . \quad (2.25)$$

The braces $\langle \dots \rangle$ represent the ensemble averaging process. As noted, this particular process began at time $t = t_0$. We can form another ensemble average beginning at time $t = t_0 + \Delta t$ such that $Y_1(t_0) = Y_2(t_0 + \Delta t)$. If these two ensembles are equal and in fact, are equal to any other ensemble created, we call $Y(t)$ a stationary process. Finally, if each record of the ensemble is statistically equivalent to every other record of the ensemble such that we can replace an ensemble averaged process with a time average over a longer time interval of a single representative record, this process is considered "ergodic". An ergodic process is one in which ensemble averages may be replaced with time averages and vice-versa. In summary, this study concerns the examination of a fully developed channel flow in which the defining statistics concern stochastic processes which may be considered as stationary and ergodic.

The most general statistical function of a variable $V(\mathbf{x}, t)$ can be represented as the space-time correlation covariance as represented by,

$$C_{u,u_i}(\mathbf{x}, \mathbf{x}', t, t') = \langle \overline{u_i(\mathbf{x}, t) u_j(\mathbf{x}', t')} \rangle \quad (2.26)$$

where the braces $\langle \dots \rangle$ again, represent either a time average or a suitable ensemble average according to the above definitions. The auto-correlation is defined for $i = j$ and the cross-correlation for $i \neq j$. If C_{u,u_i} is a stationary function of time, and homogeneous in space, then C_{u,u_i} is only a function of the time difference, $\tau = t' - t$ and the separation vector $\xi = \mathbf{x}' - \mathbf{x}$ such that,

$$C_{u,u_i}(\xi, \tau) = \langle \overline{u_i(\mathbf{x}, t) u_j(\mathbf{x} + \xi, t + \tau)} \rangle \quad (2.27)$$

To give meaning to the averaging process, we may use the definitions of "stationarity" and "ergodicity" to define C_{u,u_i} by,

$$C_{u,u_i}(\xi, \tau) = \lim_{T \rightarrow \infty} \frac{1}{T} \int_0^T u_i(\mathbf{x}, t) u_j(\mathbf{x} + \xi, t + \tau) dt \quad (2.28)$$

It's very difficult to measure the full space-time correlation covariance, since equation (2.27) or (2.28) indicate an average over an infinite spatial domain. If one had an array of transducers separated in space, one may average each one in time, store on some medium such as a hard disc or tape, then perform the spatial integration. However, for velocity and pressure, the integration is three and two dimensional respectively, a process not altogether easily accomplished. What is usually done in the laboratory, is to compute the time covariance only, at a fixed spatial separation distance $\xi = s_i$ such that,

$$C_{u,u_i}(s_i, \tau) = \lim_{T \rightarrow \infty} \frac{1}{T} \int_0^T u_i(t) u_j(s_i, t + \tau) dt \quad (2.29)$$

where the cross-correlation is for $i \neq j$ and the auto correlation is for $i = j$. Often, it is more convenient to examine the space-time correlation functions with their Fourier transform pair variables (\mathbf{k}, ω) by the following transformation of C_{u,u_i} .

$$\Phi_{u,u_i}(\mathbf{k}, \omega) = \int \int \int \int_{-\infty}^{\infty} C_{u,u_i}(\xi, \tau) \exp[-m(\mathbf{k} \cdot \xi + \omega \tau)] d\tau d\xi \quad (2.30)$$

$$m = \sqrt{-1}$$

Equation (2.30) is referred to as the full auto/cross-spectra density function, depending on $i = j$ and $i \neq j$ respectively. Finally, the Fourier transform pair is complete by inverse Fourier transforming equation (2.30) to obtain the covariance once again.

$$C_{u_i, u_j}(\xi, \tau) = \frac{1}{(2\pi)^4} \int \int \int \int_{-\infty}^{\infty} \Phi_{u_i, u_j}(\mathbf{k}, \omega) \exp[m(\mathbf{k} \cdot \xi + \omega\tau)] d\omega d\mathbf{k} \quad (2.31)$$

One of the parameters of most interest in this study is the *rms* pressure of the fluctuations at the wall. The auto-covariance of the pressure may be defined by,

$$C_{pp}(\tau) = \lim_{T \rightarrow \infty} \frac{1}{T} \int_0^T p(t)p(t+\tau) dt \quad (2.32)$$

and if $\tau = 0$, we have,

$$C_{pp}(0) = \lim_{T \rightarrow \infty} \frac{1}{T} \int_0^T p(t)^2 dt \quad (2.33)$$

For no spatial separation, the fourier transform of the covariance of pressure as defined via equation (2.30) is,

$$\Phi_{pp}(\omega) = \int_{-\infty}^{\infty} C_{pp}(\tau) \exp[-m(\omega\tau)] d\tau \quad (2.34)$$

and it's Fourier transform partner is,

$$C_{pp}(\tau) = \frac{1}{(2\pi)} \int_{-\infty}^{\infty} \Phi_{pp}(\omega) \exp[+m(\omega\tau)] d\omega \quad (2.35)$$

If we set $\tau = 0$, we obtain the additional relation for *rms* pressure as,

$$C_{pp}(\tau = 0) = P_{rms}^2 = \frac{1}{(2\pi)} \int_{-\infty}^{\infty} \Phi_{pp}(\omega) d\omega \quad (2.36)$$

One may note, that there are three methods of obtaining the *rms* pressure squared; by a long time average of the square of the pressure signal, evaluation of the auto-covariance function at $\tau = 0$, or by integrating the auto-spectrum $\Phi(\omega)$ over all frequencies. Note, all three general functions are mathematically related however, laboratory hardware usually determines which function is more easily obtained. In the case of buried noise within the pressure signal itself, one or more methods may be eliminated due to the contamination. Assuming that $p(t)$ contains noise, a simple time average is contaminated and thus equation (2.36) may be the only way to obtain P_{rms}^2 , provided an accurate measurement of $\Phi(\omega)$ is obtained. This issue will be discussed further in chapter three.

Of particular interest is the cross-spectral function of the wall pressure Φ_{p_i, p_j} between two transducers separated over a spatial distance ξ in the flow direction. The streamwise coherence

function, γ^2 , is derived by normalizing the magnitude squared of $\Phi_{p,p}$, with the square of the auto spectrum as demonstrated below.

$$\gamma_{p,p_i}^2 = \frac{|\Phi_{p,p_i}|^2}{\Phi_{p,p_i}^2} \quad (2.37).$$

Bull (1967) found this function to decay exponentially when plotted versus the cross spectrum phase, and appears to universally represent similarity scaling.

For a propagating (or convective) field, the phase of the cross-spectrum has been shown by Blake (1984) and Farabee (1986) to be proportional to the convective speed, $U_c(\omega, \xi)$. This relationship can be expressed by,

$$U_c(\omega, \xi) = -\frac{\omega \xi}{\alpha(\omega, \xi)} \quad (2.38)$$

where $\alpha(\omega, \xi)$ is the narrow band phase which, due to the dispersive nature of turbulence, is not necessarily a linear function of frequency. The convection velocity U_c for the pressure producing eddies, as defined by equation (2.38), represents the convective speed of all wavenumber scale components contained within a narrow frequency band centered at the frequency, ω .

Prior to the last decade, a single convection speed for the turbulence was determined for all scales and frequencies by analyzing the results from the cross-correlation covariance of two hot wire sensors separated in space or time. Consider equation (2.28) for the fluctuating component of velocity in the flow direction over space and time. Following the previously established conventions, this is the auto correlation ($i = j$) over one spatial coordinate for all time and can be represented by,

$$C_{uu}(\xi, \tau) = \lim_{T \rightarrow \infty} \frac{1}{T} \int_0^T u(x, t) u(x + \xi, t + \tau) dt \quad (2.39)$$

This total function is impossible to measure instantaneously. However, suppose the following process is performed. First, various values for time delay are chosen, e.g. $\tau = n\tau_o$ and the distance ξ continuously varied. Secondly, the similar but opposite operation is performed, that of choosing fixed $\xi = n\xi_o$ but evaluated for all time. Therefore, the following relations for the space correlation at successively fixed τ_o 's and time correlation for successively fixed ξ_o 's are represented respectively as,

$$(fixed \tau_o) = C_{uu}(\xi, \tau_o) = \lim_{T \rightarrow \infty} \frac{1}{T} \int_0^T u(x, t) u(x + \xi, t + \tau_o) dt \quad (2.40)$$

$$(fixed \xi_o) = C_{uu}(\xi_o, \tau) = \lim_{T \rightarrow \infty} \frac{1}{T} \int_0^T u(x, t) u(x + \xi_o, t + \tau) dt \quad (2.41)$$

Equations (2.40) and (2.41) for various ξ_i 's and τ_i 's are illustrated in figure 2.1. As shown, both covariances illustrate the convective nature of turbulence. A convection velocity U_{c_t} obtained from figure 2.1a by the value of $\xi = \xi_{max}$ for the maximum in each hump for each τ_o is defined as,

$$\frac{\partial C_{uu}(\xi, n\tau_o)}{\partial \xi} = 0 \longrightarrow U_{c_t} = \frac{\xi_{max}}{\tau_{on}} \quad (2.42)$$

Similarly, a related convection velocity U_{c_r} may be obtained from a similar analysis of the respective humps in figure 2.1b by,

$$\frac{\partial C_{uu}(n\xi_o, \tau)}{\partial \tau} = 0 \longrightarrow U_{c_r} = \frac{\xi_{on}}{\tau_{max}} \quad (2.43)$$

Equation (2.39) is represented in figure 2.2 and may be obtained from either equation (2.40) or (2.41) by summing over all τ_o 's or ξ_o 's respectively. As indicated in figure 2.2, the two definitions for convection velocity are not the same. As shown, the contours as represented in this figure (and in real turbulence) are elongated and somewhat curved in the $\tau\xi$ -plane. Only in isotropic turbulence (invariant scales) within which Taylor's hypothesis holds (frozen pattern with no temporal rate of change in the pattern), are these two definitions equal.

As a final remark, equation (2.40), and hence the convection velocity U_{c_t} as defined by equation (2.42) is difficult if not impossible to measure. What is more easily obtained and reported in the literature is to evaluate equations (2.41) and (2.43) for U_{c_r} as illustrated in figure 2.1b. Referring to the curves in this figure, one may note that the peak for $\tau = 0$, besides being of higher intensity, has a much narrower peak and sharper roll off than for larger values of spatial separation. This broadening of the so-called "hump" with increasing spatial separation shows that the correlation is due to larger structures extending over a wider region of the flow field. Thus the eddy field is convected downstream with the larger structure remaining coherent, while the higher frequency smaller scale structure loses its identity.

2.3 Macro/Micro Length and Time Scales

As mentioned previously, characterizing the scales of turbulence over both space and time is of extreme importance in furthering our knowledge of this random process. The correlation

function is defined by dividing the covariance function by the mean square value σ^2 . Taking the time correlation of velocity as defined by equation (2.41) for zero separation results in,

$$R_{uu}(\tau) = \frac{C_{uu}(\tau)}{\sigma_u^2} \quad (2.44)$$

which is illustrated in figure 2.3. This function represents a measure over time of how long the velocity is correlated with itself for all structures within the flow. A macro time scale, τ_{max} , can be defined by integrating equation (2.44).

$$\tau_{max} = \int_0^\infty R_{uu}(\tau) d\tau \quad (2.45)$$

τ_{max} is a measure of the maximum amount of time over which the eddies remember their path. We may also define a minimum or micro time scale, τ_{min} , by fitting a parabola to the function in equation (2.44) starting at time $\tau = 0$ and evaluating the 2nd derivative.

$$(i) \quad R_{uu}(\tau) = 1 - \frac{\tau^2}{\tau_{min}^2} \quad (2.46a)$$

$$(ii) \quad \left[\frac{d^2 R}{d\tau^2} \right]_{\tau=0} = \frac{-2}{\tau_{min}^2} \quad (2.46b)$$

Similar relations exist for macro and micro spatial scales, as L_x and l_x respectively and are defined by,

$$L_x = \int_0^\infty R_{uu}(\xi) d\xi \quad (2.47)$$

$$l_x = \left[\frac{-2}{\left[\frac{\partial^2 R}{\partial \xi^2} \right]_{\xi=0}} \right]^{\frac{1}{2}} \quad (2.48)$$

The macro-spatial scale L_x is a relative measure of the size of the eddies containing most of the energy and/or the longest distance over which eddies of a given size are correlated, and l_x is an approximate measure of the minimum scale at which dissipation occurs. Kraichnan (1956) argued that integration of the pressure correlation function $R_{pp}(\tau)$ over a flat plate (and channel) should be zero, hence for pressure, no macro time scale can be computed. Hansen, *et al.* (1987) showed that this might not be true, that channel flows appeared to be able to support pressure scales of infinite length at fixed frequency. However, neither hypothesis gives an alternative definition via pressure statistical functions. One can only define a pseudo-macro scale τ_o , defined as that value of time τ where the time correlation function $R_{pp}(\tau) = 0$ at its first zero crossing. From Taylor's hypothesis, one can define a macro length scale as,

$$L_x = U_o \tau_o \quad (2.49)$$

where U_o is either the convection velocity or maximum velocity in the flow. For the micro scales of length and time, a similar analysis as outlined in equation (2.46) and figure 2.3 may be attempted for the pressure correlation. However, in practice, the effort expended is somewhat subjective and requires creativity on the part of the researcher, because there are usually only a few points defining $R_{pp}(\tau)$ close to zero. Therefore, using an analysis first put forward by Taylor (1938), a relation for the time micro-scale τ_{min} can be defined as,

$$\frac{1}{\tau_{min}^2} = \frac{2\pi^2}{\sigma^2} \int_0^\infty f^2 \Phi(f) df \quad (2.50)$$

and using equation (2.49), a micro-length scale l_x can be defined as,

$$l_x = U_o \tau_{min} . \quad (2.51)$$

These macro and micro scales are computed and further discussed in chapter 5.

2.4 Relevant Measured Time-Dependent and Statistical Quantities

In order to characterize the kinematics of the flow for the physical experiment, the mean value of velocity in the flow direction $\bar{U}(x, z)$ and the fluctuating component $u(x, z, t)$ were computed from the instantaneous data set $U(x, y, z, t)$. This data set was obtained via laser Doppler velocimetry and is explained in detail in the next chapter. The longitudinal pressure gradient $d\bar{P}_o(x)/dx$, along the channel center line, was measured directly during each Reynolds number experimental run from which the wall shear stress and shear velocity could be calculated via equation (2.14).

A five element array of flush mounted pressure transducers were recorded simultaneously in time, at various flow velocities. These transducers only respond to the fluctuating component as represented by $p(x, z, t)$, and will be discussed in more detail in the next chapter. A number of first-order and second-order multi-dimensional time/statistical functions have been discussed. Intuitively, one may hope that most relations presented can feasibly be measured. In a realistic sense, all that is measured is the time dependent pressure at the wall and the time dependent velocity at various points within the flow field. These data are either processed immediately with dual channel analyzers, or digitized, stored on some suitable medium and processed later in an appropriate manner. In this experimental study, the wall pressure $p(x, z, t)$ was recorded simultaneously for five channels of data for each Reynolds number. This data was stored on digital tape, and processed later by software developed by the author. The highest order

statistical function obtained in this study is the second order 2-dimensional auto/cross spectral density function $\Phi_{pp}(\xi_x, f)$ of the wall pressure fluctuations. All other 2nd order statistical functions, such as the space-time covariance, as defined by equation (2.41), are derived from this function via Fourier transformation, and all first order relations, such as the probability density function, are obtained directly from $p(x, z, t)$.

Below is a summary of all values, either measured directly or computed, that are used in this study. The details of measuring or computing these parameters will be given in the next chapter.

$U(x, y, z, t)$	streamwise velocity
$u(x, y, z, t)$	streamwise velocity fluctuation
$\bar{U}(x, y, z)$	streamwise mean velocity
u_{rms}	root-mean-square of streamwise velocity fluctuations
$\frac{d}{dx} \bar{P}_o(x, t)$	static pressure gradient
$\Phi_{pp}(f)$	pressure frequency spectrum
p_{rms}	root-mean-square of the pressure fluctuations
$\Phi_{p_i, p_j}(\xi, f)$	pressure cross-spectrum
$\alpha_{p_i, p_j}(\xi, f)$	cross-spectrum phase
$U_c(\xi, f)$	narrow-band convection velocity
L_x, l_x	Macro, micro length scales
T_o, τ_{min}	Macro, micro time scales

2.5 Statistical Error Definitions

The full space-time power spectral density functions may be computed by Fourier transforming correlation covariance functions through equation (2.30) or by direct Fourier transformation of the time history records. Since the introduction of finite Fourier transform algorithms around 1965, the latter approach has dominated due to the faster processing times. For instance, the time to compute the correlation covariance through equation (2.29), then Fourier transforming into spectral space, typically takes approximately N^2 calculations where N is

the number of ensemble averages. The advent of the Cooley-Tukey algorithm in 1965 for the calculation of a complex Fourier series requires approximately $N \ln(N)$ calculations. Special firmware has been designed with programmed instructions for fast-Fourier-transformation and are the primary instructional set within dual channel analyzers used in the laboratory.

However, these computations are only estimates and not the actual or true values of the complete functions, as one always deals with finite time records. Estimates of the errors in computing such functions have been derived by Bendat and Piersol (1978,1980). These errors form two classes described as bias and random. Bias errors are systematic errors that appear with the same magnitude and at the same frequencies from one analysis to another. For instance background pump noise or vibrational energy transferred through walls to the transducer contribute to bias errors. Random errors, on the other hand, are considered a haphazard scatter in the results and are due to averaging operations conducted over a finite time window or number of ensembles. Bendat and Piersol have shown biasing errors to be second order, thereby contributing less overall decay to spectral estimates. For the broad band spectrums (typical of velocity and wall pressure spectral functions), random errors have more significance. The non-dimensional error estimates ϵ , for the spectral functions computed in this experimental study, are listed below with N equal to the total number of ensembles or records and N_p equal to the total number of points per record.

$$\text{auto - spectrum} \dots \epsilon[\Phi_{pp}(\omega)] = \frac{1}{\sqrt{N}} \quad (2.52)$$

$$\text{cross - spectrum} \dots \epsilon[\Phi_{pp}(\xi, f)] = \frac{1}{\gamma(\xi, f)\sqrt{N}} \quad (2.53)$$

$$\text{coherence} \dots \epsilon[\gamma^2(\xi, f)] = \frac{\sqrt{2}[1 - \gamma^2(\xi, f)]}{\gamma(\xi, f)\sqrt{N}} \quad (2.54)$$

$$\text{phase} \dots \epsilon[\alpha(\xi, f)] = \frac{[1 - \gamma^2(\xi, f)]}{\gamma(\xi, f)\sqrt{N}} \quad (2.55)$$

$$\text{fluctuations} \dots \epsilon[p_{rms}^2] = \sqrt{\frac{2}{NN_p}} \quad (2.56)$$

All of the quantities listed on the righthand side of the above equations are considered to be the true functions. Their values are not known a priori, so the common practice is to insert the calculated values for these functions. As mentioned, the finite time records available in most analyses are the primary contributor to the random error, hence all the error definitions above are shown to be proportional to N , the number of records or ensembles. While the error in the

auto spectrum is proportional only to N and that for the *rms* of the fluctuations proportional to $N N_p$, all the other error estimates are functions of the true coherence between two signals and are also functions of frequency. In either case, to decrease the error, hence improving the confidence level in the accuracy of obtaining all the functions, it is apparent from equations (2.52) to (2.56) that the larger the value of N , the more accurate are the computed estimates. In the present study, the computational and physical experiments had values of N equal to 2048 and 1750 respectively. This results in error estimates of 0.024 and 0.022 for the power spectral density function for the physical channel flow and numerical simulation experiments respectively.

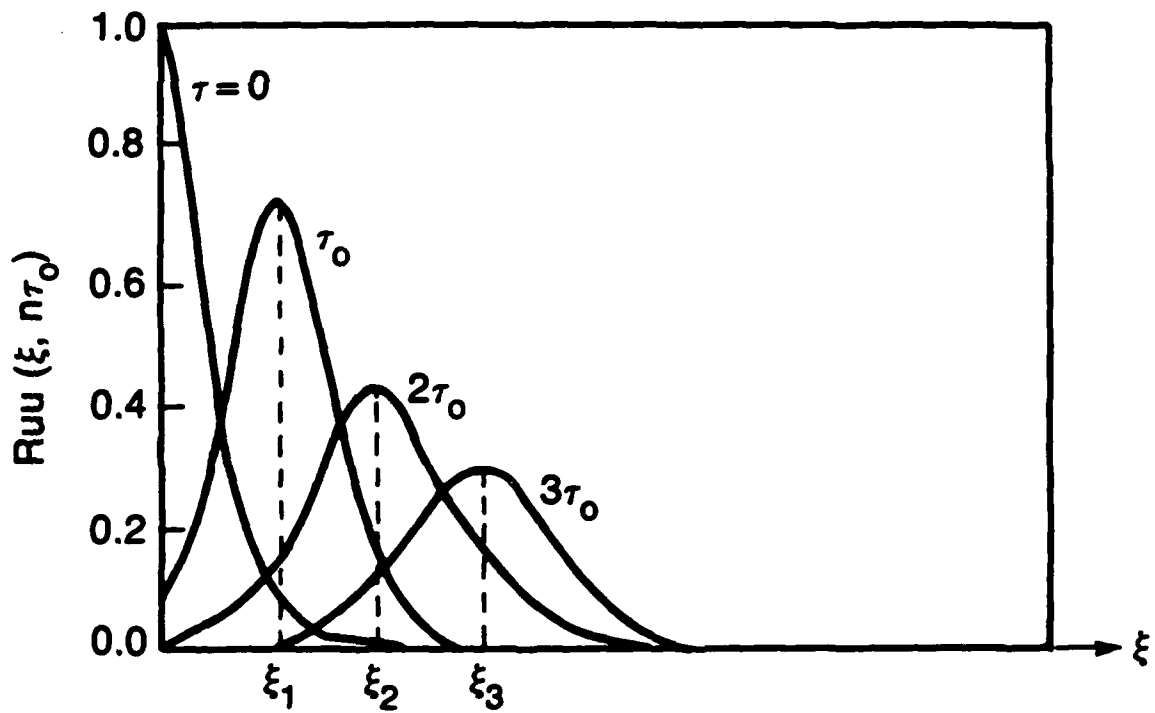


FIGURE 2.1a. SPACE-CORRELATION FOR FIXED TIME DELAY

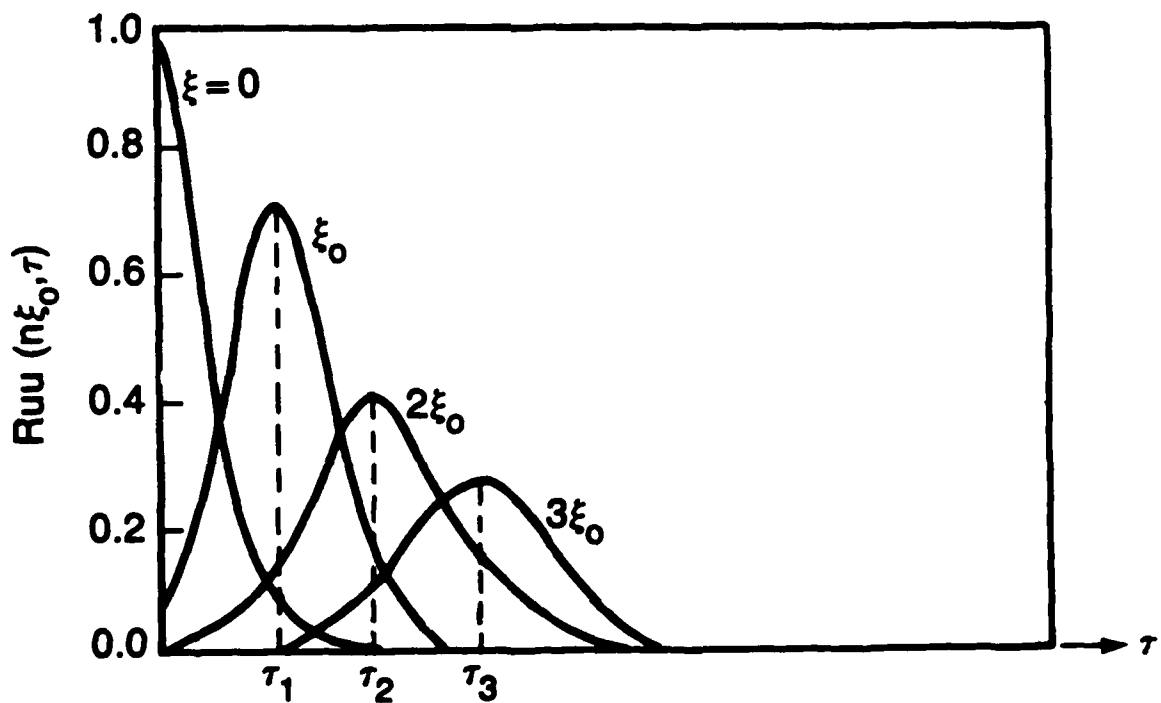


FIGURE 2.1b. TIME-CORRELATION FOR FIXED SPATIAL SEPARATION

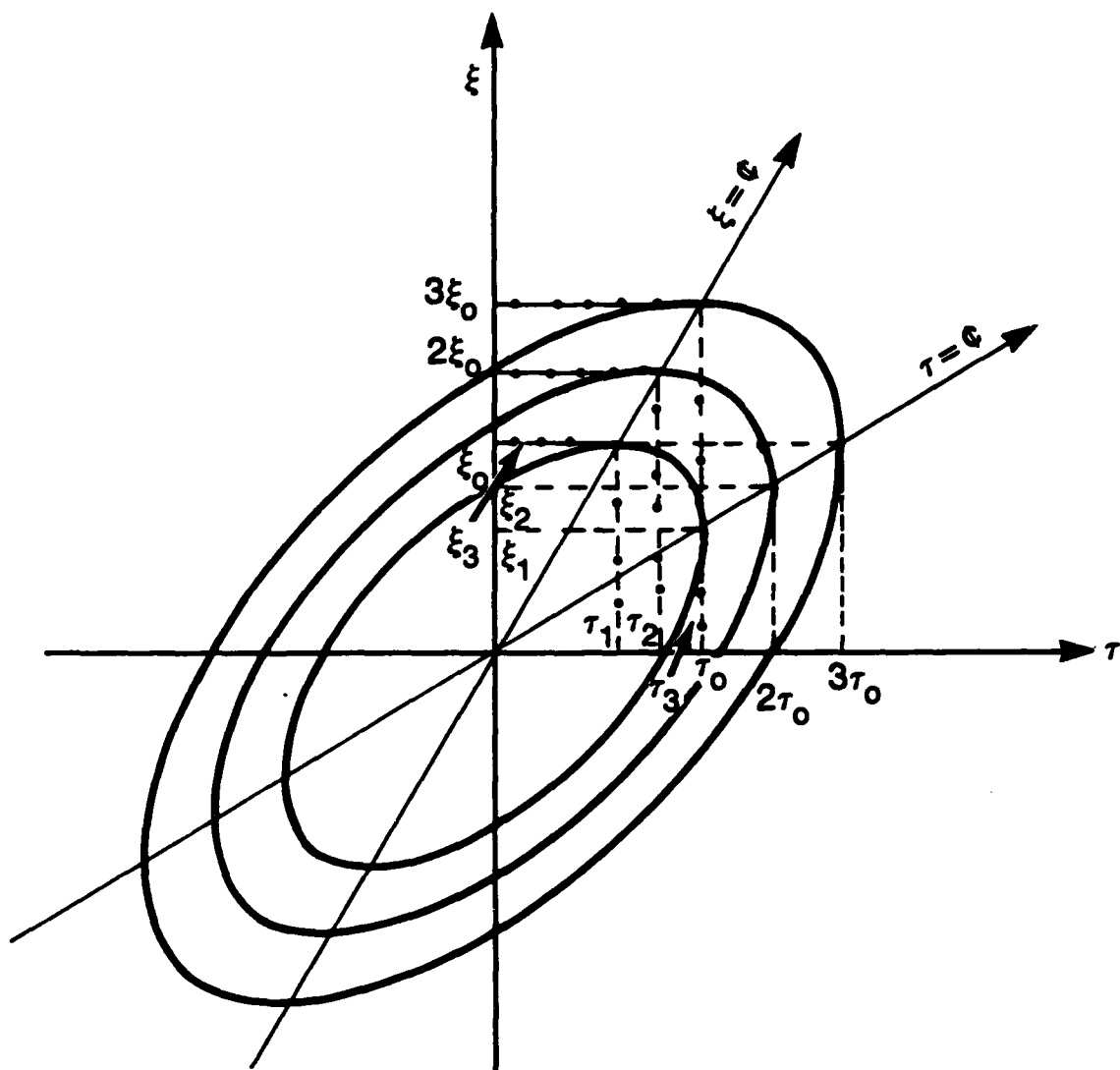


FIGURE 2.2. FULL SPACE-TIME COVARIANCE CONTOURS $R(\xi, \tau)$

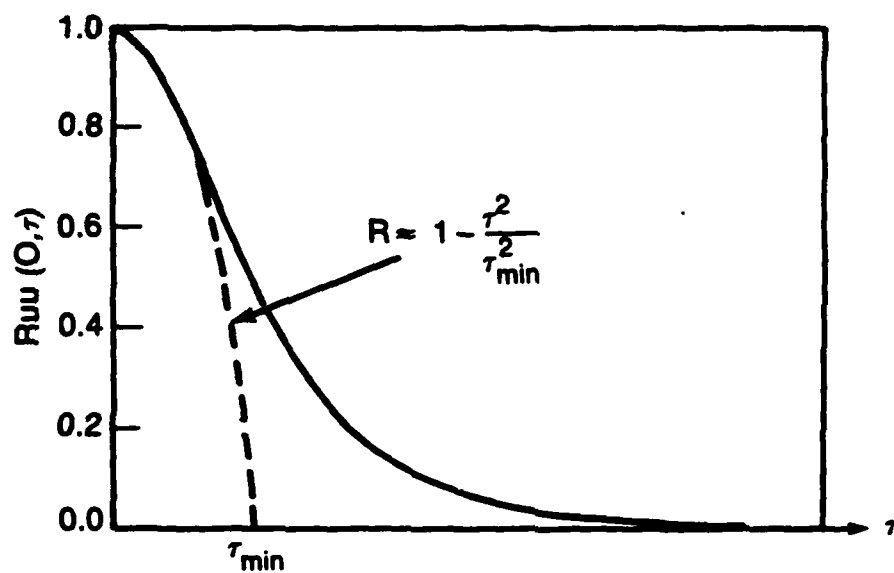


FIGURE 2.3. AUTO TIME-CORRELATION COEFFICIENT FOR VELOCITY (zero spatial separation)

CHAPTER 3 DESCRIPTION OF PHYSICAL AND COMPUTATIONAL EXPERIMENTS

3.1 Physical Experiment

Upon the conception of this experimental endeavor, a number of critical elements had to be considered. The first was to choose a facility that would ensure the presence of a fully developed two-dimensional turbulent flow with low centerline turbulence intensity level, such that boundary layer variables (both dynamic as well as kinematic) could accurately be measured. Secondly, due to the small intensity levels of the wall pressure being made, this facility should have low noise characteristics, in terms of facility related vibration and propagating acoustic noise which typically contaminate wall pressure measurements in liquid flow environments. Thirdly, the facility should accommodate test plates of various configurations and retain an uncontaminated flow characterization, not withstanding numerous insertions of such devices. Finally, the facility should have a wide range of operating conditions.

While the aforementioned specifications may appear formidable, they represent the basis for performing high quality measurements, particularly of a generic nature, to facilitate accurate comparisons with similar experiments. In particular, it was mentioned previously that these experimental results would serve to validate the correctness of more recent numerical simulations which solve the full Navier-Stokes equations in the same geometrical configuration. We can not therefore, overemphasize the importance of ensuring that the above designated criteria be strictly enforced.

3.1.1 Channel Description

The chosen facility was originally constructed in 1978, at the Naval Research Laboratory, under the auspices of the Office of Naval Research (ONR) compliant coating research program of study. A unique feature characteristic of this facility is that it operates in a blow-down configuration to eliminate contaminating noise due to structure vibration and/or vibrationally induced acoustic phenomena which are typical of a recirculating system. The flow through the channel can be driven by a gravity head alone or by a combination of increasing air pressure and gravity head which serve to produce a constant discharge rate or driving pressure.

Figure 3.1 shows a schematic of the NRL water channel in its present configuration. The major features of the facility are a pressure tank, upstream liquid reservoir, turbulence management section, entrance section for the developing turbulent flow, the test section and a downstream reservoir. All of the features, other than the pressure tank and upstream reservoir, are enclosed in a temperature controlled, acoustically isolated laboratory. The pressure tank has a volume of $14.16m^3$ with a working pressure of $552kpa$ ($80psig$). It is equipped with an inlet, outlet, relief valve, drain, pressure gage and an inspection manhole. The pressure tank is continuously charged to its working pressure with flow control valves at the outlet for regulating the discharge pressure. The upstream liquid reservoir is a stainless steel tank approximately $10m$ high, with a diameter of $3m$ and a volume of $28.4m^3$ ($7000gal$). There are five ports of differing sizes to accommodate a primary inlet and outlet and for various other instrumentation purposes. The tank is filled through a $5.08cm$ diameter pipe leading to the bottom of the reservoir. The outlet, which couples at the same location as the fill pipe, is a $10.15cm$ copper pipe which is routed inside the laboratory through a flow control valve to the turbulence management section. At the downstream end of the facility is a reservoir for collection of the working fluid. This is an open tank of welded steel construction with a total capacity of $28.4m^3$ ($7000gal$).

In figure 3.2, a more detailed schematic indicates the interior components of the channel. The turbulence management section consists of a number of sectional screens and honeycombs with an entrance component having a contraction ratio of approximately 7 to 1. The developing turbulent boundary layer proceeds through a constant cross-sectional area member, approximately 4 meters in length, which has an aspect ratio of 18 to 1 with a channel height of $2h = 2.54cm$ ($1inch$). The test section contains a number of large plates within which smaller test windows or transducer plates may be arranged in many different configurations. These windows/plates allow for the placement of small pressure probes or the non-intrusive access of the beams of a laser Doppler anemometer. The ratio of downstream distance of the measurement point to the half-height of the channel x/h , is 320. This value of x/h is well within the region of fully developed turbulent channel flow (Hussain and Reynolds 1975).

The side walls of the channel are constructed from $2.54cm$ high by $10.16cm$ ($1 \times 4 inches$) wide continuous pieces of clear plexiglass. For single point velocity measurements, an LDV system may enjoy access through these side panels if necessary. The entire channel system is located approximately $1.22m$ ($4ft$) off the floor on massive aluminum I-beams. The massive supports ensured that a minimal amount of vibrational energy would be transferred through

to the channel inner walls and subsequently, the working fluid. The test section is described in more detail later in this chapter.

The above components coupled with a full reservoir and the charged pressure tank, provide a range of velocities at the test section of 0.22 to 2.44 m/sec (0.72 to 6.0 ft/sec) corresponding to Reynolds numbers based on channel half width ($R_h = U_{avg}h/\nu$) of 3000 to approximately 30,000.

3.1.2 Operational Characteristics

The basic principle of operation is to control the bulk flow rate in the test section by maintaining a constant total dynamic head or driving pressure from the inlet to outlet. This has typically been characterized as a "blow-down" facility. By monitoring the pressure at some point in the upstream reservoir and subtracting the pressure at the channel exit, a differential (dynamic) driving pressure, characteristic of a specific bulk or average velocity can be continuously monitored. As mentioned previously, there is a large upstream liquid reservoir which provides the working fluid. However, the quantity of fluid is finite and, as the flow proceeds through the system, this measured pressure decreases as the fluid level drops in the reservoir. In order to maintain a constant driving pressure, air is added above the liquid at such a rate as to compensate for the liquid deficiency. From the equation of continuity (for incompressible flow), we may define the following relations.

$$\text{flow rate} = Q(t) = A_r V_r(t) = A_c V_c(t) = \text{Constant} \quad (3.1)$$

$$V_r(t) = -\frac{dH(t)}{dt} \quad (3.2)$$

Here, Q is the discharge rate, A_r and $V_r(t)$ are the cross-sectional area and average velocity in the upstream reservoir and A_c , $V_c(t)$ are the corresponding values in the channel. $H(t)$ is the height of the liquid as a function of time. Combining equations (3.1) and (3.2), results in,

$$V_c(t) = \frac{A_r}{A_c} V_r(t) = -\frac{A_r}{A_c} \left(\frac{dH}{dt} \right) \quad (3.3)$$

By monitoring the height of the liquid fluid as a function of time (hence the reservoir's velocity), equation (3.3) shows a simple relation for determining the channel's velocity. For a fixed starting level of liquid, one would obtain the same velocity for all runs. Therefore, as shown in figure 3.1, a flow control valve is inserted in front of the turbulence management section. By choosing various openings of the valve, one may obtain a number of velocities as indicated previously.

A Celesco model 455 differential pressure transducer is used to effect this monitoring function. This transducer requires a specific stainless steel diaphragm for each pressure range of operation and can be statically calibrated for each run if necessary. For the blowdown procedure, a 10psig diaphragm is inserted within the transducer and subsequently calibrated as the reservoir is being charged with working fluid (A calibration curve for this transducer is shown in the next section.). The output is 0 to 10 voltsDC with a frequency response good to 4000Hz. In order to facilitate the monitoring of this pressure and subsequent calculation of average velocities, an HP-200 series lab scientific computer with a multi-channel 721 multi-processor is utilized. The Celesco transducer output is sampled in time at a 1000Hz with 500 pts taken over half-second periods and averaged such that at time t_j , dH/dt may be calculated.

Figure 3.3 shows typical results of the monitoring instrumentation for four different constant velocities (Reynolds numbers). The height of the liquid reservoir, monitored over time, is recorded with the respective lines for each velocity representing a least squares best fit to the data. As the equation of continuity suggests, the data is linear to a great deal of accuracy; better than 1% repeatability for the same velocity. With respect to the velocity range indicated previously, the total amount of fluid available resulted in run times from 15min to over an hour for the highest to lowest velocities respectively.

3.1.3 Test Section

The channel contains large removable sections that provide access within the channel as well as a platform for the insertion of smaller test plates. Thus the experimenter has the ability to design arbitrarily any desirable test plate/probe combination to insert within the flow system. For this experiment, a 7.97cm (ID) hole was drilled within the center of one of the removable sections with 8 symmetric bolt holes for fastening purposes. A small test plate 7.97cm (OD) in diameter was designed for insertion of the small flush-mounted transducers. Figure 3.4 indicates the location and orientation of this test plate with respect to the large removable section, and figure 3.5 presents a detailed illustration of the placement of holes for the transducers. As shown, there were 20 holes drilled 0.17 cm in diameter in a linear array approximately 0.20cm apart. This linear array was offset from the centerline by 2.54cm with a similar hole aligned with the first hole in the array, symmetrically placed the other side of the centerline. This spanwise transducer would be used for noise cancellation purposes. Only 5 transducers were available for this experimental study, with four inserted within the linear array.

The eight symmetric bolt holes provide a means to rotate the plate to differing angles of theta (with respect to the streamwise direction) to extract more detailed wavenumber dependence if desired. For this experiment, data was taken at the theta angle of 0 degrees only and will be characterized as inline or streamwise data.

Since only four transducers were placed in the flow direction, the additional holes were filled with *rtv*, smoothed even with the surface and lightly sanded with emery cloth to exact a flush surface. The entire plate was anodized to prevent rust and/or additional corrosive deposits from adhering to the surface.

As indicated in figure 3.4, the large removable plate was 4.445cm thick and also indicates that the test plate was of a similar thickness. In order to ensure a flush mating of both plates, the test plate after fabrication, was inserted within the large removable section and sanded down to a tolerance of 24.5 μ m (microns). An O-ring maintained a water-tight seal once the two plates were inserted within the flow channel.

3.1.4 Wall Shear Stress Measurements

The geometry being investigated with rectangular cross-section, is known as plane Poiseuille flow when the aspect ratio is large, and the flow is steady and incompressible. If one chooses a differential volume located at that point where the flow is considered fully developed and analyzes the applicable surface forces, one may obtain the well known relation for wall shear stress as represented by,

$$\tau_{wall} = -h \frac{dP_o}{dx} \quad (3.5)$$

Here, h is the channel half-width, P_o is the static pressure and x is the spatial coordinate in the flow direction. Thus by an appropriate measurement of the pressure gradient within the channel at each respective Reynolds number, the wall shear stress and hence the shear velocity, $u^* = \sqrt{\tau_{wall}/\rho}$ may be determined. A number of 1/4 inch taps are placed along the side wall of the channel, approximately 0.3048m apart. Each tap was connected in parallel to a Celesco model 451 differential transducer containing a 0.1psig stainless steel diaphragm. This type transducer is simple to calibrate. A manometer was strategically placed at the channel test section and coupled to the pressure taps via appropriate tubing. Distilled water was added to the manometer at various heights above the channel centerline which provided a simple means for calibration. Figure 3.6 shows a typical calibration curve for this transducer as well as the previously mentioned model used for monitoring the height of water in the upstream

reservoir. A least squares curve was fitted to the data in each case, and as shown, the linear characteristics of the transducers were validated.

During a particular channel run at constant velocity, the pressure gradient transducer was systematically switched through each of the 12 pressure taps and a time history of the transducer output was recorded. An average for each record was then obtained and plotted versus channel location. Figure 3.7 indicates the linearity throughout all velocities tested and further substantiates that the channel's velocity is being maintained constant. Since the static pressure is linear, the slope of each line (a constant) may be used in equation (3.5) to determine the wall shear stress and hence shear velocity, for each Reynolds number investigated. Jones (1976) performed an extensive study demonstrating that high aspect ratio plays an extremely important role in determining the friction factor ' λ '. The friction factor is defined by,

$$\lambda = \frac{4\tau_{wall}}{Q} \quad (3.6)$$

Jones showed that in order for data from differing aspect ratio ducts to demonstrate similarity for turbulent flows, the Reynolds number based on hydraulic diameter must be modified. Using the following definitions,

$$D_h = D_{hydraulic} = \frac{4 \text{ Area}}{\text{Perimeter}} \quad (3.7)$$

$$R_{D_h} = \frac{U_{avg} D_h}{\nu} \quad (3.8)$$

the friction factor λ , can be plotted vs. $R_{d_h}^*$ which is defined by Jones as,

$$R_{d_h}^* = \Psi(A_s) R_{D_h}. \quad (3.9)$$

$\Psi(A_s)$ represents a function of aspect ratio A_s , which Jones was able to determine for various sized rectangular ducts. Jones further showed that to second order, this function could be represented by the following.

$$\Psi(A_s) = \frac{2}{3} + \frac{11}{24A_s} \left(2 - \frac{1}{A_s} \right). \quad (3.10)$$

In figure 3.8, typical data for the Reynolds numbers investigated have been plotted together with the well known relations of Prandtl and Blassius.

3.1.5 Measurement and Data Acquisition of the Mean Flow and Turbulence

Before making any pressure measurements of a generic nature, a characterization of the channel's velocity was desirable. The purpose being to ensure the two-dimensionality of the flow and that no extraneous large scale structure from the side walls interfered with the core flow.

Velocity was measured with an argon TSI laser Doppler velocimeter (LDV) model No. 9100-10 which was a 3-component (5 beam) system operating in backscatter mode. Originally, it was desired to pass the beams through a window located in one of the removable plates opposite the pressure transducer test plate. However, when the first measurements were attempted, it was found that the closest position that the probe volume could be placed to the wall was on the order of 0.025cm which was half the length of the ellipsoid characterizing the shape of the probe volume. This corresponded to a Y^+ value of approximately 100, which was in the outer region of the boundary layer completely ignoring the viscous sub-layer and buffer layer. The optics which were available prevented reducing this characteristic dimension unless first passing through a beam expander. Doing so however, resulted in a reduction in the focal length, thus preventing going through the window. It was decided that the clear glass making up the side walls of the channel, provided suitable access for two beams lying in a horizontal plane. By passing the beams through the 3.75 beam expander module, one could reduce the ellipsoid diameter to approximately 0.015mm , resulting in a Y^+ value on the order of 5 to 15 depending on the velocity. This did not allow for a complete characterization of the viscous sub-layer, but the buffer layer was well indicated.

An optical table 1m by 2m provided a flat bed upon which the entire optical train as well as the laser itself was placed. The optical table rested on the two dimensional segment of a milling machine which provided accurate measurements to within 0.025mm in two directions of a horizontal plane. The entire apparatus then rested on an aluminum frame connected at three points with stepping motors. This provided a simple method of aligning the two beams in a horizontal plane plus providing profile capability in the vertical direction to within 0.015mm .

The two beams which passed through the side walls were taken from the blue beam of an argon laser having a wavelength of 488nm . Both beams lay in a horizontal plane and one was shifted with a bragg cell by 2MHz such that the fringes would appear optically to move in the opposite direction to the mean velocity. After exiting from the laser, both beams pass through the optical train approximately 22mm apart then pass through the beam expander module.

At the exit from the final lens, both beams are 80mm apart, have an included angle of 18deg with a final focal length of 455mm. At the intersecting point of the two beams, an ellipsoid is formed with a characteristic length and diameter of 0.15mm and 0.03mm respectively. This resulted in being able to traverse to the wall as close as 0.015mm in the vertical direction.

In backscatter mode, the reflected light from the probe volume was collected by the return optics, focused on a photo-multiplier tube with an appropriate analog signal sent to a model 9898 TSI counter. This counter included all appropriate instrumentation for post processing of the frequency shifted beams and scattered light to include validation of the particle, counting of fringe crossings and tabulation of the time between validated bursts. This information was then sent in real time to an HP-600 computer and stored for further analysis at a later time. At each station chosen in a velocity profile for each respective run, 12,800 validated points were collected, stored on hard disc and the probe volume traversed to the next profile station. These data could then be processed for mean and fluctuating components of velocity, \bar{U} and u respectively. Figure 3.9 shows a schematic of the test section with the location of the two coincident beams. Three stations were chosen to investigate and are indicated by the points A,B and C in the diagram. As mentioned earlier, the channel is 18 inches wide, and these station points were chosen to bracket the inner core of flow as far as the beam focal length would reach. Station A,B and C correspond to 5, 8 and 11 inches from the inside of the near wall and bracket the area of the small wall pressure test plate. Three profiles were taken at each location to check repeatability. Figure 3.9 also indicates a traverse labeled "a - - - - a" which corresponds to the path made by the focal point of the two beams, from the near side wall into the flow at various distances from the bottom or top wall. These traverses were inserted to substantiate that flow was indeed two dimensional and that no side wall effects interfered with the core flow. For more detailed information on the general theory of LDV operation and that more specific to the model 9100-10, the reader is referred to Durst *et al.*(1981) and TSI (1985).

3.1.6 Measurement and Data Acquisition of the Wall Pressure Fluctuations

Five small transducers were embedded flush at the wall within a small test plate in the test section. These transducers are model 8514-10 piezo-electric sensors manufactured by ENDEVCO. Their nominal sensitivities as reported by the manufacturer, were $-227dB$ referenced to $\frac{1.0volt}{\mu pa}$ with a flat frequency response out to 140kHz. The active area of the transducer, as reported by Galib and Zandia (1984), is approximately 0.5mm. This dimension gives a ratio of

h/d_t equal to 25/1, and a viscous scale, $d^+ = (d_t u^*)/\nu$ in the range 20 to 40. The signals from each transducer were amplified to a suitable level, low-pass filtered to prevent aliasing, and then simultaneously sampled in time, digitized and stored on tape for post processing. Hence, for each velocity run, simultaneous records in time of all five transducers were recorded.

The data/acquisition was accomplished with a Quad Systems, Inc.(QSI) 16 channel model 721 data processor. This unit includes a 12-bit A/D converter, 16 sample holds, a variable quartz clock providing sampling frequencies from 0.5 to 500kHz resulting in an overall throughput storage capability of 23,000 samples/sec. The storage medium was a cipher tape drive utilizing IBM compatible phase encoded (PE) formatting and stored the data as two-byte integer words in 2's complement binary on a 10 inch reel. The versatility of the system was realized by its large storage capacity (approximately 25 mega-words), and the capability of the tape medium to be read by almost any tape reader that has the ability to read variable length records on 1600 bpi 10 track 1/2 inch tape. Figure 3.10 illustrates the overall pressure measuring system. For the Reynolds numbers investigated, a sampling frequency of 4kHz was found sufficient to contain all relevant information. The overall throughput was therefore $5 \times 4,000 = 20,000$ samples/sec which was effectively handled by the tape drive's throughput processor.

The manufacturer's reported specifications on these transducers are generally not realizable in the laboratory due to the additional impedances contributed by the various pieces of instrumentation used for amplification and/or filtering. In addition, as will be addressed in more detail later, due to the nature of some of the statistical functions necessary to be calculated, it was imperative to have an accurate estimate of the sensitivity of each transducer during each respective run. In order to satisfy any curiosity about bandwidth or amplitude limitations, all transducers were calibrated in a small J-11 piston actuated standtube calibrator filled with water. The calibrator could be operated over a range from 40Hz to 10kHz and each transducer was connected to all expected instrumentation with appropriate amplification and filter bandwidths preset. These small transducers are very fragile hence, susceptible to destruction by frequent removal from the test plate for subsequent calibrations. Therefore, since the flow within the channel is considered homogeneous in the plane of the wall, it was only necessary to carefully remove a single transducer for calibration. During subsequent runs, comparison with the other transducers on a continuous basis afforded updated calibrations. Figure 3.11 shows the individual calibrations of each transducer over a bandwidth of 500Hz,

and figure 3.12 shows the power spectral density (PSD), $\Phi(f)$ of three representative transducers during typical Reynolds number runs of $R_h = 10,000$ and $15,000$. As indicated, other than spurious electronic signals seen by each transducer, virtually identical results are obtained throughout the examined bandwidth.

3.1.7 Software Approach for Spectral Computations

All transducer data was recorded simultaneously in time and transferred to a VAX 780 computer. At the Naval Research Laboratory, these computers act as front end processors to a CRAY X-MP/24 super computer. The data were transferred to the CRAY through the VAX front ends, and software was written to analyze the time dependent data. For each velocity run, the data were read into appropriate arrays and the respective transducer sensitivities applied immediately. The software computed the power and cross spectral densities and their Fourier transform pair, auto and cross correlation functions, together with all coherence and phase information where appropriate. As an example of the speed of the CRAY processing, the software upon execution could process all data from one Reynolds number run, providing all possible combinations of frequency spectra and time correlation functions (as indicated in section 2.3) for more than 12 transducers in approximately 2 1/2 minutes. More than 100 files could be generated and stored simultaneously for each velocity run.

The choice of using the software approach was predicated on the ability of securing almost immediate turn-around on processed data. This allowed for various combinations of transform size and number of ensemble averages to be investigated to extract as much relevant information as possible. One of the goals of this experimental study was to compare a physical experiment with a computational experiment. This software method of analysis provided compatibility with the processing of both sets of data. As a final comment, the cancellation methodology outlined in the next section, was more easily applied to the data of the physical experiment by software processing.

3.1.8 Cancellation Methodology

Wambsganss and Zaleski (1970) first introduced a temporal subtraction scheme in an attempt to cancel low frequency contaminating noise within fully developed annular flow. Refinements were made by Wilson *et al.* (1979) and the present author in 1981. If the contaminating noise was acoustic in origin and could be assumed to propagate as a plane wave, this temporal

subtraction scheme worked quite well, provided pressure signals were dealt with. However, one very important assumption implicit within these methods but "not" explicitly pointed out in this past work, is the fact that "any" cancellation scheme involving the addition and/or subtraction of transducer output signals, a priori assumes that the individual transducer sensitivities must be equal. This seems trivial, but as shown below, there has been a very subtle misconception in the past work related to transducer output and sensitivity.

First, assume a simple 2 transducer arrangement as depicted in figure 3.13 within a rectangular channel or along a flat plate. U represents the velocity in the streamwise direction and transducers 1 and 2 are separated transverse to the flow velocity. The distance between the transducers indicated as l is very large ($l \gg 0$) such that the signal due to turbulence at transducer 1 is not correlated with the turbulence at transducer 2. The assumption is further made that the contaminating noise whether narrow band acoustic in origin, or of a wide band random phenomena, is fully correlated at each location with itself but not with the signal due to turbulence. Assume that the pressure signal at either location is the sum of the signals due to noise, "n" and turbulence "t" as represented by the following relation.

$$p_j = t_j + n_j = p_{t,j} + p_{n,j} \quad (3.11)$$

Note, the key point being made is that equation (3.11) refers to "actual" pressure signals and "not" voltage signals. In most analyses, the temptation is strong to assume that sensitivity is just a constant, that may be applied at any point in the processing of data that is convenient for the researcher. When the desired output deals with transformed quantities such as obtained from Fourier transforms, this is not necessarily true. Using b_j and e_j as the sensitivity and voltage respectively, the following relations can be formed.

$$\text{(total pressure)} \quad p_j = b_j e_j \quad (3.12a)$$

$$\text{(pressure due to turbulence)} \quad p_{t,j} = b_j e_{t,j} \quad (3.12b)$$

$$\text{(pressure due to noise)} \quad p_{n,j} = b_j e_{n,j} \quad (3.12c)$$

and,

$$p_j = b_j e_j = b_j e_{t,j} + b_j e_{n,j}. \quad (3.13)$$

In the laboratory, the voltage signals e_j , $e_{t,j}$, and $e_{n,j}$ are the components usually considered rather than the pressures themselves. In fact the whole field of transducer technology is geared to transforming the physical entities of pressure, force, length and time (to name a few) to an easily measured voltage or current signal with appropriate sensitivity.

The following conventions are used. Lowercase letters will represent the signals in temporal space, i.e., as a function of time, and capitalized letters will refer to their Fourier transforms into spectral space. The braces $\langle \dots \rangle$ represent the expected value over all ensembles and the superscript $*$ represents the complex conjugate of a Fourier transform. Φ_{pp} and Φ_{ee} will represent the auto or cross spectrums of the total pressure and voltage signals respectively. As an example, the auto spectrum of the pressure at a transducer 'j' can be represented as,

$$\begin{aligned}\Phi_{p,p_j} &= \langle P_j^* P_j \rangle = \langle (T_j + N_j)^* (T_j + N_j) \rangle \\ &= \langle (T_j^* T_j) + (N_j^* N_j) \rangle \\ &= \Phi_{p_t, p_t} + \Phi_{p_n, p_n},\end{aligned}\tag{3.14}$$

Assuming the transducer signals are due to voltages only, then the total sensor signal is,

$$e_j = e_t + e_n,\tag{3.15}$$

and the Fourier transform in spectral space results in the following.

$$\begin{aligned}\Phi_{e,e_j} &= \langle E_j^* E_j \rangle = \langle (E_t + E_n)^* (E_t + E_n) \rangle \\ &= \langle (E_t^* E_t) + (E_n^* E_n) \rangle \\ &= \Phi_{e_t, e_t} + \Phi_{e_n, e_n},\end{aligned}\tag{3.15}$$

Furthermore, it can be shown that,

$$\Phi_{e_t, e_{t,j}} = \frac{1}{b_j^2} \Phi_{t,t},$$

and,

$$\Phi_{e_n, e_{n,j}} = \frac{1}{b_j^2} \Phi_{n,n},$$

hence,

$$\Phi_{p,p_j} = b_j^2 \Phi_{e,e_j} = b_j^2 [(\Phi_{e_t, e_{t,j}}) + (\Phi_{e_n, e_{n,j}})].\tag{3.16}$$

The temporal subtraction scheme based on the assumptions given, consists of performing a temporal subtraction between the signals from transducers 1 and 2 and then correlating the resulting subtracted signal with either transducer. In other words, the power spectrum desired can be represented as, $\Phi_{(p_1 - p_2)p_1}$. Bear in mind that the assumptions state that the turbulence at locations 1 and 2 are not correlated with each other, and the noise is correlated with itself

and at either location, but not with the turbulence. Performing the required algebra results in the following.

$$\begin{aligned}
 \Phi_{(p_1-p_2)p_1} &= \langle (P_1 - P_2)^* P_1 \rangle \\
 &= \langle (T_1 + N_1 - T_2 - N_2)^* (T_1 + N_1) \rangle \\
 &= \langle T_1^* T_1 + N_1^* N_1 - N_2^* N_1 \rangle \\
 &= \Phi_{p_1 p_1} + \Phi_{p_{n_1} p_{n_1}} - \Phi_{p_{n_2} p_{n_1}}
 \end{aligned}$$

The last two terms are assumed equal and therefore cancel resulting in,

$$\Phi_{(p_1-p_2)p_1} = \Phi_{p_1 p_1} \quad (3.17)$$

If the same analysis is performed on the voltage signals, with proper substitution of the sensitivities, the following equation is obtained.

$$\Phi_{(p_1-p_2)p_1} = \Phi_{p_1 p_1} + \left(1 - \frac{b_1}{b_2}\right) \Phi_{p_n p_n} \quad (3.18)$$

As indicated, equations (3.17) and (3.18) are the same, "if and only if" the sensitivities b_1 and b_2 are equal. It makes no difference whether the subtraction is performed in "temporal" or "spectral" space. The problem arises due to the researcher conducting analyses in which the real signals (with proper units) are being dealt with on paper, whereas in the laboratory, voltage signals are the entities being recorded.

The above monolith seems simple, but in reality poses enormous possibilities of error when dealing with multi-sensor arrays. For this experimental study, the sensitivities of all five transducers would have to be maintained constant and equal throughout every experimental run. This was virtually impossible due to the finite time allowed for each experimental run as well as the limited instrumentation available. However, if the transducers have been consistently calibrated, such that precise knowledge of their sensitivity is known at all times, then the software approach to processing the data as presented above provides a convenient means for applying the sensitivities to each channel of data as it is read back into the analysis program. In these circumstances, the actual "pressures" are being manipulated without introducing any errors.

To backtrack slightly, the temporal subtraction scheme outlined above works quite well, provided the contaminating noise is acoustic in origin and propagates as a plane wave across any cross-sectional area of the channel. This assumption is quite restrictive and in particular,

doesn't provide a means of cancelling random vibrational energy that may interfere with the transducer signal. Horne and Handler (1989) have presented a unique cancellation scheme utilizing the concept of a "Wiener" filter (Wiener, 1949). This filter was designed originally to cancel wide band frequency signals in electrocardiography and the broad-band interference in the sidelobes of an antenna array and assumes that a signal free reference is available which represents the contaminating noise. In applying the filter technology to the measurement of wall pressure fluctuations, certain assumptions provided the author with a unique derivation of error relationships which precisely dictated the maximum error possible in the calculation of auto and/or cross spectral properties.

To briefly summarize, transducer 1 is considered to be the signal free reference in this experimental study. It is assumed to be separated from the other transducers in the linear array, a distance sufficient to insure zero correlation of turbulence. In addition it is assumed that the channel represents truly homogeneous turbulent flow, such that the auto spectral densities at each location are identical. As a final assumption, the noise at any location is assumed to be uncorrelated with the turbulence at neighboring locations. Note, no stipulation has been put upon the propagation characteristics of the noise, whether it is acoustic in origin, single frequency or random by nature. The only assumption made, is that the noise represented at each location has "finite" coherence with the noise located at transducer 1, and that this coherence is measurable. The results of the cancellation scheme are presented below for the auto and cross spectral densities Φ_{p_i, p_i} and Φ_{p_i, p_j} of the turbulence respectively. The reader may refer to Horne and Handler (1989) for a more detailed presentation of the method.

$$\text{Auto Spectrum} \longrightarrow \Phi_{p_i, p_i} = \Phi_{p, p} (1 - \gamma_{1i}^2) \quad (3.19)$$

$$i = 2, 3, 4, 5$$

$$\text{Cross Spectrum} \longrightarrow \Phi_{p_i, p_j} = \Phi_{p, p} - \frac{\Phi_{p_1 p_i}^* \Phi_{p_1 p_j}}{\Phi_{p_1 p_1}} \quad (3.20)$$

$$i = 2 \text{ only, and } j = 3, 4, 5 \text{ only.}$$

The power spectral densities in equations (3.19) and (3.20) are computed from the sensor signals themselves and the order of the indices is imperative. Note, other than the denominator in the second term of equation (3.20), the quantities computed are complex variables with $\Phi_{p_1 p_i}^*$ representing the complex conjugate of this cross spectrum respectively.

The above two relations were used extensively in this study to obtain true measurements of the power spectral densities, coherence and phase for the physical experimental data. The results thus obtained provide new information not yet published and confirm existing theories on the ' ω^2 ' dependence at low frequencies for the wall pressure fluctuation amplitude.

3.2 Computational Experiment

The wavenumber-frequency spectrum of turbulence-induced wall pressure fluctuations is of both fundamental as well as practical interest. As mentioned previously, this spectrum may provide insight into the fundamental structure of turbulent flow in the near-wall region. From a practical point of view, it may allow prediction of the small amplitude vibration response of a structure to turbulence-induced wall pressure fluctuations. In the past, however, this spectrum has proven somewhat elusive due to its difficulty in being measured. The numerical simulation experiments offer significant promise in this area.

3.2.1 Methodology of Solution

The governing equations for the current DNS work at NRL begin with equation (2.6) written in vector notation as,

$$\frac{\partial \mathbf{U}}{\partial t} + \mathbf{U} \cdot \nabla \mathbf{U} = - \nabla \frac{P}{\rho} + \mathbf{g} + \nu \nabla^2 \mathbf{U} \quad (3.21)$$

By using the vector identity,

$$\mathbf{U} \cdot \nabla \mathbf{U} = \nabla \left(\frac{\mathbf{U} \cdot \mathbf{U}}{2} \right) - \mathbf{U} \times \boldsymbol{\Omega} \quad (3.22)$$

the time dependent Navier-Stokes equations in the so-called rotational form are obtained as given by,

$$\frac{\partial \mathbf{U}}{\partial t} = \mathbf{U} \times \boldsymbol{\Omega} - \nabla \left(\frac{P}{\rho} + \frac{\mathbf{U} \cdot \mathbf{U}}{2} \right) + \mathbf{g} + \nu \nabla^2 \mathbf{U} \quad (3.23)$$

From continuity, the following incompressibility relation is obtained,

$$\nabla \cdot \mathbf{U} = 0. \quad (3.24)$$

Equations (3.23) and (3.24) form a non-linear set of 4 equations for the four unknown variables, u, v, w and p . In these two equations, ν equals the kinematic viscosity, $\boldsymbol{\Omega} = \nabla \times \mathbf{u}$ equals the vorticity, and \mathbf{g} represents a known body force. A pseudo-spectral solution technique is

used to solve for the velocity and pressure fields. Velocity components are expanded in Fourier series in the streamwise and spanwise directions and Chebychev polynomials in the wall-normal direction. All spatial derivatives are evaluated in the transform domain, after which inverse fast Fourier transforms are employed to transform the solution for one time step to the physical domain. The solution is moved forward to the next time step using the Adams Bashforth time stepping algorithm. Fast Fourier transforms are then used to move this updated solution back into the transform domain, where spatial derivatives are again evaluated spectrally. In carrying out the solution, the flow was assumed to be initially laminar. After time $t = 0$, a large unstable disturbance was added to the laminar velocity field. The establishment of fully-developed conditions required approximately 4000 time steps. The pressure at both upper and lower walls for all points in the computational grid was obtained from equation (2.7), and presented to the author by his colleagues for analysis. The reader is referred to Handler, *et al.* (1989) for a more definitive description of the methodology. In any event, this investigation seeks only to compare and/or critique the results from a typical calculation (particularly the wall pressure fluctuations), rather than comment on the accuracy of the technique used.

3.2.2 Description of Physical Model

For the data to be presented, computation continued until a fully developed channel flow was obtained. The computational volume included 16 points within the flow direction x , 33 points in the wall normal direction y , and 64 points in the transverse direction z , lying in the wall. Hence, on both the upper and lower walls of the channel, there were a total of $2 \times (16 \times 64) = 2048$ separate realizations for the wall pressure. At each of these 2048 computational points, 512 full realizations in time, of velocity and pressure were calculated and stored on tape. These given parameters somewhat limited the spectral analysis. Since only 512 time points were computed, this provided only 257 points in the frequency domain to be resolved. In addition, each computation point was treated as an ensemble, with all points added together to give 2048 averages. In a statistical evaluation, this does not translate into a true 2048 ensemble average. Many of the points used are well within the correlation length for the wall pressure at the wall and therefore are not true statistically independent records, as described in chapter 2. The calculation was performed at a Reynolds number based on shear velocity and half-width of the channel as,

$$R^+ = \frac{u^+ h}{\nu} = 125. \quad (3.25)$$

The physical experiment had an R^* value ranging from approximately 500 to 1000, or 4 to 8 times larger. In contrast, most of the experimental work to date, has values two orders of magnitude or greater, on the order of R^* greater than or equal to 5,000.

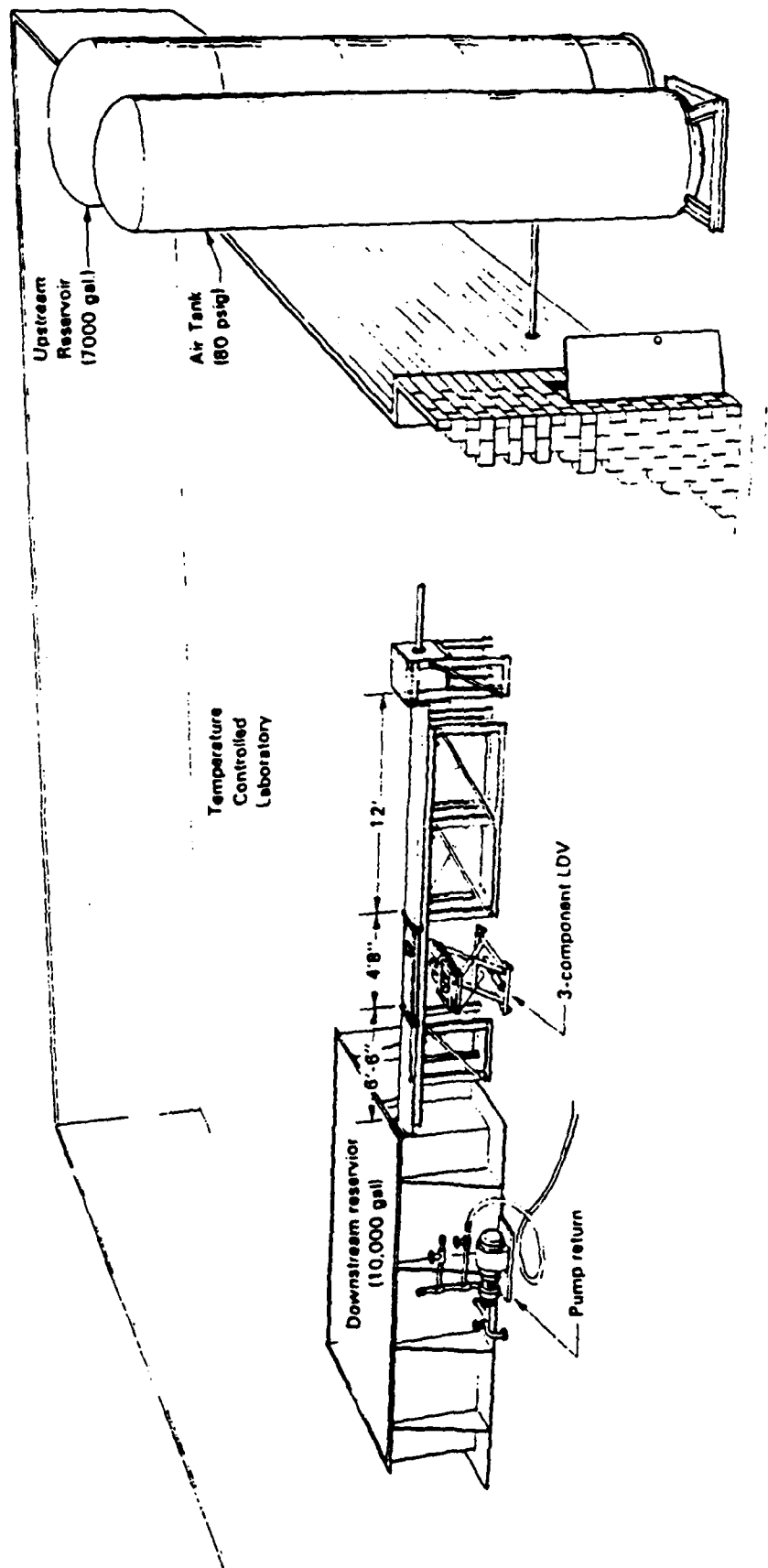
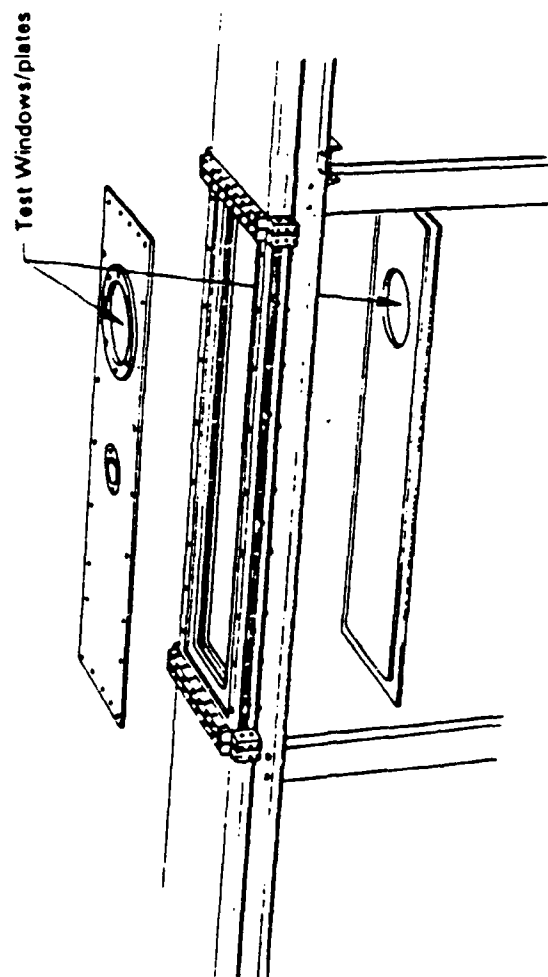
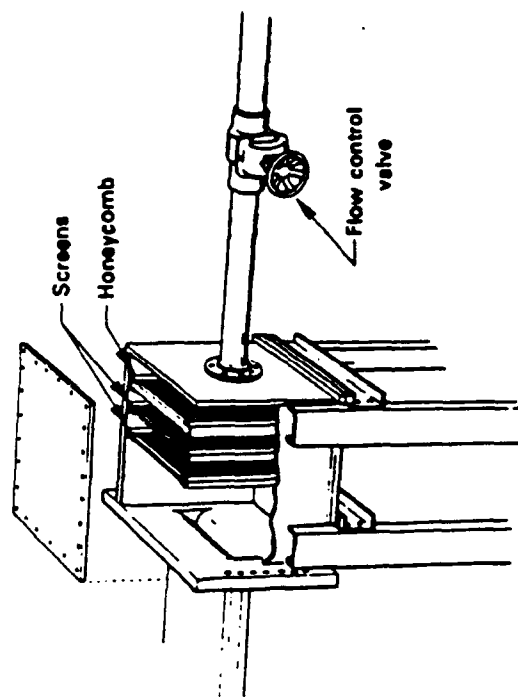


FIGURE 3.1. RECTANGULAR WATER CHANNEL FACILITY



TEST SECTION
(Aspect ratio 18":1")



Turbulence Mgmt. Sections

FIGURE 3.2. TURBULENCE MANAGEMENT AND TEST SECTIONS

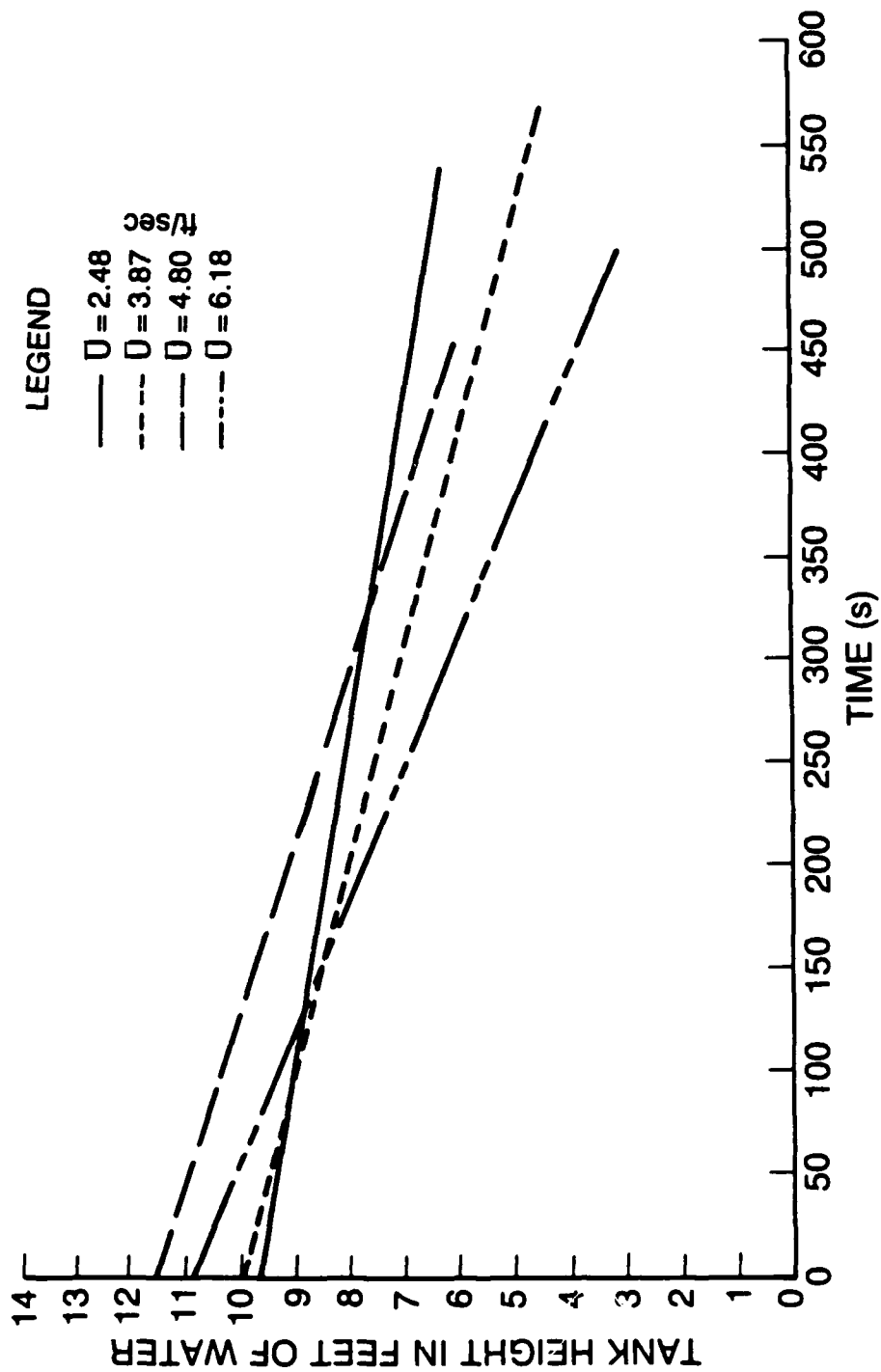


FIGURE 3.3. CHANNEL FLOW BULK VELOCITY CONTROL

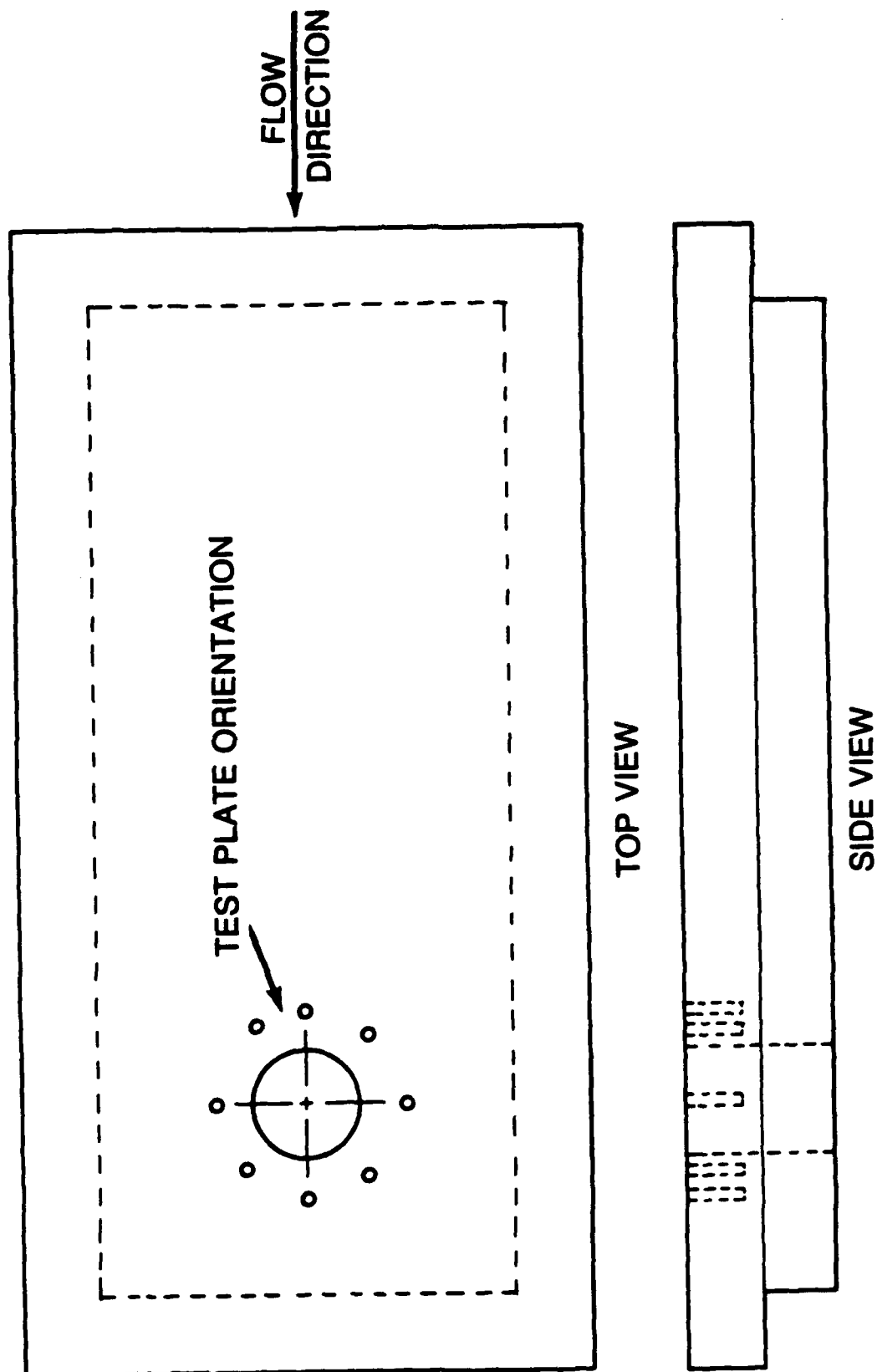


FIGURE 3.4. TEST SECTION CONFIGURATION

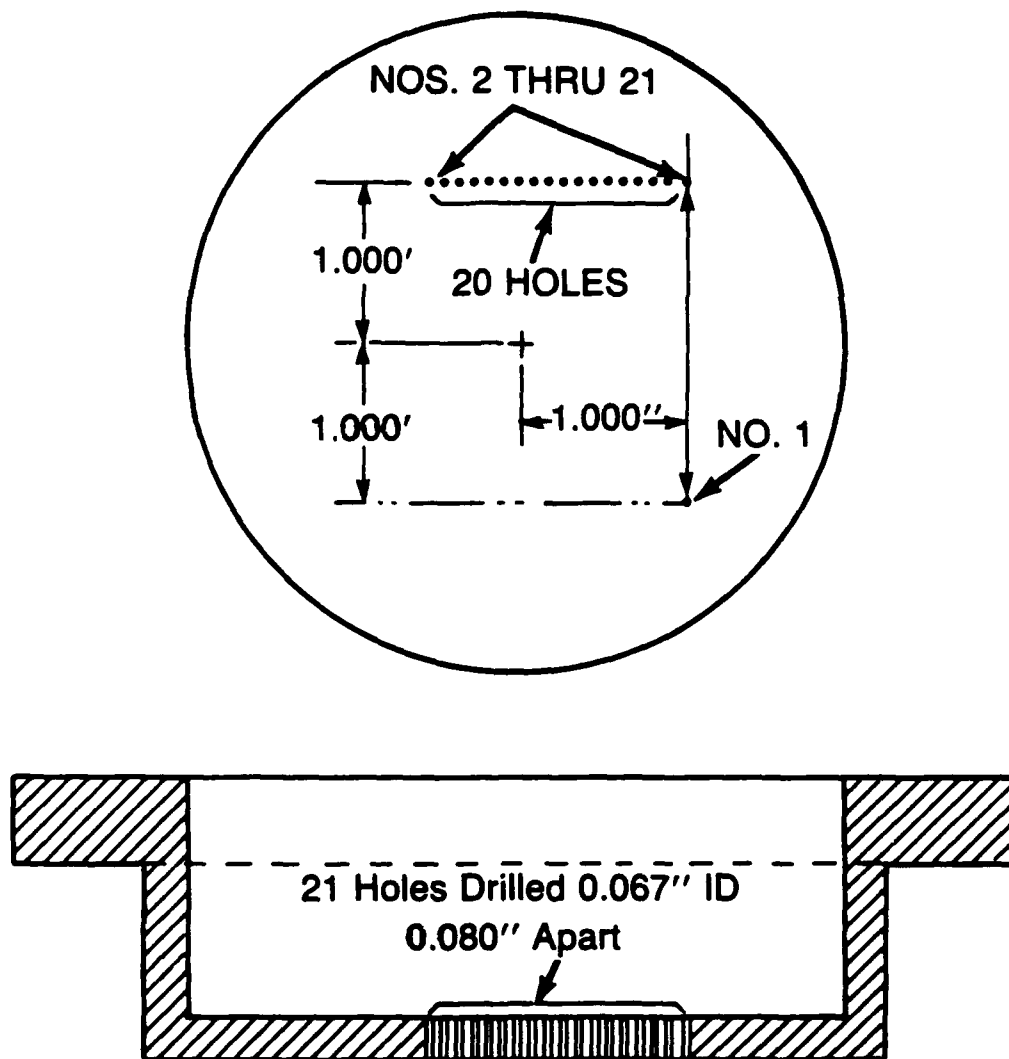


FIGURE 3.5. TEST PLATE WITH PRESSURE TRANSDUCER TAPS

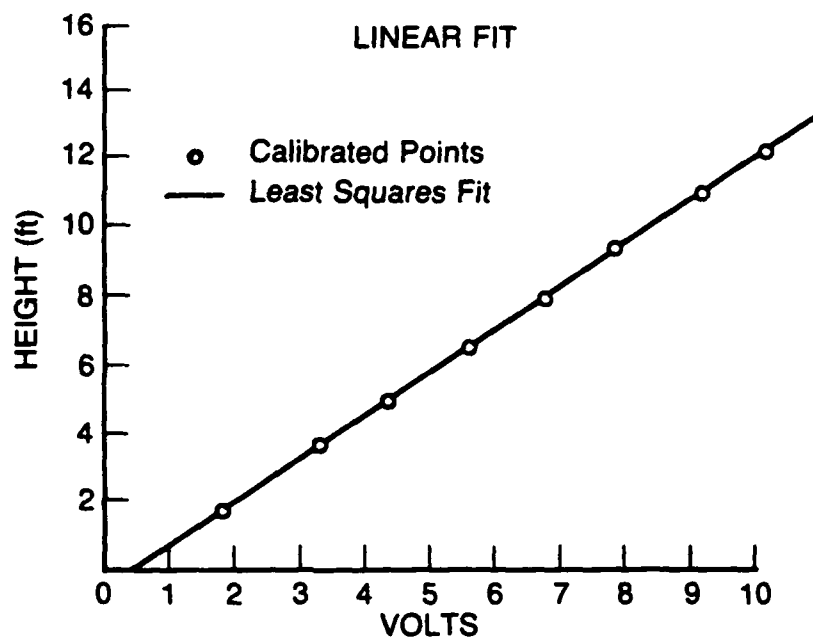


FIGURE 3.6a. TRANSDUCER CALIBRATION FOR BULK VELOCITY CONTROL

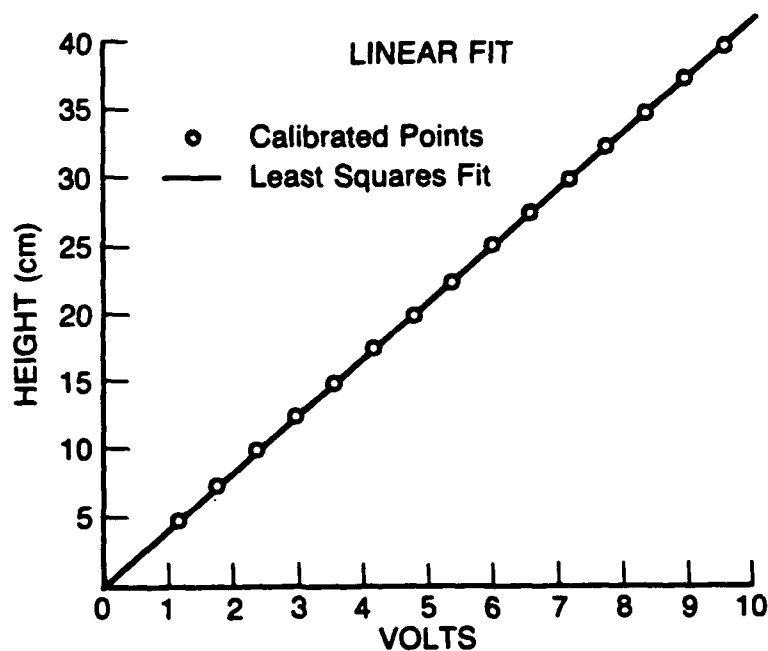


FIGURE 3.6b. TRANSDUCER CALIBRATION FOR CHANNEL PRESSURE GRADIENT

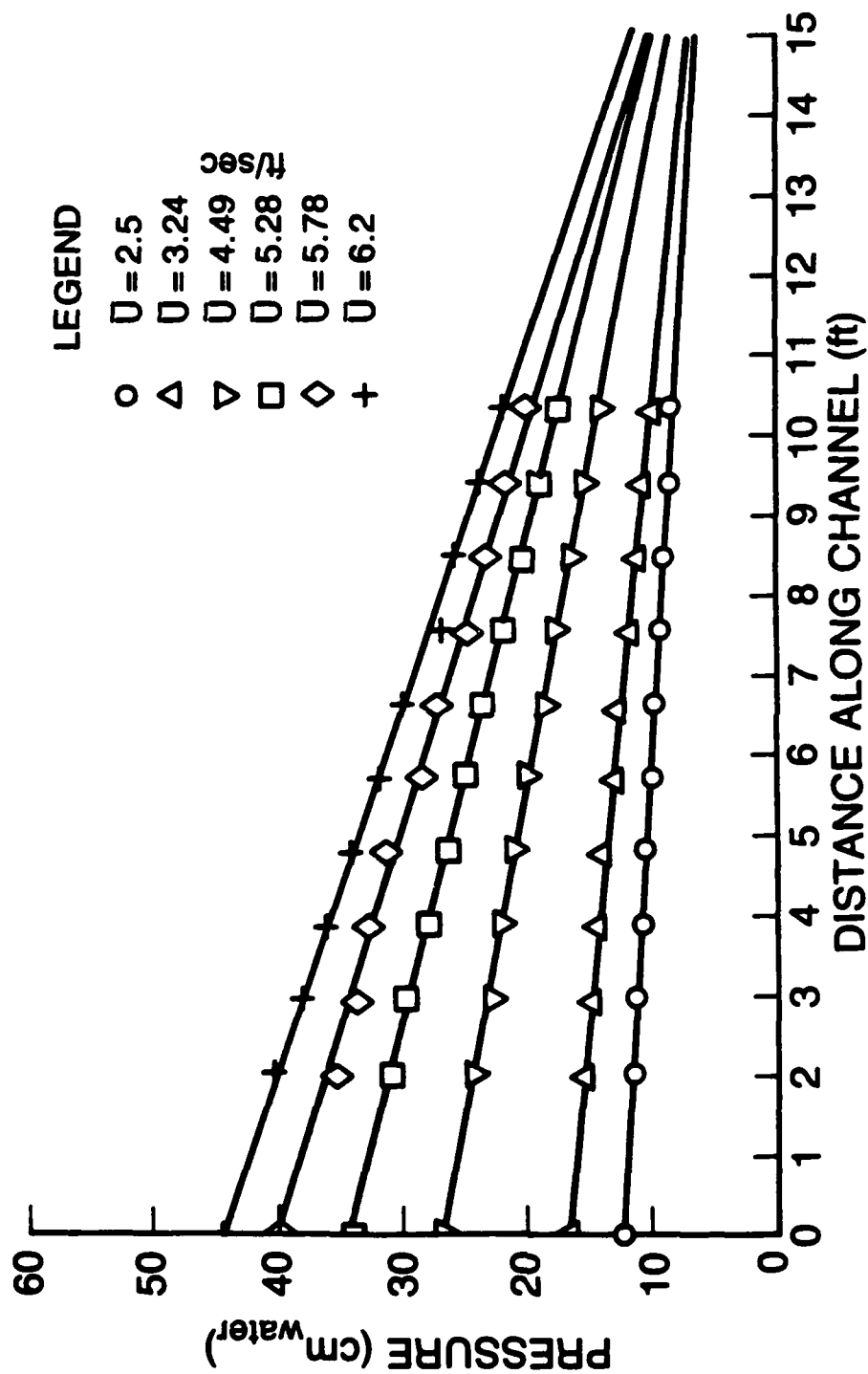


FIGURE 3.7. CHANNEL PRESSURE GRADIENT USING MULTIPLE TAPS FOR A RANGE OF BULK VELOCITIES

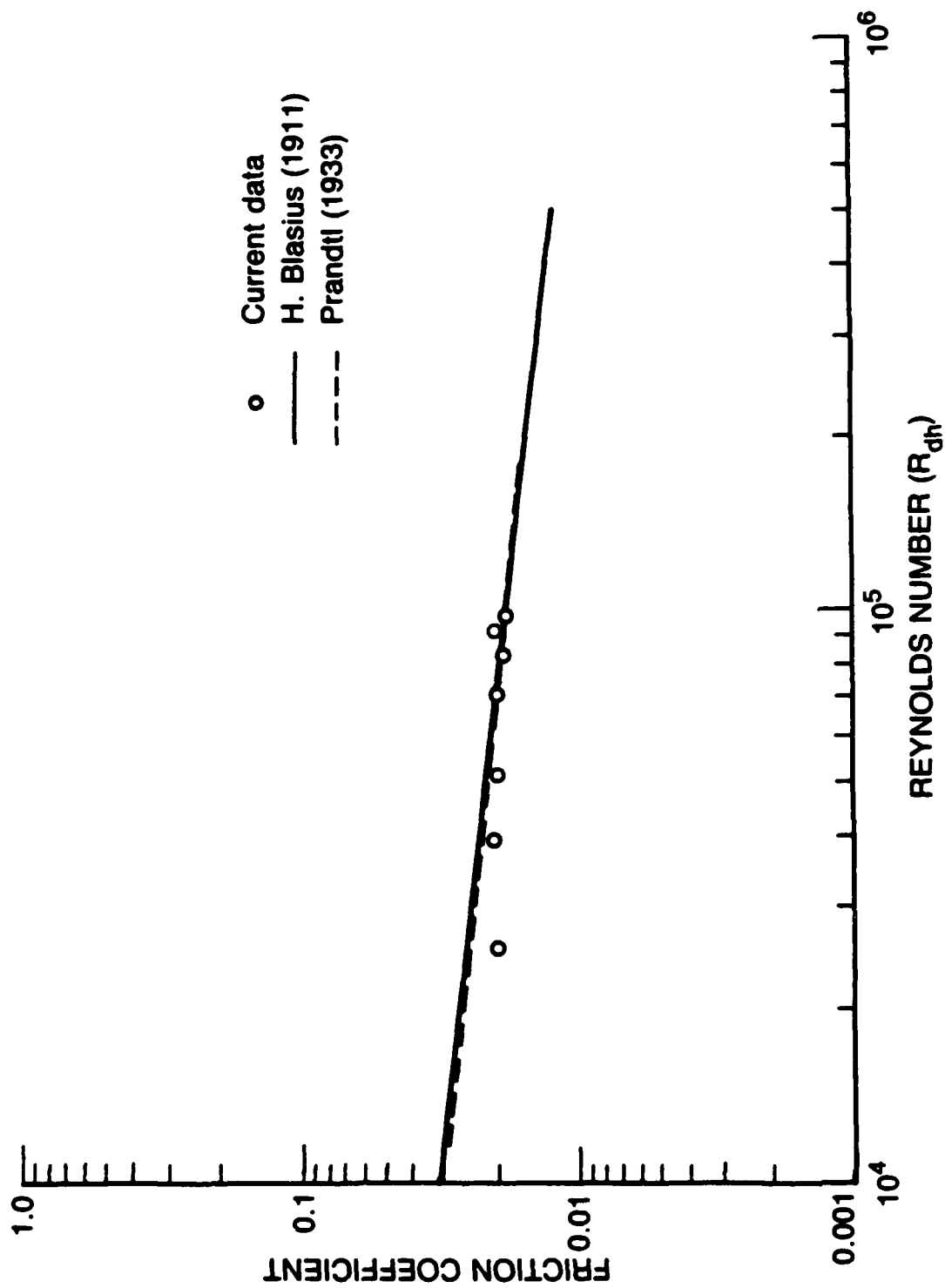


FIGURE 3.8. FRICTION COEFFICIENT FOR RECTANGULAR CHANNEL

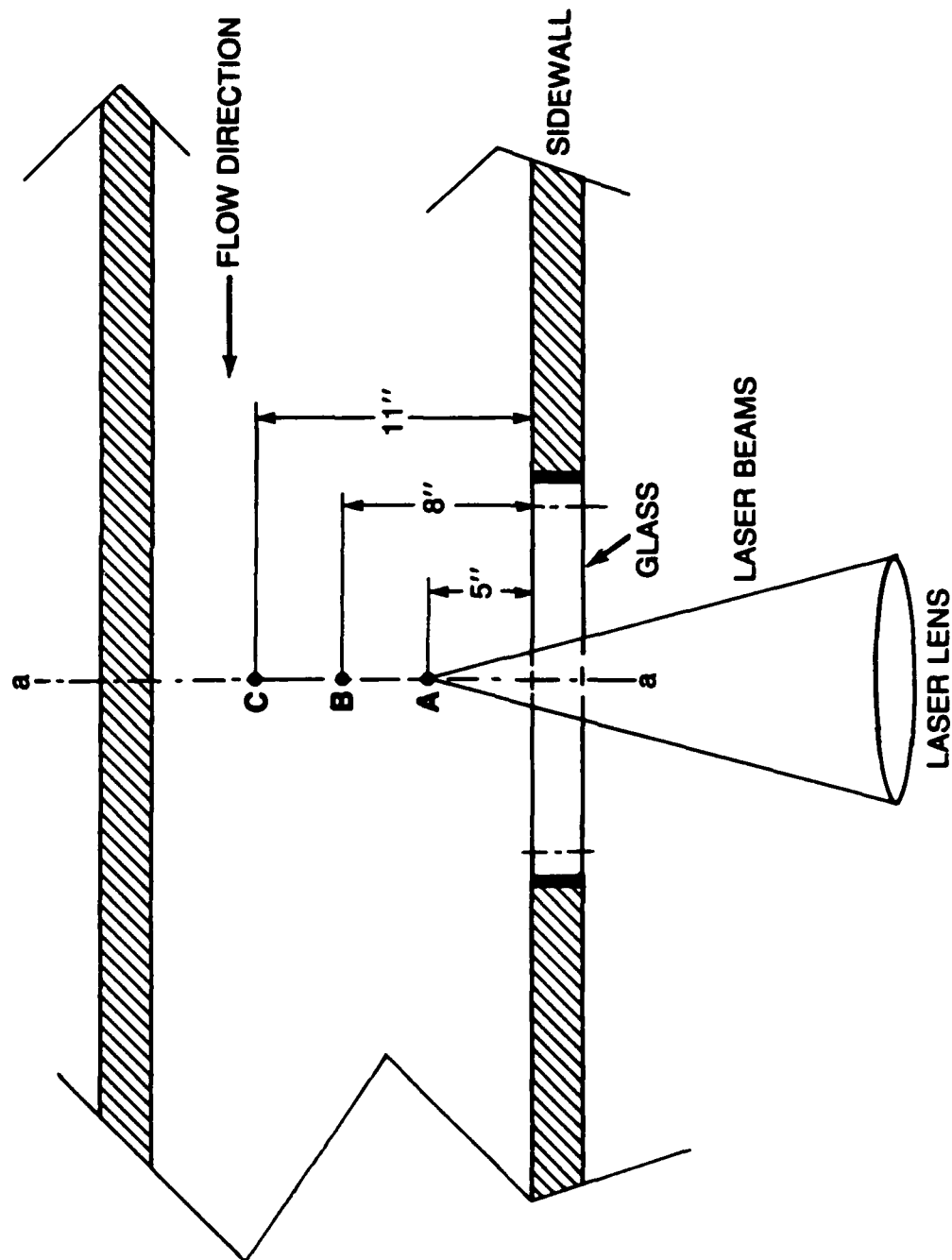


FIGURE 3.9. SCHEMATIC OF LDV ORIENTATION w/RESPECT TO TUNNEL SIDEWALLS

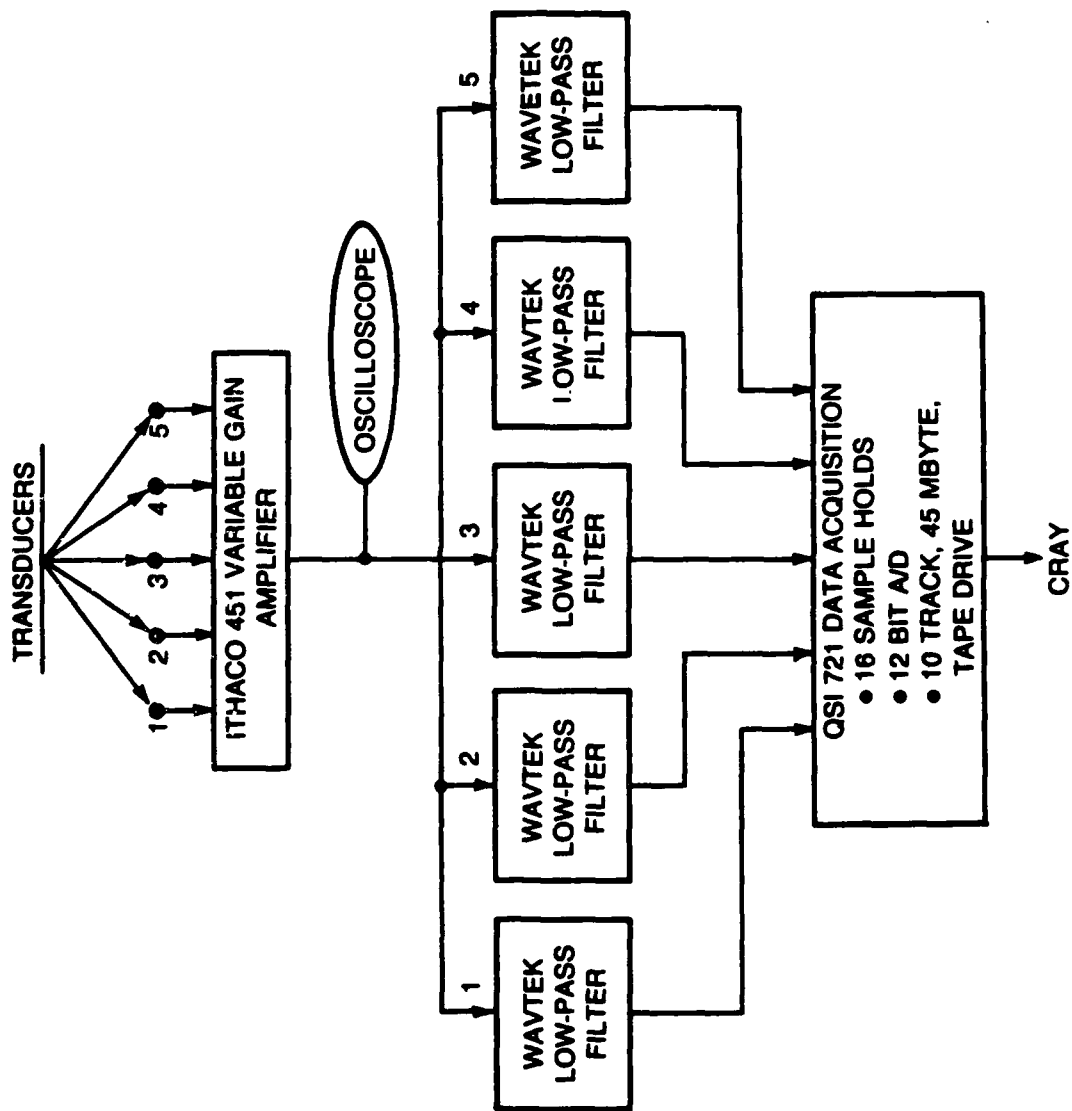


FIGURE 3.10. BLOCK DIAGRAM OF WALL PRESSURE DATA ACQUISITION

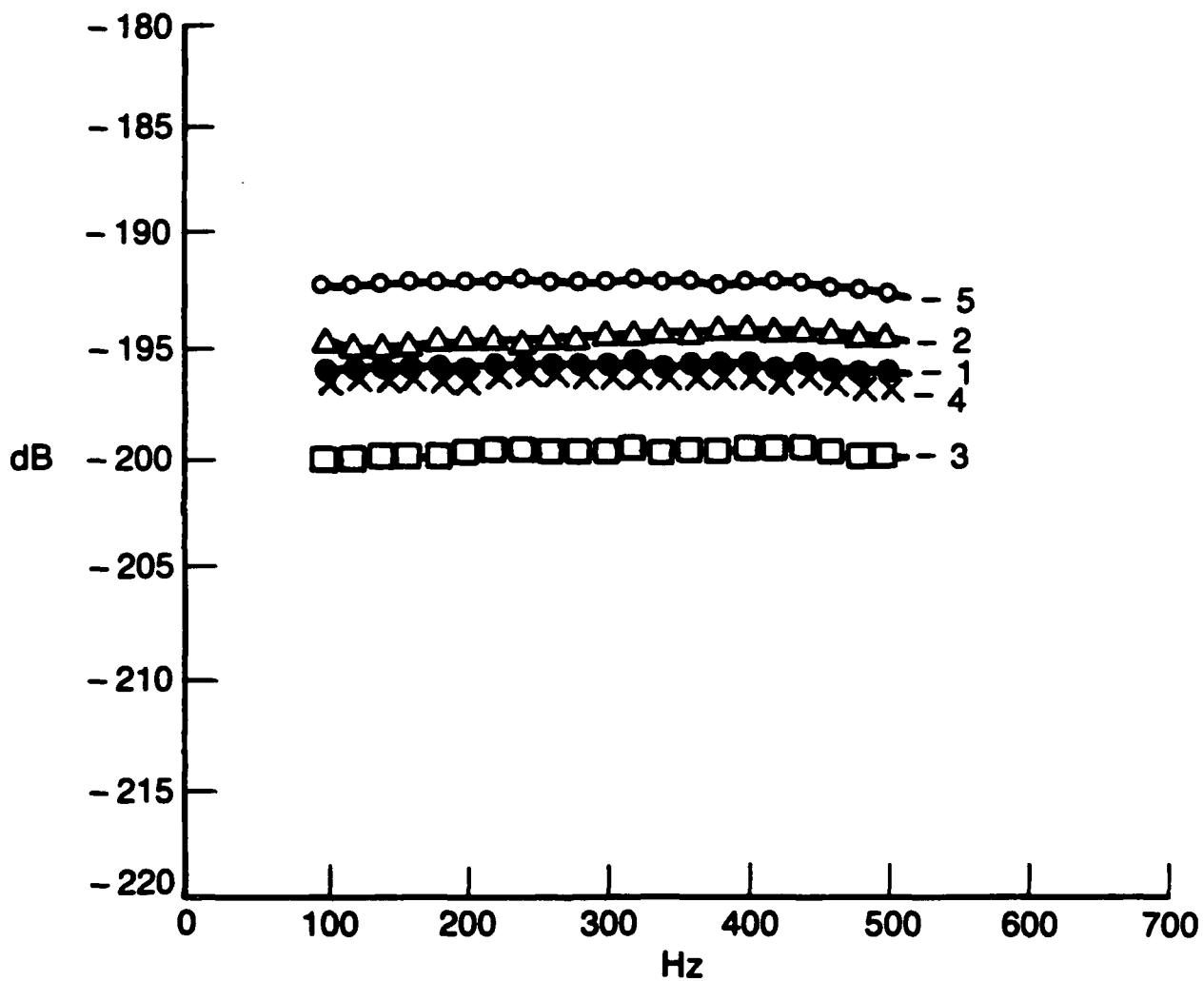


FIGURE 3.11. DYNAMIC CALIBRATION OF WALL PRESSURE TRANSducers

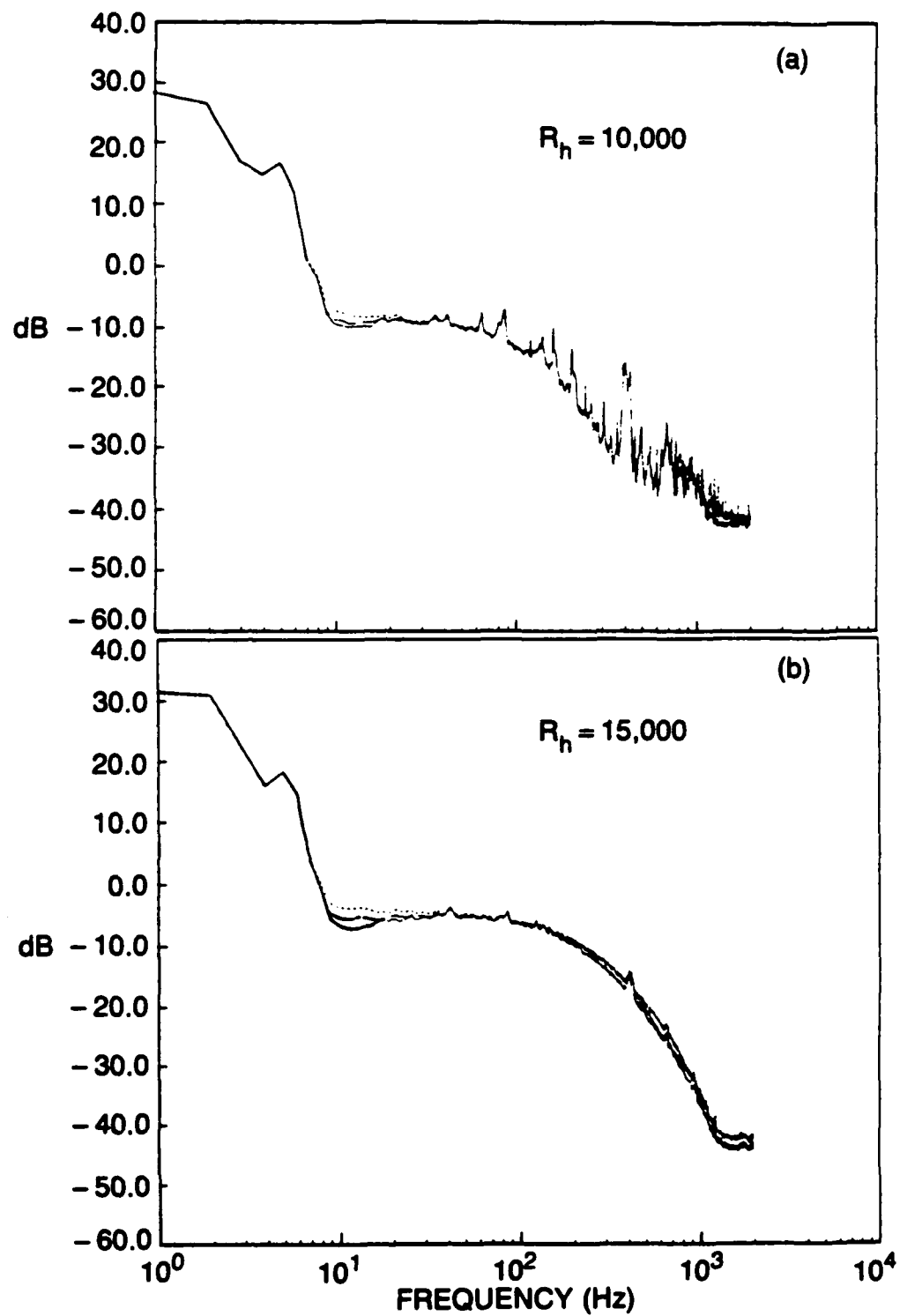


FIGURE 3.12. POWER SPECTRAL DENSITY OF THREE TRANSDUCERS AT TWO REPRESENTATIVE REYNOLDS NUMBERS

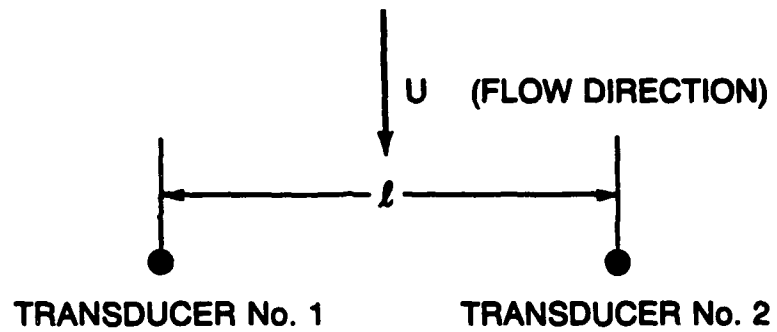


FIGURE 3.13. TRANSDUCER ORIENTATION FOR CANCELLATION

CHAPTER 4 EXPERIMENTAL RESULTS FOR VELOCITY

4.1 Introduction

This chapter presents the results for the streamwise mean velocity and its fluctuating *rms* value \bar{U} and u respectively, for the physical and computational experiments. The objectives of these measurements were to establish that both experiments represented a fully developed turbulent channel flow for the Reynolds numbers investigated. Furthermore, it was also important to establish that the large aspect ratio of the channel for the physical experiment ensured that no transverse variations in the turbulent structure interfered with the flow's two-dimensionality. As pointed out in chapter 3, the LDV system was limited to a single component in the flow direction since the side wall plexiglass permitted access to only two beam. Although limited, it was felt that these measurements were sufficient to establish that the physical experiment demonstrated fully developed turbulent flow.

The data obtained for the computational experiment included profiles of the mean and fluctuating components of velocity as a function of the distance normal to the wall. These data were averaged over the time period of the computational run as well as the entire computational box. The justification for this averaging technique lies in the assumption that if the flow is considered fully developed, then horizontal planes represent statistically independent samples of homogeneous turbulent flow. Due to the finite correlation lengths which exist in both streamwise and transverse directions for turbulent flow, statistical independence is not strictly met thereby introducing a source of random error. These profiles were represented as $\bar{U}(y)/u^*$ and $u(y)/u^*$ respectively, as a function of $Y^+ = yu^*/\nu$. As mentioned, the governing Reynolds number for the computational experiment was the value $R^* = 125$, which was based on the shear velocity u^* , channel half-height h , and kinematic viscosity ν , respectively. These three parameters provide all that is necessary to derive other profile characterizations which are outlined in table 4.1.

Profiles were taken in the rectangular channel of the physical experiment at three transverse locations labeled as *A*, *B* and *C*. These profiles were taken a number of times to insure their repeatability. Position *B* was approximately located on the channel's center line, at 8 inches from the near side wall and were those measurements compared with the computational experiment. Four Reynolds numbers were investigated at each station and were characterized as $R_h = U_{avg}h/\nu = 5000, 10000, 15000$ and 20000 respectively. Pertinent characteristics

describing representative profiles at each location are presented in table 4.2. It should be noted that the Reynolds numbers of the physical experiment were significantly higher than the computational experiment.

Table 4.1 Parameters for Computational Experiment

<i>Given :</i>	$U_j^+ = \bar{U}(y)/u^*, N \text{ values}$	$Y_j^+ = yu^*/\nu, N \text{ values}$
	$u_j^+ = u(y)/u^*, N \text{ values}$	$R^* = u^*h/\nu$
<i>Derived :</i>	$U_o/u^* = U_N^+$	$u(y)/\bar{U}(y) = u_j^+/U_j^+$
	$\bar{U}(y)/U_o = U_j^+/U_N^+$	$y/h = Y_j^+/R^*$
	$[U_o - \bar{U}(y)]/u^* = U_N^+ - U_j^+$	$R_h = U_N^+ R^*$
	$u(y)/U_o = u_j^+/U_N^+$	

It should be noted that the velocity measurements and wall pressure measurements for the physical experiment were not taken at the same time. Some of the same instrumentation was used in the characterization of velocity and pressure and precluded simultaneous measurement in some cases. In addition, the complexity of obtaining both types of data, which involved constant monitoring of a number of controlling parameters (indicated by various readout devices), permitted only one type of data (velocity or wall pressure) to be obtained at any one time. Therefore, the velocity data was taken first at the Reynolds numbers specified. Later, when the wall pressure data was investigated, it was found that the lower velocity runs provided pressure intensities of such low magnitude that the pressure sensors could not resolve the pressure signature adequately, due to their limited dynamic range. It will be shown in chapter 5, that only the larger three Reynolds numbers could be investigated along with an additional higher Reynolds number at $R_h = 25000$.

Table 4.2 Governing Parameters for Physical Experiment

R_h	station	u^*/U_o	R^*	$U_{avg}(m/sec)$
5,000	A	.0509	373	0.457
5,000	B	.0511	375	0.448
5,000	C	.0503	369	0.448
10,000	A	.0482	560	0.719
10,000	B	.0480	563	0.719
10,000	C	.0477	559	0.722
15,000	A	.0460	839	1.158
15,000	B	.0451	836	1.125
15,000	C	.0454	834	1.131
20,000	A	.0446	1015	1.417
20,000	B	.0447	1015	1.396
20,000	C	.0443	1010	1.408

4.2 Mean Velocity Profiles

The mean velocity profiles $U(y)/U_o$, as a function of distance from the wall y/h representing all four Reynolds numbers, are shown in figures 4.1 to 4.4 for the physical experiment. For comparison purposes, a laminar flow profile for the same flow configuration is also shown. In comparison with laminar flow, all profiles for each Reynolds number demonstrate the fuller shape which is characteristic of typical fully developed turbulent flows.

Observation of the data show that no variation across the channel is apparent with excellent agreement among the three stations. An interesting anomaly may be noted in relation to resolution at the wall. As one examines figures 4.1 thru 4.4, resolution with respect to the wall normal coordinate 'y' appears to get worse as the Reynolds number increases. As the velocity increases in the channel, so does the data rate of detected particles passing through the probe volume. However, larger particles which obliterate the signal from the probe volume are also more numerous and create what is termed "shot noise" to the photo multipliers, thus reducing the signal to noise ratio. As the flow moves from low to high Reynolds number, one obtains first less noise but low data rate and finally high data rate, but too much "shot noise" or flare up; hence moving away from the wall is required. This phenomenon is indicated in figure 4.4 by showing the closest distance to the wall available as $y/h = .04$ in comparison with

a value of .01 in figure 4.2. Secondly, by examining each station, *A*, *B* or *C*, one may note *B* appears to give the best resolution regardless of Reynolds number. This can be explained by the following argument. Station *A* is close to the side wall and allows reflections from the plexiglass to interfere with the signal. As the beams are traversed towards station *C*, a greater length of beam travels through the flow environment and requires the photo multipliers and related instrumentation to be more discriminating in validating particles. Both situations reduce the signal to noise ratio of the LDV system resulting in poorer resolution. By examining each of the figures, station *B* appears to represent the best compromise between both anomalies.

In order to establish more resolutely the two-dimensional nature of the flow, the laser probe volume was positioned at the two distances from the wall of $y/h = 0.2$ and 1.0 . At each position, the probe volume was traversed across the channel from approximately 2 thru 12 to 14 inches from the near wall for the two middle Reynolds numbers of $R_h = 10000$ and 15000 . These profiles are presented in figures 4.5 and 4.6 with the location of stations *A*, *B* and *C* also indicated. No gross interference from the side wall can be detected until the probe volume approached approximately 4 inches to the wall as indicated by the results at $R_h = 10000$ in both figures. The slight variations noticed are due to the slight movement of the probe volume as the beams move through the side wall. As the beams pass through the plexiglass at different locations, small imperfections cause the beam to diffract and change its path. This results in the probe volume moving to a slightly different location from that expected. This effect becomes more pronounced the closer the beams are moved towards the wall due to the presence of a higher shear gradient. This is indicated by the slight waviness in the profiles which is somewhat more noticeable in figure 4.5 than figure 4.6, as expected.

Figure 4.7 takes the results from station *B* at all Reynolds numbers and compares them with those from the computational experiment. In this figure, the measurements of Hussain and Reynolds (1975) and Laufer (1951) are indicated where the Reynolds numbers are appropriate. Two conclusions may be drawn from the comparison. First, the data of the physical experiment are in excellent agreement with other reported investigations at similar Reynolds numbers. The data of Laufer and Hussain were also taken in rectangular channels with aspect ratios of 12 and 18, respectively. Secondly, the Reynolds number dependence corresponding to outer variable scaling is well indicated.

The data taken along the channel centerline (station *B*) is compared with the computational results in figure 4.8 using inner variable scaling for the classical "Law of the Wall" profiles. The solid line represents the following equation derived by Spalding (1961),

$$Y^+ = U^+ + \exp(-\kappa B) \left[\exp(\kappa B) - 1 - \kappa U^+ - \frac{(\kappa U^+)^2}{2} - \frac{(\kappa U^+)^3}{6} \right] \quad (4.1)$$

with the constants κ and B equal to 0.40 and 5.5 respectively. Also shown in figure 4.8 are the different regions of a typical boundary layer governed by a wall-bounded turbulent flow. The linear sublayer ($U^+ = Y^+$) covers the range $0 < Y^+ < 5$, the buffer layer covers the range approximately $5 < Y^+ < 40$ and the log-law region from $40 < Y^+$ to $y \leq 0.2h$. These three regions cover the inner layer of the boundary layer. The outer or "velocity defect" region exists for $y/h > 0.2$. All the profiles in figure 4.8 collapse on the solid line and appear to merge smoothly from the log-law region to the inner sublayer region. As shown, the limited spatial resolution due to the instrumentation, only gave a few points in the buffer layer for the mid-range Reynolds numbers, but qualitatively the overall behavior is in excellent agreement with the classical results. At larger values of Y^+ , there exist differing values depicting the onset of the wake or "velocity defect" region for each profile. The computational data appears to terminate at $Y^+ = 90$, with Y^+ values of 200, 400, 600 and 800 for the physical Reynolds number flows of 5000, 10000, 15000 and 20000, respectively.

To better illustrate this defect region, the profiles of all five flows are plotted with outer variables in figure 4.9 as $[U_o - U(y)]/u^*$ versus y/h . The defect region is well indicated, beginning at y/h approximately equal to 0.2, with the profiles becoming more concave and fuller with decreasing Reynolds number as the wall is approached.

4.3 Streamwise Velocity Fluctuations

The turbulence intensity profiles at station B for all Reynolds numbers of the physical experiment are shown in figures 4.10 and 4.11 along with the computational results. These data are plotted as a function of the centerline velocity U_o in figure 4.10, and the local velocity $U(y)$ in figure 4.11. A definite Reynolds number dependence is demonstrated, with the peak value increasing and moving away from the wall with decreasing Reynolds number. The data presented in both figures show good agreement with similar experiments conducted in other large aspect ratio channels.

The *rms* values of fluctuating velocity are plotted with inner variable scaling in figure 4.12 as $U^+ = \bar{U}/u^*$ versus $Y^+ = yu^*/\nu$. The data of Kreplin and Eckelmann (1979) and Clark (1968) are shown for comparison. The overall behavior exhibits trends similar to other classic

studies in that the results increase monotonically away from the wall, peak at Y^+ values of between 13 to 18, and then slowly decrease to the value measured at the channel centerline. The rate at which the results decrease is Reynolds number dependent as shown in the literature. It should be noted that the peak value measured is limited by the transducer used. In most cases, hot films or hot wires are used in which case the length of the wire (or film) limits the scale of fluctuations capable of being measured. Kreplin and Eckelmann used hot-film sensors in oil for which the effective sensor length was as low as two viscous units. In the present study, the LDV represents a non-intrusive probe (producing no obstruction to the flow), so it can be argued that the probe volume diameter is the limiting dimension. The beam diameter of .005 inches corresponds to approximately 10 viscous units for the larger Reynolds number and should not be a limiting factor.

The peak value of about 2.8 to 3.0 obtained in the physical experiment is well within the range measured by other investigators and occurs at a Y^+ value of about 15. The computational results peak in the same approximate location from the wall but the peak is somewhat lower, reaching a value of only 2.5. Kreplin's data had an R^* value of approximately 390 which was close to those values of the physical experiment at the low Reynolds number of 5,000 but some 3 times larger than the value, $R^* = 125$ of the computational experiment. Although qualitatively both experimental data presented here agree reasonably well with that reported in the literature, either the computational experiment demonstrates a Reynolds number effect not shown before, or has not yet reached full development.

The results presented in figures 4.10 and 4.11 support this argument. As mentioned previously, scaling the fluctuations with outer and local variables should show a peak value increasing as the Reynolds number decreases. Relative to the physical experiment and the data of Laufer, Clark and Kreplin, the peak in the computational experiment is somewhat lower than the trends would seem to indicate. The computational grid may not have been of a sufficient length nor the code run-time of sufficient duration to fully develop this profile. The assumption of statistical independence mentioned in the previous section may also be contributing to this effect. This becomes an important factor because the source terms contributing the most to the wall pressure field occur closest to the wall at Y^+ values less than 40. One could well argue that the simulated experiment has not reached its fully developed state in a spatial sense, or is still experiencing transition. These ideas will be addressed further in chapter 5 where the data for the wall pressure field will be presented.

Hussain (1983) discussed the important role which the initial condition plays in the development of a turbulent boundary layer and the necessary conditions for a fully developed turbulent profile. For channel flow, these conditions can be represented as; 1) a mean profile of the proper shape, 2) a mean profile indicating a log-law and defect region of proper extent when plotted with respect to inner variables, 3) a peak in the turbulence intensity level of $u/u^* = 2.5 \pm 10\%$ at $Y^+ = 15$, and 4) an intensity profile which monotonically decreases to the centerline value. Based on these characteristics, figures 4.1 thru 4.12 clearly show the physical experiment to be fully developed. The intensity values, although somewhat high and low for the physical and computational experiments respectively, are certainly within the ranges outlined above by Hussain. A more detailed critique of the computational data was given by Handler *et al.* (1989) and will be addressed in chapter 5 in relation to the wall pressure.

4.4 Shear Velocity

A parameter of critical importance in evaluating the development of turbulence profiles is the shear velocity ' u^* '. An additional criterion to those outlined by Hussain (1983) in relation to a channel flow, is a linearly decreasing static pressure throughout the fully developed flow region thereby exhibiting a constant pressure gradient. In most external boundary layer experiments, the shear velocity is not measured but rather inferred by forcing the mean velocity to conform to the "law of the wall", given by equation (4.1). In addition, recognizing that the viscous sublayer close to the wall must result in a linear profile, the shear velocity is sometimes calculated from the slope at the wall from the relation,

$$\rho u^{*2} = \mu \left(\frac{\partial U}{\partial y} \right)_{y=0} \quad (4.2)$$

Each parameter inferred or otherwise determined by assumptions about the flow, incurs the risk of introducing additional errors. For the present physical experiment, the pressure gradient was measured directly as outlined in chapter 3. For each Reynolds number, the static pressure gradient differential was recorded in time during the full experimental run and averaged with the use of equation (2.2). The value of shear velocity for each Reynolds number is plotted in figure 4.13 in terms of $R^* = u^*h/\nu$ versus the channel center-line Reynolds number $R_h = U_ch/\nu$. The numerical experimental value of 125 is also shown and the solid line represents the data of Hussain (1975) which was found to correlate with the relation,

$$R^* = 0.1079 (R_h)^{0.911} \quad (4.3)$$

The results of both the computational as well as the physical experiments are in excellent agreement with this correlation.

In summary, the results presented from both experiments suggest the following conclusions:

- o The mean velocity profiles of the physical experiment demonstrate a fully developed two-dimensional channel flow throughout the core region of the duct.
- o The turbulence intensity profiles with respect to outer and local variables, show a Reynolds number dependence consistent with other investigations for the physical experiment.
- o The peak in the *rms* level u/u^* is approximately 2.8 to 3.3 and occurs at $Y^+ = 15$, in good agreement with accepted values in the literature.
- o The location of the channel test section shows an ideal constant pressure gradient resulting in constant values for shear velocity for each Reynolds number of the physical experiment.
- o The computational experiment demonstrates similar agreement for the mean velocity, but shows somewhat retarded development with respect to the fluctuating component $u(y)$.

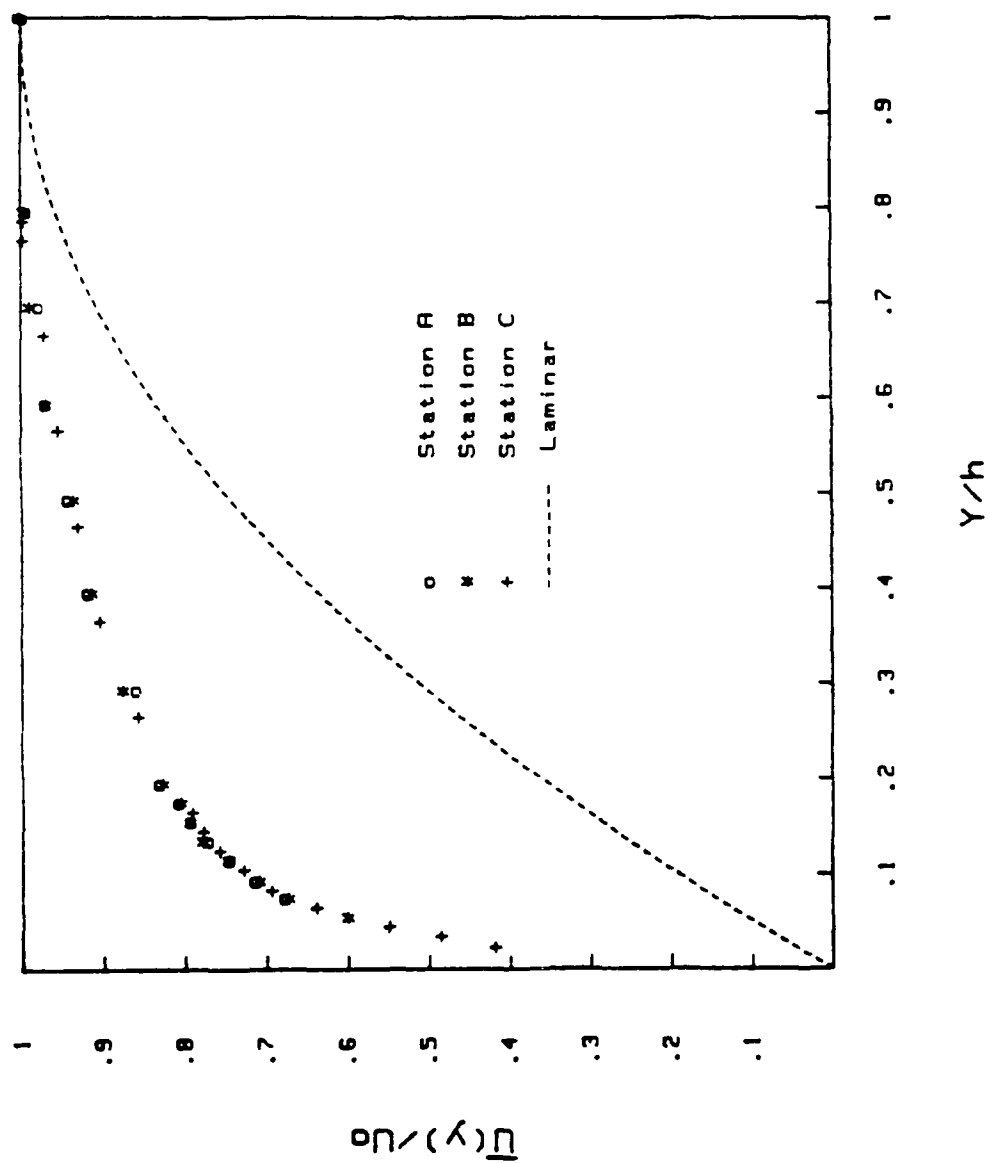


FIGURE 4.1 Velocity Profile at $Rh = 5,000$ at Each Station Across the Channel.

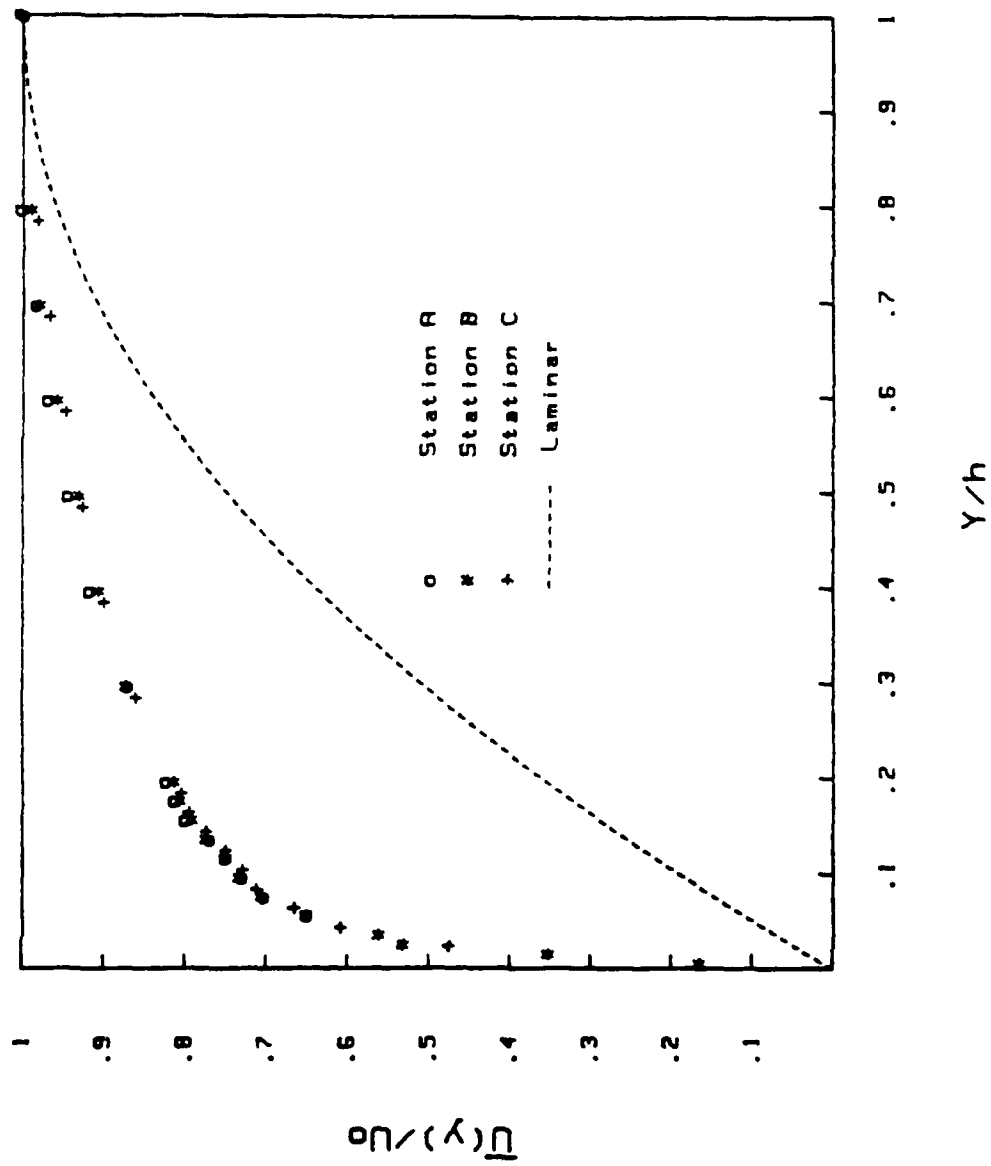


FIGURE 4.2 Velocity Profile at $Rh = 10,000$ at Each Station Across the Channel.

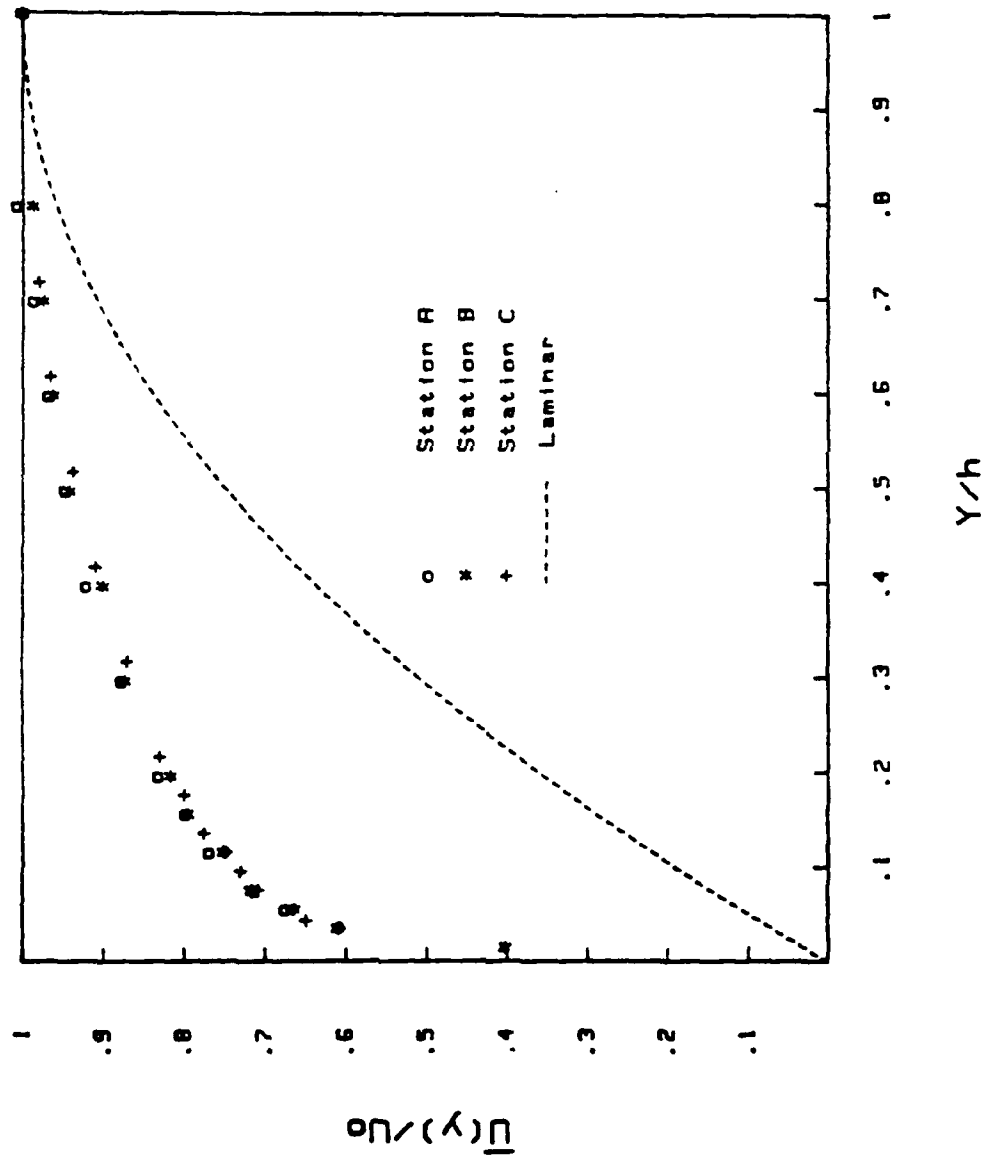


FIGURE 4.3 Velocity Profile at $Rh = 15,000$ at Each Station Across the Channel.

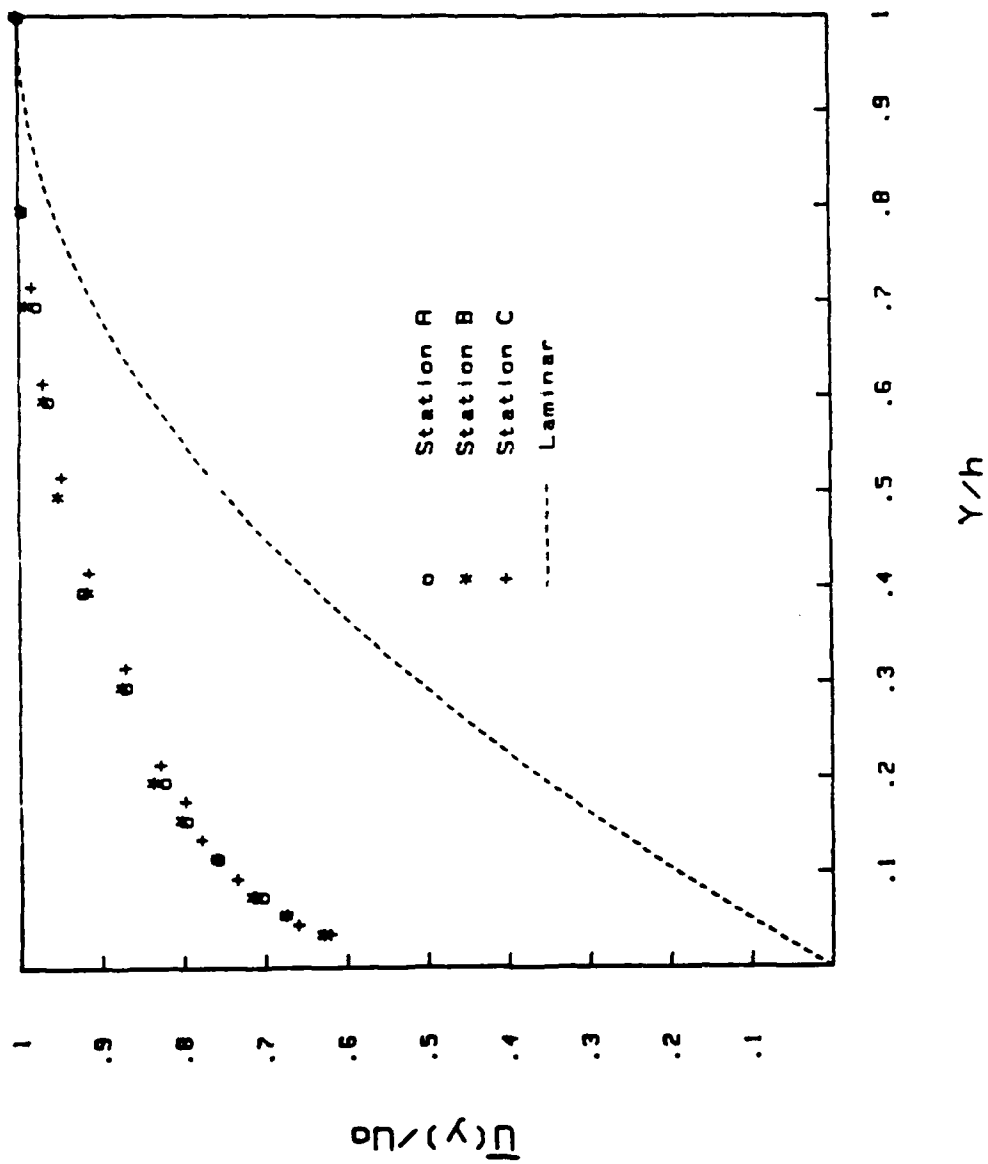


FIGURE 4.4 Velocity Profile at $Rh = 20,000$ at Each Station Across the Channel.

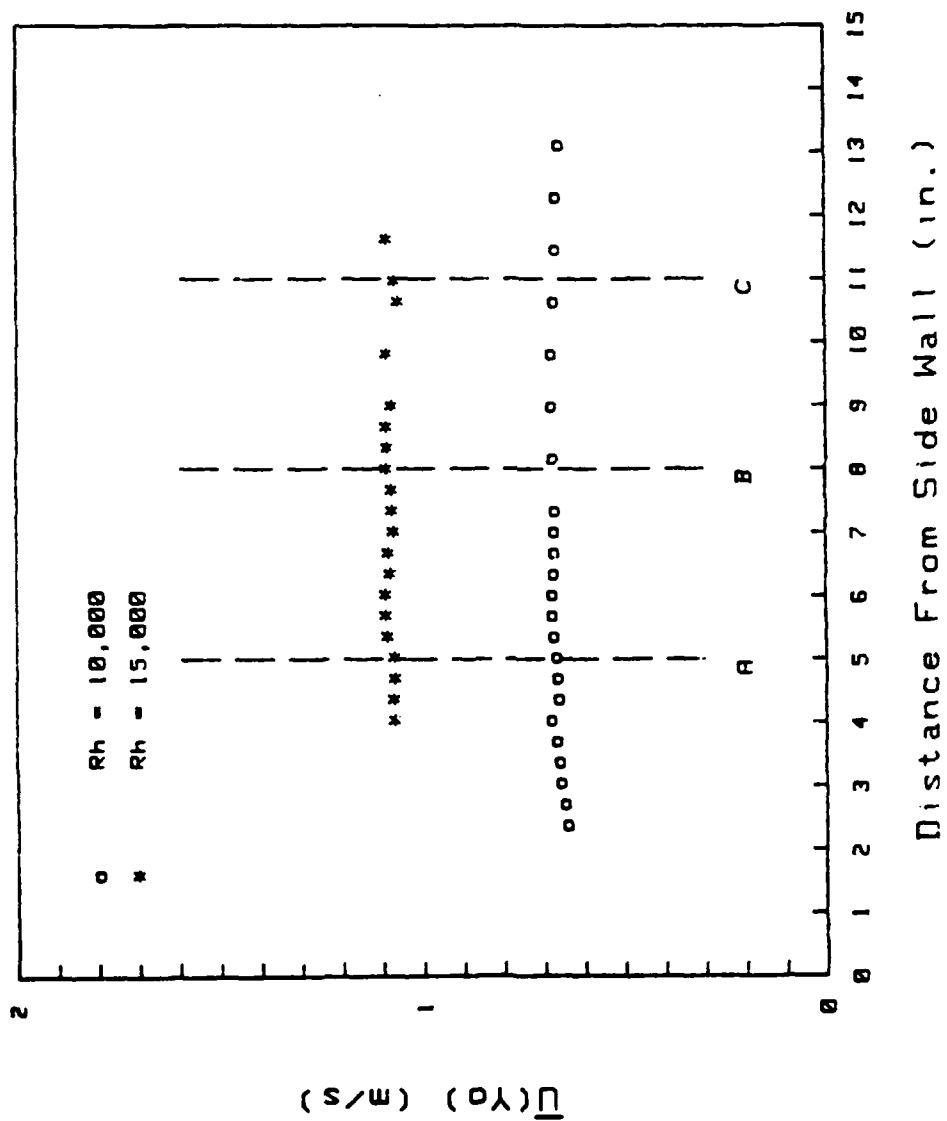


FIGURE 4.5 Velocity Profile Across Channel at
 $Y_0 = 0.1$ inches From Upper Wall.

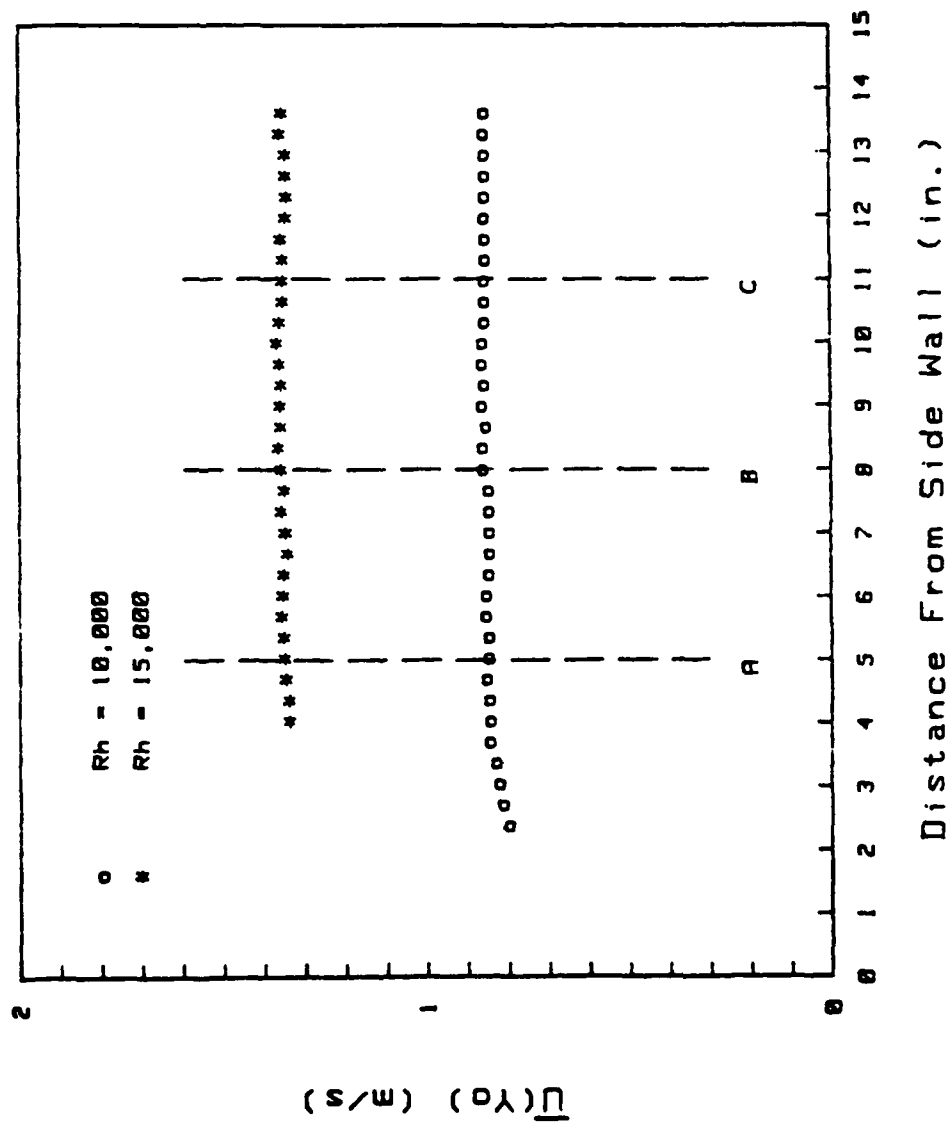


FIGURE 4.6 Velocity Profile Across Channel at
 $Y_0 = 0.5$ inches From Upper Wall.

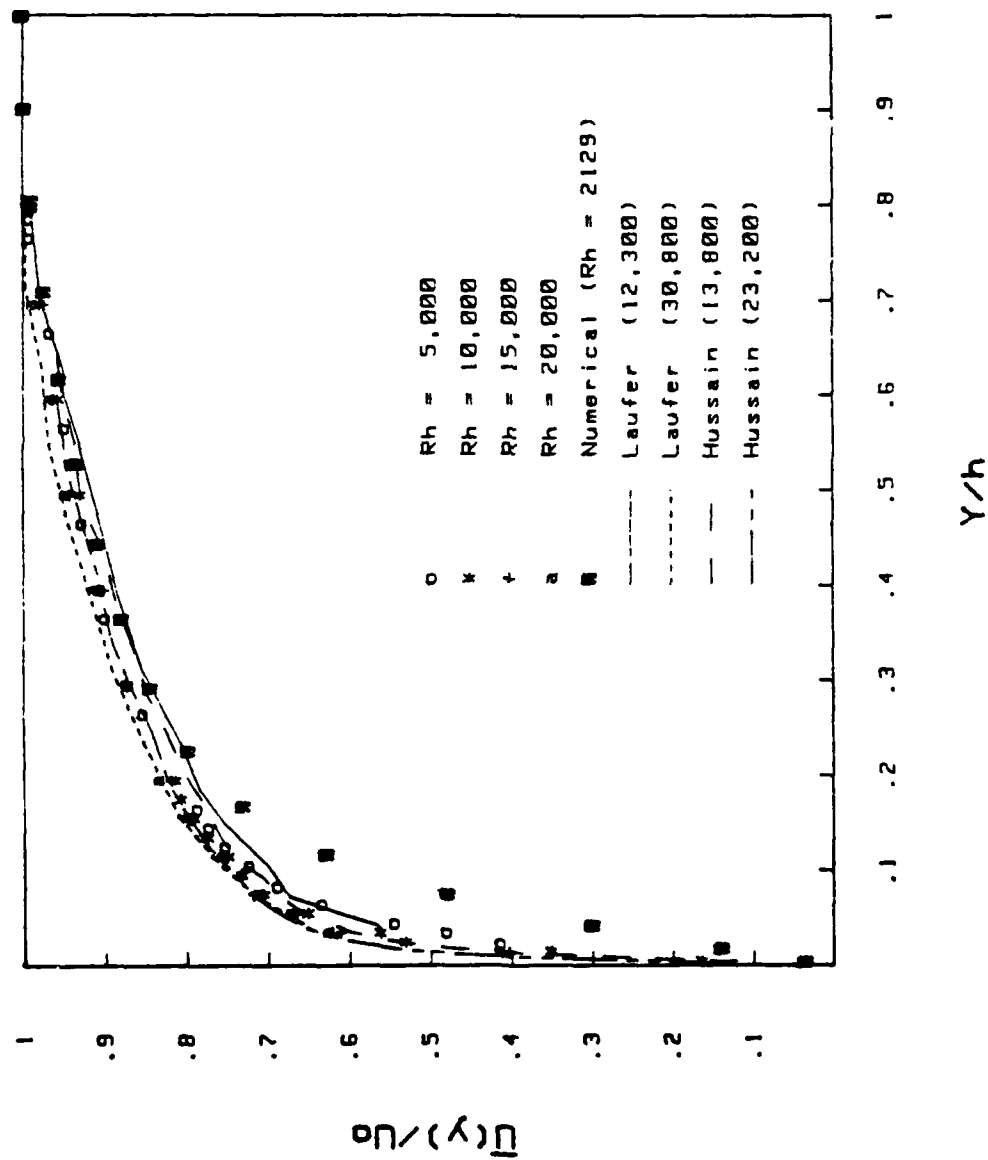
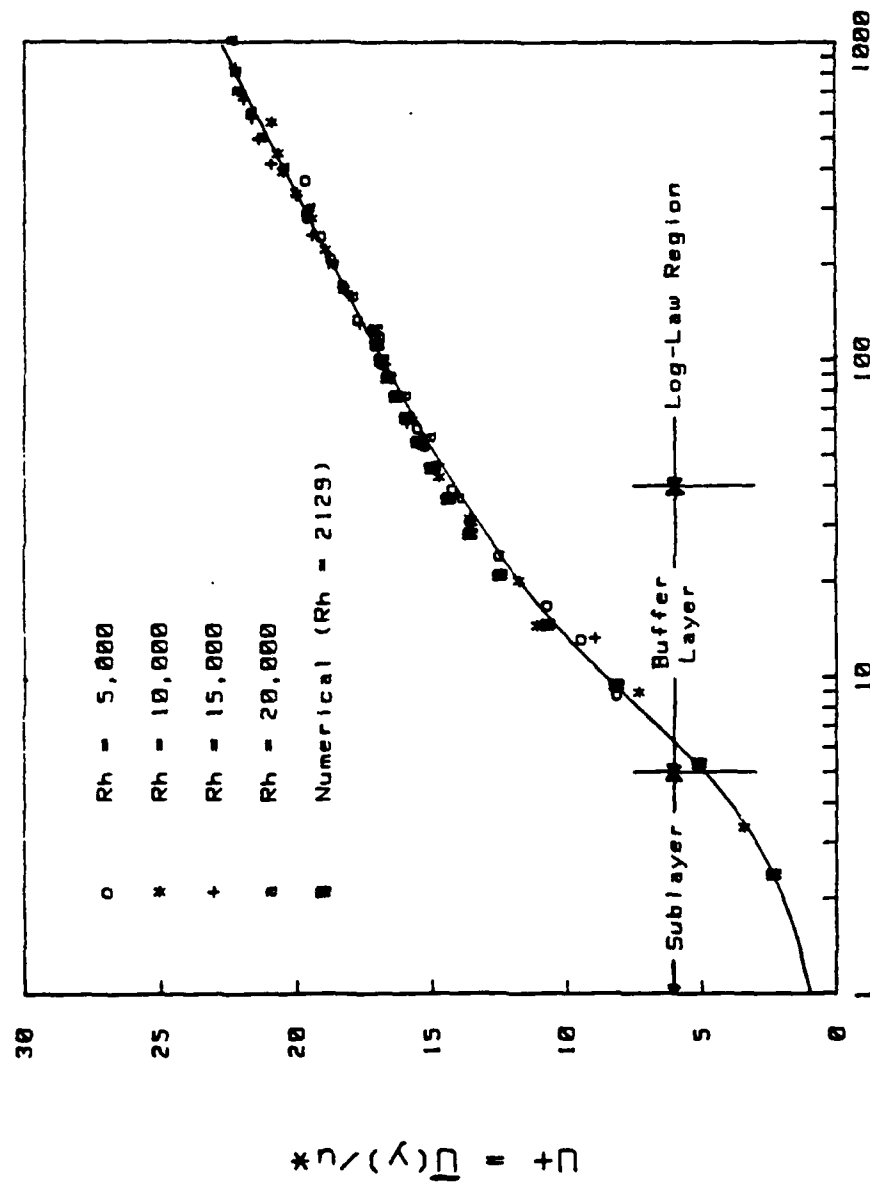


FIGURE 4.7 Velocity Profile at Station B for All Reynolds Numbers, to Include Numerical Data.



$$Y^+ = yu^*/Nu$$

FIGURE 4.8 Universal Velocity Profile at All Reynolds Numbers Including the Numerical Data.

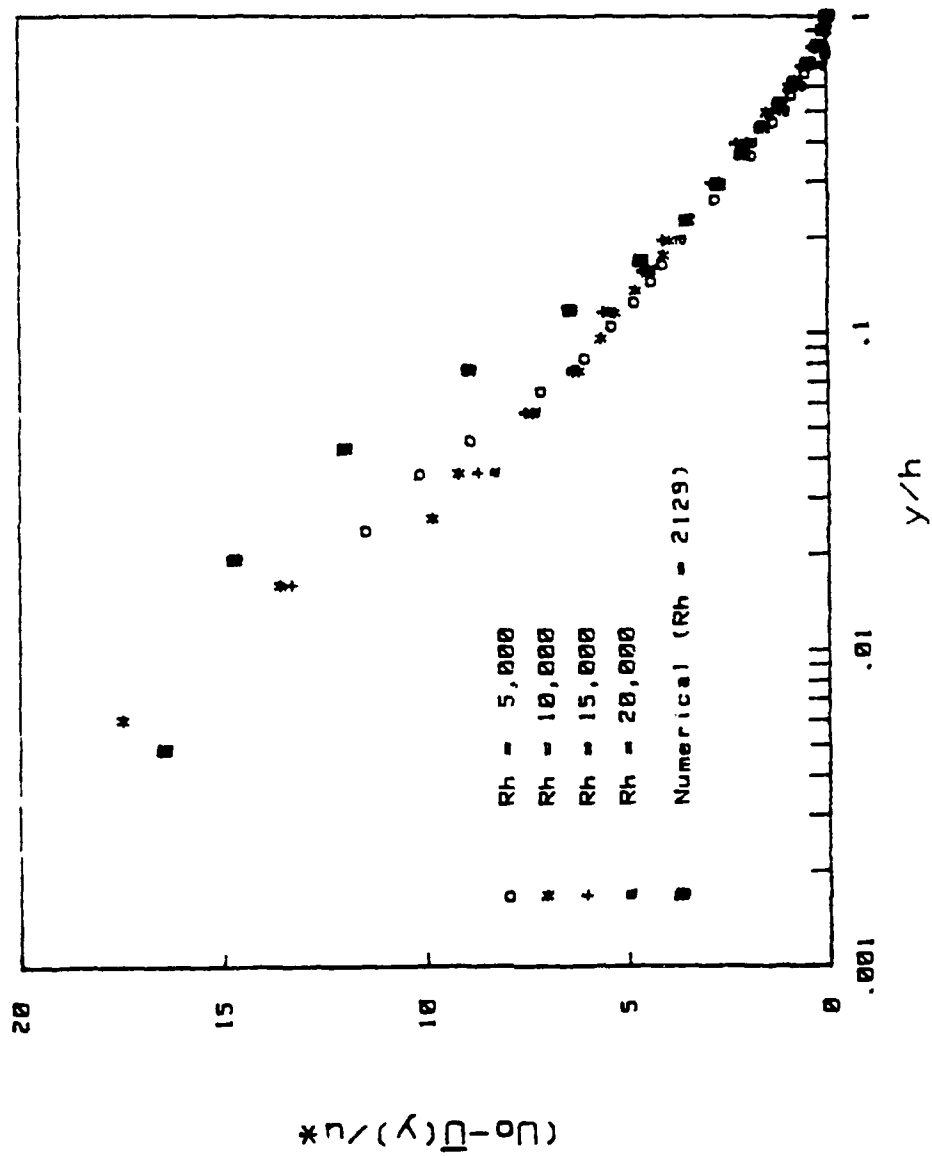


FIGURE 4.9 Velocity Defect for All Data.

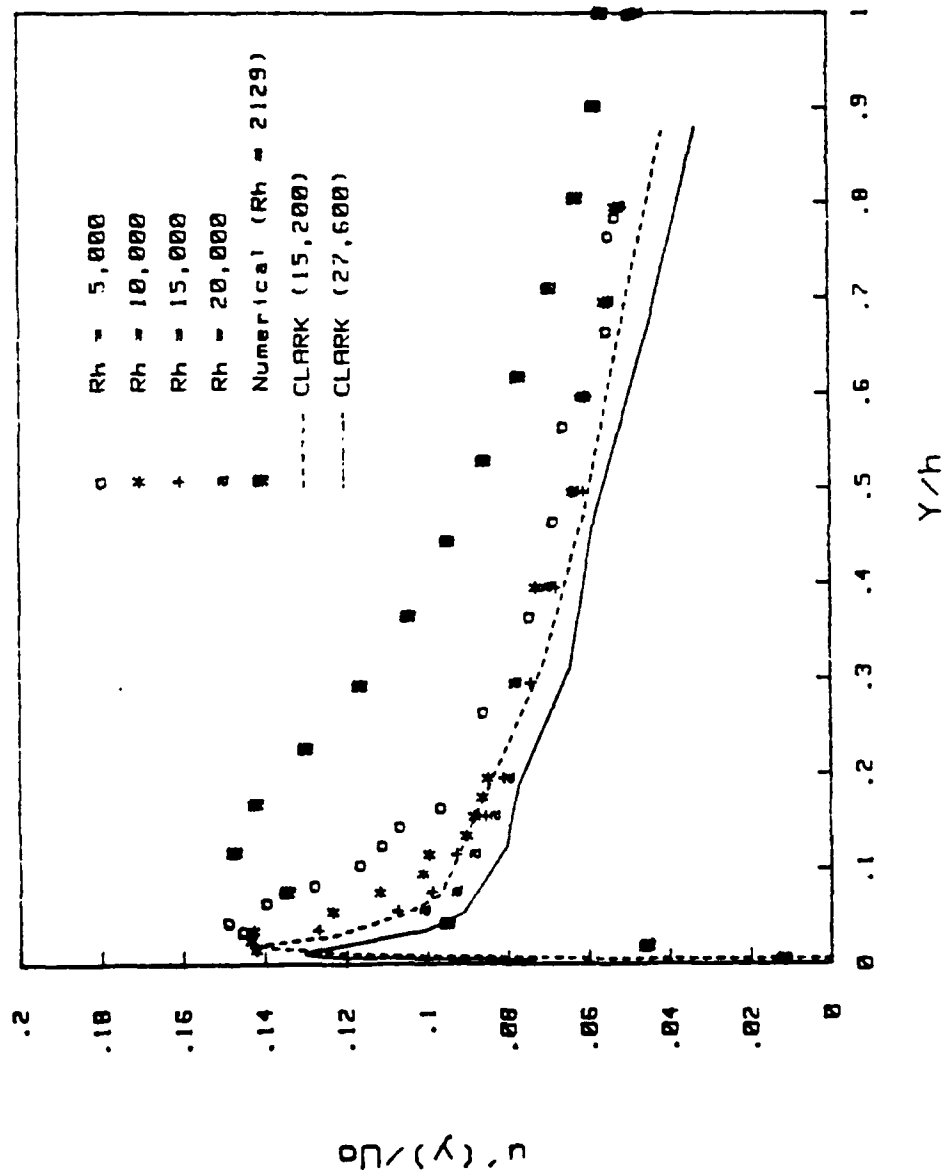


FIGURE 4.10 RMS Profile Versus Outer Variables.

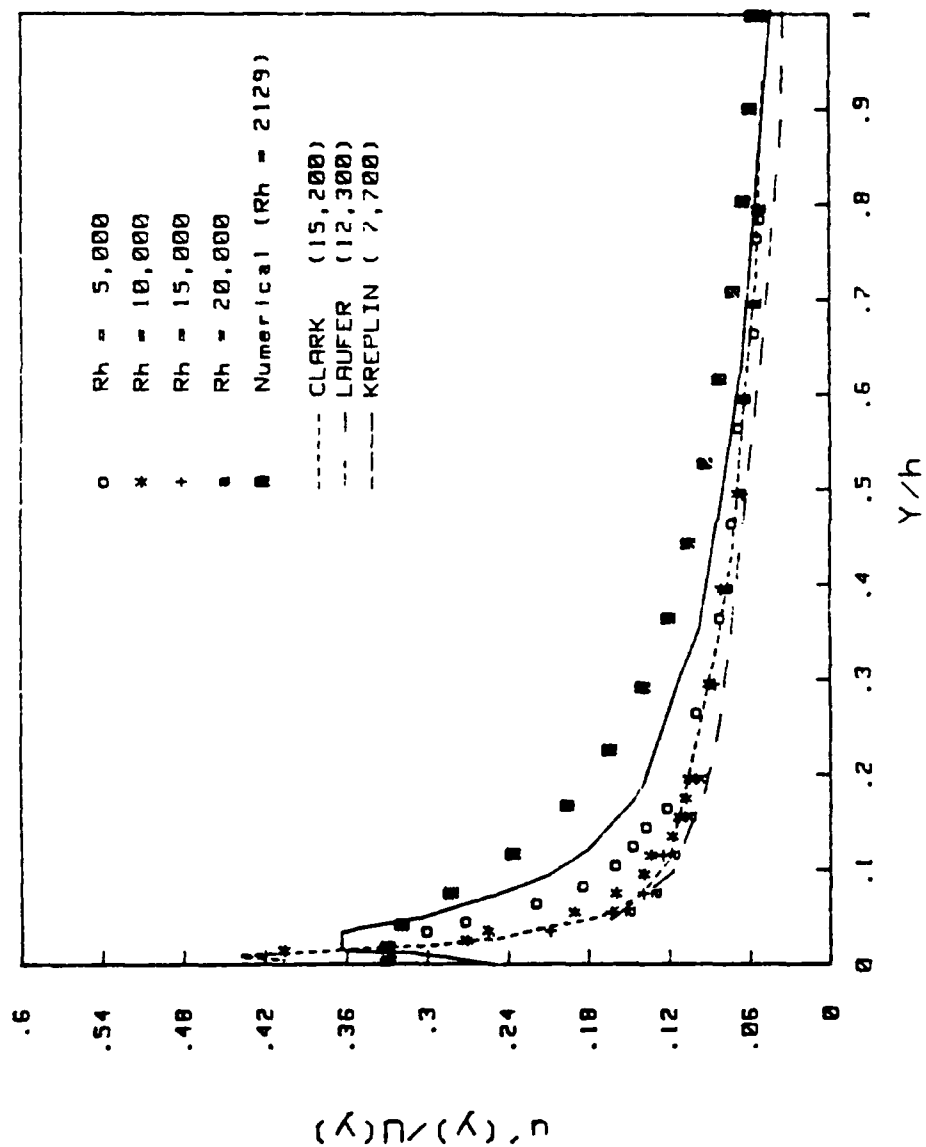


FIGURE 4.11 RMS Profile Versus Local Variables.

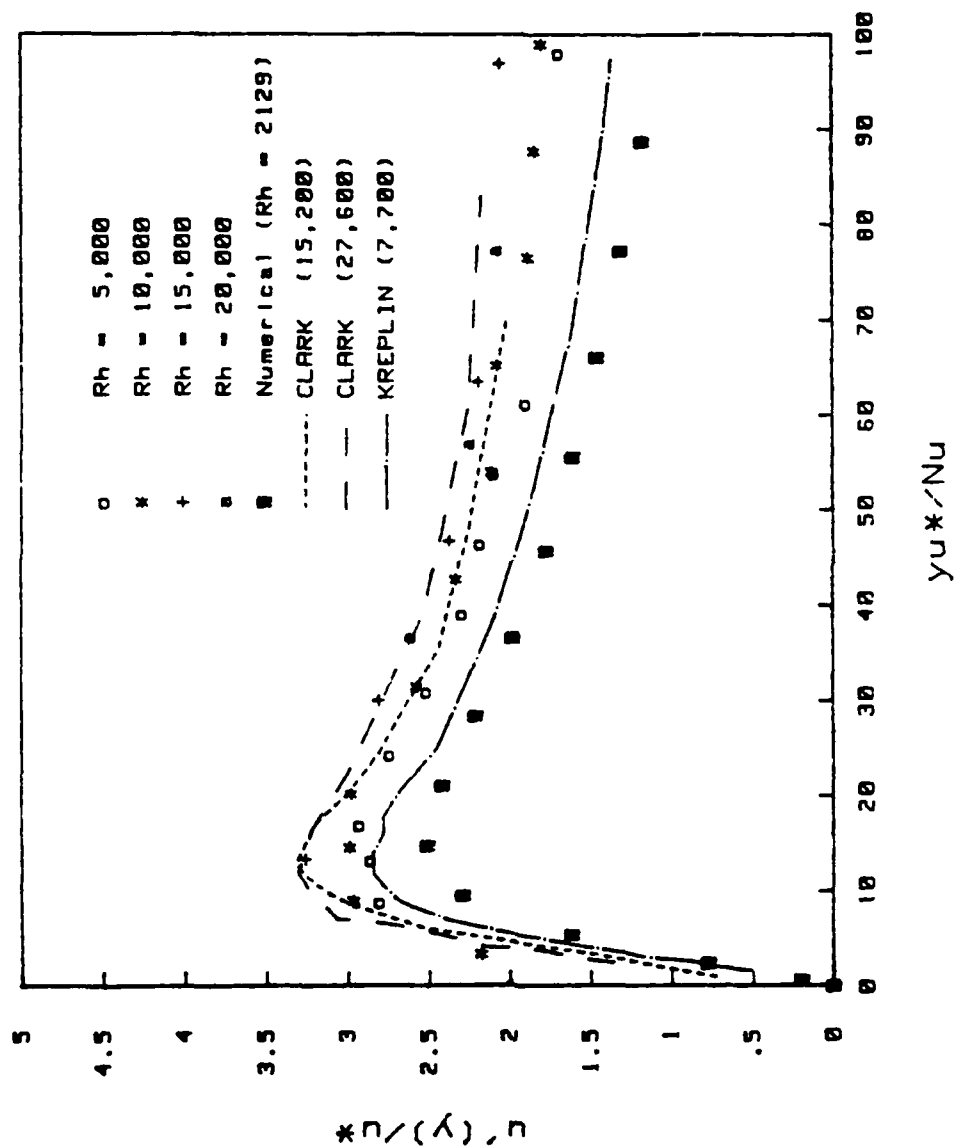


FIGURE 4.12 RMS Profile Versus Inner Variables.

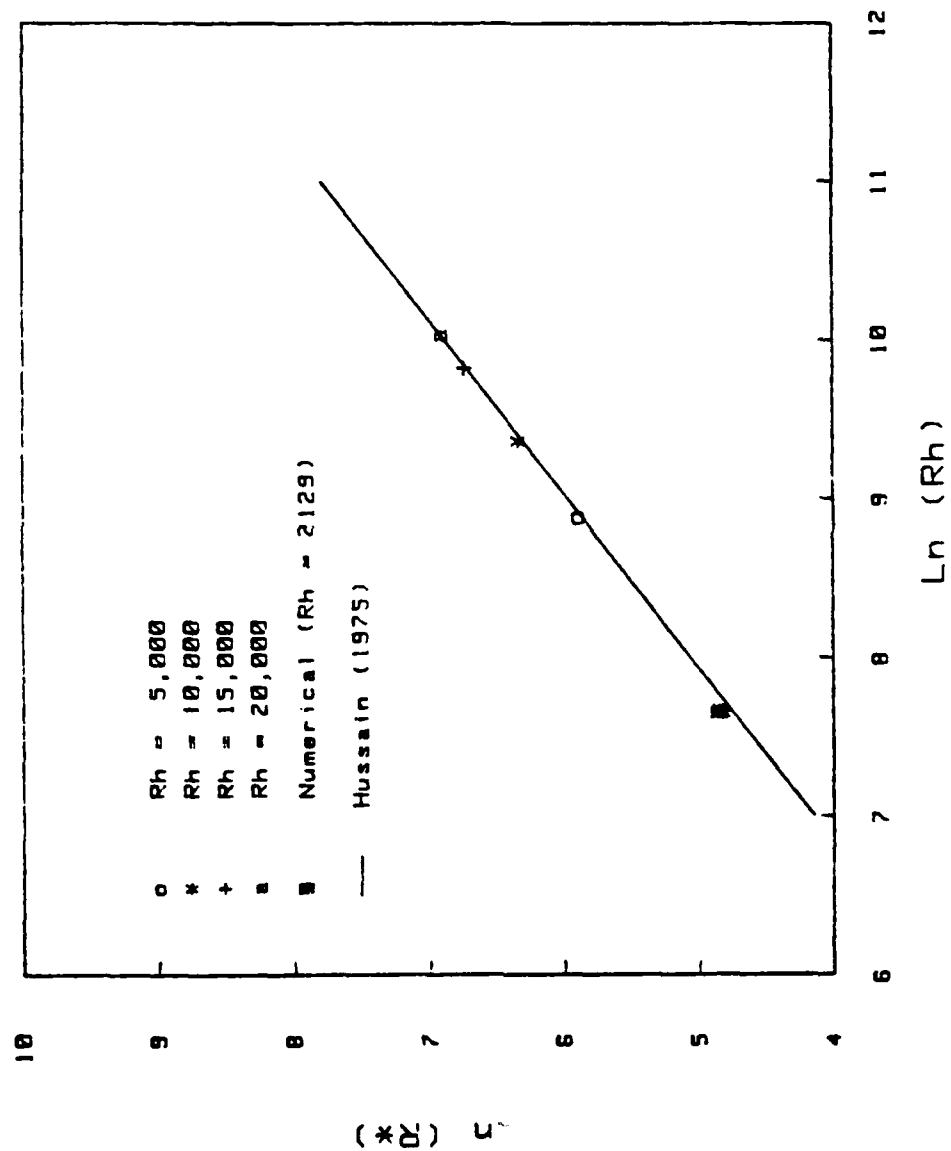


FIGURE 4.13 Friction Velocity Versus Reynolds Number.

CHAPTER 5 EXPERIMENTAL RESULTS FOR PRESSURE

5.1 Introduction

This chapter presents a comparison of the results obtained for the wall pressure field for both the physical and computational experiments which is the primary focus of this study. There are a number of valid reasons for examining duct flows at low Reynolds numbers. First (and foremost), the recent theoretical work related to Direct Numerical Simulation (DNS) experiments has generated excitement in the research community in that a great deal of information appears to be available without the overhead of maintaining large, complicated laboratory facilities. However, this excitement has also introduced a cloudy issue, in that successful evaluation of a computational experiment requires accurate comparison with an identical physical experiment with all parameters matching, before addressing issues not yet resolved. This means that not only should the kinematic properties of the flow, such as mean velocity, turbulence intensity and Reynolds stress profiles be in agreement, but both the spatially averaged "scalar" properties such as the total wall shear stress τ_{wall} , p_{rms}/τ_{wall} , p_{rms}/Q , and the more detailed spectral characteristics of the wall pressure field should also be in agreement.

As first postulated by Kraichnan (1956), the pressure generated at the wall is the summation of kinematic turbulent source terms throughout the boundary layer with over 80% of this contribution taking place within the near wall buffer region ($Y^+ < 50$). The Poisson integral equation for the wall pressure represents an "averaging" process which tends to smooth out small discrepancies not exactly matched in the velocity field. Therefore, if the spectral content of the wall pressure field (including convection velocity, scales of motion and decay rates) does not match between the two comparative experiments, it could be argued that the numerical simulation does not represent a generic flow in entirety. Whether the fault lies with assumed initial and/or boundary conditions, or that the simulation is not considered "mature" enough in spatial or temporal space, are issues to be resolved.

Secondly, because of the computer limitations due to spatial resolution and complex boundary conditions, computational experiments are limited at this time to internal (duct or channel) flows at very low Reynolds numbers. As mentioned in chapter 1, virtually all past investigations of the wall pressure field have been conducted in external flow environments simulating flat plate boundary layers. The few studies done within internal configurations, Clinch (1969), Wambsganss and Zaleski (1970), Wilson *et al.* (1979), and Horne and Hansen (1981), have been

confined to pipe or annulus geometries at Reynolds numbers 2 to 3 orders of magnitude larger than the computational experiment. Therefore, the generation of a detailed data base in a physical configuration specifically tailored to the computational scheme provides for the first time, an informational basis for comparison. In addition, the results presented also show distinct features of duct flows such as length scales, time scales and decay rates which differentiate them from external boundary layers.

The wall pressure signature was recorded for the physical experiment at five locations on the bottom wall of the channel for Reynolds numbers, $Re_h = 10000, 15000, 20000$ and 25000 . Transducers 2 to 5 were located in-line with the flow direction, approximately 5.1cm off the channel centerline. Transducer 1 was located 5.1cm on the opposite side of the channel centerline and aligned with transducer 2 in the same cross-sectional plane. The distance between transducers 1 and 2 resulted in a transverse separation of $\xi_z/h = 4$ which was considered sufficient to ensure zero correlation of turbulent energy between these transducers and hence transducer 1 was used for noise cancellation as outlined in chapter three. The separation distances in the flow direction for transducers 2 thru 5 were in multiples of $\xi_x/h = 0.16$, with the largest distance possible at $\xi_x/h = 0.48$. During each run, all five transducers were recorded simultaneously together with the pressure gradient, and digitally stored on magnetic tape. This data was then transferred to a VAX 780 computer to be processed by software developed for data analysis.

The digital/software approach for data analysis, in contrast to utilizing a spectral analyzer, was superior for a number of reasons. First, for comparison purposes, both experiments could be analyzed via the same method. Secondly, a number of combinations of transform size in Fourier space could be chosen when analyzing the physical data, in order to optimize the best choice combination between spectral accuracy and resolution. According to Bendat and Piersol (1980), and outlined in chapter 3, the accuracy in measuring all spectral statistical functions is inversely proportional to N , the number of ensemble averages obtained. However, due to the limited number of points recorded in time, higher resolution in spectral space requires a larger transform size (larger set of time points), resulting in an overall lower number of ensemble averages. Performing this analysis on a computer with almost immediate graphical output provides the researcher with enormous convenience. A third reason for this approach was also outlined in chapter 3 and is related to cancellation. The largest potential source of error in cancellation schemes involving additions and subtractions in either "real" or "spectral" space, is that representative voltages are used rather than the actual pressure signals. Hence, errors are

introduced proportional to the sensitivity ratios of the channels being analyzed. In a realistic sense, it is virtually impossible to apply the actual sensitivity constants to each channel being investigated within the laboratory environment. On the other hand, having the entire data sets stored on a computer where the analysis is going to be performed, provides a convenient means for dealing with the actual pressure signals by applying the appropriate sensitivities to each channel as the data is being read back into the analysis program.

Table 5.1 lists the various combinations of record size and resulting ensemble averages that were investigated for the physical experiment together with that possible for the computational experiment. For instance, set 1 indicates 512 time points per record size, with a resolution of 7.81 Hz. The total number of points recorded in time during an experimental run at any Reynolds number, divided by the 512 points required per record, resulted in 3500 ensemble averages. Sets 1 thru 6 represent the possibilities investigated for all Reynolds numbers.

Table 5.1 Possible Record Size and Ensemble Averages

Set	N_{time} (time pts)	$N_{frequency}$ (frequency pts)	$N_{average}$ (ensemble averages)	Resolution (Hz)
1	512	257	3500	7.81
2	1024	513	1750	3.91
3	2048	1025	875	1.95
4	4096	2049	450	0.98
5	16384	8193	110	0.24
6*	(.....)	1061	110/875	0.24/1.95
Numerical	512	257	128/2048	~ 7.81

* Set # 6 was a combination of sets 3 and 5

5.2 Correction Analysis and rms Pressure Levels

5.2.1 Auto-Spectrum Levels and Magnitude Squared Coherence

Representative auto-spectra from transducer 2 for all four Reynolds numbers in the physical experiment are presented in figures 5.1 thru 5.4. These figures indicate the direct output (uncorrected) from the transducer, the corrected version using the technique outlined in chapter 3, and the background noise level with all turbulence removed. These results were taken

from data set 2 in table 5.1 because the number of time points and ensemble averages gave an expected accuracy in the auto-spectrum on the order of 2.4 % and the resolution obtained was sufficient to show effective cancellation. A number of interesting features are indicated. All four Reynolds numbers show that although the channel attempts to minimize acoustic and/or background facility generated noise by operating in a "blowdown" mode, a very intense contaminating noise level exists for frequencies less than approximately $10Hz$. An analysis was conducted to determine if organ pipe resonances were present in the system, but the frequencies computed were at least an order of magnitude larger than calculated.

In order to better illuminate the lower frequency region, separate runs were made at each Reynolds number over a bandwidth of $100Hz$, with a resolution of approximately $0.1Hz$. The results showed three distinct frequencies located at approximately 1, 5 and $10Hz$ respectively, with their intensities decreasing for each successively larger frequency component. Despite extensive analysis, no sources for these contaminating frequencies could be isolated. Accelerometers were placed on the test section at a number of locations to determine if structure vibration was being transmitted to the fluid within the channel. There was virtually zero coherence with the accelerometer output and that of the pressure transducers, and no peaks were indicated at these three distinct frequencies. It was surmised that the large upstream reservoir might be the source. In order to maintain constant velocity during each run, high pressure air is discharged in the top of the tank to ensure a constant overall dynamic pressure. One possible explanation is that a very low frequency, slow moving pressure bubble is created in the upstream tank, due to the interaction of the high pressure air with the free surface of the contained water. This low frequency bulk wave is then transmitted acoustically to the channel test section within the flowing fluid.

Another interesting feature indicated in these figures is the limited dynamic range of the transducers used. Figure 5.1 shows that at a Reynolds number of 10,000, the high frequency end of the spectrum is dominated by electronic noise, and the correction scheme fails to adequately cancel the three distinct contaminating frequencies at the low end. It should be noted however, that further examination of figure 5.1 shows that cancellation works rather well at high frequencies where turbulence is present, but lower in intensity than the electronic noise evident. This supports the hypothesis that the "Wiener" cancellation scheme presented in chapter 3 is not only "not" bandwidth limited but that it produces excellent results, provided the level of the contaminating noise is within $20dB$ of the desired signal. If one accepts the

hypotheses of Panton (1980) and Chase (1980), that the low frequency end of the wall pressure signature should drop off as ω^2 , then the ratio of amplitudes over a decade in frequency would result in an approximate drop of 20dB in amplitude. Figure 5.1 has a maximum around -10dB at around 10Hz and therefore should drop to about -30dB at approximately 1Hz. The intensity of the contaminating noise is on the order of 50 to 60dB higher in this range and therefore requires extreme cancellation. The lack of effectiveness at this low Reynolds number is not considered to be a failure of the correction scheme. In chapter 3 the assumptions of "homogeneity" and "signal-free" reference were critical to obtaining accurate cancellation. For very low Reynolds numbers, the length scales and decay rates of turbulence, particularly the large scale components at low frequency, might be large and slow enough to extend transversely past the limited separation of transducers 1 and 2. Hence, part of the turbulence itself is being cancelled or otherwise modified. Examining the other three Reynolds numbers shows that cancellation is adequate and the overall background noise level in the channel is approximately 10 to 20dB below the turbulent energy spectrum levels.

In order to show the full range of the cancellation scheme and to better illustrate the three contaminating frequencies, the composite data set 6 from table 5.1 is shown in figure 5.5 for all four Reynolds numbers. This data set combines two analyses, one with a resolution of 1.95Hz and one with a resolution of 0.244Hz with 875 and 110 ensemble averages respectively. The merging of these two sets is apparent in figure 5.5 by the obvious waviness starting at 10Hz and lower. The most interesting information depicted in figure 5.5, is the apparent universal drop-off in spectrum level proportional to frequency with a slope of 1.7 ($f^{1.7}$). Although an ω^2 dependence resulting in 20dB difference in amplitudes is not exactly matched, it is more likely a result of the lower spectral accuracy, due to an ensemble average that at most, only gives an expected error good to approximately 10 percent. In either case, figure 5.5 presents "new" information for internal flow geometries and validates past and present theoretical suppositions for similar frequency dependence for external flows.

Finally, figures 5.6 thru 5.9 show representative results for the magnitude squared coherence γ^2 , for the combinations of transducers 1 : 2, 2 : 3, 2 : 4 and 2 : 5 for all Reynolds numbers. These figures are obtained from data set 2 in table 5.1 for illustrative purposes and serve to indicate two important points. First, the decay in intensity levels as well as loss in coherence with frequency at increasing separation for transducers 2 thru 5 in the flow direction is distinct for all Reynolds numbers. Secondly, the solid line represents the coherence between transducer 1, which was used as a cancellation source, and transducer 2 which was the lead transducer in

the linear array. The separation of these two transducers by $\xi_z/h = 4$ was sufficient to ensure zero correlation of turbulence in a cross-sectional plane for the largest three Reynolds numbers. Examination of all four figures demonstrates that in reality, correction need only be applied for frequencies below approximately $10Hz$. In addition, as pointed out in Horne and Handler (1989), the potential error resulting from a non-signal free reference is specifically determined by the noise coherence level. The maximum error possible is equivalent to $3dB$, when the magnitude squared coherence is equal to unity. This is certainly indicated in figures 5.6 to 5.9. within experimental and computational error.

5.2.2 Root-Mean-Square Pressure Levels (*rms*)

As pointed out in chapter 3, there are three methods of computing the rms level of the wall pressure depending on the method of analysis chosen. The primary method is to utilize equation (2.18) and average the time history data directly, provided there is no low frequency contaminating noise. The second and third methods depend on whether the correlation covariance is solved for, as represented by equation (2.32), or whether the power spectral density is computed directly by Fourier transforming the pressure signals and integrating the auto-spectrum via equation (2.36). All three methods must give the same results, and in reality, the last two are identical as the correlation covariance and spectral density functions are Fourier transform partners.

For the physical experiment, data set 6 was analyzed in order to take advantage of the cancellation scheme to obtain an accurate representation of a generic channel flow as is possible to date. As shown in the previous figures 5.1 to 5.9 it was not possible to average the time history records to obtain p_{rms} , due to the high intensity low frequency noise present in each signal. Therefore, the corrected spectra were integrated throughout the frequency range using equation (2.36), but modified for frequency, as shown by,

$$p_{rms}^2 = \int_0^{\infty} \Phi_{pp}(f) df \quad (5.1)$$

(Note that $\Phi_{pp}(\omega)$ differs from $\Phi_{pp}(f)$ by the factor 4π). As a check of the method of analysis, the raw, uncorrected data time histories were averaged and compared with the integrations of the uncorrected auto-spectrums for which identical results were obtained. The *rms* levels are presented in table 5.2 as ratios p_{rms}/Q and p_{rms}/τ_{wall} together with other related characteristics describing all flow configurations investigated.

Table 5.2 Parameters Governing Both Experiments

Type	U_{avg}	$\frac{p_{rms}}{\tau_{wall}}$	$\frac{p_{rms}}{Q}$	$\frac{u^*}{U_{avg}}$	d^+	R^*
Physical	2.48	2.84	0.0174	0.056	23	572
	3.87	2.12	0.0106	0.050	32	806
	4.80	2.36	0.0108	0.048	38	955
	6.18	2.26	0.0092	0.045	46	1156
Numerical		1.32	0.0092	0.059	~ 40	125

It should be noted, as pointed out in chapters 3 and 4 that the physical experiment was really a composite of two experiments; one in which the kinematic (velocity) data was documented and the second for which the wall pressure results were obtained. In the wall pressure experiment, no values for the centerline velocity were possible as the value for U_{avg} was the only variable recorded. Therefore, the average velocity was used to normalize the *rms* pressure by calculating a dynamic pressure term as represented by $Q = \frac{1}{2}\rho U_{avg}^2$. Because there is no ratio of U_{avg}/U_∞ generally accepted within the literature for channel flows, actual measurable values were used to determine these ratios.

Figure 5.10 shows the values of p_{rms}/Q taken from table 5.2, plotted versus transducer diameter normalized by the viscous length scale ν/u^* . Included are the measurements of Blake (1970), Schewe (1983), and Farabee (1986). It is not clear what value to use for d^+ for the computational results, even though the value of $d^+ \sim 40$ is indicated in table 5.2. The separation distance between computational grid points in the flow direction is $\xi_x u^*/\nu = 40$, and limits the smallest scales resolvable. As shown in figure 5.10, both experiments agree quite well with the excellent data of Blake and Schewe, and the more recent data of Farabee. It should be noted however, that Blake's, Schewe's and Farabee's data were obtained from experiments conducted within flat plate boundary layers.

5.3 Spectral Features of Channel Flow Wall Pressure

5.3.1 Single Point Frequency Spectra

The single point frequency spectra were measured and noise cancellation techniques applied at all five locations in the channel test section. Except for the lowest Reynolds number at 10,000, all other results demonstrated turbulent homogeneity and produced similar results at all Reynolds numbers. The single point frequency spectra at the Reynolds numbers $R_h = 15,000$

and 25,000 were chosen to compare with both the computational experiment and flat plate data from the literature. These Reynolds numbers were approximately 7 and 12 times larger than the computational experiment respectively, and table 5.2 indicates their values for R^* as 806 and 1156. Figures 5.2 and 5.4 show that the intensity level of the pressure fluctuations was sufficiently above the background noise and the corrected results show good cancellation of the low frequency acoustic contamination.

The velocity fluctuations throughout the boundary layer comprise the source terms for the wall pressure fluctuations. If one examines the length and time scales which appear to collapse the pressure spectra to those scales characteristic of the turbulent boundary layer, it may be possible to determine the specific origins of these source terms. Detailed information which quantify these regions more explicitly must be obtained from cross-spectral information. However, at least in a global sense, single point data may be examined to determine orders of magnitude.

Figures 5.11 thru 5.16 show the single point pressure spectra normalized by three sets of variables commonly used in the literature. For these and subsequent plotted results, the following relations were used.

$$U_{avg}/U_{\infty} = 0.84 \quad (5.2)$$

$$\delta/\delta^* = 7 \quad (5.3)$$

$$\delta/h = 1 \quad (5.4)$$

$$\text{physical hydraulic diameter}, \frac{d_h}{2h} = 1.89 \quad (5.5)$$

$$\text{computational hydraulic diameter}, \frac{d_h}{2h} = 2.00 \quad (5.6)$$

It must be noted, that the above relations are used only to compare the experimental results with typical data in the literature which represent flat plate boundary layers and for which these parameters are usually measured and have a certain significance. Although there has been no acceptable value for U_{avg}/U_{∞} reported in the literature, examination of the velocity data for the physical experiment presented in chapter 3 indicates that the above value given by equation (5.2) is reasonable. Figure 5.11 shows the frequency spectra scaled on the outer flow length and velocity scales δ^* and U_{∞} respectively, in the form,

$$\frac{\Phi_p(\omega)U_{\infty}}{Q^2\delta^*} \text{ vs. } \frac{\omega\delta^*}{U_{\infty}} \quad (5.7)$$

This is usually termed "outer-variable" scaling and uses a time scale δ^*/U_∞ associated with the outer part of the boundary layer. Examination of the results from the physical experiment reconfirm the ω^2 dependence at low frequencies mentioned in section 5.2.1. The time scale could be thought of as a combination of a velocity scale U_∞ , and a length scale δ^* (or δ), which are characteristic of the outer flow, large scale, slower moving structure (low frequency). Despite both the physical and numerical data indicating an ω^2 dependence, the normalization used does not collapse both experimental sets of data exactly for very low frequencies. In a channel, the outer flow consists of that structure which exists and/or occupies the entire channel cross-section, hence the centerline velocity and channel half-height U_∞ and h respectively, certainly constitute proper velocity and length scales for normalization of the pressure spectra amplitudes. For the flat plate flows of Blake (1970) and Farabee (1986), U_∞ and δ^* represent proper outer flow variables, but again, no collapse of the data is readily apparent between the two internal/external flow regimes.

Figure 5.12 shows the frequency spectra scaled on a combination of inner and outer flow variables in the form,

$$\frac{\Phi_p(\omega)U_\infty}{\tau_{wall}^2\delta^*} \text{ vs. } \frac{\omega\delta^*}{U_\infty} \quad (5.8)$$

A time scale associated with the outer flow is used, but the wall shear stress is now incorporated to normalize the intensity of the wall pressure fluctuations. Corcos (1963), Blake (1970) and Farabee (1986) have all shown that the maximum in the wall pressure spectrum should occur at $\omega\delta^*/U_\infty$ approximately equal to 0.3. The flat plate boundary layer data indicated in figure 5.12 substantiate this value, but the channel flow data from both the physical and numerical experiments do not agree with this result. Figure 5.13 modifies the data in figure 5.12 by computing a hydraulic diameter given by,

$$\text{Hydraulic diameter, } d_h = \frac{4 \text{ Area}}{\text{Perimeter}}. \quad (5.9)$$

The value of d_h/h equals 4.0 and 3.8 for the computational and physical experiments respectively. As shown in figure 5.13, the maximum in the channel flow data does peak at $\omega\delta^*/U_\infty = 0.3$. However there is a marked difference between internal and external flows as indicated by the flat plate data of Blake (1970) and Farabee (1986). If one were to use the hydraulic diameter only on the x-axis in figure 5.13, the agreement at $\omega\delta^*/U_\infty = 0.3$ is met as shown in figure 5.14, but major differences still exist within the low frequency region.

A number of points can be made from the collective examination of figures 5.11 thru 5.14. First, scaling only on outer flow variables does appear to collapse the data between the two

flow configurations, internal and external provided hydraulic diameter is used. This is somewhat subjective, as there is virtually no information in the literature at low frequency. Second, normalization of the wall pressure fluctuations with τ_{wall} in mixed (inner-outer) variable scaling does collapse the spectrum amplitudes for internal and external flows separately, and the maximum in the spectrums does appear to be universal at $\omega\delta^*/U_\infty = 0.3$, provided internal flows can be characterized by hydraulic diameter. Third, the most interesting feature with mixed variable scaling is the important role that the wall shear plays in establishing the magnitudes of the low frequency pressure fluctuations. This implies that inner flow length scales are much different between the two regimes. Fourth, the computational experiment demonstrates marked degradation at low frequencies. The ω^2 dependence appears to be indicated, but the breadth of the spectrum at low frequencies is not of sufficient bandwidth to collapse this data with the physical experiment. This is a result of insufficient time history data and the periodic boundary conditions interfering with the flow. Finally, neither of the two sets of variable normalization hold for the high frequency portion of the spectra. This is not unexpected because smaller scale structures corresponding to higher frequencies exist within the inner layer of the boundary layer and have a time scale of ν/u^{*2} . Collectively, these results show that external and internal flow configurations constitute two physically different flow regimes whose outer and inner flows are "not" similar.

Figure 5.15 scales the high frequency portion of the wall pressure fluctuations on inner variables. The velocity scale is u^* and the length scale is represented by ν/u^* . Both the physical and computational data sets collapse in the region $0.4 < \omega\nu/u^{*2} < 1$. This region is represented by an $\omega^{-7/3}$ dependence, as shown by Schewe (1984). There is a discrepancy in the computational data at $\omega\nu/u^{*2} \sim 1$. The shape of the numerical spectrum appears to change slope sharply beyond this frequency, which is typical of reduced resolution due to finite transducer size in physical experiments. One of the critical aspects of DNS calculations as shown by Reynolds (1989), is that the grid resolution size must be small enough to resolve both the largest and smallest eddies that are dynamically significant to the flow. The grid size for the computational experiment is represented by $x^* = \xi_x u^*/\nu = 40$. From table 5.2, $u^*/U_\infty = .059$. As this region of the boundary layer is very close to the wall, an assumption of convection velocity $U_c/U_\infty = 0.5$ is not unreasonable. Using these values, a cut-off frequency due to finite 'computational' resolution could be determined as,

$$\left[\frac{\omega\nu}{u^{*2}}\right]_{cutoff} = 0.5 \frac{2\pi}{x^* u^*/U_\infty} = 1.33. \quad (5.10)$$

Apparently, the discrepancy between the physical and computational experiments at very high frequencies, is a result of the relatively poor resolution capability resulting from the computational grid size.

Figure 5.16 shows the computational spectrum compared with the physical experiment Reynolds number $R_h = 15,000$ from the composite data set 6 and set 1 which also had 512 time points per ensemble record. Clearly, the only discrepancies in the software approach for the physical data is in that region where the higher resolution had only 100 averages. This is common in power spectra that do not contain enough time points to achieve sufficient accuracy. The amplitudes exhibit a waviness and have not settled down to their steady state values. As a final note, the wall pressure spectrum from the computational experiment exhibits a number of peaks in the low frequency region. Similar to the physical experiment, these peaks represent noise and are a result of the periodic boundary conditions in the DNS calculations. This phenomenon will be addressed further in section 5.4.

5.3.2 Cross-Spectral (two-point) Pressure Measurements

Measurements of the two-point space-time statistics of the wall pressure field aid in quantifying the convective properties more fully and provide insight into the size of the eddies representative of the inner and outer flow. The magnitude of the cross-spectrum is expressed in normalized form as the square-root of the magnitude-squared coherence function, as outlined in chapter 2, equation (2.37). For each successive streamwise separation, the phase of the cross-spectrum represents a narrow-band interpretation of the convection velocity and has the form,

$$U_c = \frac{-\omega \xi_x}{\alpha(\omega, \xi_x)}. \quad (5.11)$$

For flow in the streamwise direction, Taylor proposed that the cross spectrum phase can assume a physical meaning when expressed as,

$$-\alpha = \frac{\omega \xi_x}{U_c} = \frac{2\pi \xi_x}{\lambda_x}. \quad (5.12a)$$

or

$$-\alpha = \frac{\omega \xi_x}{U_c} = k_x \xi_x. \quad (5.12b)$$

where $k_x = 2\pi/\lambda_x$. As shown, the phase can be interpreted as a non-dimensional wave number. By plotting the magnitude of the coherence versus the phase, an indication of the decay of the dominant pressure producing eddies of a specific size λ_x may be obtained.

Two-point measurements were made for the physical experiment at three streamwise separations characterized by $\xi_x/h = 0.16, 0.32$ and 0.48 . The computational experiment's grid spacing provided ratios of $(\xi_x/h)_j = j(0.32)$ with $j = 1, 2, \dots, 15$. Only 128 ensemble averages were possible for the computational experiment when calculating the cross-spectrum. In addition, the short length of the computational box resulted in the periodic boundary conditions affecting adversely the phase information, therefore, only the physical experimental data for coherence will be displayed. Figures 5.17 to 5.19 present the streamwise coherence plotted versus the phase $\alpha(\omega, \xi_x)$ for the largest three Reynolds numbers. Bull (1967) proposed that the streamwise coherence exhibited an exponential decay of the form,

$$|\gamma(\omega, \xi_x)| = \exp\left[-C_o\left(\frac{2\pi\xi_x}{\lambda_x}\right)\right], \quad (5.13)$$

and this relation is indicated in each figure. Bull found a value for C_o equal to approximately 0.12. For other flat plate flows in the literature, C_o has taken on values from 0.1 to 0.2 and appear to decrease as the Reynolds number increases. The more recent study of Farabee (1986) found values of $C_o = 0.145$ and 0.125 . In figures 5.17 to 5.19, the values indicated are larger, ranging from 0.27 to 0.18 and do exhibit this same Reynolds number dependence. Bull found that the streamwise coherence decayed to a value of 0.05 when $\alpha(\omega, \xi_x)$ equaled 24.5. Using equations (5.12a) and (5.13), he obtained the relation,

$$\xi_x \sim 4\lambda_x. \quad (5.14)$$

This suggests that the largest eddies of size λ_x lose coherence upon being convected 4 times their size. Similar results were found by Willmarth and Wooldridge (1962) and Farabee (1986). However, the data of the physical experiment presented here show that eddies of a specific size λ_x lose all their coherence, upon being convected a distance 2 to $2\frac{1}{2}$ times their respective sizes. For example, taking the value $C_o = 0.22$ from figure 5.18 and evaluating the term in brackets from equation (5.13) where $|\gamma(\omega, \xi_x)| = 0.05$ results in,

$$\xi_x = 2.2\lambda_x. \quad (5.15)$$

This implies a faster decay rate for internal flow geometries versus external flat plate boundary layers which have no constraining wall to limit the size of the boundary layer thickness δ . This

suggests that channel flows which are characterized by a fixed length scale (either $2h$ for ducts, or D the diameter in pipes) force eddies of a specific size to decay in half the distance for internal flows versus external. It is not clear whether this has been previously observed since the pipe flow experiments of Bakewell (1963) and Clinch (1969) were broadband analyses for which transducer resolution was affected by cancellation effects.

In duct flows, to a large extent, it has been proposed that turbulence is characterized primarily by what goes on close to the wall rather than in regions closer to the centerline. The outer intermittent region of external flows represented by boundary layers have been hypothesized to be different than the region existing at the channel centerlines. This is substantiated somewhat by the kinematic results from chapter 4, in that the viscous sub-layer, buffer, and log-law regions are very similar to those results reported for external flows. However, the shorter decay lengths and lower intensity values for all frequencies in the pressure spectra for channel flows gives evidence that both internal and external boundary layers are fundamentally different.

5.3.3 Convection Velocity (narrow-band)

A narrow band analysis of the convection velocity is performed by solving equation 5.11 for each separation distance between transducers. For both experiments, these results are presented in figures 5.20 to 5.23 scaled on outer variables h and U_∞ , and in figures 5.24 to 5.27 scaled on the inner variable time scale ν/u^* .

The most distinguishing feature displayed by these results is the Reynolds number dependence. First, at all Reynolds numbers (including the computational experiment), the convection velocity decreases to zero with decreasing frequency. This is a trend first measured by Blake (1970) and Wills (1970) and predicted by Chase (1980) and recently confirmed by Farabee (1986). Because this trend is indicated no matter the size of transducer separation, the implication is that a finite lower frequency limit exists for which there is measurable coherence. Referring to figures 5.17 to 5.19 this is shown clearly by the drop in coherence at low frequency. As Farabee showed, equation (5.13) can achieve unity, either by ω going to zero or ξ_x going to zero. The coherence going to 1, as ξ_x goes to zero, is a required result, since the cross-spectrum essentially becomes the auto-spectrum for which $\gamma = 1$ for all frequencies. However, if γ goes to 1 as ω goes to zero, this implies that low frequency components remain coherent over very long distances, without being distorted by the flow, which is not physically realizable. Thus,

as figures 5.17 to 5.19 show, there is a loss of coherence with decreasing frequency, and as the convection velocities support, there is a finite frequency for which structure at all wavenumbers exist within the channel and are convected downstream. Secondly, for all Reynolds numbers, the convection velocity assumes higher values for larger separation distances, implying that as the transducer separation increases, smaller scale structure has decayed and all that remains is the larger size eddies which physically must exist further out into the flow and are subject to a higher velocity. Thirdly, at a fixed frequency, say $\omega h/U_\infty = 0.3$, as the Reynolds number increases, even smaller scale structure exists within the flow and is convected downstream. This is sensed by the transducers, by registering an even higher convection velocity, from a value of U_c/U_∞ equal to 0.65 for the low Reynolds number, to a value of 0.98 at a Reynolds number of 25,000. The convection velocity ratio at the smaller separation seems to asymptote at large frequencies to a value of approximately 0.55 and for the larger separations, a value closer to 0.75.

The computational experiment exhibits the same Reynolds number dependence as shown by the physical experiment, except for the relative peak values and magnitude dependence on separation distance. As mentioned previously, the cross-spectrum phase was very difficult to measure, due to the low number of ensemble averages available and interference from the periodic boundary conditions. Therefore, the only expectation was to confirm the Reynolds number dependence from this set of data. Figures 5.24 to 5.27 show the same information just discussed, except they are scaled on the inner variable time scale, $\nu/u^*{}^2$.

In section 5.3.2, an assumption was made that $k_x = \omega/U_c(\omega)$ which is Taylor's hypothesis that a unique convection velocity exists that relates the wavenumber of a certain fluctuation to its frequency. Figures 5.20 to 5.27 show that the convection velocity varies with ξ_x/h . This supports the belief that the pressure field is dispersive, in which fluctuations of approximately the same size may convect at different velocities depending on their location within the flow. This idea was explicitly shown by Wills (1970) who spatially transformed his cross-spectral measurements into contour plots showing both the dispersive nature of the wall pressure field and that for decreasing frequency, U_c/U_∞ should tend to zero.

5.4 Temporal Features of Channel Flow

5.4.1 Correlation Analysis (broadband)

As shown in the previous sections, a narrow-band analysis consists of evaluating the cross-spectral density functions in narrow frequency bandwidths. Assuming that Taylor's hypothesis holds, this provides a means for evaluating the properties of the wall pressure field for all wave numbers contained within a narrow frequency band centered at ω . The space-time correlation function is the Fourier transform of the cross-spectra for which all phase information is lost. The retained information consists of the relative measure of correlation of the large scale components, and the distances and limits in time for which they remain coherent. In addition, a broad band convection speed can be determined for all scales and frequencies by the proper interpretation of this function.

For the most part, a broadband analysis does not provide very much detail about the turbulence present and/or its relationship to the wall pressure. On the other hand, one of the goals of this experimental endeavor was to evaluate the wall pressure results from a DNS calculation by comparing with those of the physical experiment. All information extracted from both experiments should be considered valuable. In addition, one of the assets of the software approach to analysis, was to evaluate both experiments via the same approach. As mentioned, the computational experiment had indications of low frequency noise contamination and the possibility of resolution problems due to insufficient grid size. The temporal features, as obtained through the Fourier transform of the cross-spectral density function, will substantiate these observations more clearly.

The space-time correlation functions for the physical experiment are presented in figures 5.28 to 5.31 for all four Reynolds numbers as a function of τ , the separation in time. Figure 5.32 contains similar results for the computational experiment as a function of T^* , a non-dimensional time. As mentioned previously, there was a low frequency contamination centered at approximately 1, 5 and 10 Hz, respectively for all four Reynolds numbers. This low frequency noise had such large amplitudes, that it completely swamped the time signals. The single point auto-spectra presented in section 5.3.1 showed a contamination over the low range of frequencies which were 30 to 50dB higher than the rest of the spectrum levels. When Fourier transforming frequency spectra, large amplitudes, particularly at low frequencies, tend to mask the overall output. This can be observed in figures 5.28 to 5.31, by the almost solid horizontal lines at the top of each figure. These lines represent the Fourier transforms of the "un-corrected" spectrums.

The other four curves represent the fourier transforms of the "corrected" cross-spectral density functions from section 5.3.2. It was speculated in section 5.2.1 that the separation between the two lead transducers 1 and 2 for the low Reynolds number at 10,000 was insufficient for total cancellation of the contaminating noise. This is evident in figure 5.28 by the somewhat arbitrary coefficients obtained at each maximum. The higher Reynolds numbers, for which cancellation produced excellent results, clearly show the dominant characteristic of the wall-pressure field as a convecting pattern which rapidly loses coherence. Although there were not sufficient transducers to obtain a much broader separation in the streamwise direction, the three separations presented do indicate slight asymmetries for each successive correlation as represented by a dispersive field.

The results from the computational experimental results presented in figure 5.32 show similar behavior for the first nine separational grid points. Asymmetry in each successive correlation is somewhat subjective to isolate, however, this is consistent with a very low Reynolds number flow which would only be weakly dispersive. The most interesting feature in the computational results is the indication of periodicities at large time separations for each correlation. This is a direct result of the periodic boundary conditions used within DNS calculations. If the computational box over which the flow is being computed is too small for the Reynolds number being investigated, the flow senses or feels this periodicity. This same periodicity was observed in the single point spectra of the computational results in figures 5.11 thru 5.16 as the individual peaks at low frequency. This periodicity represents noise, and is very similar to that observed in the physical experiment. The only method of eliminating it, is to increase the box size such that it is much larger than the size of the largest structure remaining correlated. In section 5.3.2 it was found that the structure at all wavenumbers (wavelengths) decay over distances between 2 and $2\frac{1}{2}$ times their size. For the computational experiment investigated, the box size was 5, 2 and 5 units in the x, y, z directions, respectively. Because $y = 2h$, then $x = 5$ corresponds to a computational box only $5h$ units long in the x direction. In order to eliminate the periodicity in the boundary conditions from interfering with the results, this box size should be increased by a factor two to four times its present size.

In order to more explicitly compare the two experiments, a comparison was made based on outer and inner unit time scales. Figures 5.33 and 5.34 use a time scale h/U_∞ associated with the outer flow, and figures 5.35 and 5.36 use a time scale ν/u_*^2 associated with flow close to the wall. Figure 5.33 shows the largest three Reynolds numbers for the physical experiment at their respective values of r_1/h separation. Two distinct features are present as a function of Reynolds

number. First, all three separations show a frozen convection pattern. In other words, each successive correlation is coincident about its value of r_1/h for all Reynolds numbers. Secondly, the correlation coefficient has the highest value and broadest curve for the smallest Reynolds number at the first separation, but as the flow convects and decays, all curves approach a similar shape and intensity. Figure 5.34 shows a comparison between the computational experiment and the lowest Reynolds number at $R_A = 15,000$ for the same separation, $r_1/h = 0.32$. The computational experiment indicates a higher intensity and broader shape at this separation, consistent with the previous information. It may also be noted, that the physical experiment supports the decay properties shown in section 5.3.2 via a narrow band analysis with virtually all turbulence decaying within two non-dimensional length units.

Figures 5.35 and 5.36 show similar trends when non-dimensionalized on an inner time scale. The difference is that a convecting pattern is observed based on Reynolds number. The same trend indicated earlier is observed relative to intensity levels, but the largest Reynolds numbers include much smaller length scales with resulting smaller time scales and show a pseudo moving convection pattern. Again, the similar trend is observed in figure 5.36 for the computational experiment, with its time scale being much larger at its lower Reynolds number than for the larger Reynolds numbers of the physical experiment. The moving convecting pattern can be explained by the differing values of ξ^* of each experiment. In figures 5.33 and 5.34, each successive correlation hump is at the same r_1/h value which does not change with Reynolds number. For figures 5.35 and 5.36, each experiment incurs a different value for the shear velocity u^* , hence $\xi^* = r_1 u^* / \nu$ has ever increasing values from the computational experiment through the physical experiment. To summarize, the computational experiment represents similar results to the physical experiment which are consistent with its lower Reynolds number. However, its limited computational box size, contributed to a much larger decay rate than expected with the periodic boundary conditions contributing noise at the larger time separations, hence lower frequencies.

Figure 5.37 presents the convection velocity based on a broadband approach. In other words, the time for the maximum to occur at each successive separation in the curves of figures 5.33 thru 5.36 is combined with the separation distance to obtain a convection velocity according to equation (2.43). Similar to the results of Bull (1967) and Blake (1970), the convection velocity increases with separation for both experiments. Both Bull and Blake showed that the broadband convection velocity should begin about $U_c/U_\infty = 0.5$ and increase with separation to an asymptotic value of about 0.75. The computational results are somewhat influenced by

the periodicity interfering with their intensity levels, and the physical experiment did not have enough separations to reach an asymptotic value. On the whole, the results of both present experiments are consistent with those in the literature.

5.4.2 Length and Time Scales

As postulated by Kraichnan (1956), the integration of the auto-covariance function for pressure over a flat plate to include the wall of a channel, should be equal to zero such that no net force per unit area would be present. However, Hansen *et al.* (1987) argued that channel flows can support very large scale low frequency structure such that this integration is finite. Because the spatial correlation as defined by equation (2.47) was not obtained, a macro-length scale could not be defined via this analysis. Therefore, the evaluation of the auto correlation functions at the first 'zero' crossing for each Reynolds number of the physical experiment were obtained as an approximation for macro-time scales and are indicated as,

$$R_h = 15,000 \longrightarrow \mathcal{T}_{o_1} = 6.25 \text{ (msec) },$$

$$R_h = 20,000 \longrightarrow \mathcal{T}_{o_2} = 8.50 \text{ (msec) },$$

$$R_h = 25,000 \longrightarrow \mathcal{T}_{o_3} = 6.75 \text{ (msec) }.$$

From Taylor's hypothesis, one can define a macro-length scale L_x from equation (2.49) by assuming that the largest structure existing in the flow is proportional to the maximum velocity and the maximum time scale. The scales for the three highest Reynolds numbers are,

$$R_h = 15,000 \longrightarrow L_{x_1}/h = 0.66 ,$$

$$R_h = 20,000 \longrightarrow L_{x_2}/h = 1.10 ,$$

$$R_h = 25,000 \longrightarrow L_{x_3}/h = 1.14 .$$

These scales give a relative measure of the size of the largest eddies which exist in the flow and contain most of the energy. They are also indicative of the longest distance over which large eddies are correlated. From section 5.3.2 and 5.4.1, it was shown that eddies of a specific size λ_x decay in a distance approximately $2 \frac{1}{2}$ times their size in channel flows. The macro-scales indicated above suggest that it is the limiting dimension of a channel ($2h$) which controls the size and extent over which structure exists and remains coherent. For the computational experiment, the total box size of $\Delta x = 5h$ would seem to be only twice as long as the correlation

length scale for the largest eddies. Thus, only two statistically independent points in the flow direction would be appropriate for ensemble averaging purposes with 16 in the 'z' direction. Therefore, instead of an accurate statistical average of 2048 ensembles for the auto spectral density function, one only obtains approximately 16 which, according to equation (2.52) gives an error of,

$$\epsilon[\Phi_{pp}(f)] = 0.125. \quad (5.16)$$

Finally, using Taylor's analysis presented in equations (2.50) and (2.51), the time and length micro scales were computed and are listed below.

$$R_h = 15,000 \longrightarrow \tau_{min_1} = 1.21 \text{ (msec) },$$

$$R_h = 20,000 \longrightarrow \tau_{min_2} = 0.93 \text{ (msec) },$$

$$R_h = 25,000 \longrightarrow \tau_{min_3} = 0.56 \text{ (msec) } ;$$

$$R_h = 15,000 \longrightarrow l_{x_1}/h = 0.128 ,$$

$$R_h = 20,000 \longrightarrow l_{x_2}/h = 0.122 ,$$

$$R_h = 25,000 \longrightarrow l_{x_3}/h = 0.094 .$$

The definition of a micro-scale is an average and certainly can be considered an upper bound on the size of the smallest eddies. The scale size analysis presented above, is general and requires further investigation of similar computations from the velocity field which the present experimental investigation was unable to provide.

5.4.3 Probability and Time Series Analysis

Schewe (1983) conducted one of the more definitive analyses on external boundary layer flows for which the transducer dimension was as small as nineteen viscous units in size, one of the smallest amongst all investigations. Schewe showed that the wall pressure intensity exceeded values as high as $p_t = 3p_{rms}$ for only one percent of the time but still contributed significantly to the overall pressure level of intensity. One of the primary concerns of this experimental investigation was that the resolution of data obtained for the physical experiment was sufficient to capture all relevant information for the small scales. Figures 5.38 and 5.39 present the probability distribution functions (PDF), as defined in chapter 2, normalized by p_{rms} and the dynamic pressure Q , for both the physical and computational experiments. The

data of Schewe is shown as well as the typical curve representing a Gaussian random function. The data from both the physical and computational experiments are in excellent agreement with Schewe's data. An analysis was conducted for both experiments to determine the percent the wall pressure exceeded $3p_{rms}$. The results of the computations showed the same one percent threshold reported by Schewe which is consistent with the PDF results presented in these figures.

Representative time records are plotted in figures 5.40 and 5.41 for the computational experiment and figures 5.42 and 5.43 for the physical experiment at the Reynolds numbers of 15000 and 25000, respectively. Although a visual analysis of time records is somewhat subjective, certain observations can be noted. A low frequency periodicity is clearly indicated in figures 5.41 and 5.42 for the computational experiment which shows the interference caused by the periodic boundary conditions used in the computation. Wall pressure fluctuations typify a very intermittent process in which short time segments with large fluctuations appear to be followed by long time segments with smaller levels of fluctuations. Events exceeding $3p_{rms}$ have short time histories and decay much faster than those of larger structures. Overall, these comments seem to be substantiated by the temporal results. If one observes the temporal data somewhat subjectively, a frozen pattern of turbulence moving at a convection velocity of $U_c = 0.70$ can be observed, as shown by the broad band analysis discussed in section 5.4.1.

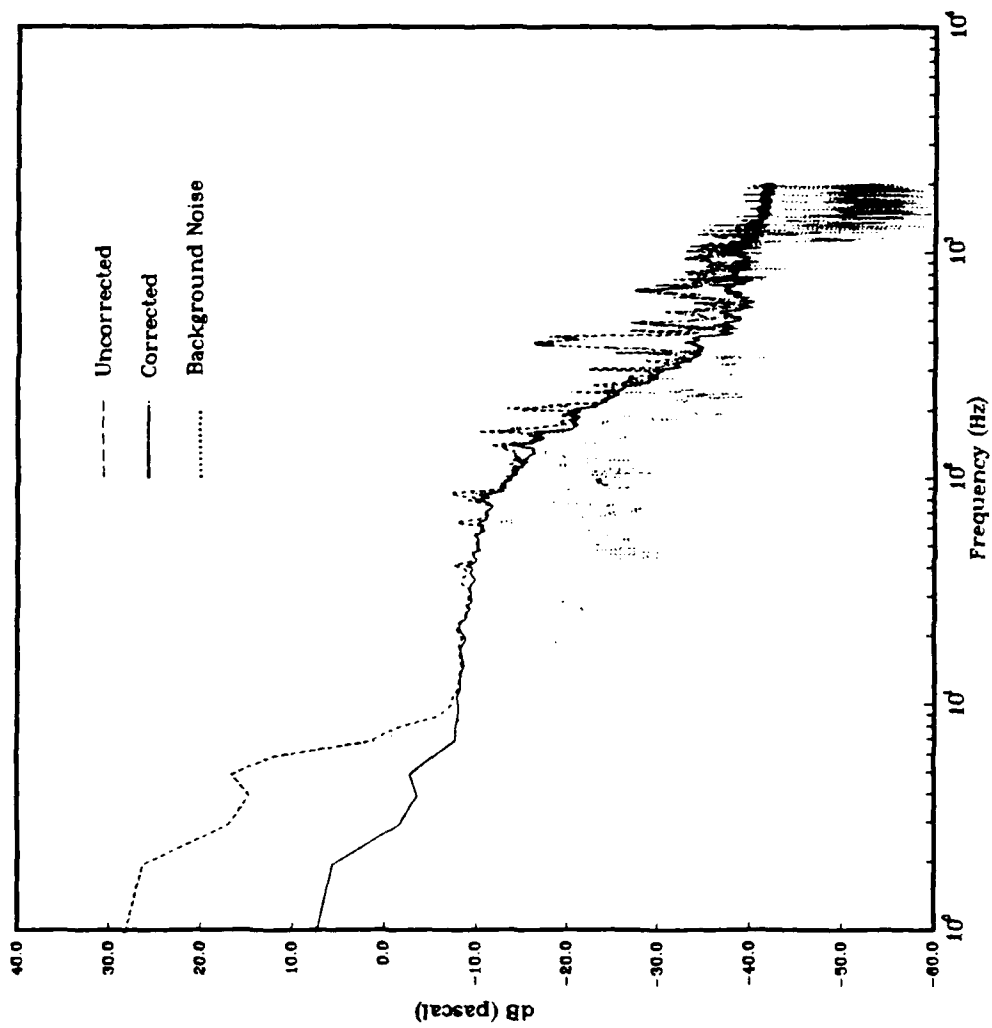


Figure 5.1 Power Spectral Density at $R_h = 10,000$

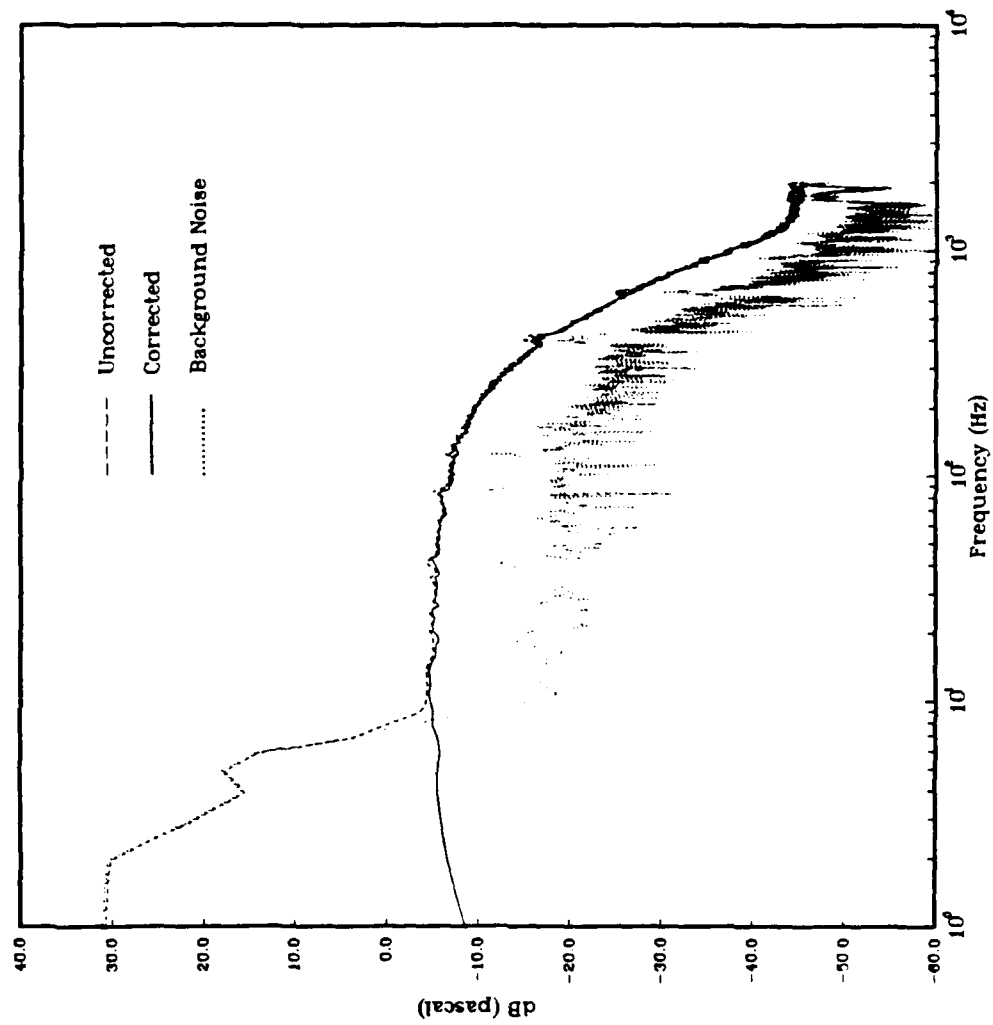


Figure 5.2 Power Spectral Density at $R_h = 15,000$

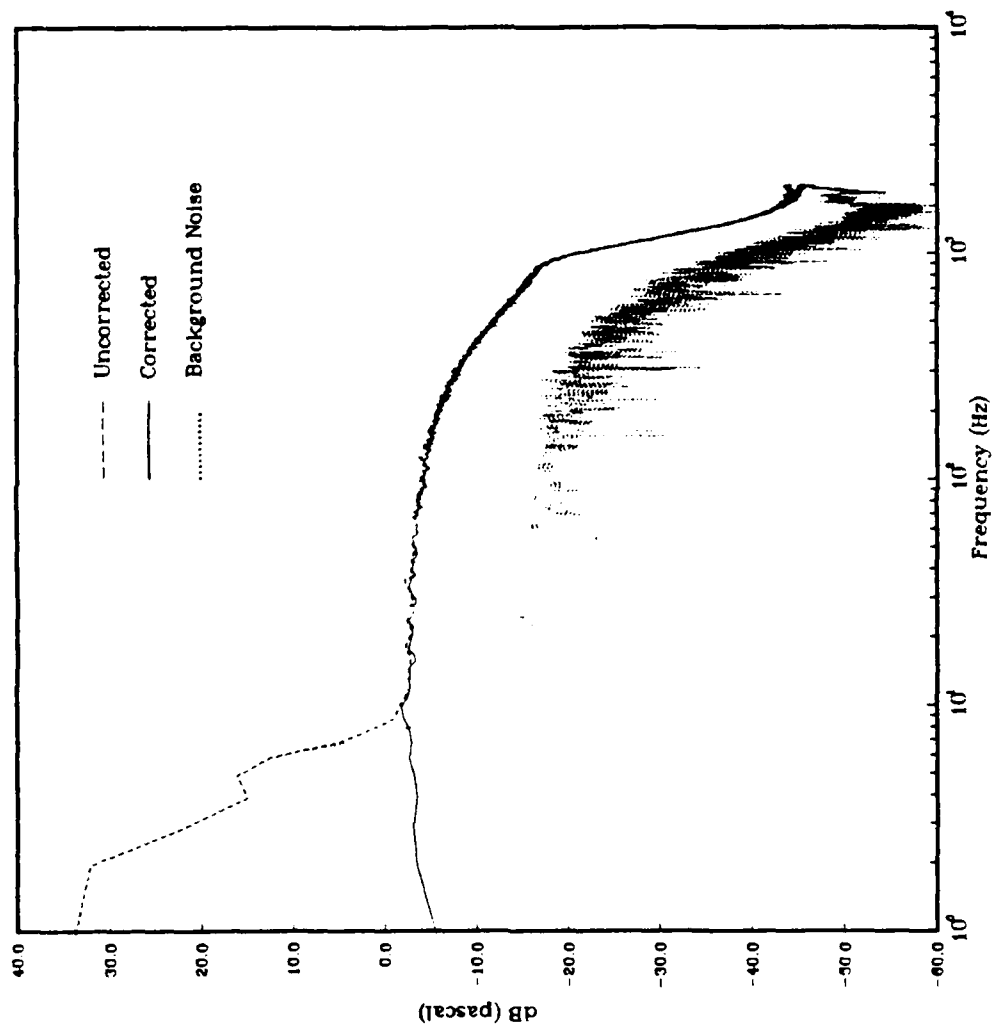


Figure 5.3 Power Spectral Density at $R_h = 20,000$

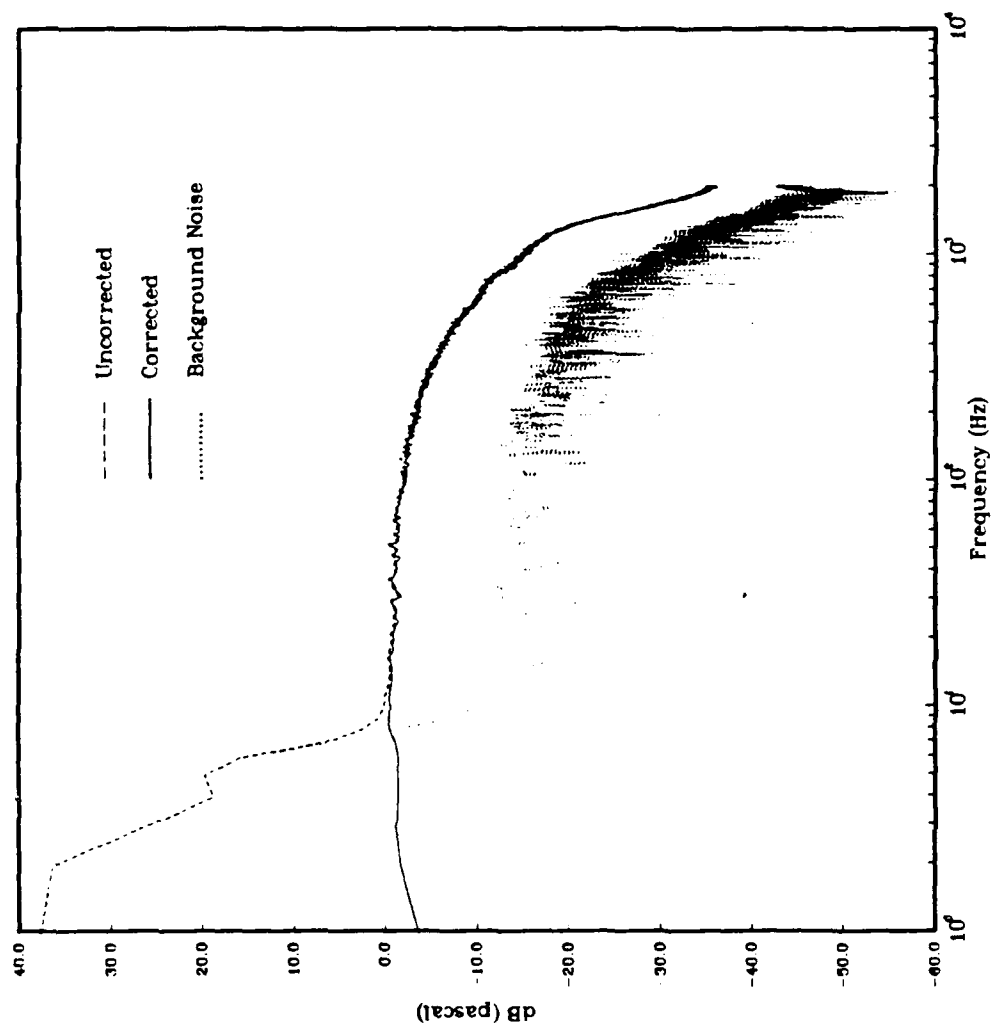


Figure 5.4 Power Spectral Density at $R_h = 25,000$

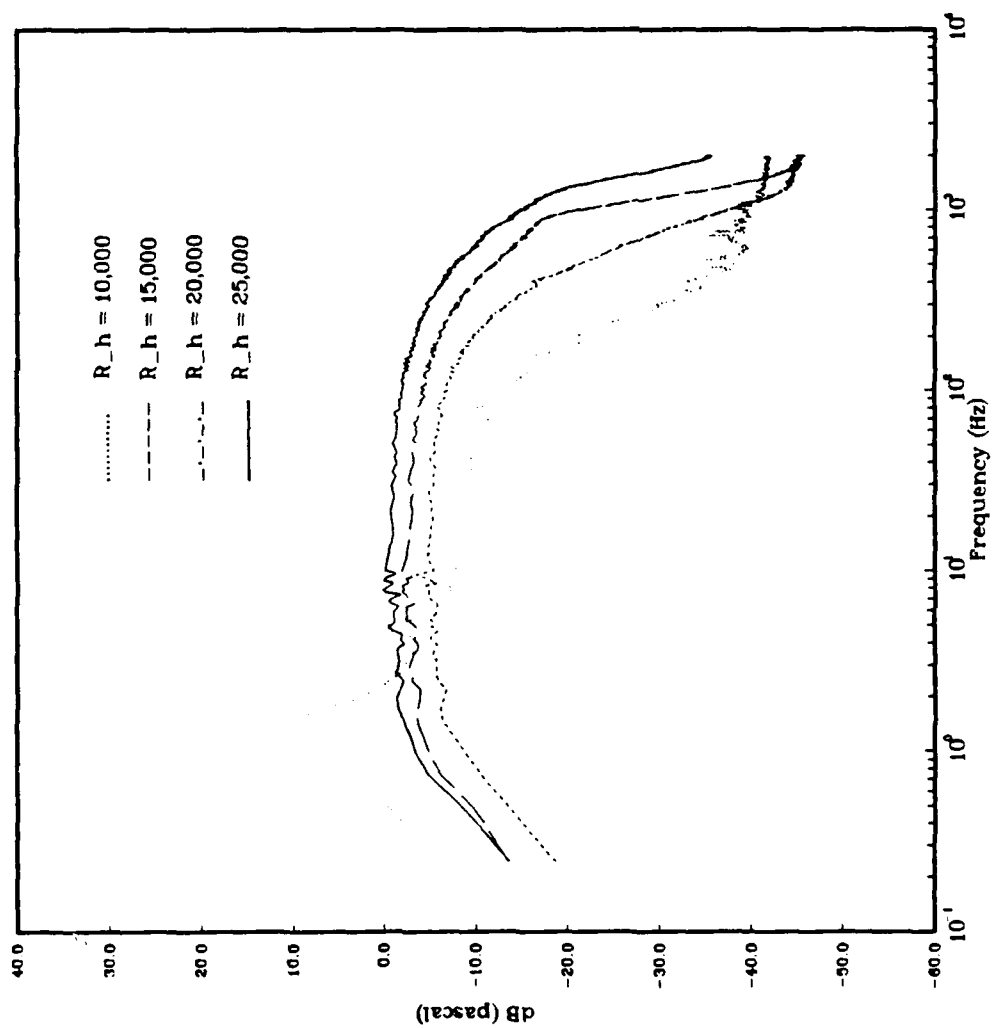


Figure 5.5 Highest Resolution Power Spectral Density (corrected)

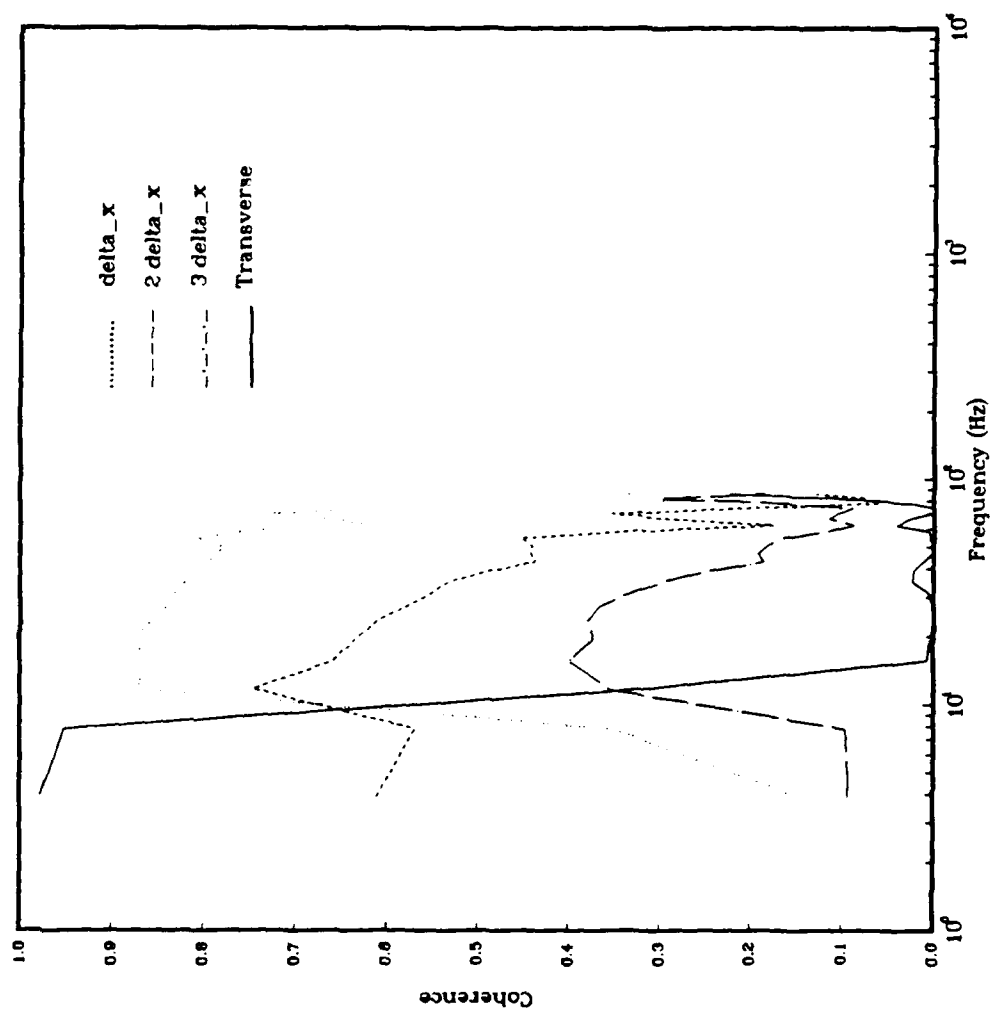


Figure 5.6 Magnitude Squared Coherence, $R_h = 10,000$.

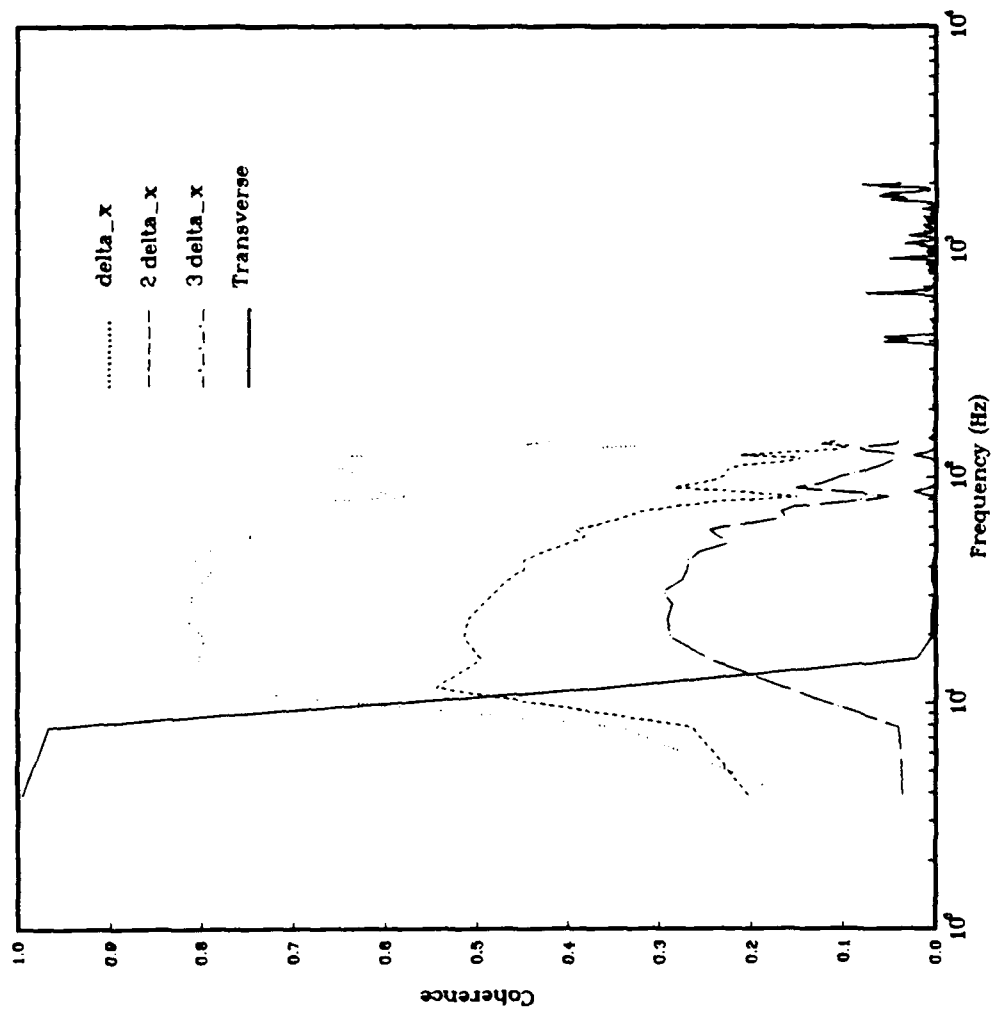


Figure 5.7 Magnitude Squared Coherence, $R_h = 15,000$.

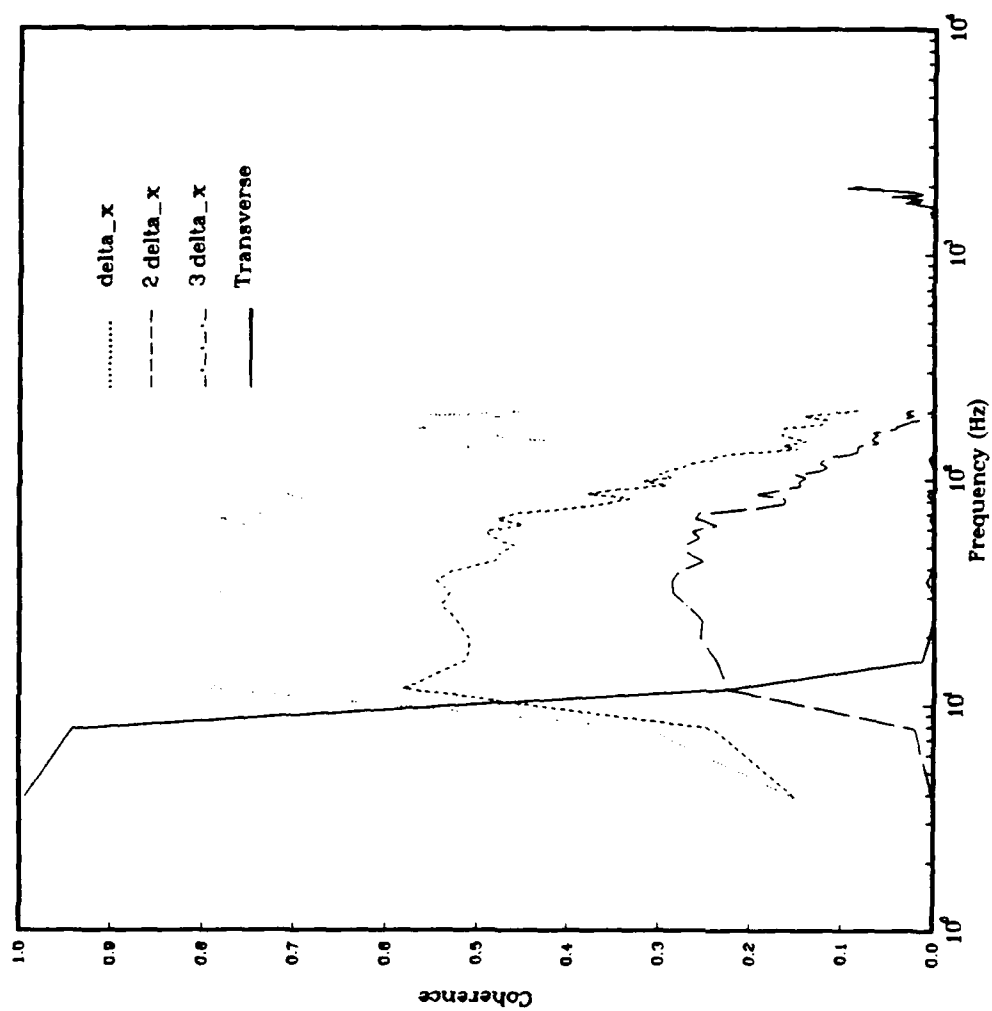


Figure 5.8 Magnitude Squared Coherence, $R_h = 20,000$.

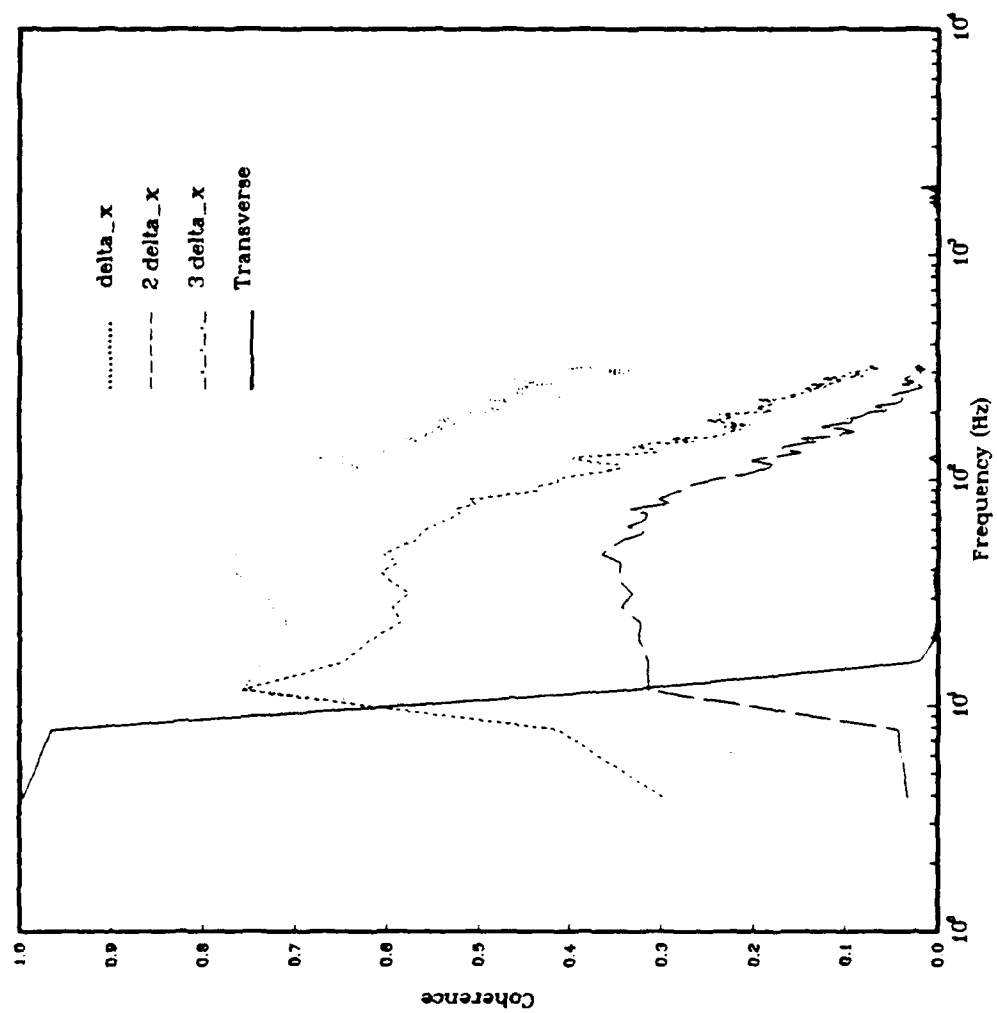


Figure 5.9 Magnitude Squared Coherence, $R_h = 25,000$.

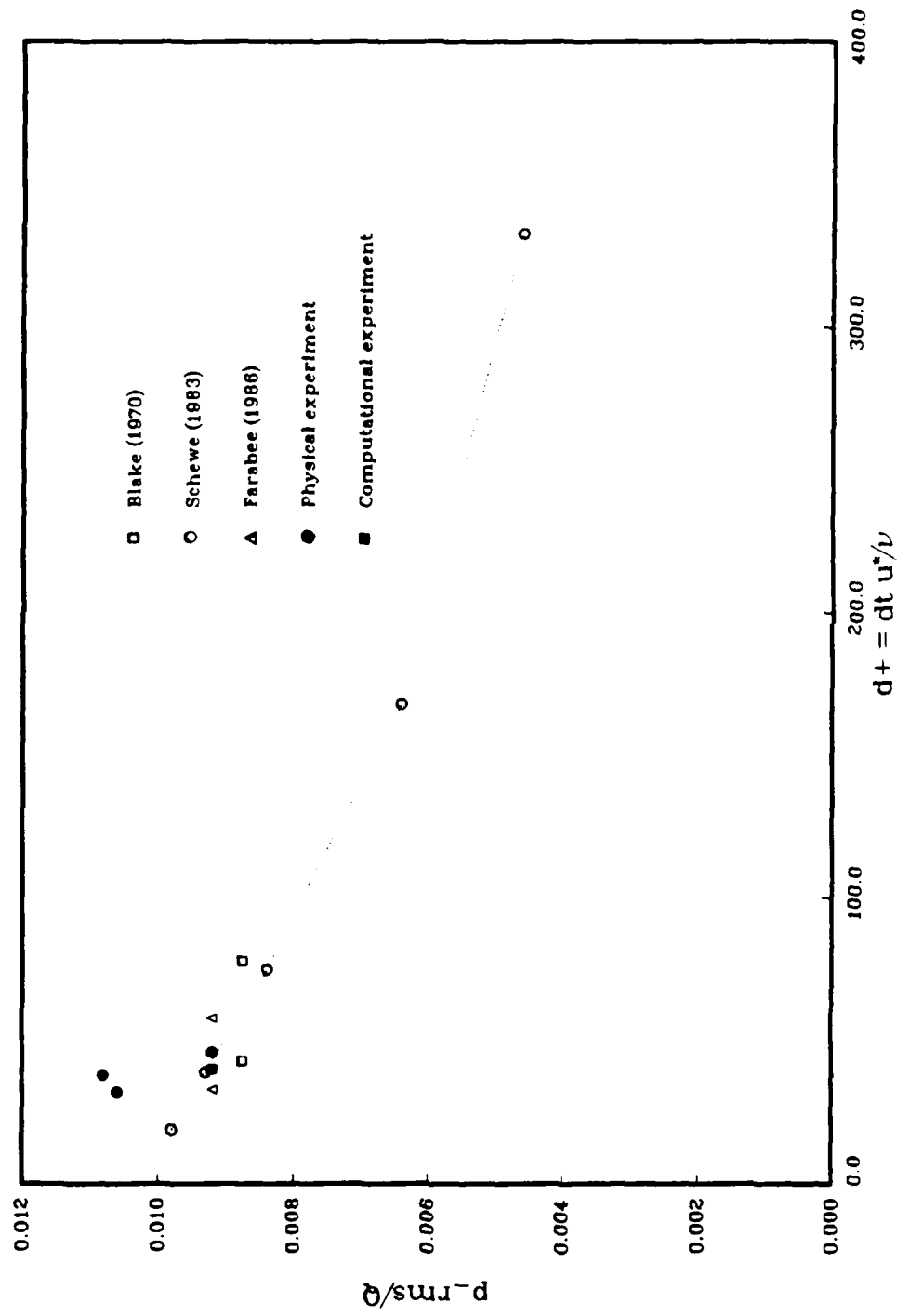


Figure 5.10 Comparison of RMS Levels

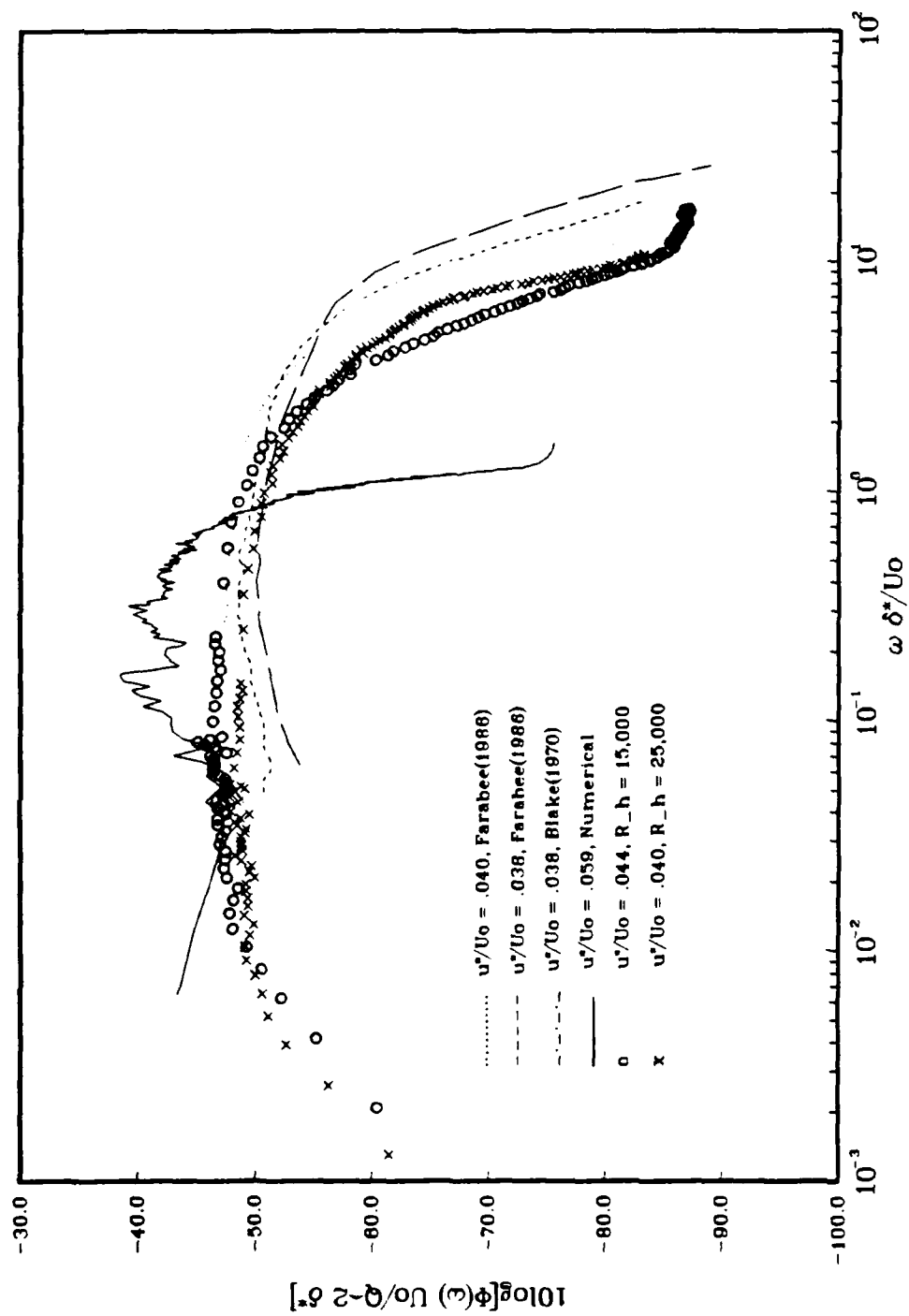


Figure 5.11 Outer Variable Similarity

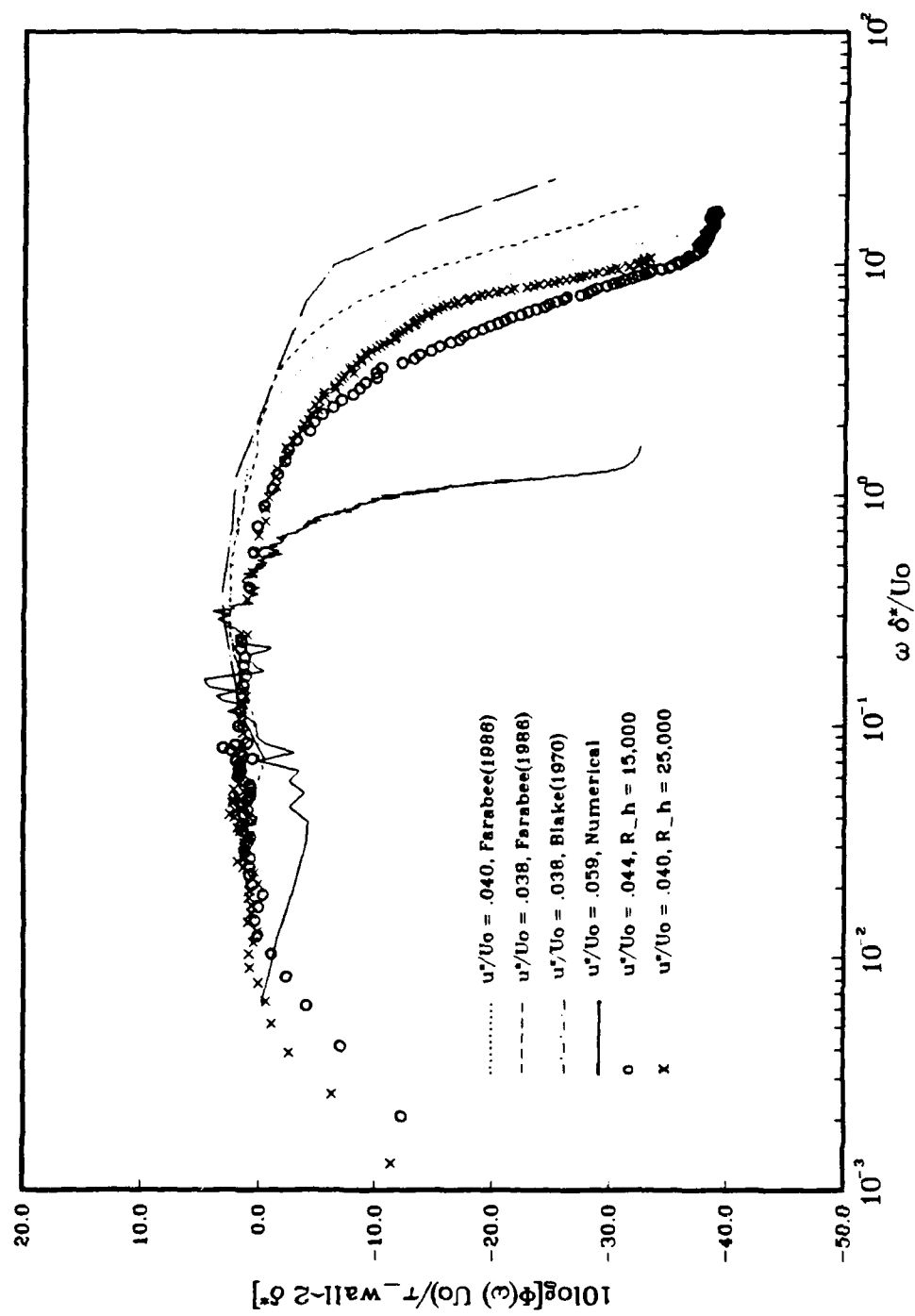


Figure 5.12 Mixed Variable Similarity

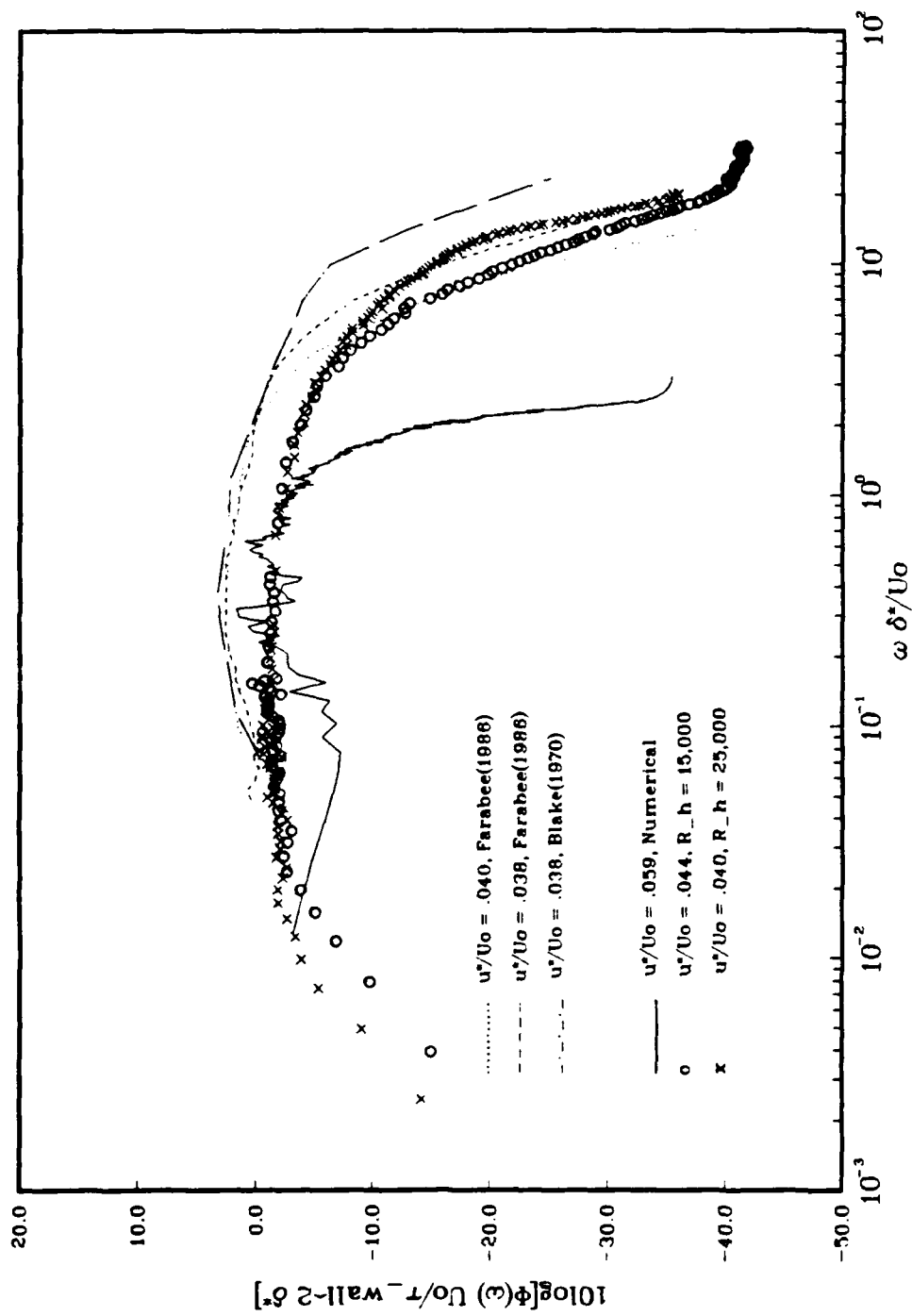


Figure 5.13 Mixed Variable Similarity With Hydraulic Diameter on Both Axes.

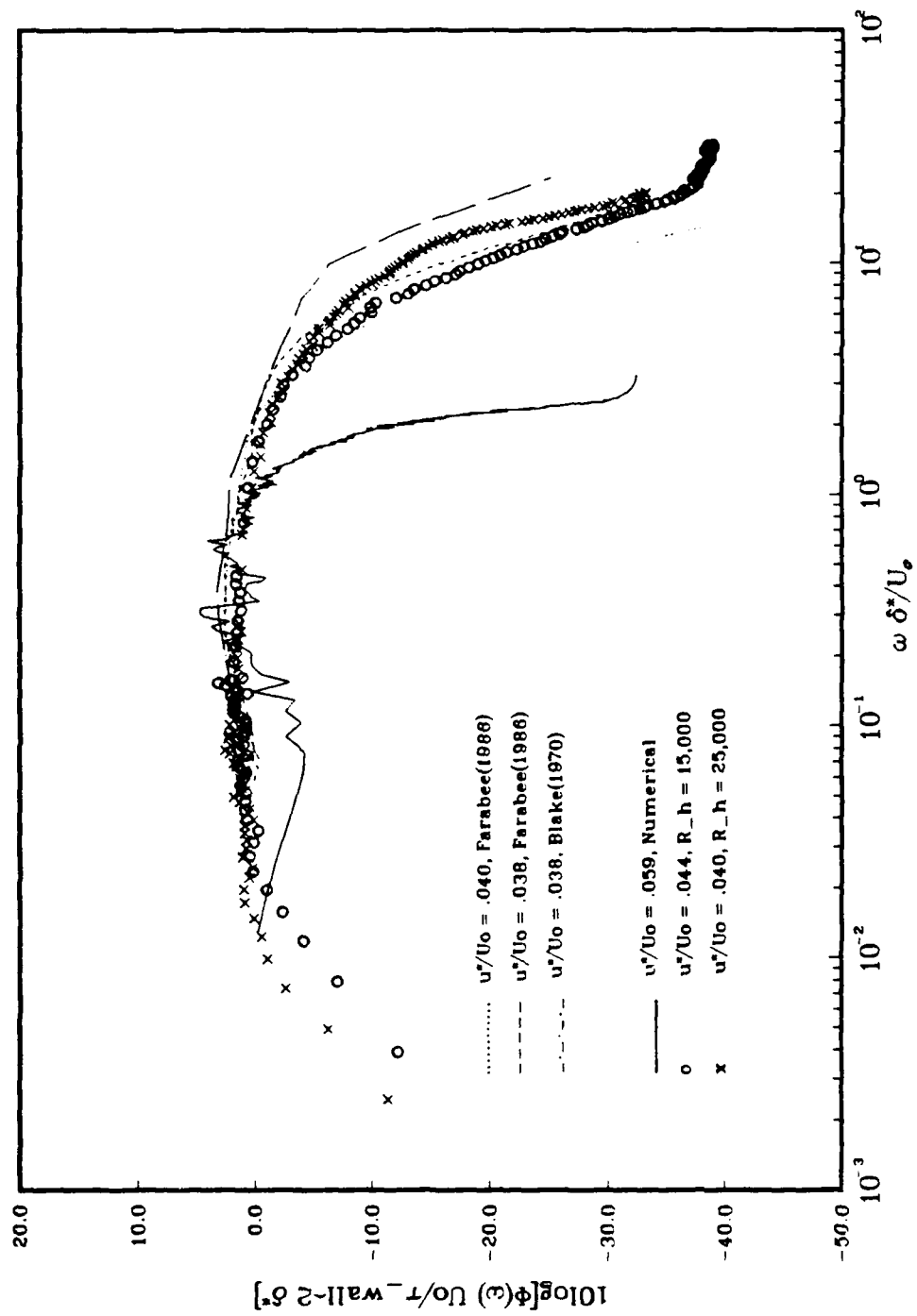


Figure 5.14 Mixed Variable Similarity With Hydraulic Diameter on X-axis Only.

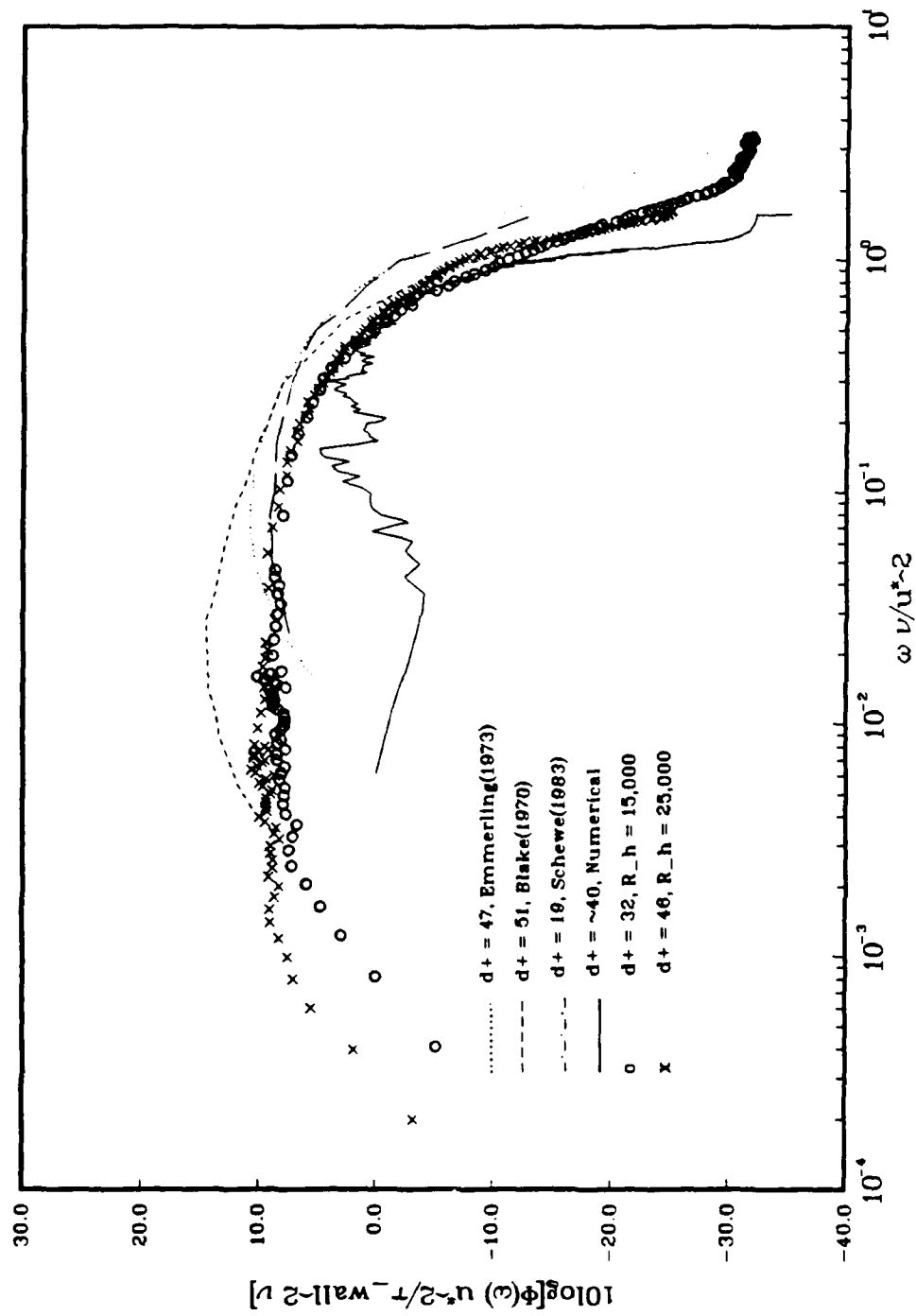


Figure 5.15 Inner Variable Similarity

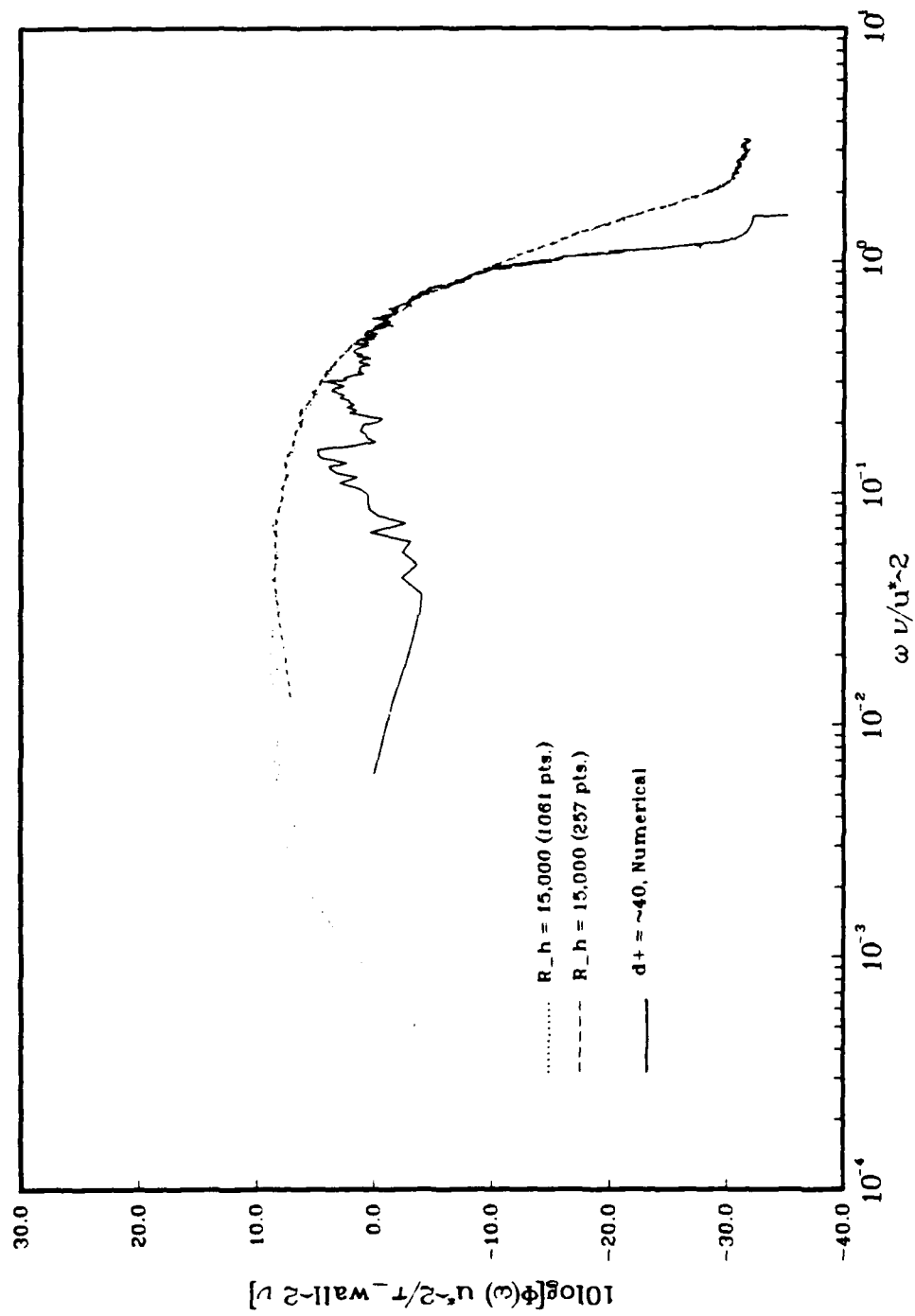


Figure 5.16 Comparison of Spectral Resolution

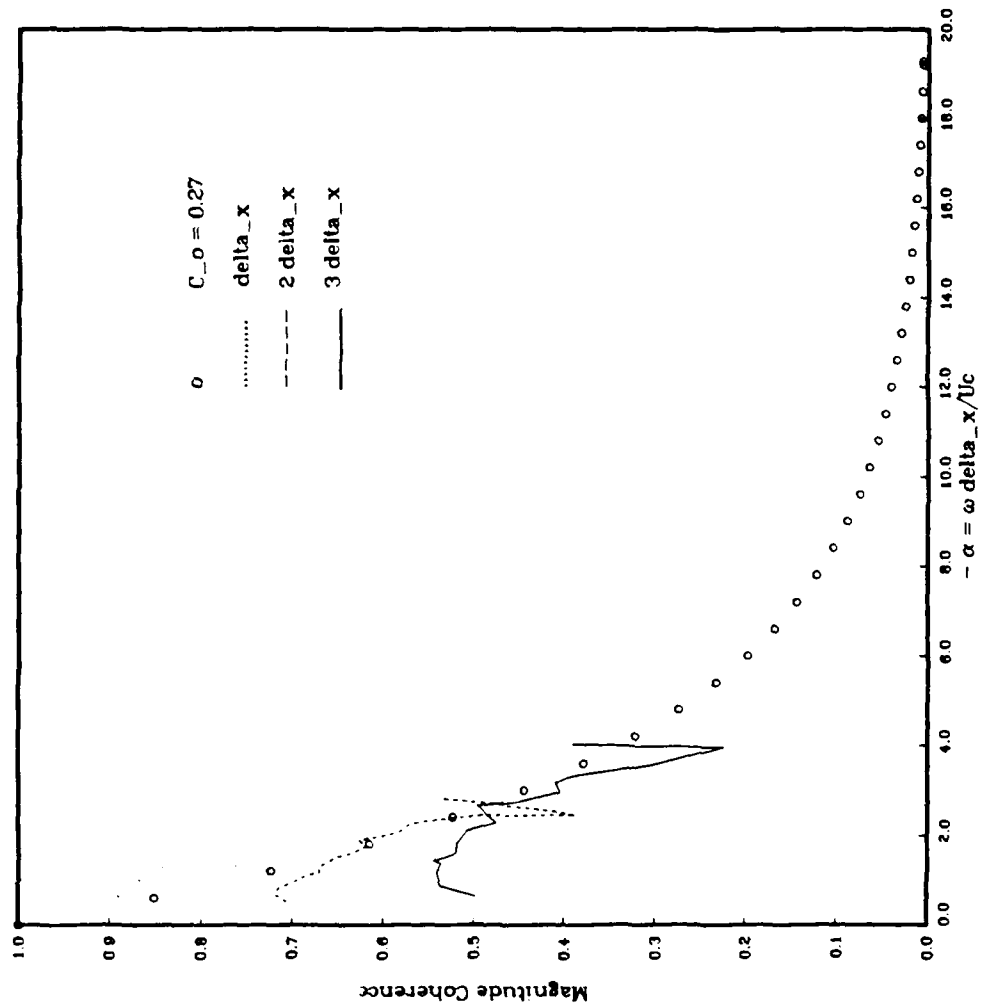


Figure 5.17 Streamwise Coherence, $R_h = 15,000$

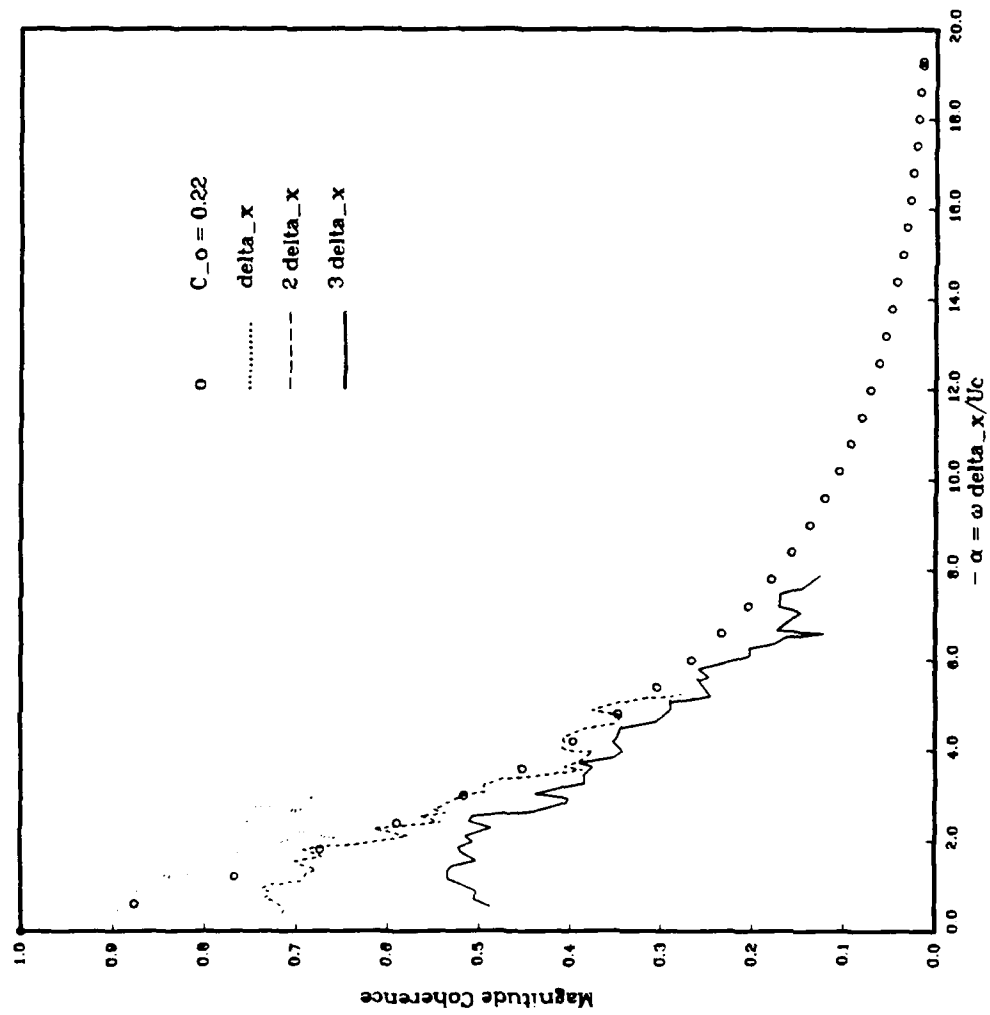


Figure 5.18 Streamwise Coherence, $R_h = 20,000$

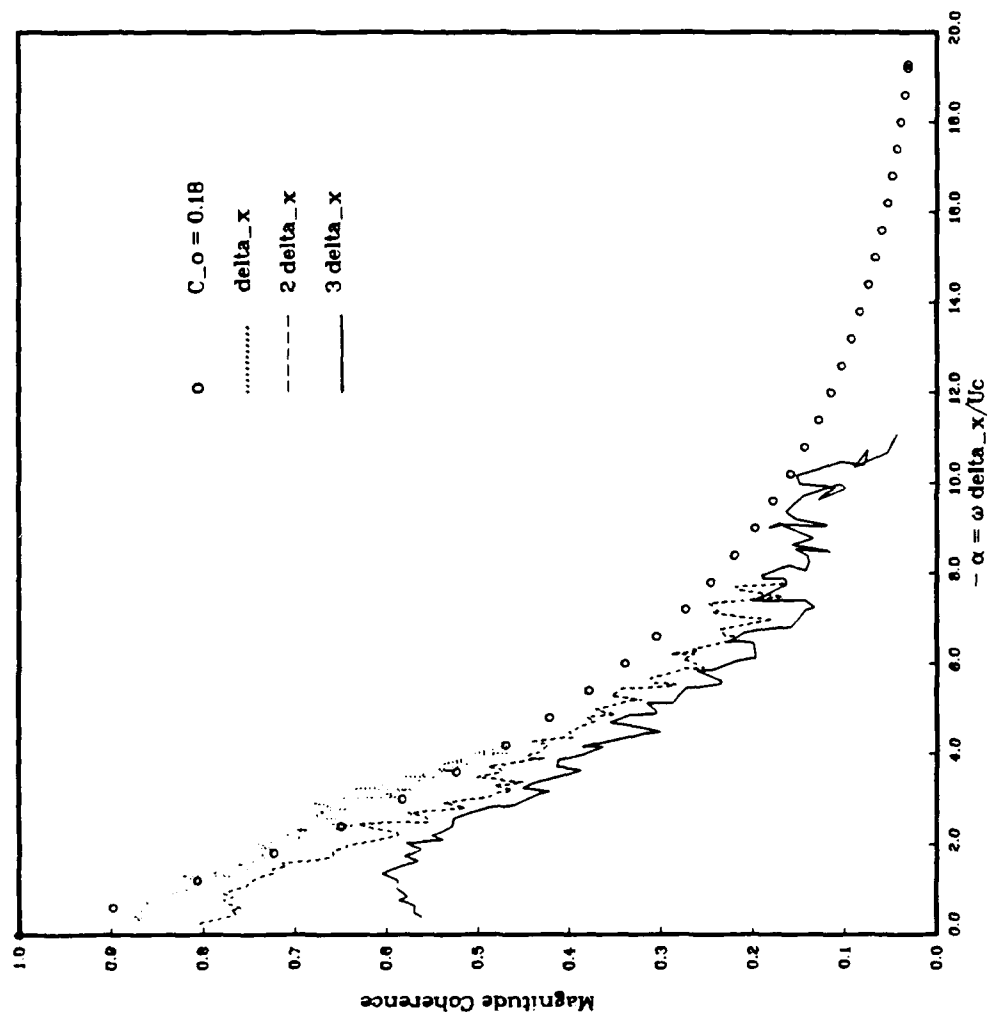


Figure 5.19 Streamwise Coherence, $R_h = 25,000$

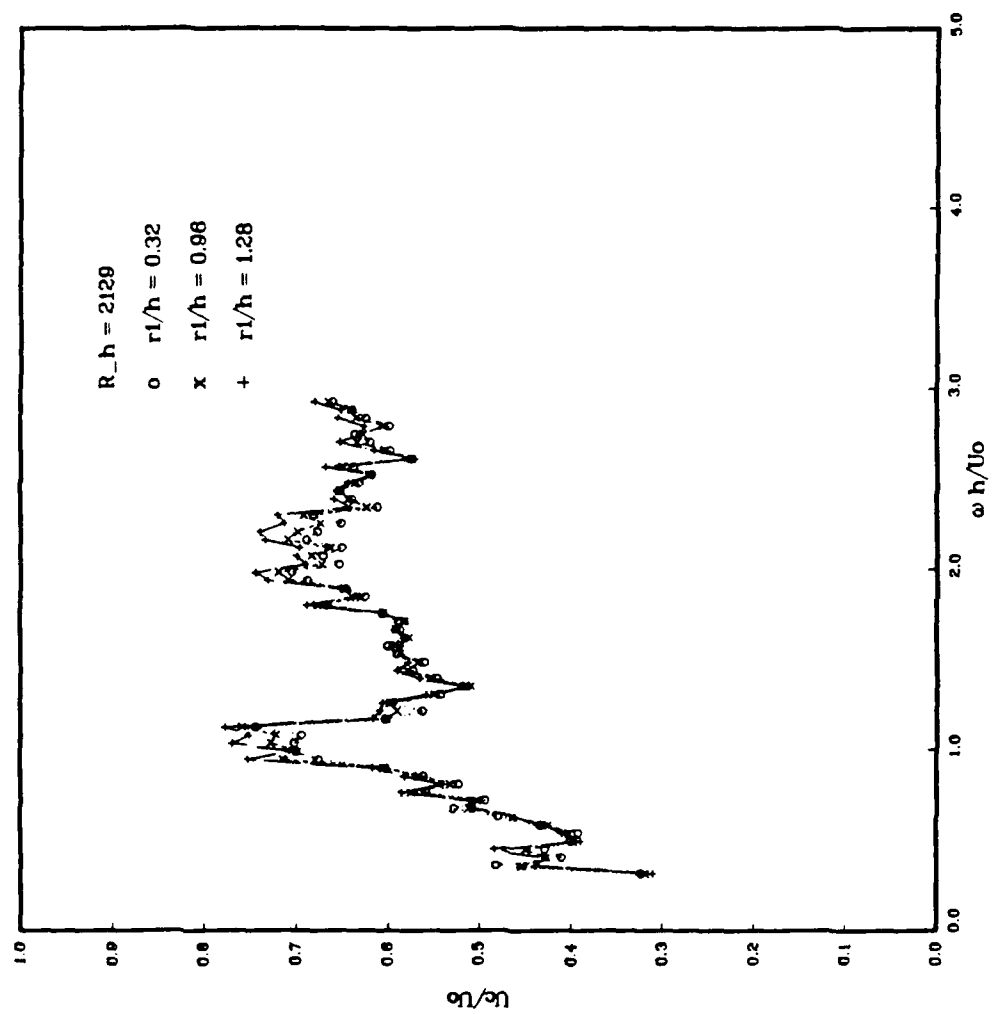


Figure 5.20 Narrow Band Convection Velocity of Computational Experiment, (Outer Units)

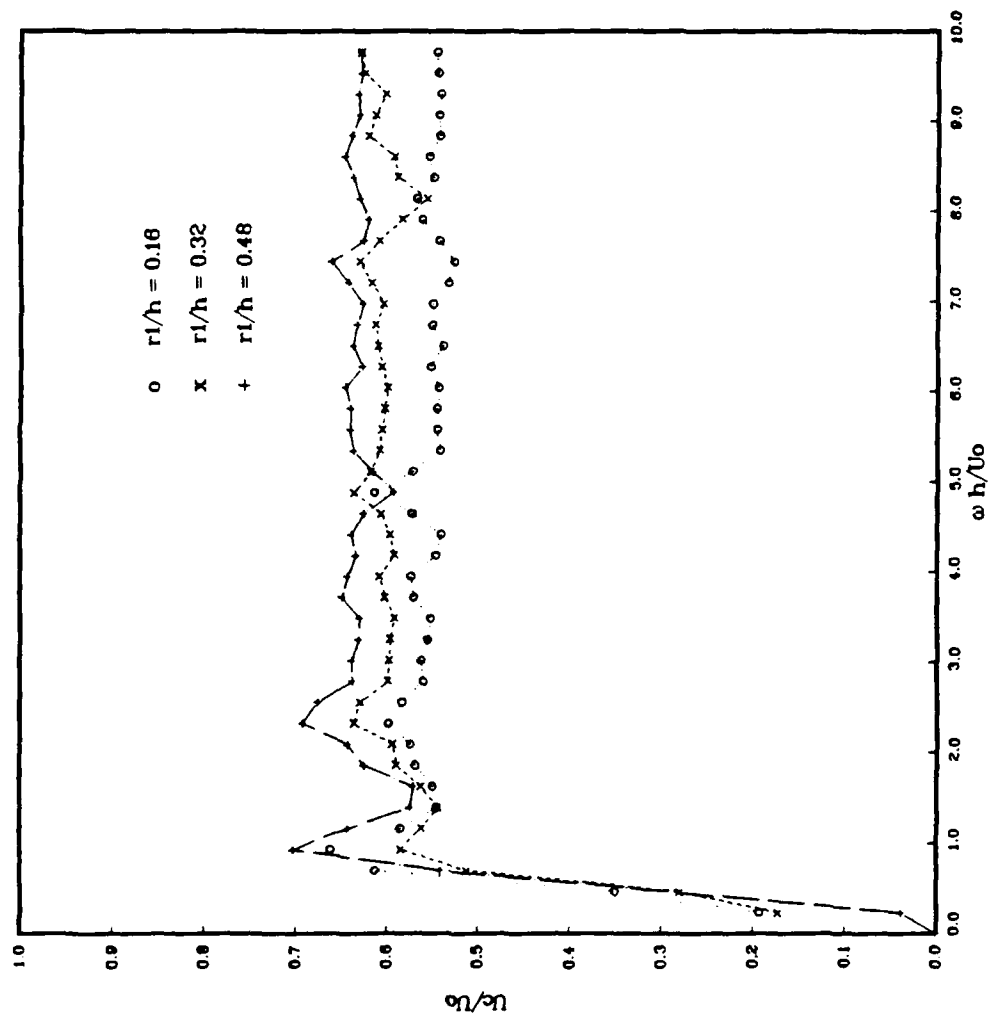


Figure 5.21 Narrow Band Convection Velocity of Physical Experiment At $R_h = 15,000$ (Outer Units)

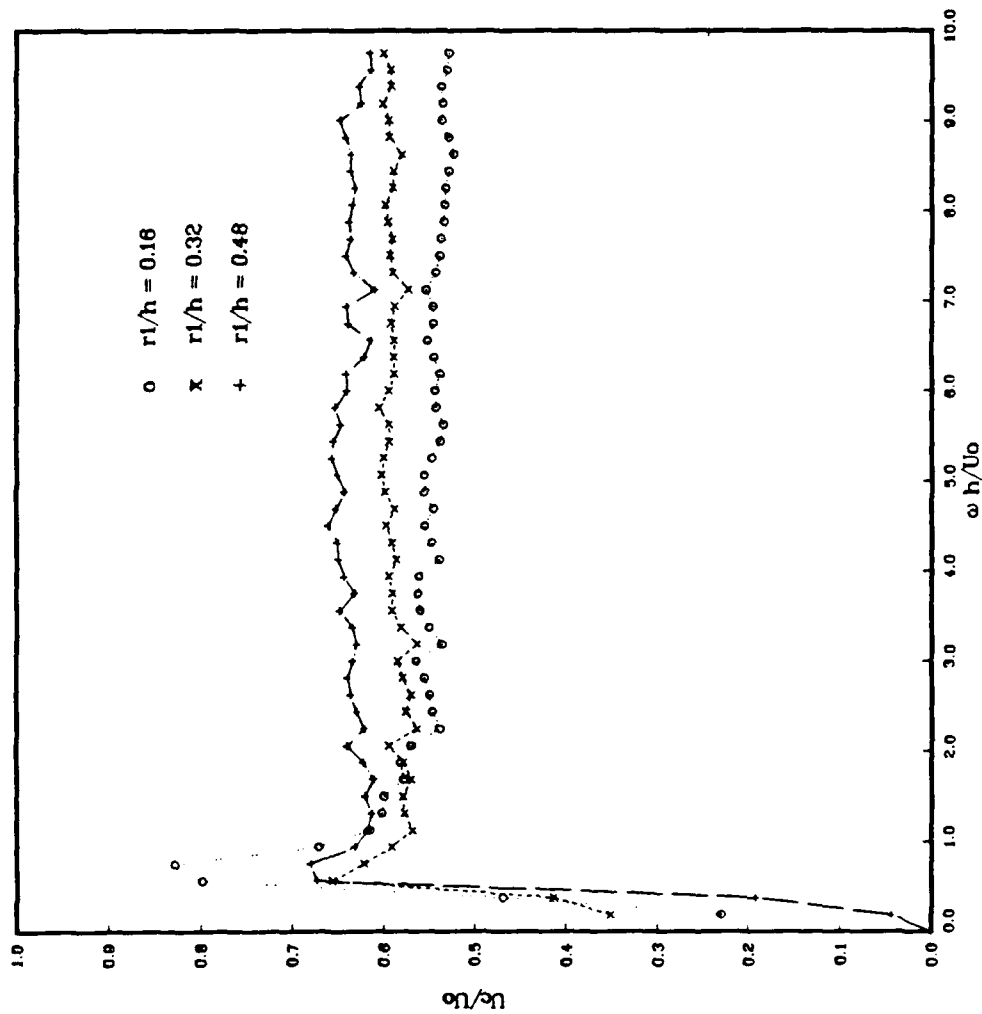


Figure 5.22 Narrow Band Convection Velocity of Physical Experiment At $R_h = 20,000$ (Outer Units)

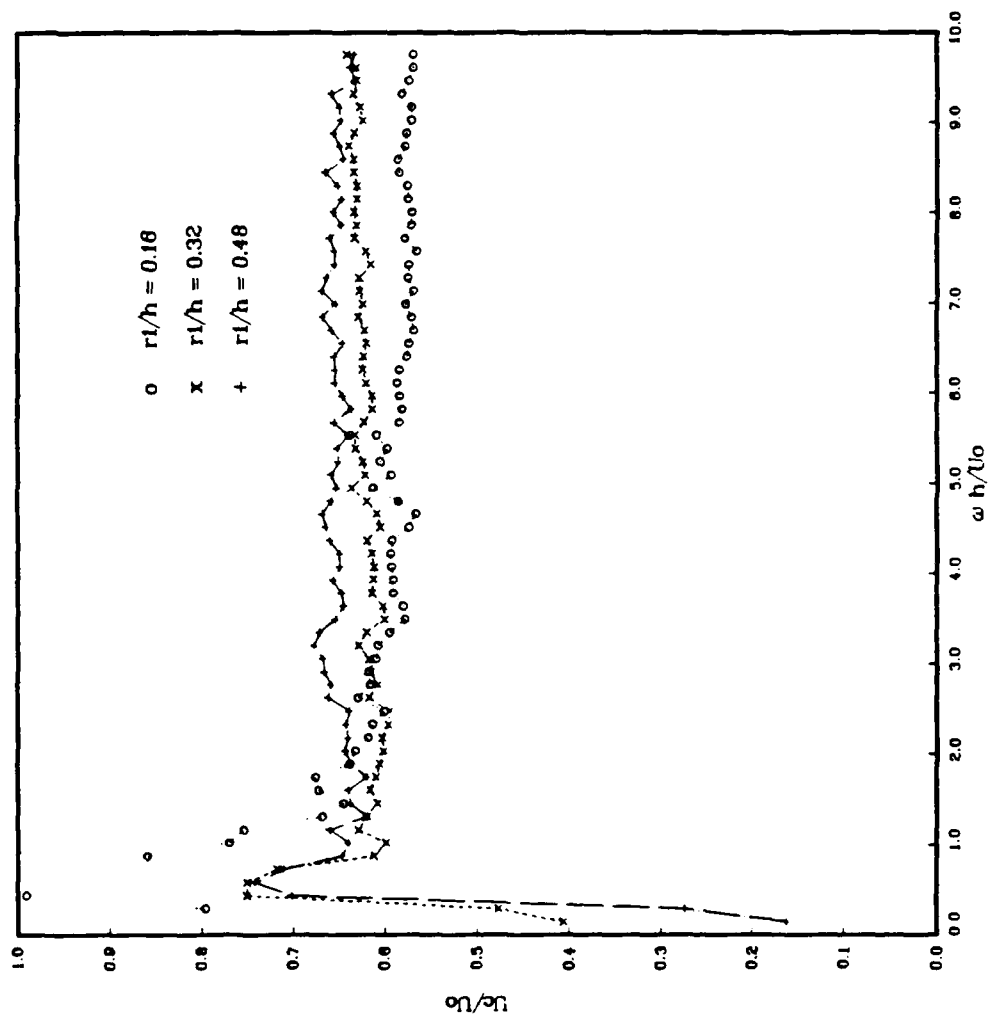


Figure 5.23 Narrow Band Convection Velocity of Physical
Experiment At $R_h = 25,000$ (Outer Units)

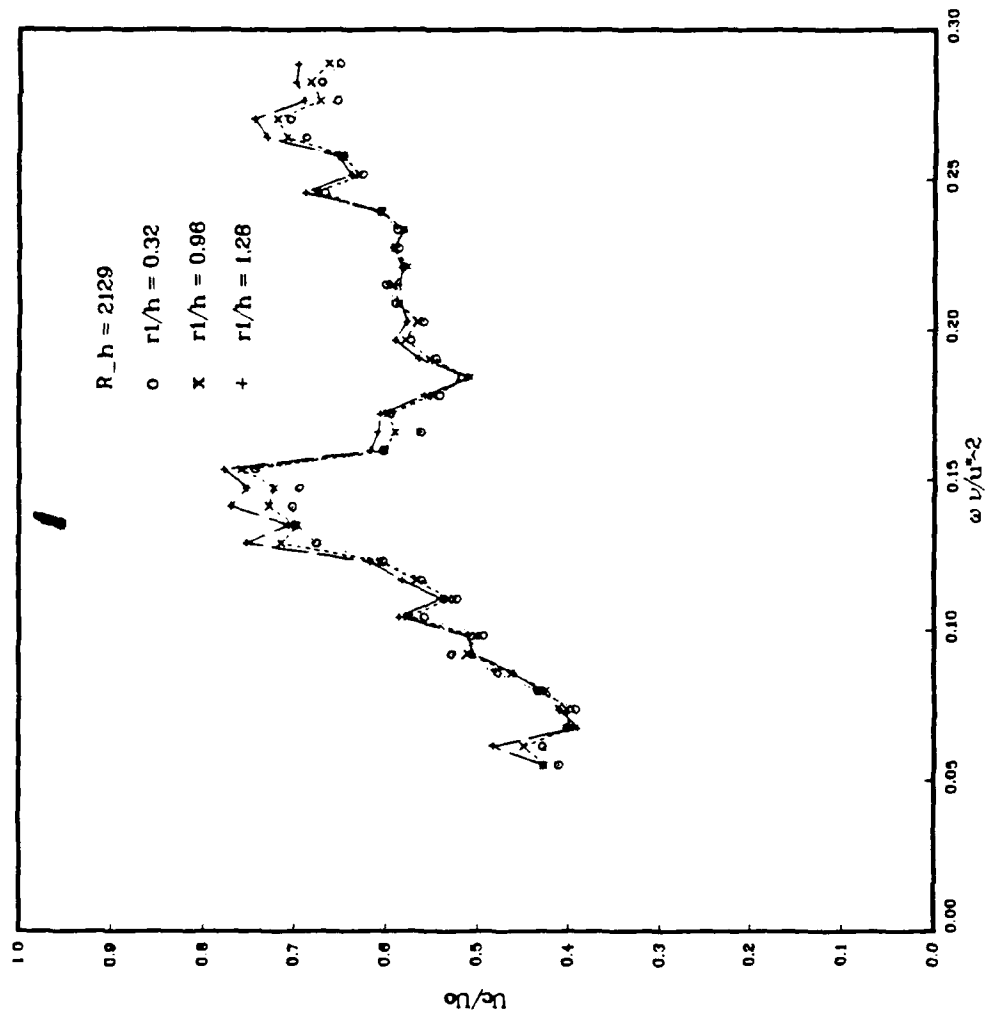


Figure 5.24 Narrow Band Convection Velocity of Computational Experiment, (Inner Units)

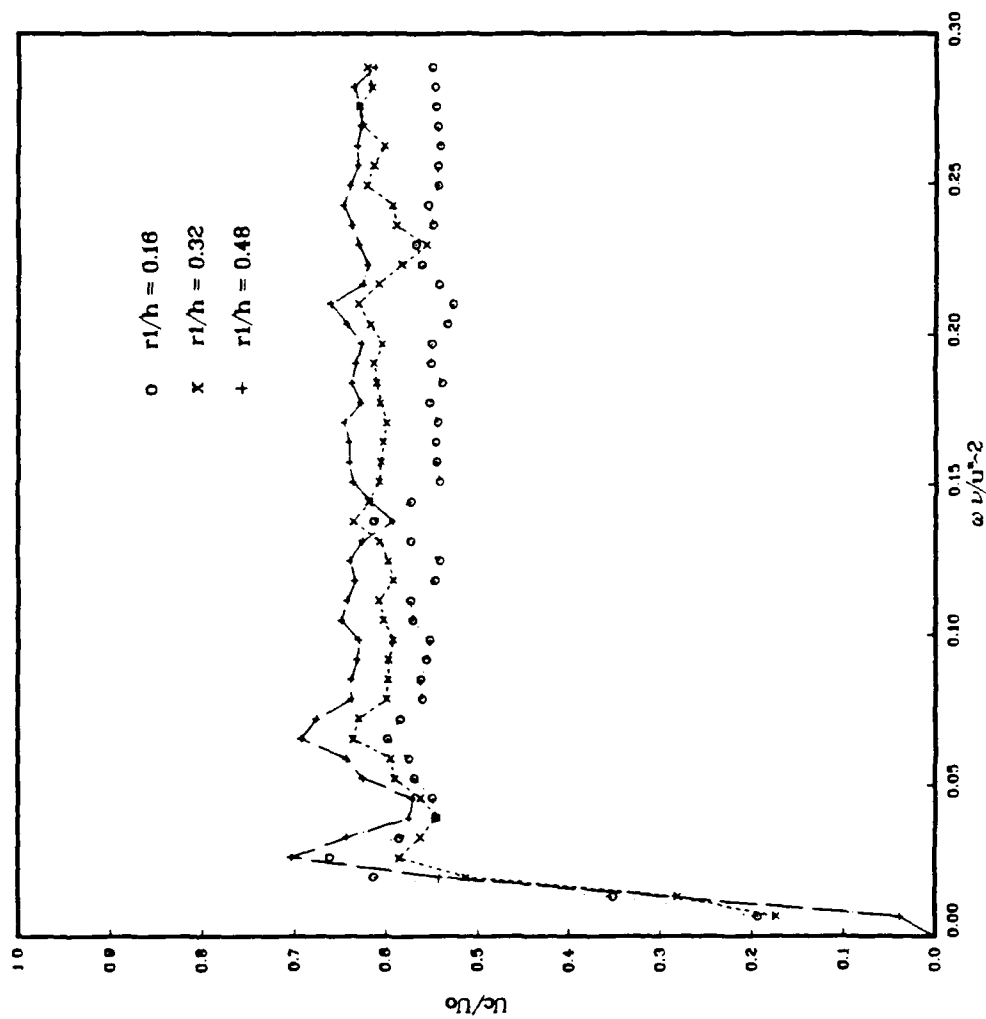


Figure 5.25 Narrow Band Convection Velocity of Physical
Experiment At $R_h = 15,000$ (Inner Units)

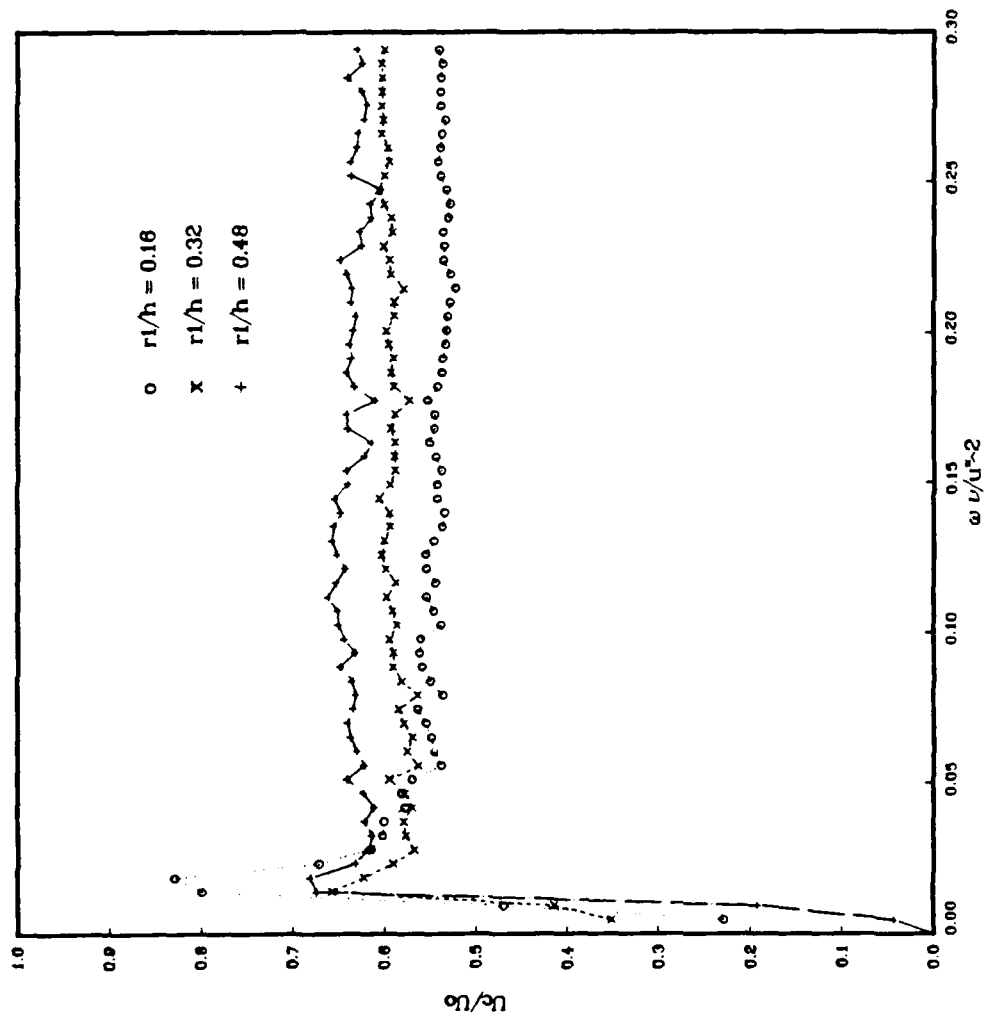


Figure 5.26 Narrow Band Convection Velocity of Physical
Experiment At $R_h = 20,000$ (Inner Units)

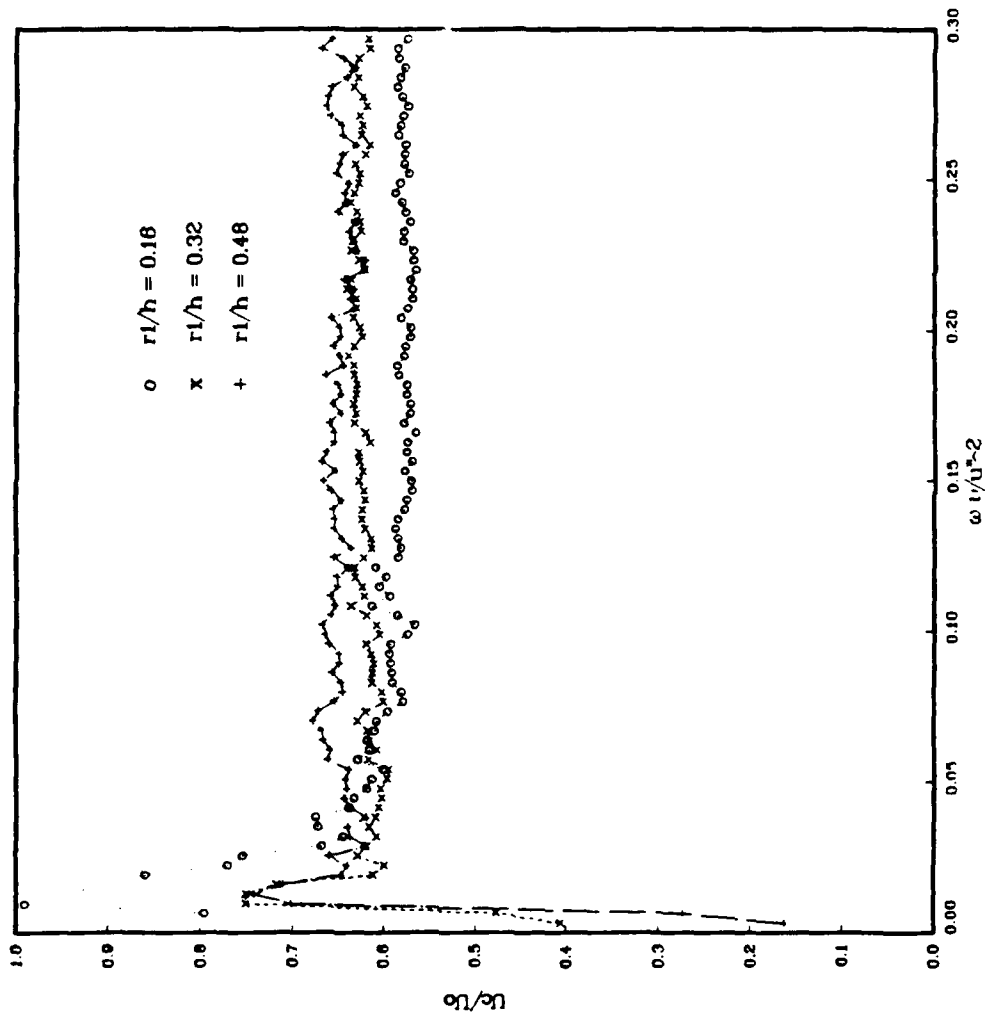


Figure 5.27 Narrow Band Convection Velocity of Physical
 Experiment At $R_h = 25,000$ (Inner Units)

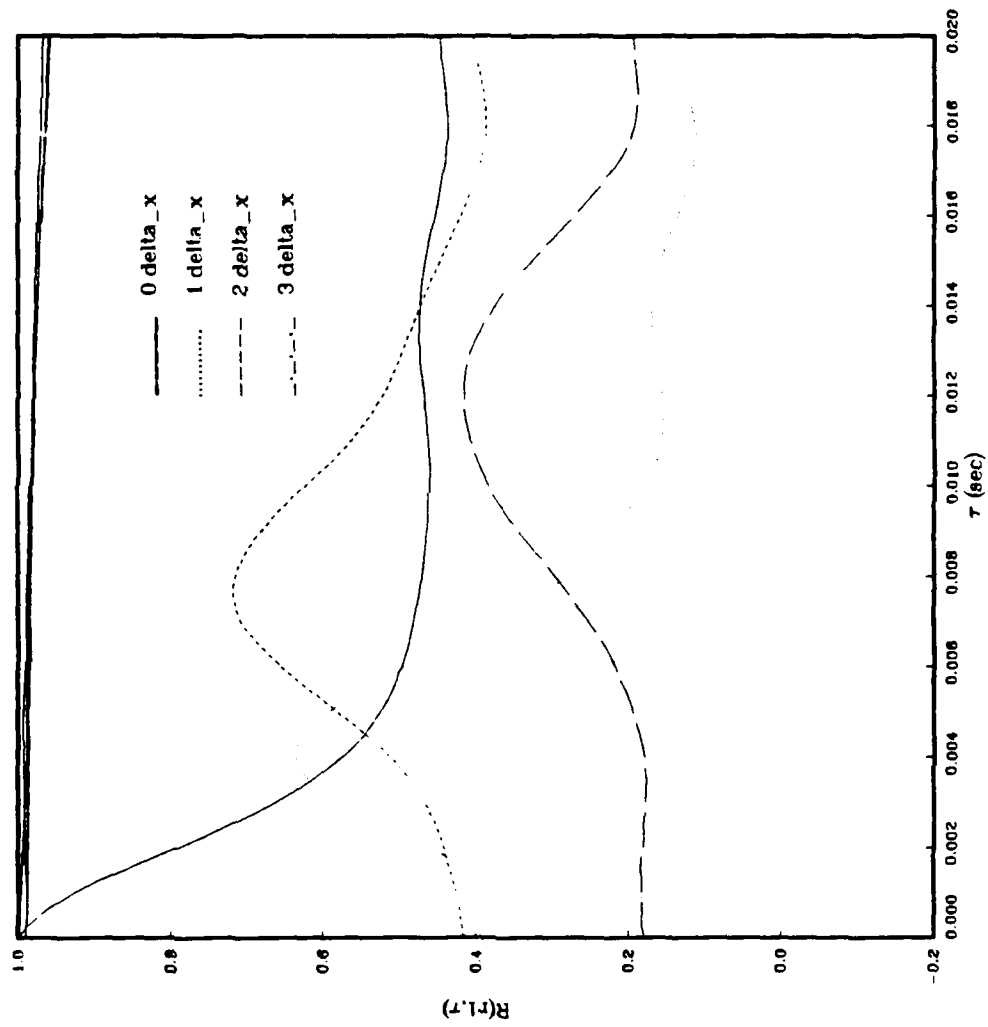


Figure 5.28 Time Correlation for Physical Experiment

At $R_h = 10,000$.

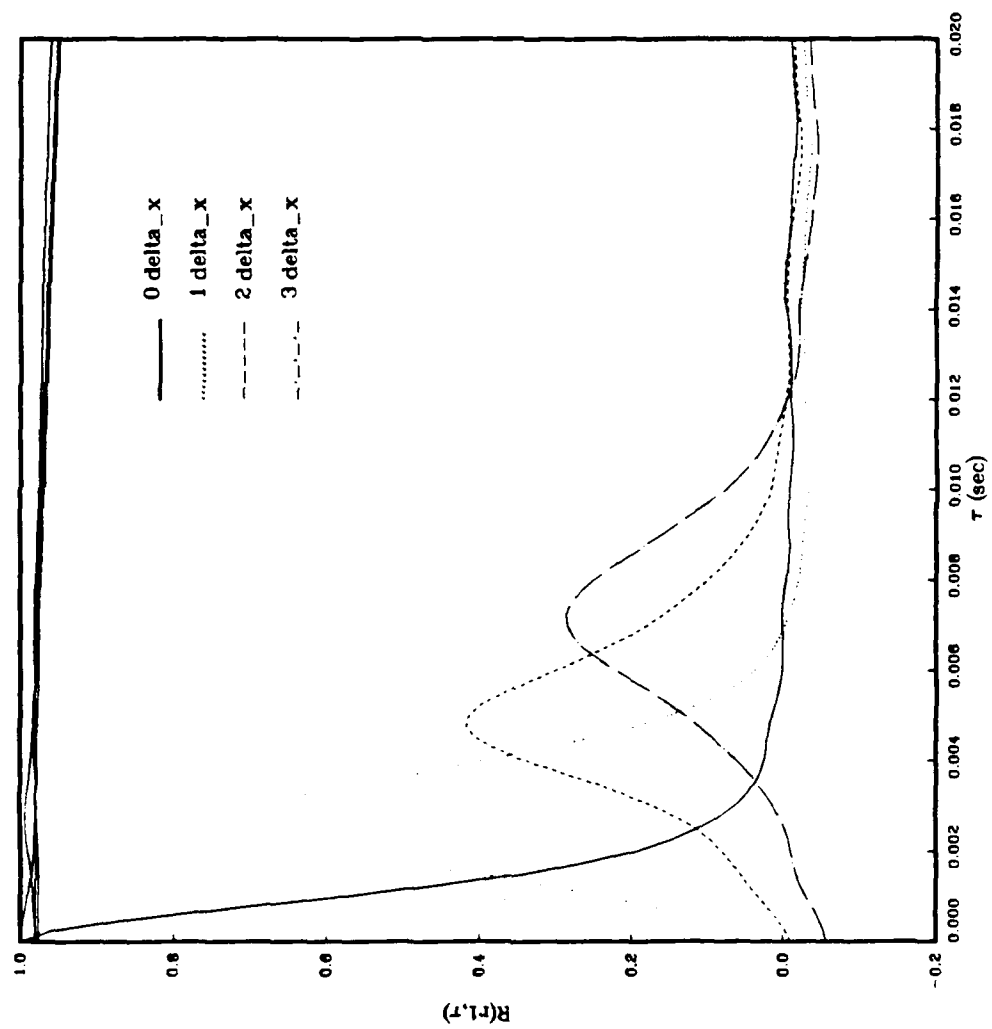


Figure 5.29 Time Correlation for Physical Experiment
At $R_h = 15,000$.

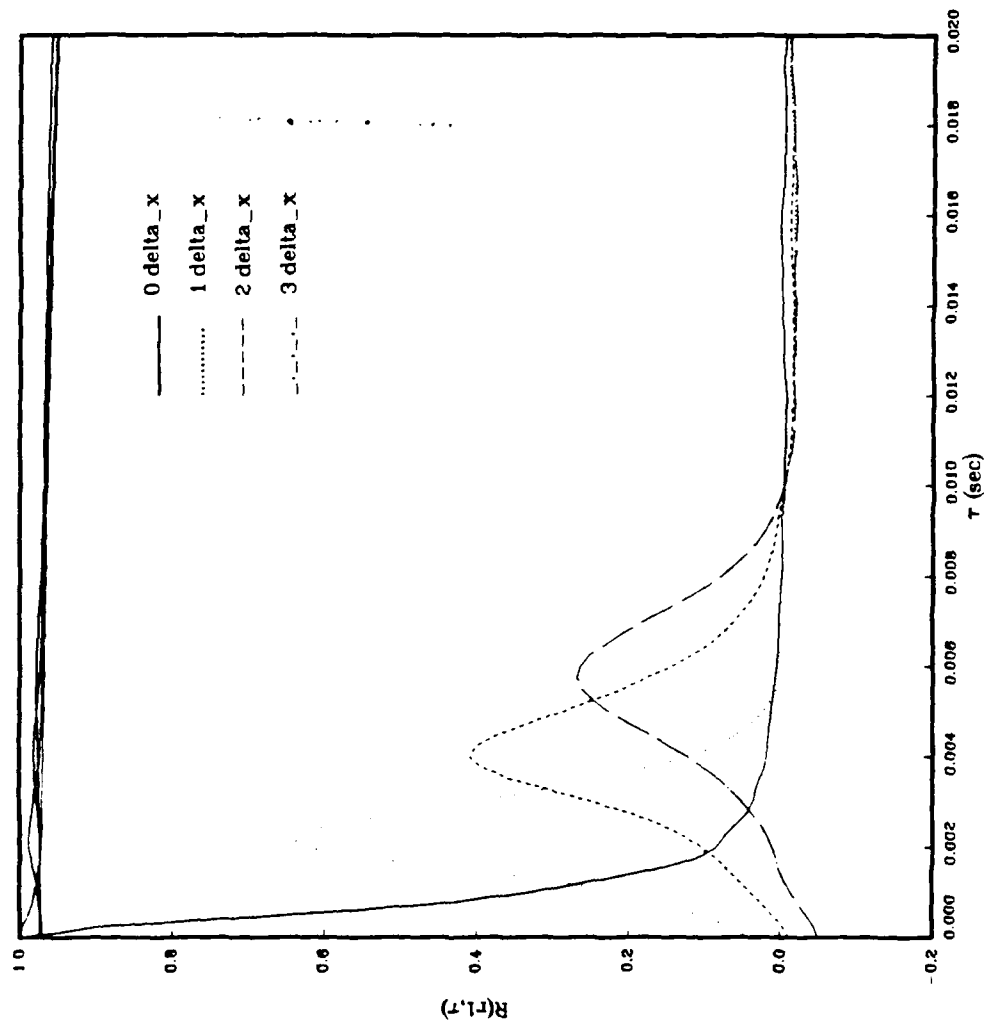


Figure 5.30 Time Correlation for Physical Experiment

At $R_h = 20,000$.

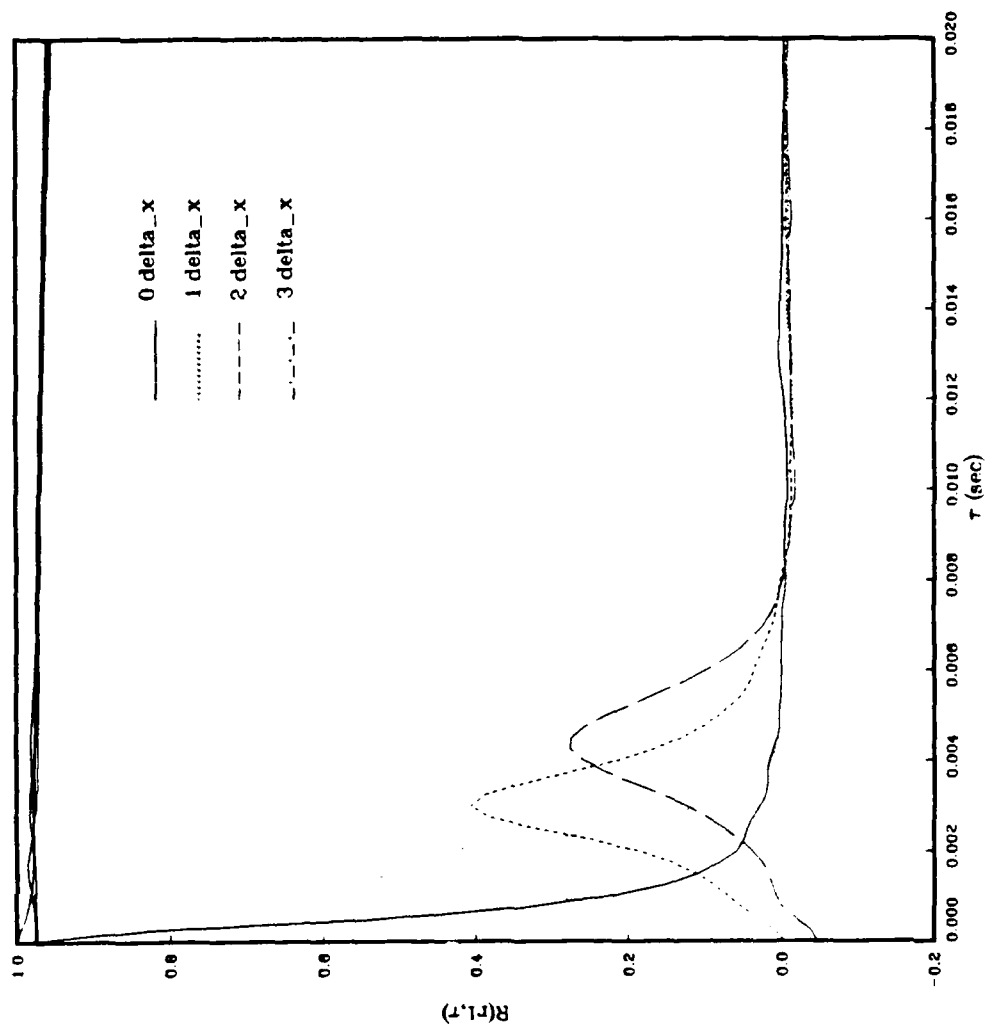


Figure 5.31 Time Correlation for Physical Experiment
At $R_h = 25,000$.

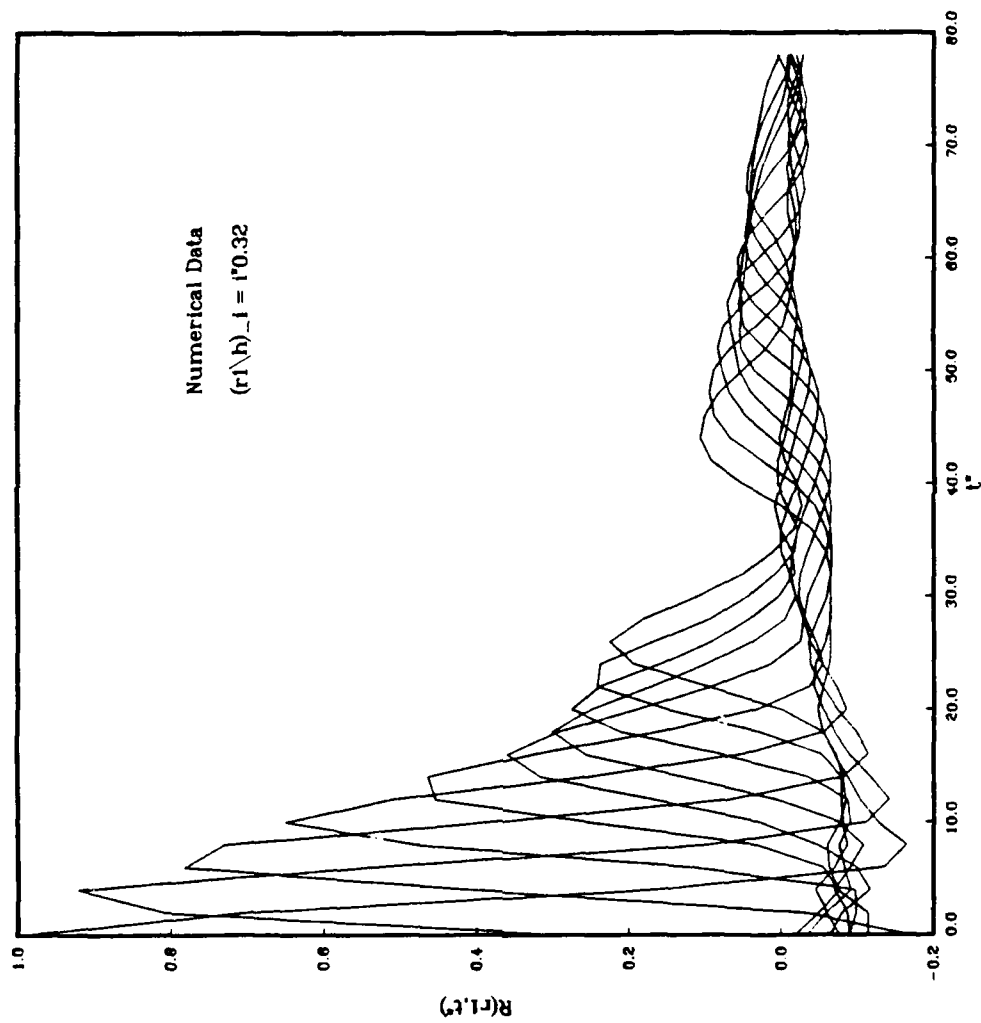


Figure 5.32 Time Correlation for Computational Experiment

At $R_h = 2,129$.

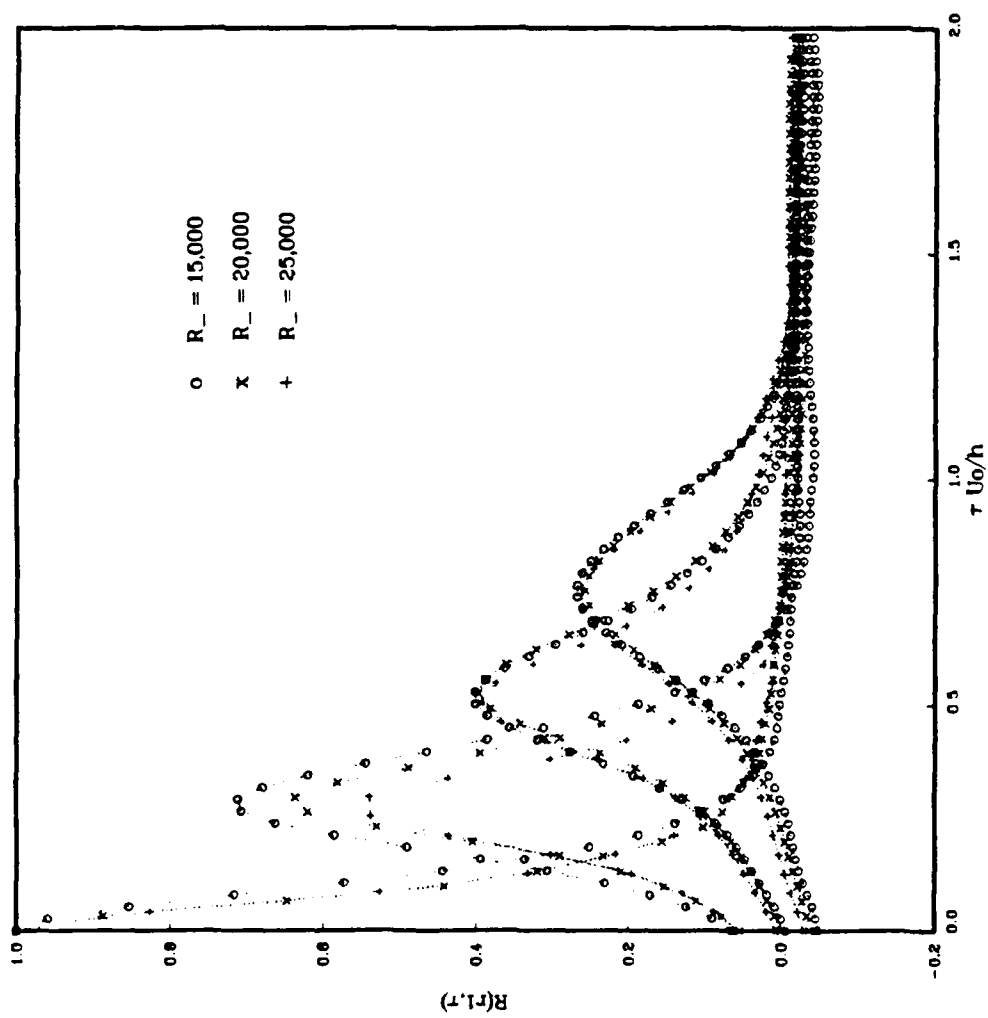


Figure 5.33 Outer Unit Correlation Versus Reynolds Number
for the Physical Experiment.

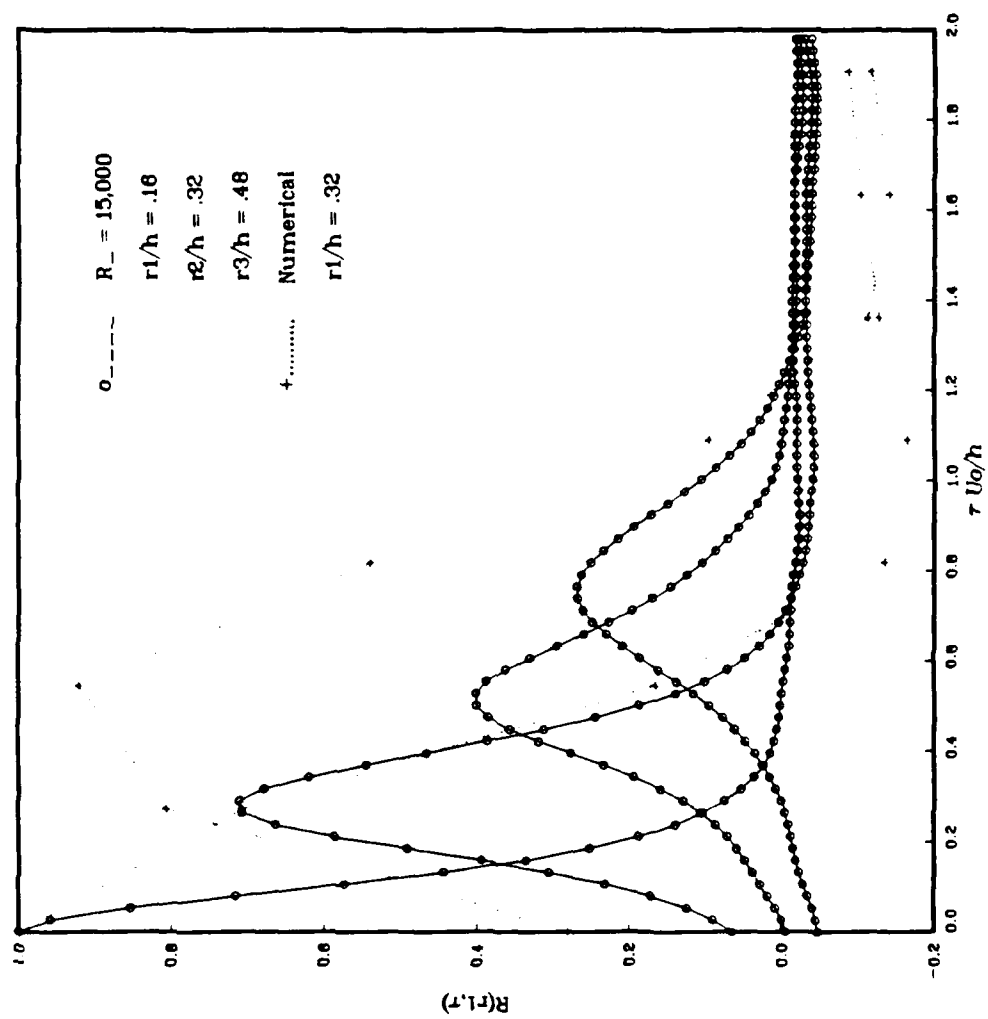


Figure 5.34 Outer Unit Correlation; Computational and Physical Experiments.

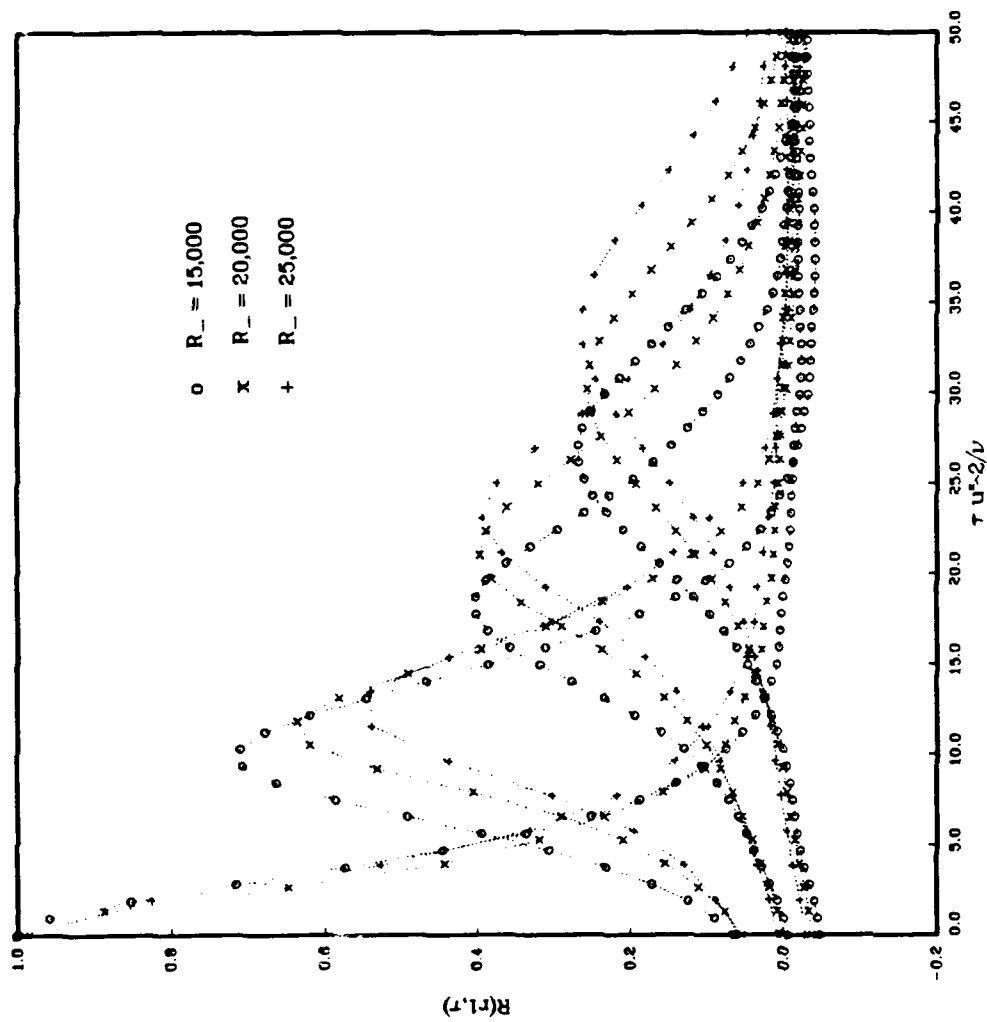


Figure 5.35 Inner Unit Correlation Versus Reynolds Number
for the Physical Experiment.

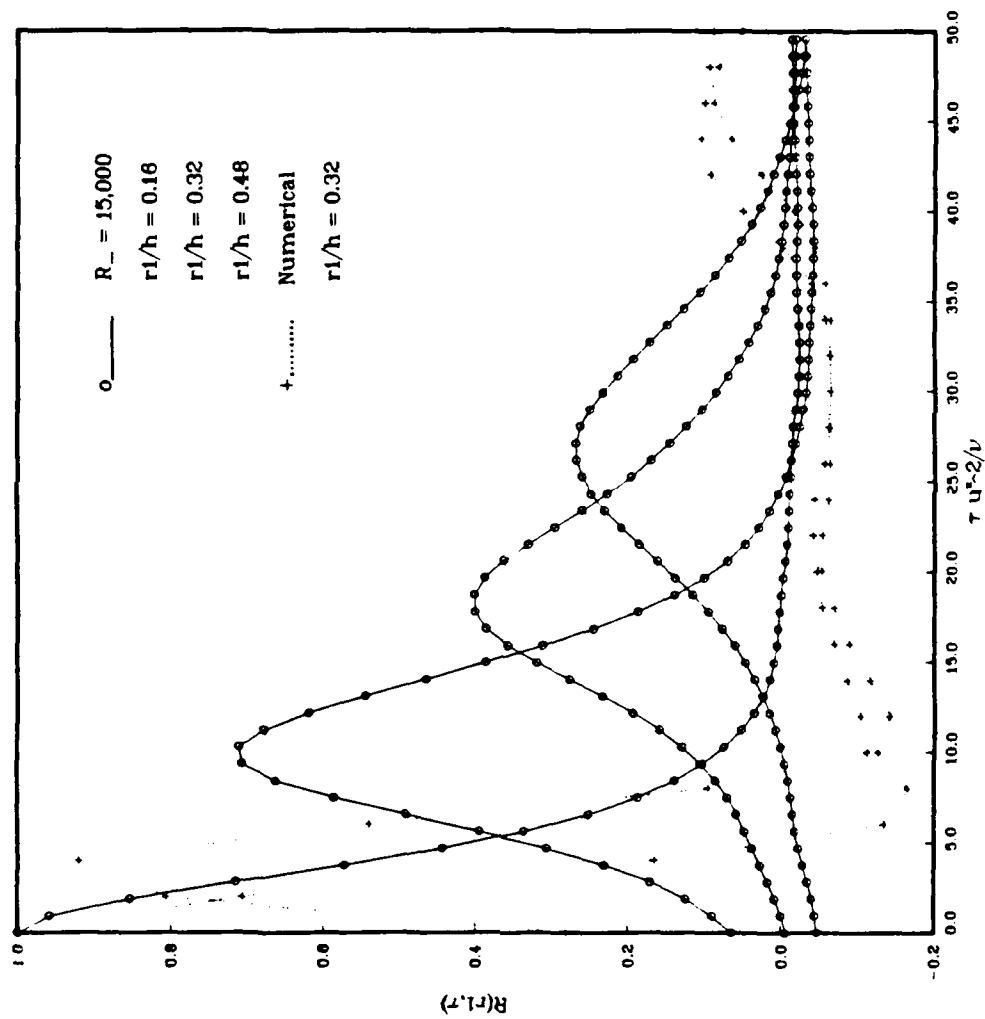


Figure 5.36 Inner Unit Correlation; Computational and Physical Experiments.

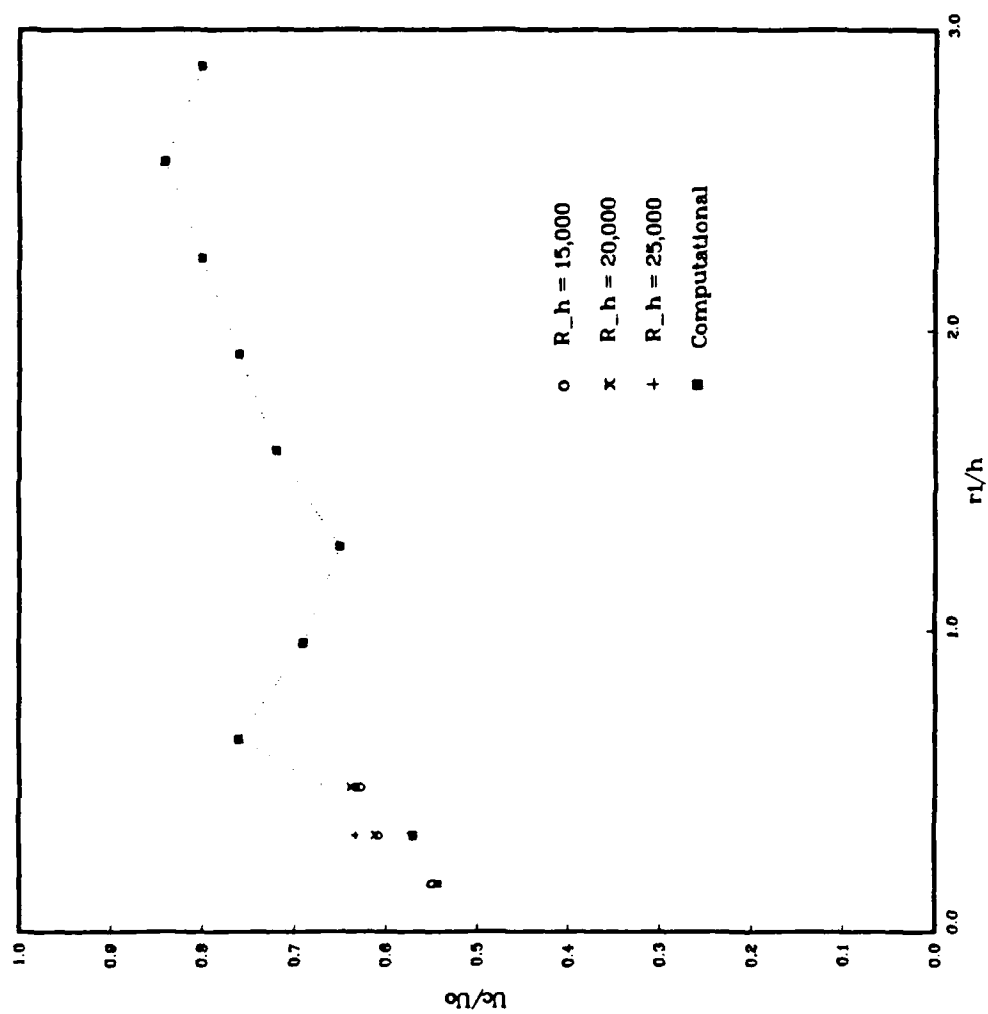


Figure 5.37 Broadband Convection Velocity for Both Experiments.

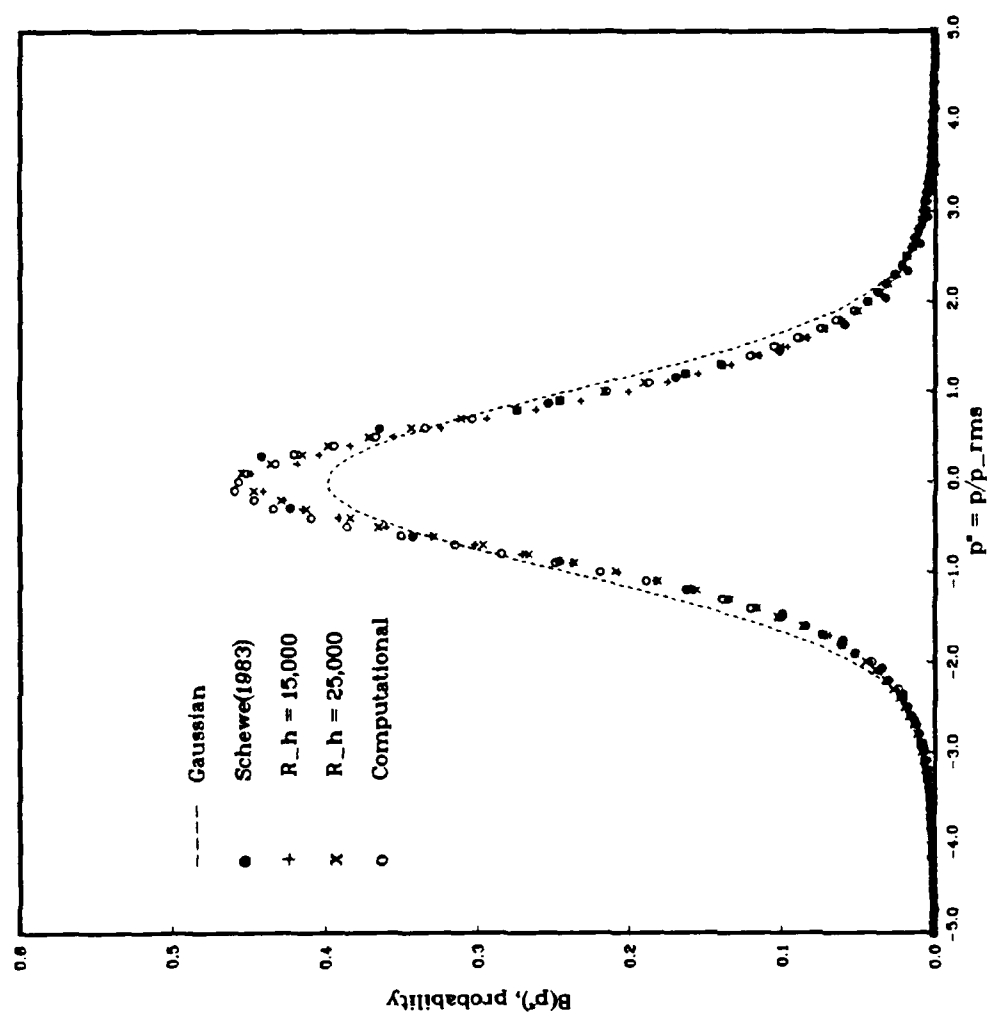


Figure 5.38 Probability Distribution Normalized with rms Pressure.

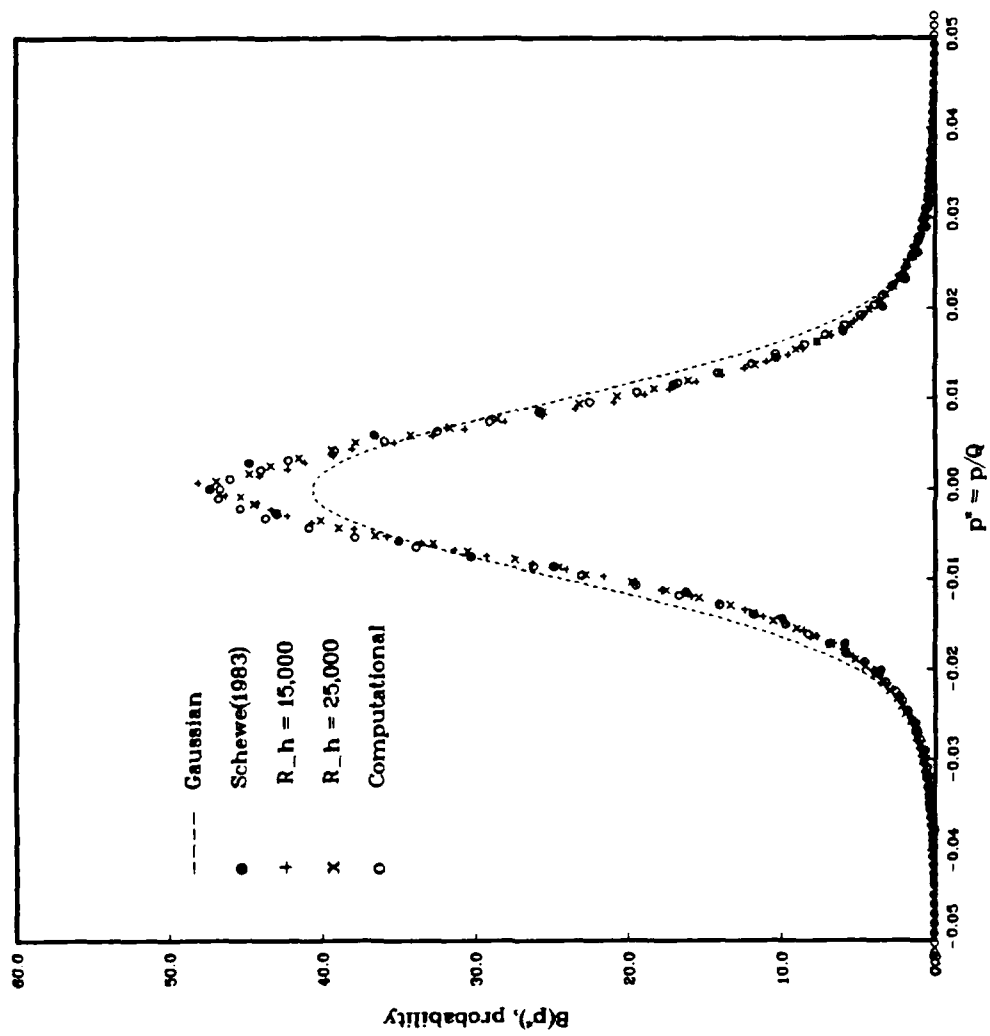


Figure 5.39 Probability Distribution Normalized with Dynamic Head.

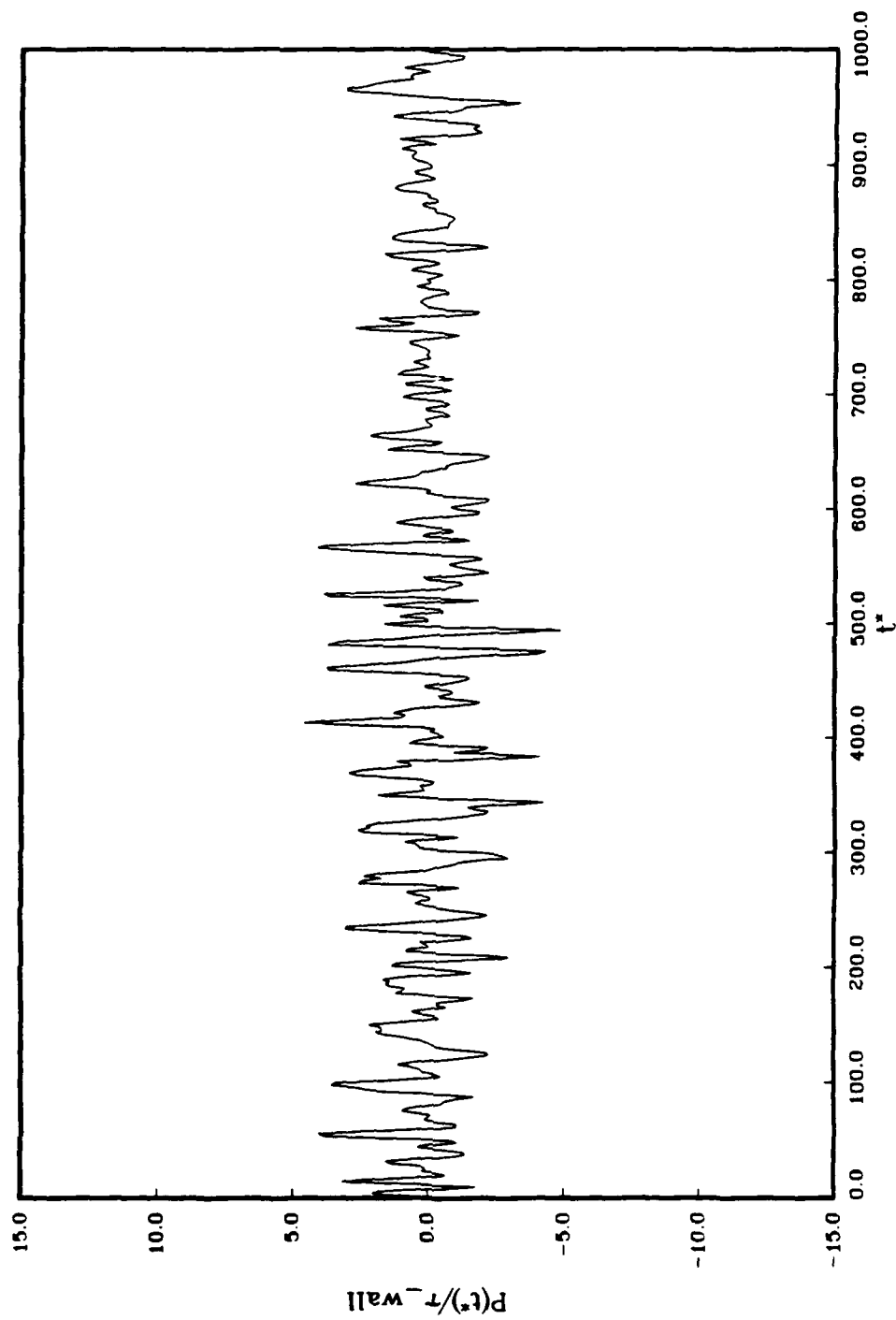


Figure 5.40 Computational Temporal Data at Station 1.

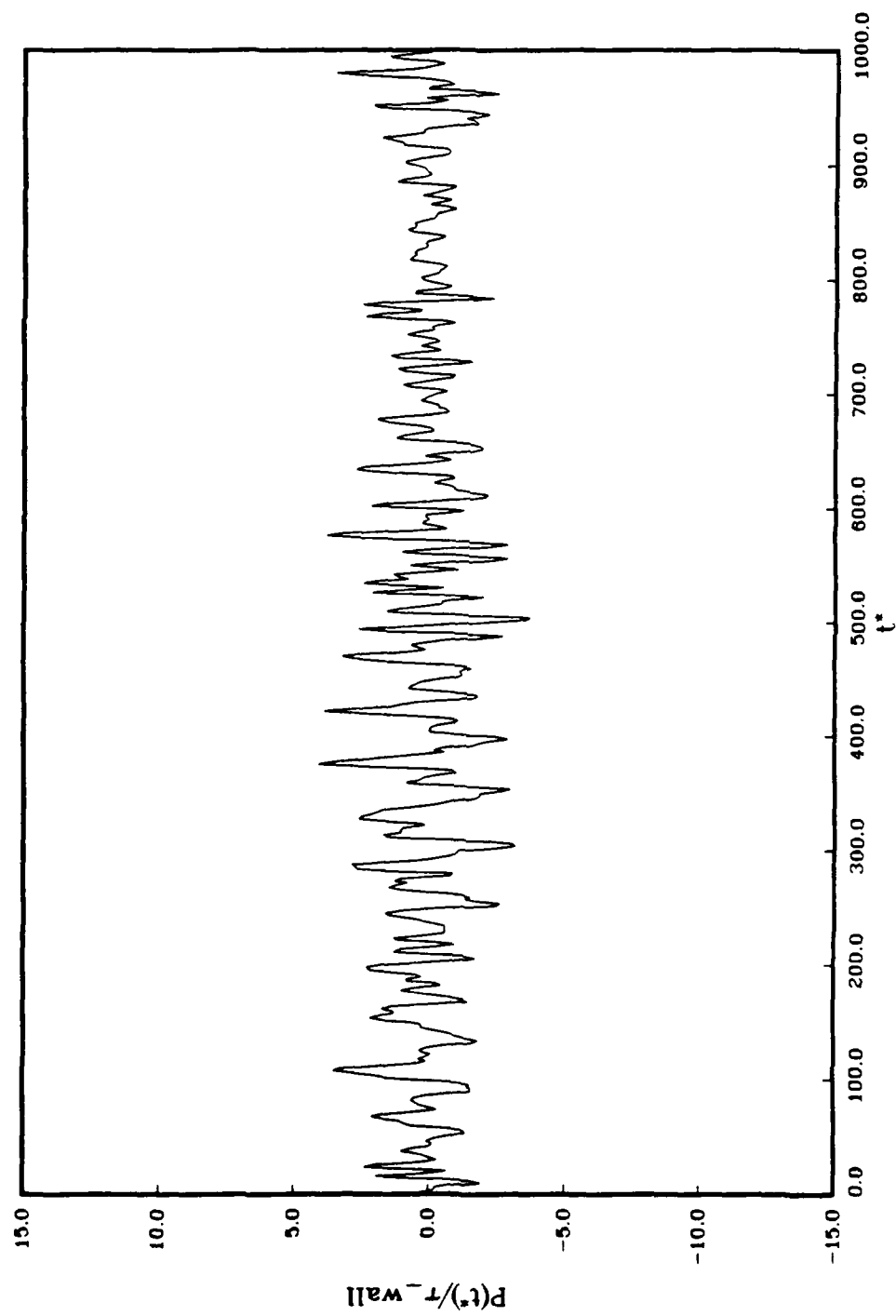


Figure 5.41 Computational Temporal Data at Station 4.

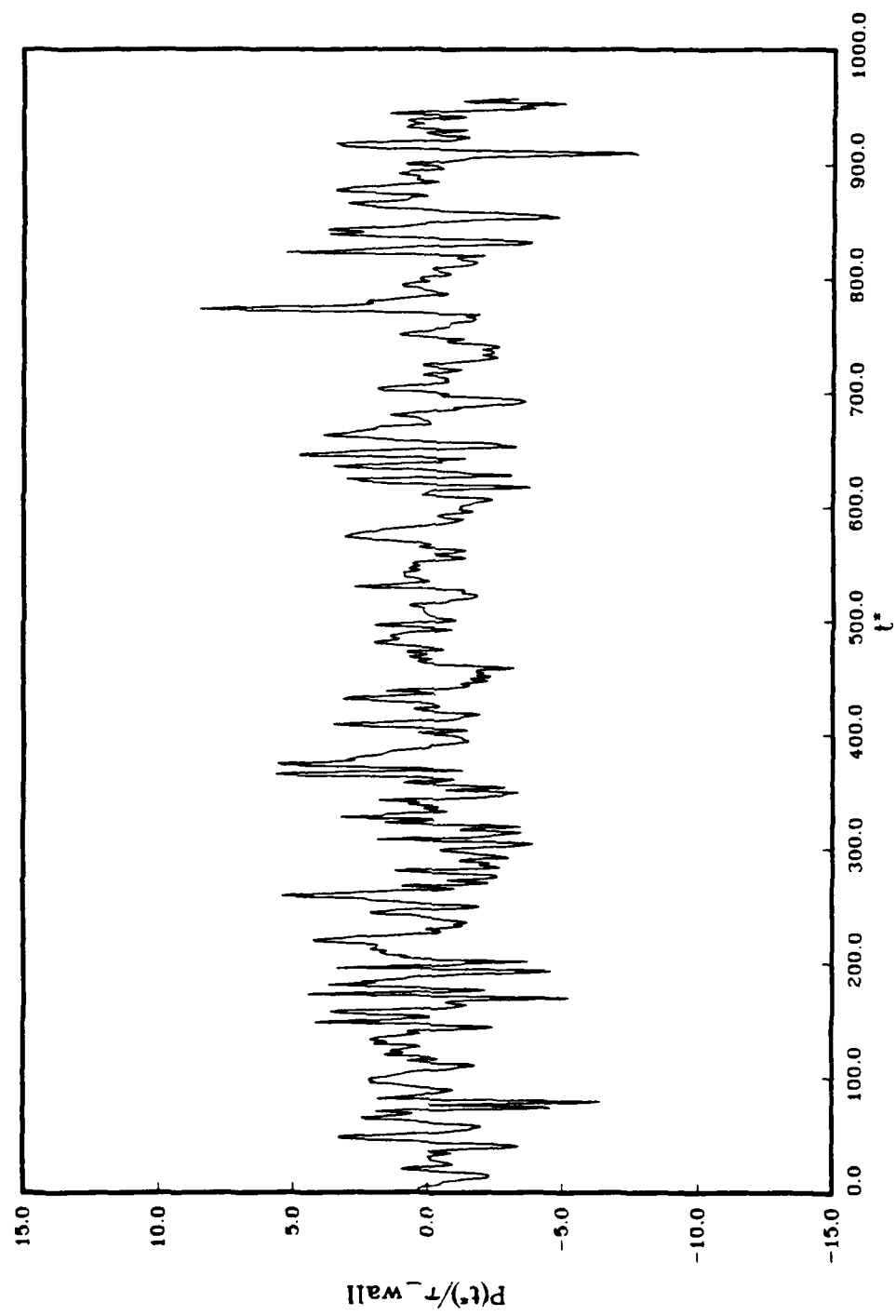


Figure 5.42 Temporal Data at $R_h = 15,000$

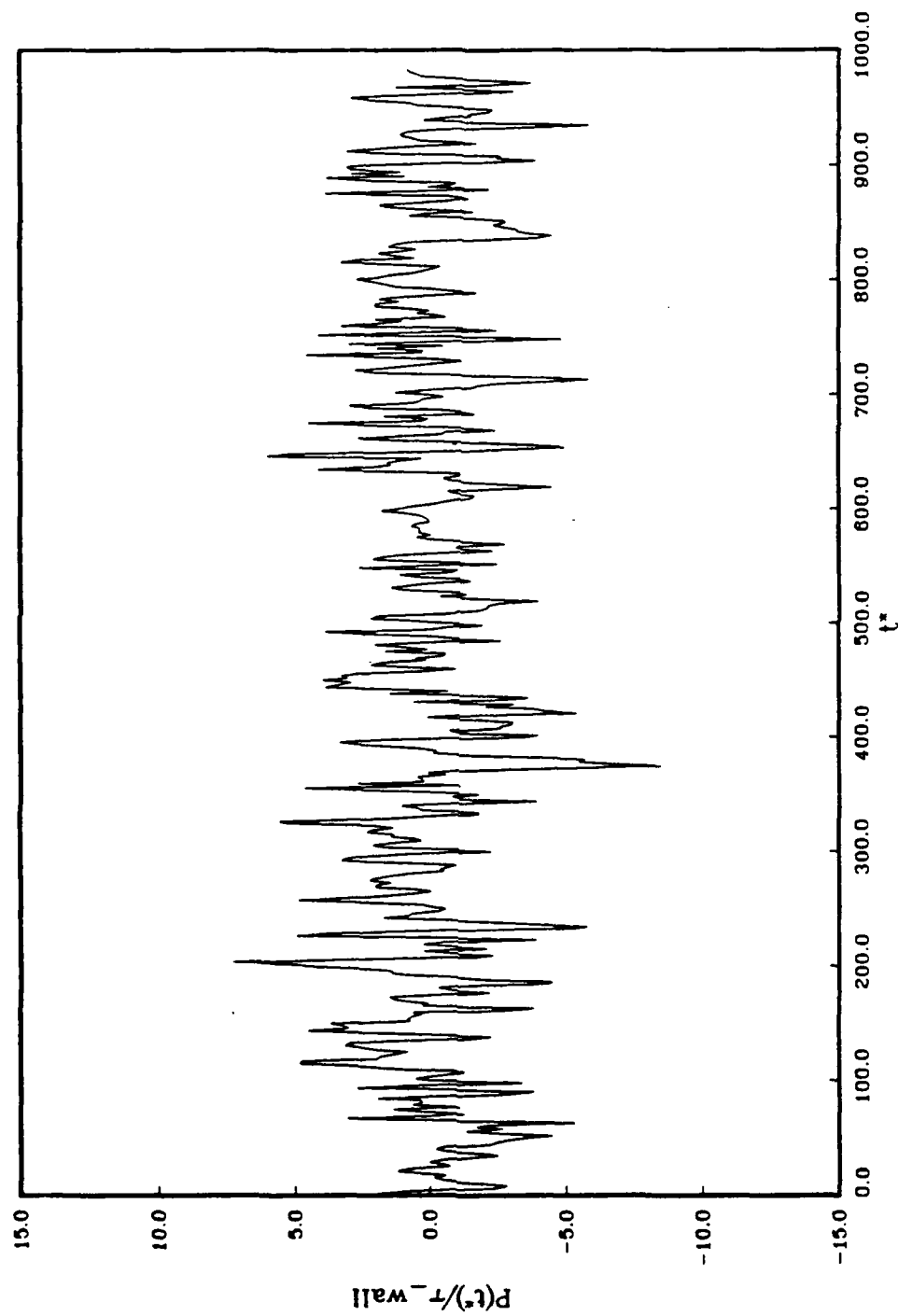


Figure 5.43 Temporal Data at $R_h = 25,000$

CHAPTER 6 SUMMARY AND CONCLUSIONS

6.1 Summary of Accomplishments

Throughout this experimental study, a number of issues of scientific merit have been raised and effort has been focused on addressing these issues. Wall pressure experiments in various flow geometries have been conducted for more than the last three decades and one might well ask "What has been learned?". Why does a characterization of "low Reynolds number" appear to be so important? In relation to pressure in an acoustic sense, has the knowledge gained in recent experiments increased our ability to discriminate against "flow noise"? Questions also have been raised from a more generic standpoint, about "internal flow" versus "external flow". For instance, do unique length, velocity and/or time scales exist for both flow geometries regardless of Reynolds number and do both flow regimes demonstrate similarity scaling? All of the above issues have played significant roles in the design of the present experiment to in some way further a basic understanding of turbulent flows.

Three major reasons can be identified from a practical standpoint to justify the examination of wall pressure fluctuations. First, a wall pressure fluctuation experiment provides a non-intrusive means for examining the fundamental physics of turbulent flows. By making the measurement at the wall, no flow disturbance is created by the introduction of pressure probes within the flow area. Distinct regions of the pressure spectrum can be investigated for scaling laws and/or decay characteristics, as represented by similarity scaling. Certain properties of the space-time correlation function may give insights into characteristic length and time scales of the underlying turbulence. Second, wall pressure fluctuation spectra provide information on fluid/structure interaction. Vibration and sound are generated by coupling phenomena which may lead to damaging fatigue if a resonance condition exists. Third, "flow noise" effects can be examined in relation to surface and sub-surface sonar platforms and towed arrays from the standpoint of contamination and detection liabilities. These issues provided the major motivation for conducting this investigation.

A recent study by Kim (1989) has raised interesting questions about the origins (source terms) of the wall pressure fluctuations. Kim analyzed the results from a DNS calculation at a larger Reynolds number ($R^* = 180$) than that of the present experiment. Decomposing the velocity into mean and fluctuating components, he split the pressure into a "rapid" part containing the mean velocity gradient and a "slow" part containing a product of fluctuating

component gradients. The rapid and slow terms come about by assuming that only the rapid part responds immediately to a change imposed on the mean field, whereas the slow part feels the change through non-linear interactions. Sometimes, the slow part is termed the "return" term because a number of researchers believe this term to be responsible for returning the Reynolds-stress tensor toward local isotropy. Kim found that, contrary to prior experimental work, the slower part was much larger in intensity than the rapid part except very close to the wall ($Y^+ < 15$). Both parts were found to contribute approximately 75 percent of the total *rms* pressure at the wall. In terms of single point frequency spectra, Kim found no distinct differences in length scales associated with the two pressures. Because the rapid part is composed of the mean velocity gradient, one would expect large contributions from the low wavenumbers and so this finding is somewhat surprising. This recent work of Kim, together with the results presented here, suggest the viability of using DNS calculations to further our understanding and interpretation of the fundamental physics of turbulent flows.

The overall objective of this research was to obtain experimentally for the first time, the statistical properties of the wall pressure fluctuations for a generic turbulent flow within a rectangular channel and to directly compare these results with those obtained from a full solution to the Navier-Stokes equations via Direct Numerical Simulation (DNS). For both the physical and computational experiments, serious limitations on the quality of the results had to be identified. For instance, facility generated noise, transducer resolution/sensitivity and Reynolds number effects played primary roles in the determination of whether the physical experiment represented true equilibrium flow conditions. Equilibrium conditions also had to be met in the computational experiment but there were additional constraints inherent in the computational technique employed. In other words, computational accuracy was directly related to the grid resolution, the size of the computational box and the extent in time over which the computation was conducted.

An extensive data base was obtained from the present physical experiment. Profiles for the mean and fluctuating components of the streamwise velocity were obtained at three locations in the spanwise direction for a range of Reynolds numbers $R_h = 5000, 10000, 15000$ and 20000 . Utilizing a new cancellation technique, a complete set of cross-spectral density measurements was obtained for the wall pressure field for Reynolds numbers ranging from $R_h = 10,000$ to $25,000$ and at streamwise separations represented by $\xi_x/h = 0.16$ to 0.48 . All data was stored on magnetic tape, then transferred to and subsequently analyzed on a CRAY super-computer.

The original time-dependent data together with the processed results are stored in CRAY tape files for easy access.

6.2 Major Conclusions

A number of issues were investigated in the process of conducting this research with the following conclusions. First, a careful characterization of what constitutes a generic equilibrium experiment for wall pressure was obtained. It was found that the physical experiment represented a generic channel flow with fully-developed profiles of streamwise mean and fluctuating components of velocity. It was further shown that the small transducers utilized in obtaining the wall pressure spectral properties provided sufficient resolution to adequately resolve all relevant information at the small scales and at high frequencies. Facility-generated noise was effectively eliminated by the application of a new cancellation technique which thereby produced new experimental results at low frequencies within internal flow geometries.

A second issue of importance was related to the physics of the flow through the examination of the fundamental nature of the wall pressure spectrum. A broadband continuous pressure spectrum with no bulges was established for the physical experiment thereby demonstrating an equilibrium channel flow. Scaling laws were shown to collapse the data over specific regions related to the predominant source terms at those respective frequencies. The single point spectra of a channel flow can be related to similar spectra obtained in fully developed pipe flow, provided the length scale used to collapse the data is based on the hydraulic diameter. Both spectra demonstrate maximum spectral levels at $fd_h/U_\infty = 1.0$, where f is the frequency (Hertz), d_h represents the hydraulic diameter, and U_∞ is the centerline mean velocity. An ω^{-2} dependence in the pressure spectrum amplitude was shown to exist at low frequencies, as has been predicted by Patton *et al.* (1980) and Chase (1980). An examination of the streamwise two-point cross-spectral results show that internal flows do exhibit similarity scaling in a manner similar to external flows, wherein an eddy of a specific size decays in a distance proportional to its size. The narrow band convection velocity was shown to approach zero at decreasing frequencies, as first shown by Blake (1970) and more recently substantiated by the extensive experimental work of Farabee (1986).

These two issues represent fundamental concerns to experimentalists, because low Reynolds number data are not well documented and are virtually non-existent for Direct Numerical Simulation channel flow experiments. A third issue representing the primary goal of this

research was to compare directly the results from both experiments. Overall, the results from the computational experiment showed good qualitative agreement with those obtained from the physical experiment. However, the results from the present research demonstrated that specific limitations can be characterized for the results obtained from the DNS experiment. First, the computational results are somewhat underdeveloped for higher order statistical functions. Two possible explanations are that the flow was not developed fully enough in time before recording the data, and that statistical errors were introduced by calculating ensemble averages via a spatial average rather than time averages based on a stationary ergodic process. Second, there were resolution problems at both ends of the frequency spectrum related to the computational technique and the related governing parameters. The small scales at high frequencies were not adequately resolved due to the insufficient size of the computational grid. This cutoff at high frequencies was denoted by the attenuation of spectrum levels for the fine-scale structure, much as has been demonstrated in physical experiments which use pressure transducers with too large a diameter. However, physically large transducers do provide some information (although attenuated), whereas the computational technique acts as a low-pass filter. The large grid spacing apparently results in the rejection of 'all' smaller scale information. Hence, the cut-off in frequency spectra, as demonstrated via inner variable scaling in figure 5.15, is much sharper than for a physical transducer with the same value of d^+ . The size of the computational box in which the simulation was carried out also affects the spectrum levels at low frequencies. As shown in chapter 5, this box size appeared to be too small. The periodic boundary conditions were sensed by the flow and thus represented "noise" peaks in the wall pressure spectrum levels at low frequencies. This interference prevented adequate resolution of the flow at low frequencies and, furthermore, it demonstrated a retardation in the decay characteristics as demonstrated by the results obtained from the physical experiment.

Finally, an issue of lesser importance but of potentially significant scientific merit was the comparison of the wall pressure results from internal flows (as represented by generic channel flows) with the results of typical outer flow regimes, such as flat plate boundary layers. The preponderance of data in the literature is represented by the latter set of experimental flows, at Reynolds numbers more than two orders of magnitude larger than those of the present investigation. It can be argued that these data represent an incorrect data base, when used to critique the accuracy of the results from DNS calculations. The results of the present research show two fundamental characteristics which differentiate external flows from internal flows. Channel flows were shown to decay at approximately twice the decay rate of external flows. Inner/mixed/outer variable scaling was found to collapse the data from both regimes separately,

but no "universal" law was found to exist which brings both internal and external flow regimes into coincidence. This was most noticeable by observing the difference in intensity levels between the spectra of internal flows versus external flows. The pressure gradient represents an "edge" or boundary condition of a flat plate boundary layer flow and, thus is controlled by the outer intermittent flow. There is no derivable relationship which, relates this outer flow phenomenon to shear stress at the wall, whereas within internal flows a direct relationship does exist. Thus, the shear velocity, which is used to define time scales of the smaller structure (locally isotropic) at high frequencies, appears to be coupled to the outer flow region for internal flows. This refutes or supports the hypothesis, depending on one's perspective, that the outer flow of the two flow regimes does not represent similar phenomena, as has been thought in the past.

6.3 Original Contributions and Concluding Remarks

This investigation has provided new information not previously recorded in the literature regarding wall pressure physics related to internal flow geometries. In particular, an extensive data base has been obtained at low Reynolds numbers and may be used to assess the quality of typical Direct Numerical Simulation (DNS) experiments. It must be noted that the data from the computational experiment used in the present study is not the only data base which exists, and certainly not the last which will be obtained. However, a careful examination of the results obtained from the physical experiment should prove useful in determining those specific governing parameters in future DNS experiments which will provide a more accurate data base for comparison.

As a final remark, the original contributions to the literature as obtained in the present research are summarized by the following:

- o A new cancellation technique was used for the first time to effectively eliminate facility-generated noise and thereby substantiate an ω^2 dependence at low frequencies, as shown by theoretical predictions.

- o The full digital analysis technique used to process the data from the physical experiment demonstrates an innovative methodology, not used previously, in the analysis of wall pressure data.
- o Baseline wall pressure data at low Reynolds numbers has been presented for the first time.
- o The comparison of the results from a Direct Numerical Simulation (DNS) experiment with the results obtained from a generic channel flow experiment has been accomplished for the first time.
- o Unique features of internal flows were examined in contrast to external flows and distinct differences were shown to exist.

REFERENCES

- Bakewell, Henry P., *et al.*, "Wall Pressure Correlations in Turbulent Pipe Flow", Naval Underwater Sound Laboratory, USL Report No. 559, 1963.
- Bakewell, H.P., "Turbulent Wall-Pressure Fluctuations on a Body of Revolution", JASA, Vol. 43, No. 6, 1968.
- Blake, William K., "Turbulent Boundary-Layer Wall-Pressure Fluctuations on Smooth and Rough Walls", JFM, Vol. 44, 1970.
- Blake, William K., "Aero-Hydroacoustics for Ships", DTNSRDC report 84/010, Volume I and II, 1984.
- Bendat, J.S., "Statistical Errors in Measurement of Coherence Functions and Input/Output Quantities", J. Sound and Vibration, 59(3), pp.405-421, 1978.
- Bendat, J.S. and Piersol, A.G., Engineering Applications of Correlation Analysis, John Wiley & Sons, 1980.
- Bull, M.K., "Wall-Pressure Fluctuations Associated With Subsonic Turbulent Boundary Layer Flow", JFM, Vol.28, part 4, 1967.
- Chase, D.M., "Modeling the Wavevector-Frequency Spectrum of Turbulent Boundary Layer Wall Pressure", J. Sound Vibration, Vol 70, part 1, 1980.
- Clark, J.A., "A Study of Incompressible Turbulent Boundary Layers in Channel Flow", Journal of Basic Engineering, Trans. ASME, Series D, Vol 90, pp 445-468, 1968.
- Clinch, J.M., "Measurements of the Wall Pressure Field at the Surface a Smooth-Walled Pipe Containing Turbulent Water Flow", J. Sound Vibrations, Vol 9(3), 1969.
- Cooley, J.W. and Tukey, J.W., "An Algorithm for the Machine Calculation of Complex Fourier Series", Mathematics of Computation, Vol. 19, No. 90, p. 297, 1965.
- Corcos, G.M., "On the Resolution of Pressure in Turbulence", JASA, 35, No 2, pp192-199, 1962.
- Corcos, G.M., "The Structure of the Turbulent Pressure Field in Boundary-Layer Flows", JFM, Vol. 18, pp. 353-378, 1963.
- Durst, F., Melling, A. and Whitelaw, J.H., Principles and Practices of Laser-Doppler Anemometry, Academic Press, 1981.
- Emmerling, R., "The Instantaneous Structure of the Wall Pressure Under Turbulent Boundary Layer Flow", Rept. No. 56/1973, Max Planck Institute fur Stromungsforschung, Gottingen, 1973

- Farabee, T.M., "An Experimental Investigation of Wall Pressure Fluctuations Beneath Non-Equilibrium Turbulent Flows", PhD dissertation, The Catholic University of America, 1986.
- Ffowcs-Williams, J.E., "Boundary-Layer Pressures and the Corcos Model: A Development to Incorporate Low-Wavenumber Constraints", JFM, Vol 125, 1982.
- Galib, T.A. and Zandina, A., "Turbulent Pressure Fluctuations With Conventional Piezoelectric and Miniature Piezoresistive Transducers", 108th Meeting of the Acoustical Society of America, Mpls., Minnesota, JASA, Suppl. 1(76), 1984.
- Handler, R.A. *et al.*, "Calculation of the Wall-Pressure Field in a Turbulent Channel Flow", Physics of Fluids, Vol 27(3), p579, 1984.
- Handler, R.A. *et al.*, "The Frequency Spectrum of Turbulent Wall Pressure Fluctuations: Comparison of Simulations With Experiments", J. of Fluids and Structures, Vol 2, p197, 1988.
- Handler, R.A. *et al.*, "Low Reynolds Number Calculation of Turbulent Channel Flow", NRL Mem. Rept. 6410, Naval Research Laboratory, 1989.
- Hansen, R.J. *et al.*, "Prediction of Turbulence-Induced Forces on Structures From Full Numerical Solutions of the Navier-Stokes Equations", J. of Fluids and Structures, Vol 1, p431, 1987.
- Hier, Jen-Yuan, "The Relation Between Wall Pressure and the Flow Field in the Wall Region of a Turbulent Boundary Layer", Ph.D. Dissertation, MIT, 1986.
- Horne, M.P. and Hansen, R.J., "Minimization of the Farfield Acoustic Effects in Turbulent Boundary Layer Wall Pressure Fluctuation Experiments", 1981 Symposium on Turbulence, University of Missouri-Rolla, 1981.
- Horne, M.P. and Handler, R.A., "Single Point Cancellation of Contaminating Noise in the Measurement of Turbulent Wall Pressure Fluctuations", In Publication, 1989.
- Hussain, A.K.M.F. and Reynolds, W.C., "Measurements in Fully Developed Turbulent Channel Flow", Journal of Fluids Engineering, Trans ASME, pp 568-580, 1975.
- Hussain, A.K.M.F., "Coherent Structures—Reality and Myth", Physics of Fluids, Vol 26(10), pp 2816-2849, 1983.
- Jones, O.C., "An Improvement in the Calculation of Turbulent Friction in Rectangular Ducts", J. Fluids Engineering, Trans ASME, pp 173-181, 1976.

- Kim, John. "On the Structure of Pressure Fluctuations in Simulated Turbulent Channel Flow". JFM, Vol. 205, pp. 421-451, 1989.
- Kraichnan ^(a), R.H., "Pressure Field Within Homogeneous Anisotropic Turbulence", JASA, Vol. 28, pp1-64, 1956.
- Kraichnan ^(b), R.H., "Pressure Fluctuations in Turbulent Flow Over a Flat Plate", JASA, Vol. 28, p. 378, 1956.
- Kreplin, H. and Eckelmann, H., "Behavior of the Three Fluctuating Velocity Components in the Wall Region of a Turbulent Channel Flow", Physics of Fluids, Vol 22(7), pp. 1233-1239, 1979.
- Landahl, M.T., "A Wave-Guide Model for Turbulence Shear Flows", JFM, Vol 29, part 3, 1967.
- Laufer, J.L., "Investigation of Turbulent Flow in a Two-Dimensional Channel", NACA report No. 1053, 1951.
- Marcus, P.S., "Simulation of Taylor-Couette Flow. Part 1. Numerical Methods and Comparison With Experiment", JFM, Vol 146, p45, 1984.
- Morrison, W.R.B. and Kronauer, R.E., "Structural Similarity for Fully Developed Turbulence in Smooth Tubes", JFM, Vol. 39, 1969.
- Orszag, S.A. and Patterson, G.S., "Numerical Simulation of Three-Dimensional Homogenous Isotropic Turbulence", Phys. Review Letters, Vol 28, p76, 1972.
- Orszag, S.A. and Kells, L.C., "Transition to Turbulence in Plane Poiseuille and Plane Couette Flow", JFM, Vol 96, p159, 1980.
- Orszag, S.A. and Patera, A.T., "Subcritical Transition to Turbulence in Plane Channel Flow", Phys. Rev. Letters, Vol 45, p989, 1980.
- Panton, R.L. and Linebarger, J.H., "Wall Pressure Spectra Calculations for Equilibrium Boundary Layers", JFM, Vol 65, part 2, 1974.
- Panton, R.L., *et al.*, "Low-Frequency Pressure Fluctuations in Axisymmetric Turbulent Boundary Layers", JFM, Vol. 97, 1980.
- Reynolds, O., Phil. Trans. R. Soc., ser. A, Vol. 186, pp. 123-164, 1895.
- Reynolds, W.C., "The Potential and Limitations of Direct and Large Eddy Simulations", Position paper, Whither Turbulence conference, Cornell University, 1989.

- Rogallo, R.S. and Moin, P., "Numerical Simulations of Turbulent Flows", Annual Review of Fluid Mechanics, pp99-138, 1984.
- Schewe, Gunter, "On the Structure and Resolution of Wall-Pressure Fluctuations Associated With Turbulent Boundary-Layer Flow", JFM, Vol.134, 1983.
- Schlichting, H., Boundary-Layer Theory, McGraw-Hill, New York, 1955.
- Schloemer, Howard H., "Effects of Pressure Gradients on Turbulent-Boundary Layer Wall-Pressure Fluctuations", JASA, Vol.42, No. 1, 1966.
- Schumann, U. and Friedrich, R., "On Direct and Large Eddy Simulation of Turbulence", Advances in Turbulence, Springer-Verlag, pp 88-104, 1987.
- Spalding, D.B., Journal of Applied Mechanics, Vol. 28, pp. 455-457, 1961.
- Taylor, G.I., Proc. Roy. Soc., London, 164A, pp.476, 1938.
- Tennekes, H. and Lumley, J.L., A First Course in Turbulence, MIT press, Mass., 1972.
- Townsend, A.A., The Structure of Turbulent Shear Flow, Camb. Univ. Press, Cambridge, 1956.
- TSI, "System 9100-10 5 Beam, 3 Component Laser Doppler Velocimeter Instruction Manual", TSI Incorporated, St. Paul Minnesota, 1985.
- Wambsganss, M.W. and Zaleski, P.L., "Measurement Interpretation and Characterization of Nearfield Flow Noise", ANL-7685, 1970.
- Wiener, N., Extrapolation, Interpolation and Smoothing of Stationary Time Series, With Engineering Applications, Wiley, New York, 1949.
- Willmarth, W.W., "Space-Time Correlations and Spectra of Wall Pressure in a Turbulent Boundary Layer", NASA-report #3-17-59W, March 1959.
- Willmarth, W.W. and Wooldridge, C.E., "Measurements of the Fluctuating Pressure at the Wall Beneath a Thick Turbulent Boundary Layer", JFM, Vol. 14, pp. 187-210, 1962.
- Willmarth, W.W. and Roos, F.W., "Resolution and Structure of the Wall Pressure Field Beneath a Turbulent Boundary Layer", JFM, Vol.22 part I, pp 81-94, 1965.
- Willmarth, W.W. and Yang, C.S., "Wall-Pressure Fluctuations Beneath Turbulent Boundary Layers on a Flat Plate and a Cylinder", JFM, Vol. 41, part 1, 1970.

Willmarth, W.W., "Pressure Fluctuations Beneath Turbulent Boundary Layers", Annual Review of Fluid Mechanics, No 7, 1975.

Wills, J.A.B., "Measurements of the Wave-Number/Phase Velocity Spectrum of Wall Pressure Beneath a Turbulent Boundary Layer", JFM, Vol. 45, part 1, 1970.

Wilson, R.J., Jones, B.G. and Roy, R.P., "Measurement Techniques of Stochastic Pressure in Annular Flow", Sixth biennial Symposium on Turbulence, University of Missouri-Rolla, October 1979.